From biogenesis to synaptic organization : developing tools to study AMPAR-associated proteins

Diogo António Bessa Neto

To cite this version:

Diogo António Bessa Neto. From biogenesis to synaptic organization : developing tools to study AMPAR-associated proteins. Neurons and Cognition [q-bio.NC]. Université de Bordeaux, 2021. English. NNT : 2021BORD0314 . tel-03562221

HAL Id: tel-03562221
https://theses.hal.science/tel-03562221

Submitted on 8 Feb 2022

THÈSE PRÉSENTÉE

POUR OBTENIR LE GRADE DE

DOCTEUR DE
L'UNIVERSITÉ DE BORDEAUX

ÉCOLE DOCTORALE DES SCIENCES DE LA VIE ET DE LA SANTE

SPÉCIALITÉ NEUROSCIENCES

Par Diogo António BESSA NETO

From biogenesis to synaptic organization: developing tools to study AMPAR-associated proteins

Sous la direction de : Dr. Daniel CHOQUET

Soutenue le 6 Décembre 2021

Membres du jury :

Daniel CHOQUET	Directeur de recherche	Université de Bordeaux	Directeur de thèse
Eric BOUÉ-GRABOT	Directeur de recherche	Université de Bordeaux	Président
Ana Luísa CARVALHO	Professeure associée	Universidade de Coimbra	Rapporteur
Pierre PAOLETTI	Directeur de recherche	Ecole Normale Supérieure	Rapporteur
Ivana NIKIĆ-SPIEGEL	Chargée de recherche	Eberhard Karls Universität Tübingen	Examinateur
Markus SAUER	Professeur	Julius-Maximilians-Universität Würzburg	Invité

Interdisciplinary Institute for Neuroscience (IINS)
CNRS UMR 5297
Université de Bordeaux
Centre Broca Nouvelle-Aquitaine
146 rue Léo Saignat
33076 Bordeaux (France)

De la biogénèse à l'organisation synaptique: mise au point d'outils pour étudier les protéines auxiliaires des AMPAR

Résumé

Dans le système nerveux central, la transmission synaptique excitatrice rapide est principalement médiée par les récepteurs de l'acide α-amino-3-hydroxy-5-méthyl-4-isoxazolepropionique (AMPAR). Les AMPAR sont des récepteurs homo ou hétéro tétramériques assemblés à partir de combinaisons de quatre sous-unités, GluA1-4 qui forment un pore. Celui-ci s'assemble en un complexe macromoléculaire avec plusieurs protéines structurellement non apparentées, les protéines auxiliaires des AMPAR. Plus de 30 protéines auxiliaires différentes ont été identifiées. Celles-ci exercent un large éventail de fonctions sur le récepteur : stabilisation, exportation du réticulum endoplasmique (ER), trafic, ancrage synaptique, modulation du canal. Malgré leur importance pour le bon fonctionnement des récepteurs et, par conséquent, pour la transmission synaptique, leurs fonctions restent mal connues. Le principal facteur limitant a été le manque d'outils, soit pour visualiser directement la protéine cible sans compromettre sa fonction, soit pour étudier directement la dynamique de son interaction avec le récepteur dans des cellules vivantes.

La protéine ferric-chelate reductase 1-like (FRRS1l) a été désignée comme un acteur clé au cours des premières étapes de la biogenèse des AMPAR, mais les mécanismes à l'origine de ce rôle putatif étaient inconnus. Récemment, il a été montré que FRRS1l, parmi d'autres protéines interagissant avec l'ER, participe aux différentes étapes de l'assemblage des AMPAR. Cependant, la dynamique de ce processus est inconnue.

D'autre part, la famille des protéines régulatrices transmembranaires d'AMPAR (TARP) a été découverte au début des années 2000 et a été identifiée comme le médiateur clé du trafic des AMPAR et de la régulation de leurs propriétés biophysiques. Malgré les nombreux travaux réalisés, il manque encore des outils permettant d'étudier et de visualiser les TARP de surface sans compromettre et déstabiliser leur interaction avec les AMPAR. De plus, l'un des plus grands débats autour des sous-unités auxiliaires (en particulier les TARP), est de savoir si les sous-unités auxiliaires se dissocient ou non des complexes AMPAR à la membrane plasmique. Cette question est particulièrement importante car la dissociation des sous-unités auxiliaires pourrait potentiellement conduire à la réorganisation des complexes macromoléculaires des AMPAR, et ainsi façonner la transmission médiée par les AMPAR.

L'objectif général de ma thèse était de développer de nouveaux outils pour étudier la dynamique des AMPAR et des protéines interagissant avec les AMPAR, en particulier la protéine FRRS1l et les TARP $\gamma 2$ et $\gamma 8$. Tout d'abord, je discuterai des stratégies que j'ai adoptées pour dévoiler le rôle de FRRS1l au cours des premières étapes de la biogenèse des AMPAR. En particulier, je rapporte le développement de nouveaux outils pour étudier l'interaction entre les AMPAR et FRRS1l en utilisant le transfert d'énergie par résonance de Förster (FRET) basé sur la microscopie d'imagerie par fluorescence (FLIM). Mes résultats montrent que non seulement les AMPAR et FRRS1l interagissent directement dans les cellules vivantes, mais aussi que la carnitine palmitoyltransferase 1c (CPT1c), protéine résidant dans l’ER, coopère et améliore l'assemblage de FRRS1l et des AMPAR, comme cela a été suggéré précédemment. Deuxièmement, j’ai développé un nouvel outil pour marquer les TARP de surface dans les neurones vivants en utilisant la combinaison de l'expansion du code génétique avec le marquage par clic. Grâce à cet outil, nous avons pu démontrer l'organisation différentielle de surface de γ2 et γ8 à la fois dans des neurones hippocampiques dissociés et dans des cultures de tranches d'hippocampe. De plus, en utilisant la microscopie à super-résolution, nous avons démontré que γ2, mais pas γ8, est organisé en nanodomaines dans les synapses, comme précédemment rapporté pour les AMPARs.

Mots clés: récepteurs AMPA (AMPAR), sous-unités auxiliaires, Förster énergie de résonance de transfert (FRET) microscopie, expansion du code génétique, chimie-click, super-resolution microscopy

From biogenesis to synaptic organization: developing tools to study AMPAR-associated proteins

Abstract

In the central nervous system, fast excitatory synaptic transmission is mainly mediated by α-amino-3-hydroxy-5-methyl-4-isoxazolepropionic acid receptors (AMPAR). AMPAR are homo-tetrameric or hetero-tetrameric receptors assembled from different combinations of four core subunits, GluA1-4. These pore-forming subunits then form a macromolecular complex with several structurally unrelated proteins, the AMPAR-auxiliary proteins. To date, more than 30 different auxiliary proteins have been identified. Those are known to exert a wide range of functions on the receptor: from receptor stabilization, endoplasmic reticulum (ER)-export, trafficking, synaptic anchoring, to channel gating modulation. Despite their relevance to proper receptor function and consequently to synaptic transmission, there is still a vast lack of knowledge on their function. So far, the major limiting factor that has hampered these types of studies has been the lack of tools, either to directly visualize the target protein without compromising their function or to directly study the dynamics of their interaction with the receptor in living cells.

The ferric-chelate reductase 1-like protein (FRRS1l) was identified as a key player during the early steps of AMPAR biogenesis, but the mechanisms behind its putative role were unknown. More recently, FRRS1l among other ER-interacting proteins has been shown to mediate different stages of AMPAR assembly. However, the dynamics of this process are unknown.

On the other hand, the transmembrane AMPAR regulatory proteins (TARP) family was discovered in the early 2000s and was identified as the key mediator of AMPAR trafficking and channel gating. Despite the extensive work done, there is still a lack of tools to allow the study and visualization of surface TARPs without compromising and destabilizing their interaction with AMPARs. Moreover, one of the biggest debates around auxiliary subunits (in particular TARPs), is whether auxiliary subunits dissociate or not from AMPAR complexes at the plasma membrane. This is of particular importance as dissociation of auxiliary subunits could potentially lead to the rearrangement of the AMPAR macromolecular complexes, and thus shape AMPAR-mediated transmission.

The overall goal of my PhD has been to develop new tools to study the dynamics of AMPAR and AMPAR-interacting proteins, in particular, the ER-interacting protein FRRS1l and the auxiliary subunits TARP $\gamma 2$ and $\gamma 8$. First, I will discuss the strategies I took to unveil the role of FRRS1l during the early steps of the AMPAR biogenesis. In particular, I report the development of new tools to study the interaction between AMPARs and FRRS1l using fluorescence-lifetime imaging microscopy (FLIM)-based Förster resonance energy transfer (FRET). The results here presented show that not only AMPAR and FRRS1l directly interact in living cells, as well as, the ER-resident protein carnitine palmitoyltransferase 1c (CPT1c) cooperates and enhances FRRS1l and AMPAR assembly, as previously suggested. Second, I developed a new tool to label surface TARPs in living neurons using the combination of genetic code expansion with click-labeling. Using this tool, we were able to demonstrate the differential surface organization of γ2 and γ8 both in dissociated hippocampal neurons and hippocampal slice cultures. Moreover, using super-resolution microscopy, we demonstrate that γ2, but not γ8, is organize in nanocluster within the synapses, as previously reported for AMPARs.

Keywords: AMPA receptors (AMPAR), auxiliary subunits, Förster resonance energy transfer (FRET) microscopy, click-chemistry, genetic code expansion, super-resolution microscopy

List of abbreviations

aaRS	Aminoacyltransferase
AMPAR	α-amino-3-hydroxy-5-methyl-isoxazole-propionic acid receptor
ATD	Amino-terminal domain
bAP	Biotin-acceptor peptide
BN-PAGE	Blue native polyacrylamide gel electrophoresis
CA	Cornu Ammonis
CaMKII	Calcium/calmodulin-dependent protein kinase II a
CKAMP	Cysteine-knot AMPAR modulating protein
CNIH	Cornichon
COPII	Coat protein complex II
CPT1c	Carnitine palmitoyltransferase 1c
CTD	Carboxyl-terminal domain
***d*STORM**	Direct stochastic optical reconstruction microscopy
e.v.	Empty vector
ECD	Extracellular domains
ECH	Extracellular helix
eGFP	Enhanced GFP
ER	Endoplasmic reticulum
ERAD	ER-associated protein degradation
Ex1	Extracellular loops 1
Ex2	Extracellular loops 2
FLIM	Fluorescence lifetime imaging microscopy
FP	Fluorescent protein
FRET	Förster resonance energy transfer
FRRS1l	Ferric-chelate reductase 1-like
GABA	γ-aminobutyric acid
GCE	Genetic code expansion
Glu	Glutamate
GSG1l	Germ cell-specific gene 1-like protein
HA	Hemagglutinin
iGluRs	Ionotropic glutamate receptors
KAR	Kainate receptor
LBD	Ligand-binding domain
LTD	Long-term depression
LTP	Long-term potentiation
MAGUK	Membrane-associated guanylate kinase
MAPK	Mitogen-activated protein kinase
mGluR	Metabotropic glutamate receptor

msfGFP	Monomeric superfolder GFP
ncAA	Non-canonical amino acid
NHEJ	Non-homologous end joining
NMDAR	N-methyl-D-aspartate receptor
OHSC	Organotypic hippocampal slice culture
PF	Parallel fiber
PICK1	Protein interacting with C-kinase 1
PKA	Protein kinase A
PKC	Protein kinase C
PORCN	Porcupine O-acyltransferase
PP1	Protein phosphatase 1
PP2B	Protein phosphatase-2B
PRRT1	Proline-rich transmembrane protein 1
PSD	Postsynaptic density
PylRS	Pyrrolysine aminoacyl tRNA synthetase
SCC	Schaffer collateral/commissural
SCE	Single-cell electroporation
SMLM	Single-molecule localization microscopy
SPIEDAC	Strain-promoted inverse electron-demand Diels-Alder cycloaddition reaction
SynDIG4	Synapse differentiation-induced gene 4
TARP	Transmembrane AMPAR regulatory protein
TCO	Trans-cyclooct-2-ene
TCO*A	TCO*-L-lysine
TKIT	Targeted Knock-In with Two
TMD	Transmembrane domain
WT	Wild-type

List of figures

Table of contents

Introduction

1. From the reticular theory to the existence of synapses – a historical perspective

Science is usually seen as a synonym of progress, but one cannot talk about science without mentioning controversies. Indeed, controversy can be seen as one of the foundations of science and progress. Together with the intrinsic Human curiosity, the eagerness to prove oneself believes right has led to major discoveries and paradigm shifts throughout Human history. Perhaps the most controversial and far-reaching theory was the Copernican heliocentrism model, with the Sun at the center of the Solar system, put forward by Nicolaus Copernicus in his seminal work *De revolutionibus orbium coelestium* in 1543. The theory was later perfected by the work of others, including Johannes Kepler, Galileo Galilei and, Sir Isaac Newton. But it was not until the middle of the 17th century that the majority of the scientific community accepted the Copernican theory and, not until the late 18th century that it was accepted among the public[1].

Neuroscience, as it is called nowadays, also had its share of controversies, of which major paradigm shifts led to progress. Constrained by rudimentary imaging techniques, the central nervous system was initially seen as a continuum network of specialized cells, the so-called reticular theory first postulated by Joseph von Gerlach in 1871[2]. In 1873, Camillo Golgi developed a new staining technique, the '*reazione near*' (black reaction)[3], popularly known as Golgi's stain. A game-changing technique that was about to divide the scientific community in two. Golgi, a vivid supporter of the reticular theory, demonstrated using his newly developed technique that dendrites, or protoplasmic arborizations as named at the time, ended freely rather than subdividing indefinitely as suggested in Gerlach's theory. While rejecting the existence of anastomoses in the dendrites, Golgi describes axons as an interconnected structure that gives rise to a large number of ramifications, that he describes as a 'diffuse nervous network'[4,5]. Later, using an improved version of Golgi's staining technique, Santiago Ramón y Cajal not only corroborated Golgi's observations on dendrites ending freely, as he reported that the distal dendritic branches of Purkinje cells were decorated with '*espinas*', introducing the term of dendritic spines (Figure 1a). However, contrary to Golgi, Ramón y Cajal observed that similarly to dendrites, axons also ended freely[6], suggesting that nerve cells were independent cells in contiguity rather than continuity[7,8]. This view of the central nervous system as individual cells led to the formulation of the neuron doctrine, a term introduced and popularized by Heinrich Wilhelm Gottfried von Walderyer-Hartz[9], who also coined the term neuron to refer to nerve cells[7].

In the view of the neuron doctrine, Ramón y Cajal[10] and Arthur van Gehuchten[11] attempted to postulate how nerve impulses, the action potentials, were passed from neuron to neuron. They speculated that the propagation of nerve impulses occurred exclusively from terminal bulbs to dendrites, occasionally soma, and then from soma to axons. In other words, that the transmission was unidirectional from dendrites to soma and soma to axons, which led to the formulation of the law of dynamic polarization. However, as often occurs in biology, a rigid and inflexible hypothesis tends to be wrong, and the law of dynamic polarization as it was later demonstrated by Charles Scott Sherrington was not an exception. In 1897, Sherrington demonstrated that in the central nervous system of mammals, axons possess the ability to conduct nerve impulses both ways contrary to the postulate by Ramón y Cajal[12]. He further showed that the unidirectionality of nerve impulses from neuron A to a neuron B observed in normally functioning nervous system for a given space and time are not due to axon physical properties, but rather due to a valve-like structure in the axon terminals[13], later termed synapse[14].

Over 50 years after Sherrington coined the term synapses, the first series of morphological proof of the existence of synapses arrived with the recently developed electron microscope[15]. Moreover, electron microscopy allowed to prove synapses are a morphological entity rather than only a physiological entity, as provided by the identification of synaptic vesicles; granular/vesicular elements restricted to the presynaptic terminals[16-19] (Figure 1b,c). The neuron doctrine was now validated. The understanding of the nervous system as a network of individual cells, where nerve impulses are transmitted through synapses – from the terminals of the presynaptic neuron to a postsynaptic cell separated by a thin gap, the synaptic cleft. The reticular theory had now been set aside and, a new chapter in the light of neuronal doctrine had just emerged, the synaptic transmission era.

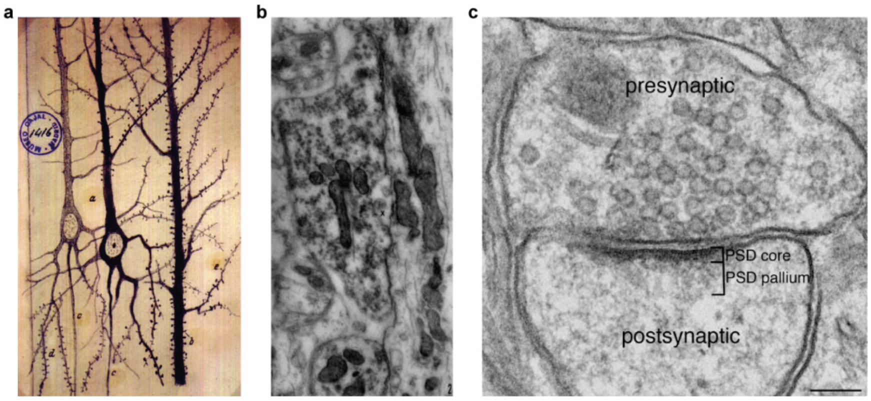

Figure 1: Synapses, from a concept to a morphological entity. (**a**) Drawing of spines on cortical cells stained using methylene blue-stained pyramidal cortical cells by Ramón y Cajal. Adapted from Glickstein (2006)[7]. (**b**) Early electron microscopy image of central synapses in rodent brain. On the left side it is possible to observe a presynaptic terminal containing synaptic vesicles and mitochondria. On the right side, a dendrite containing endoplasmic reticulum and mitochondria. Adapted from Palay (1956)[19]. (**c**) Modern electron microscopy image of excitatory glutamatergic synapses showing the synaptic vesicles at the presynaptic site, and the prominent electron-dense zone next to the postsynaptic membrane, the postsynaptic density (PSD). Adapted from Dosemeci, et al. (2016)[20].

2. Connecting the dots: an overview of synaptic transmission

The beginning of the 20th century marks a new chapter in the field of neuroscience and, as History dictates, a fierce and three-decade debate, 'the War of Soups and Sparks'[21]. The dispute between the nature of synaptic transmission: electric versus chemical. Why not both? After a couple of turns of events that made the scale tip in favour of the existence of one type of synapses over the other, the existence of both types of synapses is now accepted.

Known by their fast synchronous synaptic transmission, in the electrical synapse the pre- and postsynaptic membranes of adjacent cells are directly connected by specialized intracellular channels, the gap junctions (see also ref. [22,23]). On the other hand, in the chemical synapses, the information is transmitted from the presynaptic cell with the release of a certain class of molecules (neurotransmitters) into the synaptic cleft which in turn is detected by the postsynaptic cell. While this classic view of synapses as the preferential way of communication between neurons is well accepted, it is worth mentioning the ability of neuronal cells, including neurons, to communicate through alternative mechanisms. Of those, the ability to generate electrical fields capable of influencing the excitability of surrounding neurons[24] or, the diffusion of neurotransmitters into the extracellular space, a process known as volume transmission, which is temporally slower and anatomically broader in reach[25,26].

Given that in our team we are particularly interested in chemical synapses, more precisely glutamatergic synapses, I will exclusively introduce the topics that are related to these synapses, and that best portray the work presented here.

2.1 Chemical synapses

The electron microscopy data gathered in the early 1950s was the icing on the cake, the proof of the existence of chemical synapses. Nonetheless, the first pieces of evidence of the existence of chemical transmission came right after the introduction of the concept of synapses by Sherrington in 1897. The first pieces of evidence arrived by the hands of Thomas Renton Elliott, who in 1904 presumptively discovered the action of epinephrine as a neurotransmitter in the sympathetic nervous system[27], then Henry Hallett Dale in 1914 who postulated acetylcholine as a neurotransmitter in the parasympathetic nervous system[28]. And, later, in 1921 Otto Loewi after stimulating the frog's vagus nerve collected the fluid and used it in a dissected heart without the vagus nerve, which made the heart slow down as observed upon vagus stimulation[29]. A simple and elegant experiment with which Loewi was able to convince everybody of the existence of chemical transmission. Over the following years, several molecules have been identified as neurotransmitters: amino acids (glutamate (Glu), aspartate, D-serine, γ-aminobutyric acid (GABA), glycine, etc), monoamines (epinephrine, norepinephrine, dopamine, histidine, serotonin), acetylcholine, peptides, purines (adenosine triphosphate – ATP), endocanabinoides, peptides, gases, and acetylcholine among others[30].

Once released into the extracellular space (including synaptic cleft), neurotransmitters bind to membrane-bound receptors at the surface of the target cells, thereby initiating or inhibiting cellular functions. This concept of receptors as proteins that bind to drugs or neurotransmitters onto the cell, thus triggering or inhibiting cellular functions was initially proposed by John Newport Langley in 1905, which at the time named receptors as 'receptive substances'[31,32], whereas the term receptor was earlier introduced by Paul Ehrlich in 1900 in the context of immunology[32].

2.2 Glutamatergic synapses

Glutamatergic synapses are a class of excitatory synapses involved in the majority of synaptic transmission in the central nervous system with the neurotransmitter Glu as a catalyst. Here, the main protagonists are the glutamate receptors, a class of receptors accumulated at the postsynaptic cell responsive to Glu (and also present on the pre-synapse to regulate transmitter release). Since the cloning of the first glutamate receptor in late 1989 by Hollmann and colleagues[33], more than a dozen have been identified and are now categorized in two main types, the ionotropic (iGluRs) and metabotropic glutamate receptors (mGluRs) (Figure 2).

iGluRs are ligand-gated ion channels composed of four subunits – the pore-forming core – which in response to Glu binding open their ion channel pore allowing the influx of cations (Ca^{2+}, K^+, Na^+). This triggers a rapid depolarization of the postsynaptic membrane, which in turn initiates a signal transduction cascade in the postsynaptic cell. Perhaps one of the most interesting features of the iGluRs is their diversity of channel properties, dependent on subunit composition, and the expression profile across the mammalian brain. And, dependent on their specific agonist, iGluRs can be divided into three main groups: α-amino-3-hydroxy-5-methyl-isoxazole-propionic acid receptors (AMPARs), kainate receptors (KARs), and N-methyl-D-aspartate receptors (NMDARs)[34] which are all heterotetramers (Figure 2). AMPARs are the cornerstone of fast synaptic transmission in the central nervous system, and as the core of my work AMPARs will be further detailed in Section 3. KARs are somehow a special class of iGluRs. KARs are composed from 5 subunits, GluK1–5, and unlike AMPARs and NMDARs (with few exceptions) are expressed at both pre- and postsynaptic sites. Moreover, depending on the subunit composition, KARs can exert a (GluK2-dependent) ionotropic or a (GluK5-dependent) metabotropic function. Yet, the role of KARs during synaptic transmission remains poorly characterized[35-37]. Finally, NMDARs colocalize with AMPARs to form functional synaptic units in front of glutamate release sites. NMDARs are composed from seven subunits, GluN1, GluN2A–D, and GluN3A–B. This class of receptors is particularly unique among synaptic receptors as its activation requires not only the binding of Glu but also of a co-agonist (glycine or D-serine). At resting membrane potential, NMDARs are blocked by physiological levels of extracellular Mg^{2+}, but membrane depolarization upon rapid activation of AMPARs and KARs can release the Mg^{2+}-block. Finally, the high Ca^{2+} permeability, and the slow kinetics of NMDARs due to the slow unbinding of Glu, make NMDARs crucial for the regulation of synaptic strength. The increase of intracellular Ca^{2+} upon NMDARs activation triggers several intracellular Ca^{2+}-dependent signal cascades in the postsynaptic neurons, some of which ultimately produce either short-term or long-term changes in synaptic strength[35,38,39].

In contrast, mGluRs belong to the C class of G protein-coupled receptors and are widely distributed throughout the surface of neurons and glia. mGluRs and are divided into three groups based on the signal transduction pathway and pharmacological profile, the group I: mGluR1 and mGluR5, group II: mGluR2 and mGluR3, and group III: mGluR4, mGluR6-8 (Figure 2). Their activation triggers an intracellular G-protein response, and subsequent activation of downstream signal transduction pathways, contrary to the cation flux of iGluRs[40,41].

At hippocampal excitatory glutamatergic neurons, the mGluRs (mGluR5) are homogeneously distributed at the plasma membrane, whereas the iGluRs are clustered within the synapses at the postsynaptic density (PSD) areas. The NMDARs occupying a more central position in the PSD, and AMPARs evenly distributed in small clusters surrounding the NMDARs[42-44].

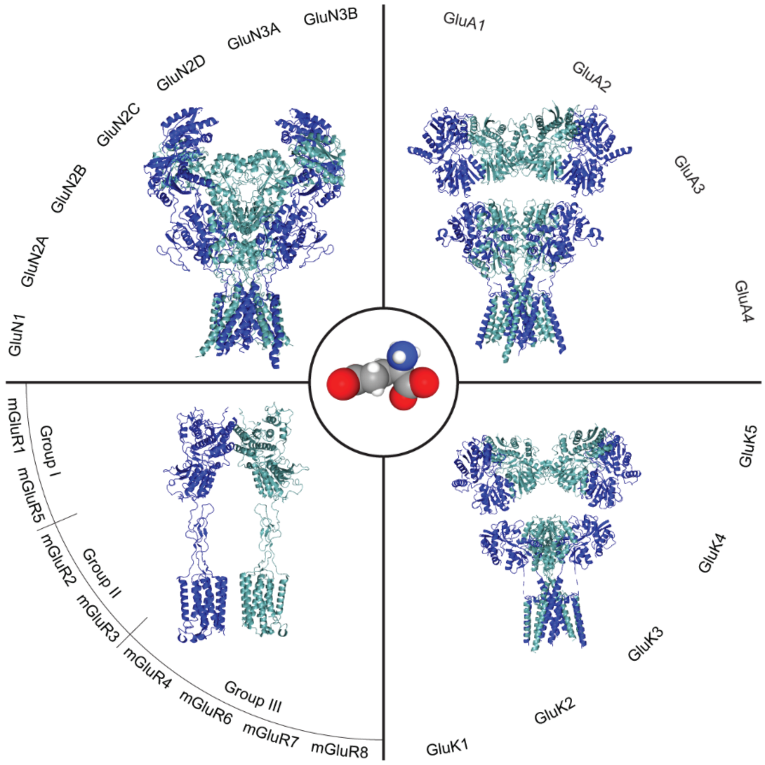

Figure 2: The family of Glutamatergic Receptors. Groups and subunits of the ionotropic and metabotropic glutamate receptors. From top left, in a clockwise direction, structure of the heterotetramer NMDAR – GluN1(light blue)/GluN2B(dark blue) (PDB: 5FXK)[45]; the heterotetramer AMPAR – GluA1(light blue)/GluA2(dark blue) (PDB: 6QKZ)[46]; the heterotetramer KAR – GluK2 (light blue)/GluK5(dark blue) (PDB: 7KS3)[47]; and dimeric mGluR5 (PDB: 6N52)[48].

2.3 The postsynaptic density

With the demonstration of the existence of synapses by EM, an unknown dark area emerged in the postsynaptic side, the PSD (reviewed in [49,50]). Identified as an electron-dense web near the postsynaptic membrane of excitatory synapses (Figure 1c), the PSD serves as an area of receptors clustering apposed to the presynaptic site[51,52]. Usually found at the tip of the dendritic spine head, PSD is a proteinaceous structure that comes in all shapes and sizes across different brain regions. It typically resembles a disk-like structure, although larger PSDs are often irregular or perforated: ~200–800 nm (mean 300–400 nm) wide and ~30–60 nm thick[53]. The number of AMPARs at hippocampal synapses is positively correlated with the PSD area, while the number of NMDARs is independent of PSD area[43,54]. Moreover, synaptic strength was shown to positively correlate with PSD area at neocortical synapses[55].

In a race against the clock to decipher PSD composition, a combined effort using gel electrophoresis from isolated PSDs, yeast two-hybrid assay, mass spectrometry led to the identification and quantification of several hundreds of proteins over the years[49,50] (Figure 3). Recently an effort was put forward to exhaustively measure precisely the amount of the major synaptic proteins at individual spines using a combination of electron microscopy and quantitative biochemistry with super-resolution microscopy[56]. Of all synaptic proteins, actin-cytoskeleton-related proteins, kinases/phosphatases, and GTPases and respective regulators make up the largest protein groups in the PSD; calcium/calmodulin-dependent protein kinase II α (CaMKII) is overall the most expressed protein[57,58] (Figure 3b,c). It should however stay in mind that such composition is not set in stone. It not only varies between different brain regions[58] and cell types, as there is a continuous molecular turnover under basal conditions with larger changes during neuronal activity[49,59,60]. Of all the different proteins, one cannot talk of PSD without mention the membrane-associated guanylate kinases (MAGUK) superfamily of scaffold proteins. Identified in the early 1990s[61,62], the PSD95 is the most studied PDZ-containing MAGUK member, as well as, the most abundant of them[58] (Figure 3b). Located close to the postsynaptic membrane[63-65] (Figure 3a), PSD95 – like all the other MAGUK family members – contains three domains, the PDZ domain(s) (PDZ1, PDZ2, and PDZ3), the SH3 domain, and the guanylate kinase-like domain[66]. The PDZ domains of PSD95 play a central role in the direct synaptic anchoring of NMDARs[67,68] and indirectly the AMPARs through AMPAR-auxiliary proteins[69-71].

Compared to other PSD proteins, PSD95 is highly stable[72,73], however, post-translational modifications, such as phosphorylation[74,75] and palmitoylation[76-78] dictate the course of PSD95 in the PSD. Importantly, PSD95 dynamics plays a crucial role during synaptic plasticity[79,80], and homeostatic synaptic scaling[81].

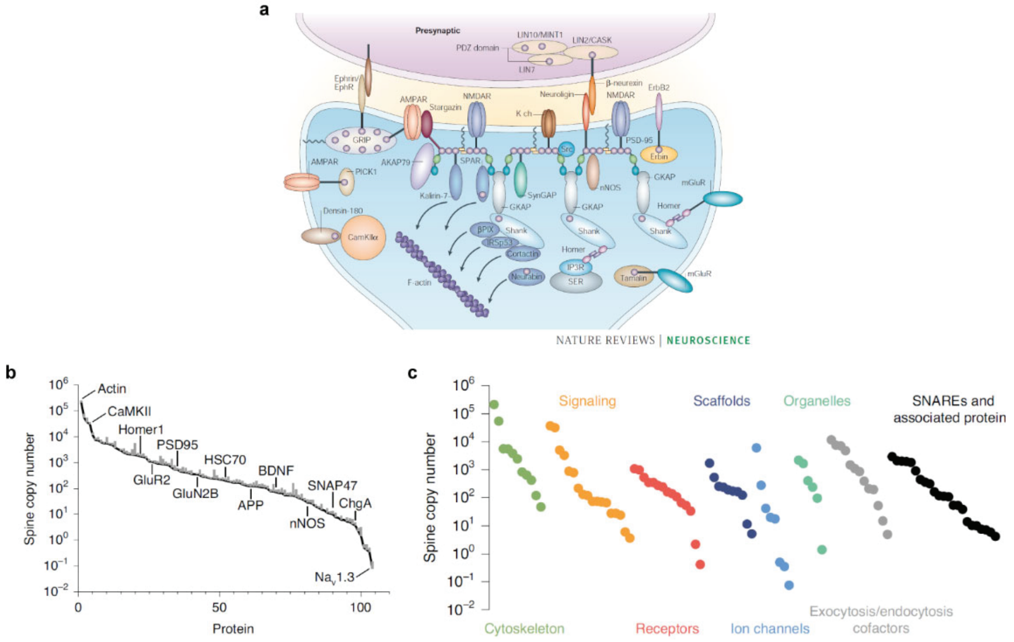

Figure 3: Excitatory PSD organization. (**a**) Schematic diagram of the organization of postsynaptic proteins at the mammalian excitatory synapse. Adapted from Kim and Sheng (2004)[66]. (**b**) Overview of the average copy number per spine for 110 proteins in hippocampal neurons. (**c**) Overview of the copy number per category. (**b** and **c**) Adapted from Helm, et al. (2021)[56].

2.4 Surfing the plasma membrane: the game-changing 2000s

After the groundbreaking 1950s, it was now the time for the 1970s to define the game. In 1966, Terje Lømo observed that upon high-frequency stimulation of presynaptic fibers of the perforant pathway a long-lasting enhancement of the postsynaptic cells of the dentate gyrus could be observed. Tim Bliss later joined Lømo, and together introduced in 1973 a new concept in synaptic transmission: the long-lasting potentiation, later renamed long-term potentiation (LTP)[82,83]. LTP is one of the several mechanisms implicated in synaptic plasticity, one that confers the ability of chemical synapses to increase their strength; LTP is widely accepted as one of the major cellular mechanisms that underlie learning and memory formation[84,85]. As there is no 'Yin' without a 'Yang', Gary Lynch and colleagues introduced in the late 70s the concept of long-term depression (LTD)[86,87], the long-lasting decrease of synaptic strength.

The 1970s were not only fruitful for the neuroscience field. A key turning point in the cell biology field arrived in the early 1970s by the hands of Seymour Singer and Garth Nicolson, who introduced in 1972 the fluid mosaic model of cell membrane structure[88]. While the model has evolved, the fundamentals remain; a lipid bilayer organized as a mosaic of several components – phospholipids, cholesterol, proteins, and in small amounts carbohydrates – that give the membrane a fluid nature.

From the early days, the central nervous system has always been a challenge to study. At that time, the understanding of central synapses arrived from fixed snapshots of those synapses, and extrapolations from observations of the neuromuscular junctions. At the transition of the decade, lateral diffusion of acetylcholine receptors was observed at the plasma membrane of neuromuscular junctions, and postulated as a key mechanism for receptor accumulation during the synaptogenesis; those observations led to the formulation of the 'diffusion-trap' mechanism[89,90]. Receptor lateral diffusion was later extended to the formation of central synapses[91], but its role during synaptic plasticity was not considered until the early 2000s. Until there, central synapses were seen as relatively statics, and changes in receptor numbers within the synapses were often attributed to endo-/exocytosis processes; reviewed in [92,93].

At the turn of the millennium, Daniel Choquet, Antoine Triller and colleagues directly established the mobility of glycine receptors and AMPARs, dethroning the simplistic view of static central synapses[94,95] (Figure 4a,b). Using single-particle tracking, they demonstrated that receptors within the synapses constantly alternate between an immobile state and mobile state, in which receptors diffuse in the plane of the plasma membrane by Brownian motion – lateral diffusion[94-97] (Figure 4c). It is now well accepted that lateral diffusion of receptors not only plays a role during synaptogenesis, as it is a crucial feature of synaptic transmission and its plasticity; reviewed in [93,98,99].

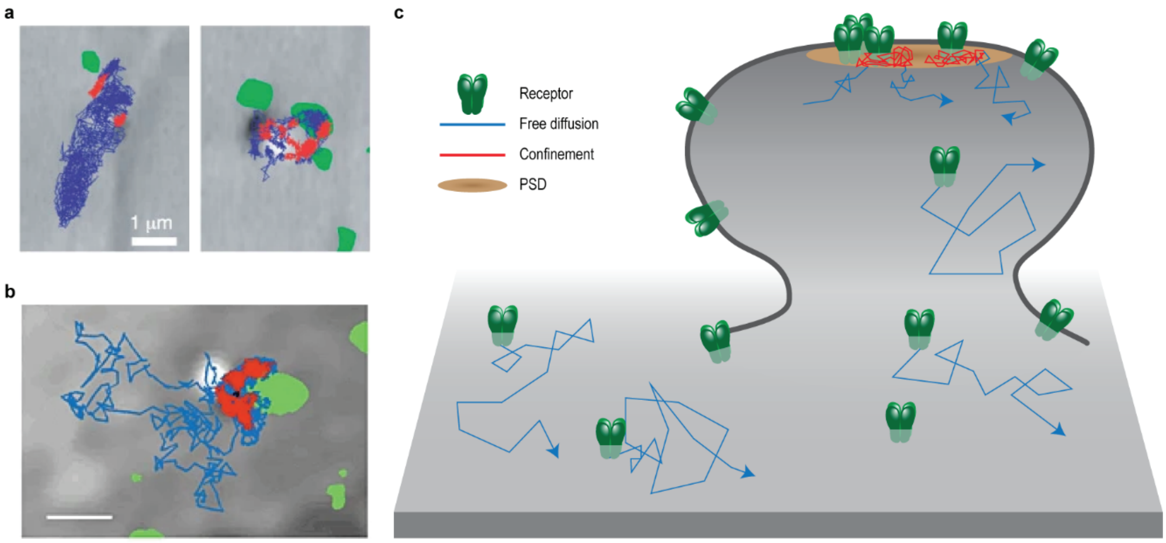

Figure 4: Receptor lateral diffusion. (**a**) Representative trajectories of AMPARs labeled with latex particles next to pre-synaptic sites stained with FM1-43 (green) in dissociated hippocampal neurons. Diffusive (free) movements in blue, and confined movements in red. Adapted from Borgdorff and Choquet (2002)[95]. (**b**) Single trajectory of a glycine receptor in dissociated motor neurons. Diffusive (free) movements in blue, and confined movements in red; in green, gephyrin, a scaffold protein present at inhibitory synapses. Scale bar: 1 µm. Adapted from Meier, et al. (2001)[94]. (**c**) Schematic representation of receptor lateral diffusion.

At the PSD (brown circle), receptors are confined and show small trajectories (red lines), however, outside the PSD, receptors are able to freely diffuse through Brownian motion, and thus present fast and long trajectories (blue lines).

Throughout my PhD, I have been working on understanding the mechanism by which different proteins regulate different aspects of the AMPAR cycle. As AMPARs are only a fraction of a much larger picture, the way I approached some of these topics was through the direct study of some of these proteins, rather than focusing on AMPARs. Therefore, the better way for me to introduce and describe AMPARs in the following section is no other than from the perspective of the AMPAR associated proteins.

3. Behind the scenes of AMPAR-mediated transmission

In 1989, while screening for kainate-gated ion channels by microinjecting mRNAs from rat forebrain in *Xenopus laevis* oocytes, Hollmann and colleagues identified what would later be termed GluA1[33]. Like all the iGluRs, AMPARs are a tetrameric complex of four homologous subunits – GluA1 to Glu4 – assembled in different stoichiometry giving rise to functionally distinct receptors[100]. Additionally, post-transcriptional modifications such as alternative splicing and RNA editing, and post-translational modifications further extend the functional diversity of AMPARs[101-105], thus contributing to the vast diversity of AMPAR gating kinetics, cation flux, and pharmacological profiles[35]. In particular, an interesting feature of the AMPAR is its potential permeability to Ca^{2+}. However, the presence of GluA2 – Arg-edited at position 607 in the pore-forming loop – subunits in the AMPAR complex confer low permeability to Ca^{2+} and insensitivity to intracellular polyamines blockers. The GluA2-containing, Ca^{2+}-impermeable AMPAR mediate the majority of AMPAR mediated transmission. While the role of Ca^{2+}-permeable AMPARs remains poorly understood, the transient recruitment of these receptors seems to play a role in different forms of synaptic plasticity, such as LTP and LTD, as well as homeostatic plasticity[106,107].

Nonetheless, this is only a small part of a much broader and intricate picture. Usually, described as the tetrameric assembly of GluA subunits, AMPAR is only the pore-forming core of a larger macromolecular complex composed of several other proteins that directly interact and determine the basic features of pore-forming subunit, the AMPAR auxiliary subunits[108]. After the identification of several new AMPAR interacting proteins, Jochen Schwenk and colleagues proposed a model in which the pore-forming core is surrounded by an ‘inner’ core composed of four proteins from a subset of the auxiliary subunits and an ‘outer’ core possibly composed of the remaining auxiliary subunits and interacting proteins[109]. Importantly, AMPAR subunit composition, as well as auxiliary subunits, vary in function of the developmental stage, brain region, and cell type[101,110,111]. In sum, an endless functional and regional diversity of receptors.

3.1 AMPAR structure

GluA subunits comprise four distinct domains: the extracellular amino-terminal domain (ATD or NTD), ligand-binding domain (LBD), transmembrane domain (TMD), and the intracellular carboxyl-terminal domain (CTD) (Figure 5a). Similar to other iGluRs, AMPAR features a symmetry mismatch between the extracellular domains and the TMD; the ATD and LBD share a 2-fold symmetry, whereas the TMD exhibit a 4-fold symmetry[112,113] (Figure 5b).

Within the AMPAR, GluA subunits are often described from subunits A–D to accurately describe their spatial position in the tetrameric receptor[112]. The extracellular domains (ECD) of AMPAR – ATD and LBD – represent the vast majority of the receptor mass, ~85%. The ATD and LBD display a 2-fold symmetry, however, symmetry mismatch is observed between the two domains as a result of the loose NTD-LBD linker that separates the domains. Therefore, while the tightly associated ATD dimers are arranged in A/B and C/D pairs, LBD symmetry occurs between A/D and B/C subunits[112,114]. The ATD encompasses 50% of an AMPAR subunit, yet its function remains unclear. ATD-deleted AMPARs are fully functional[115], but it has been suggested a crucial role of the ATD in the receptor assembly[116], clustering, synaptic localization[117-121], and fine-tuning of receptor responses[115,122], see also[123]. Worth mentioning, and in line with their high heterogeneity, distinct roles have been attributed to ATDs of different subunits. GluA2 ATD facilitates synaptic anchoring contributing for basal AMPAR-mediated synaptic transmission[119,121], but not for hippocampal LTP[120,124]. In contrast, GluA1 NTD is required for hippocampal LTP maintenance[119,120,124] through interaction with neuroplastin-65[124].

The LBD is a bilobed structure highly conserved across the different iGluRs. The LBD of iGluRs is often described as a clamshell-like structure, the D1 lobe as the upper half and the D2 lobe as the lower half of the clamshell (Figure 5a). At the receptor level, the LBD of adjacent subunits is arranged back-to-back as a dimer of dimers via de D1 lobes[35,113]. The binding of Glu at the base of the D1 lobe triggers the closure of the clamshell-like structure with an outward movement of the D2 lobe. This in turn creates tension on the LBD-TMD linker, and subsequent opening of the channel pore[125].

The TMD of AMPARs is composed of four transmembrane helices: M1-M4. The M1, M3, and M4 segments form the core of the channel pore, whereas the re-entrant M2 loop occupies the inner cavity of the channel. At the apex of the GluA2 loop lies the Gln/Arg-edited site that controls Ca^{2+} permeability and sensitivity to polyamines (Figure 5a). Also, the M4 segment from one subunit interacts with the M1 and M3 segments from adjacent subunits[35,113].

Finally, the cytoplasmic CTD presents a structure rich in phosphorylation sites and subunit-specific protein interactions. The CTD varies in length between subunits; GluA1 and GluA3 having long C-tails, and GluA2 and GluA3 short C-tails. Changes in C-tail lengths are also observed in some splice variants[126-129]. Not yet fully understood, the CTD has been pointed as a key regulator in receptor trafficking and anchoring, ultimately, synaptic plasticity and learning[98,129-131].

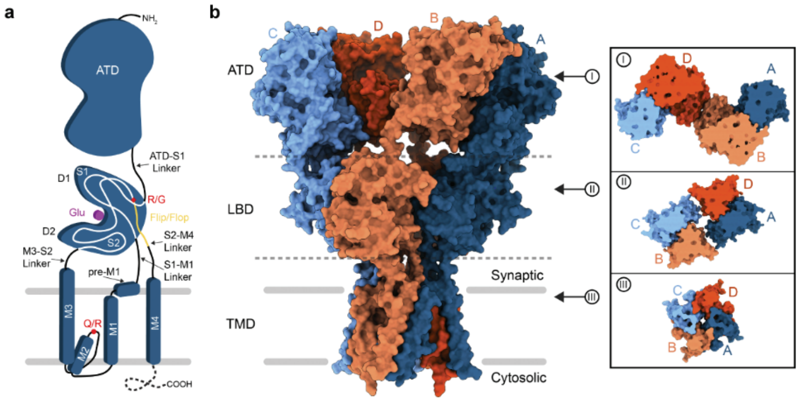

Figure 5: Architecture of AMPARs. (**a**) Topology of a single GluA subunit. The dashed line represents the CTD, which is as of yet structurally unresolved. (**b**) Structure of a homotetrameric GluA2-containing AMPAR (PDB 5WEO). Each GluA2 subunit is colored individually (A, dark blue; B, coral; C, light blue; D, dark orange). Dashed lined separates the three structurally resolved AMPAR domains: ATD, LBD, and TMD. Insets display a top-down view of slices into each domain of the receptor. Adapted from Twomey, et al. (2019)[132].

3.2 AMPAR architecture

Despite decades of study, the precise composition of native AMPARs remains poorly understood. AMPARs are known to form homo- or heteromers. Previous studies based on averaging of the entire population of receptors suggested the diheteromeric GluA1/GluA2 and GluA2/GluA3 receptors as the most abundant assemblies in the mammalian brain[133,134]. Recent work from the lab of Eric Gouaux using specific antibody fragments against GluA1, GluA2, and GluA3 subunits elucidated ten distinct native architectures of AMPAR combinations by single-particle cryo-EM[100,135]. Noteworthy is the identification of a previously uncharacterized triheteromeric GluA1/GluA2/GluA3 assembly, which, funny anecdote, represents the major population of AMPAR assembly in the whole brain[100] and the second-biggest population in the hippocampus[135]. This is of particular relevance as most of the studies take only into consideration homo or diheteromeric in their studies, and as already discussed, different combinations of GluA subunits will have different properties, and likely different auxiliary subunits assembly.

Previous work in recombinant heteromeric GluA2/Glu3 receptors suggested GluA2 at the A/C position and GluA3 at B/D position with the receptor adopting an ‘O’-like shape configuration[136], in contrast to the canonical ‘Y’-like shape configuration of the homotetrameric GluA2 receptor[112]. However, in native AMPAR[100,135], GluA2 subunits preferentially occupy B/D positions while GluA1 and GluA3 occupy the A/C positions with the receptor mostly adopting a ‘Y’-like shape configuration, as previously suggested in recombinant heteromeric GluA1/GluA2 receptor[46]. Others than ‘Y’-like shape have been previously reported, in particular, when in complex with certain auxiliary subunits (reviewed in [137]), which may have gone unnoticed in the native AMPAR studies as a result of restricted conformational flexibility imposed by the antibodies fragments or low abundance of such configurations.

3.3 The architecture of AMPAR-auxiliary subunit complexes

In neurons, however, endogenous AMPARs are often co-assembled with a large and diverse pool of >30 structurally transmembrane proteins of different families (Figure 6), of which 12 exclusively associate with AMPARs[109,110,138]. These proteins have been implicated in several aspects of the AMPAR

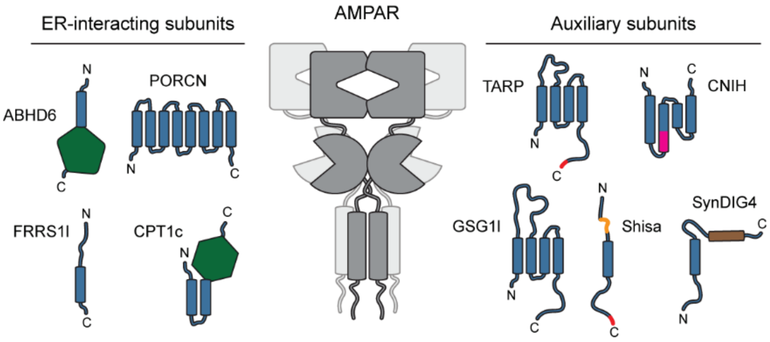

Figure 6: Topology of AMPAR interacting proteins. Topology of the transmembrane ER-interacting subunits and auxiliary subunits. In green the catalytic subunits of α/β-hydrolase domain-containing protein 6 (ABHD6) and carnitine palmitoyltransferase 1c (CPT1c); in red, the PDZ-binding motif at the C-terminus of transmembrane AMPAR regulatory protein (TARP) and Shisa family proteins; in pink, the cornichon (CNIH)2/3 specific segment; in orange, the cysteine-knot motif of Shisa family proteins; in brown, the membrane associated domain of SynDIG4. Porcupine O-acyltransferase (PORCN), ferric-chelate reductase 1-like (FRRS1l); and germ cell-specific gene 1-like protein (GSG1l).

cycle, from biogenesis, trafficking and, anchoring to channel gating and pharmacology (see Section 4). A subset of these proteins meet several of these criteria and are thus defined auxiliary subunits[108]. Moreover, the auxiliary subunits, in particular the less abundant ones, are brain-region and neuronal cell-type-specific with specialized functions[139]. Others, like the transmembrane AMPAR regulatory protein (TARP) and cornichon (CNIH) families, are widespread throughout the brain[110]. Therefore, elucidating AMPAR architecture when in complex with those different proteins is of utmost importance; recently reviewed by [132,137,140], and discussed below. Not only will this provide a more realistic and accurate picture of the AMPAR-mediated modulation of excitatory circuits, but it will also open therapeutical opportunities for the development of brain region-specific drugs based on auxiliary subunit-specific enriched AMPAR complexes[141,142].

3.3.1 The architecture of the AMPAR-TARP complex

TARPs are structured with a cytoplasmic ATD and CTD and a twisted bundle of four transmembrane helices (M1-4) connected by a short cytoplasmic loop and two extracellular loops (Figure 6). TARPs ECDs comprises a long ECD (Ex1): four β-strands (β1-4) and three flexible loops (β1–β2, β3–β4, β4–M2), and a short ECD (Ex2): one flexible loop (M3–β5) and one β-strand (β5)[132] (Figure 7). The TARP family is often subclassified in type-Ia (γ2 and γ3), type-Ib (γ4 and γ8), and type-II (γ5 and γ7) based on differences in sequence homology and functional properties[143]. However, γ5 is not considered as a canonical AMPAR-auxiliary subunit. TARPs are crucial players when it comes to AMPAR trafficking, gating modulation, ion permeation, and pharmacology[71,144-147]. Moreover, TARPs are expressed in a subunit-specific brain region-specific manner[110,148], which altogether places TARPs in the spotlight when it comes to understanding AMPAR complexes. The prototypical AMPAR-auxiliary subunit γ2, also known as stargazin, was discovered over 20 years ago thanks to the stargazer mouse[71,149,150]; a *Cacng2* (encodes the protein γ2) mutant mouse characterized by an ataxic phenotype, due to the prominent role of γ2 in cerebellar granule neurons. Lack of γ2 expression in these neurons results in impaired AMPAR surface delivery[71,149]. γ2 was the first auxiliary subunit whose structure was elucidated when in complex with homomeric GluA2 receptors[151,152] (Figure 7a). More recently, the

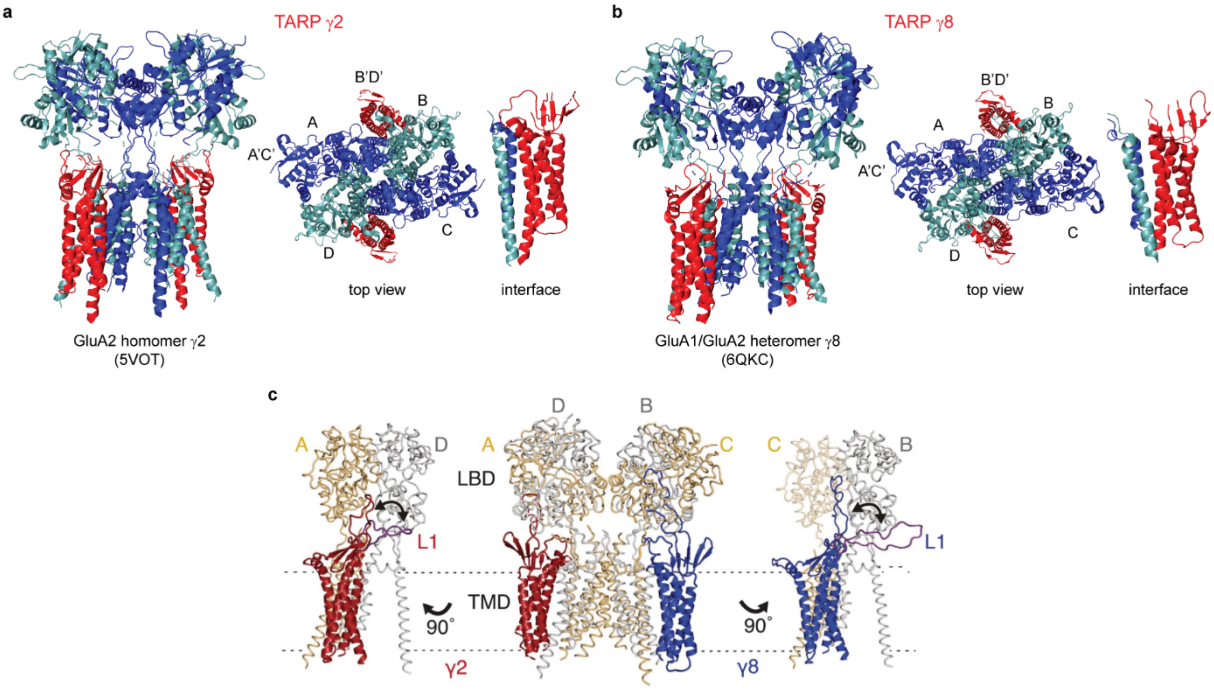

Figure 7: Architecture of the AMPAR-TARP complex. (**a**) Left panel, side view of the AMPAR visualizing the tetrameric LBD and TMD interface of a Glu2 homotetramer (GluA2 subunits positioned at AC and BD positions are coloured light and dark blue, respectively), and two γ2; middle panel, LBD top-down view depicting γ2 positioned at the B′D′ sites. Right panel, diagram of the interface between γ2 and M1 and M4 of AMPARs viewed from the side in parallel to the membrane (PDB 5VOT)[153]. (**b**) Left panel, side view of the AMPAR visualizing the tetrameric LBD and TMD interface of a Glu1/GluA2 heterotetramer (GluA1 subunits positioned at AC and GluA2 subunits positioned at BD positions are coloured light and dark blue, respectively), and two γ8; middle panel, LBD top-down view depicting γ2 positioned at the B′D′ sites. Right panel, diagram of the interface between γ2 and M1 and M4 of AMPARs viewed from the side in parallel to the membrane (PDB 6QKC)[46]. (**c**) Left panel, side view of the receptor model depicting γ2 and γ8 positioned at equivalent B′D′ sites based on the cryo-EM complex structure of the GluA2 homotetramer in complex with four γ2 subunits (PDB 5KK2). On the side panels, the predicted Ex1 of γ8 is longer than in γ2 enabling it to reach the AMPAR LBD upper lobe. TARPs ECD is not resolved, the loops are just predicted models based on the putative flexibility. Adapted from Riva, et al. (2017)[154].

architecture of γ8 in complex with the heteromeric GluA1/GluA2 receptor has been elucidated using cryo-EM[46] (Figure 7b), which accounts for the vast majority of TARP-containing AMPAR complexes in the hippocampus[110,135].

The main interaction between TARPs and AMPAR occurs at the TMD level, an interface between the M3 and M4 from the TARP and the M1 and M2 from one GluA subunit and the M4 from the adjacent subunit[151,152], and reviewed in [132]. TARPs CTD emerges from the TARP M4 and extends into the cytoplasm. Type-I TARPs share a cannonical PDZ-binding domain (Thr-Thr-Pro-Val) at the end of the CTD, while type-II TARP display an atypical terminal sequence, Thr/Ser-Ser-Pro-Cys[143]. TARPs CTD remains unresolved probably as a result of CTD truncation or conformational flexibility/heterogeneity.

TARPs are known for their ability to modulate AMPAR gating as well as pharmacology (see Section 4.3), a property that has been attributed to TARP ECD[144,154,155]. TARP-mediated AMPAR modulation is ensured by a perfect positioning, where TARPs ECD is juxtaposed to the AMPAR LBD 'clamshells'[132] (Figure 7c). Structurally, γ2 and γ8 are very similar[46,151,152] (Figure 7a,b). The most striking difference between the arrangement of these two TARPs can be observed at the β1-β2 loop, as the long β1-β2 loop of γ8 projects towards the upper lobe of AMPAR LBD[46] (Figure 7c), which could explain the different modulatory effect observed between γ2 and γ8[144,154]. A particular feature of type-I TARPs is the presence of a negatively charged extracellular helix (ECH) preceding the M2 suggested to interact with the positively charged residues on the lower lobe of the AMPAR LBD, including the Lys-Gly-Lys motif[46,151,152], implicated in AMPAR channel activation[156].

As abovementioned, AMPAR ECDs display a two-fold symmetry with the interfaces A/B and C/D being equivalent, and the same is valid for the interfaces A/D and B/C. Therefore, the four interfaces available for TARPs assembly can be broken down into two groups, the A'C' and B'D' sites. Depending on the occupied site, TARPs ECD will have access to different elements of the AMPAR LBD[132,137]. As most of the native AMPARs are heterotetramers, A'C' and B'D' sites are likely to be unique depending on the AMPAR subunit composition.

The AMPAR-TARP stoichiometry remains poorly understood. Several functional studies using recombinant AMPAR and TARPs expression predicted a mixed stoichiometry, ranging from 1-4 TARPs per AMPAR tetramer[157-159], later structurally confirmed[46,151,152]. Recently, structural data of native AMPAR complexes further confirmed a mixed stoichiometry of AMPAR-TARP complexes that can range up to four TARPs per AMPAR, with TARPs preferentially occupying the B'D' sites of AMPAR[100,135].

3.3.2 The architecture of the AMPAR-GSG1l complex

The germ cell-specific gene 1-like protein (GSG1l) is a distant homolog of TARPs within the claudin superfamily, and like TARPs and CNIHs has been proposed to constitute part of the 'core' AMPAR complex[109,160]. GSG1l folds like TARPs, and similarly, it is composed by four transmembrane helices (M1-4) (Figure 8) and five β-strands[161]. Like TARPs positioned at B'D' sites, GSG1l main interaction occurs between the M3 and M4 from the GSG1l and the M1 and M2 from the GluA subunit at positioned at the A/C site and the M4 from the GluA subunit at B/D site[161,162] (Figure 8). However, some particular differences within Ex1 domain of GSG1l and TARPs hold the differences in the modulation of AMPAR gating[163]. Overall, GSG1l Ex1 is significantly, ~50%, longer than the ones from TARPs[160], and confers GSG1l an inhibitory effect on AMPAR-mediated transmission[163]. One of the key differences is the long β1-β2 loop of GSG1l; GSG1l$_{\beta1\text{-}\beta2\text{ loop}}$: 49 amino acids versus $\gamma8_{\beta1\text{-}\beta2\text{ loop}}$: 29 aa versus $\gamma2_{\beta1\text{-}\beta2\text{ loop}}$: 17 aa[46,161]. Replacement of GSG1l β1-β2 loop with the shorter β1-β2 loop of γ2 disrupts the GSG1l-specific modulation of AMPAR recovery from desensitization[161]. Interestingly, the β1-β2 loop is poorly conserved across different TARPs and GSG1l and may play a role in the unique effects of these auxiliary subunits on AMPAR desensitization[132]. Another noticeable difference between TARPs and GSG1l is the absence of the ECH domain in the latter, which is compensated by a longer M2 that extends into the extracellular space[161].

In contrast to TARPs which can simultaneously bind up to four molecules per AMPAR tetramer, GSG1l seems to occupy up to two sites (the B'D' sites), but such observations were made using recombinant homomeric GluA2 receptors[161,162] and may be different in native AMPAR complexes.

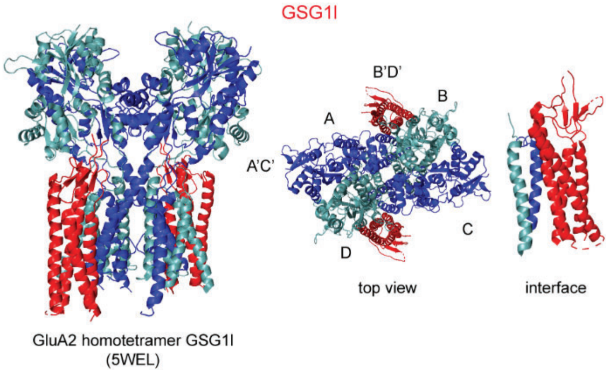

Figure 8: Architecture of the AMPAR-GSG1l complex. Left panel, side view of the AMPAR visualizing the tetrameric LBD and TMD interface of a Glu2 homotetramer (GluA2 subunits positioned at AC and BD positions are coloured light and dark blue, respectively), and two GSG1l; middle panel, LBD top-down view depicting GSG1l positioned at the B′D′ sites. Right panel, diagram of the interface between GSG1l and M1 and M4 of AMPARs viewed from the side in parallel to the membrane (PDB 5WEL)[162].

3.3.3 The architecture of AMPAR-CNIH complex

Along with TARPs, CNIHs are the most abundant AMPAR auxiliary subunits[109]. Both CNIH2 and CNIH3 were recently resolved by cryo-EM, elucidating a bundle of four transmembrane helices (M1–4) emerging from the extracellular ATD and CTD[164,165] (Figure 9). Interestingly, superimposition of claudin homologous TARP/GSG1L with CNIH2 and CNIH3 revealed a similar 3D architecture; CNIHs M1 overlies TARPs M3, CNIH3 M2 overlies TARPs M4, and so on, which somehow resembles an inverted TARP. Importantly, CNIHs and TARPs bind at the same location on AMPAR (Figure 9); while on TARPs M3 and M4 interface with AMPARs, CNIHs interface occurs at the M1 and M2 domains[137,164,165]. Perhaps, the most interesting feature about CNIHs occurs from M2 to M3. CNIHs M2 starts in the cytoplasm but fails to penetrate the extracellular space, instead, it turns 180º in the membrane connecting to the M3[164]. Additionally, CNIH M2 starts with a α-helix that is unique to CNIH2 and CNIH3[137]. As the majority of CNIH is embedded in the membrane with a small cytoplasmic domain, a direct interaction between CNIHs and AMPAR LBD is unlikely to occur[164,165]. Moreover, CNIH2 and CNIH3 contain three phenylalanine residues (position 3, 5, and 8 aa) at the ATD that were shown to be required for AMPAR gating modulation[165]. Therefore, the CNIH-induced gating modulation of AMPARs requires an interchange between CNIH M1 and M2, but the mechanism is yet to be determined. Cryo-EM data from recombinant and native hippocampal GluA1/GluA2 heterotetramers suggests a preferential occupancy of the spatially more restricted AMPAR A'C' positions by CNIH2, whereas B'D' positions are occupied, preferentially, by γ8[135,165].

3.3.4 The architecture of AMPAR-SynDIG4 complex

Synapse differentiation-induced gene 4 (SynDIG4, also known as proline-rich transmembrane protein 1 – PRRT1) is an 'outer' core auxiliary subunit[109,135]. Unlike the four-transmembrane helices-containing 'inner' core auxiliary subunits, SynDIG4 is predicted to at least one transmembrane helix with a cytoplasmic ATD and extracellular CTD – type II transmembrane protein[166] (Figure 6). Recently, Yu and colleagues identified a helix-like structure on native hippocampal AMPAR complexes likely to correspond to SynDIG4. Interestingly, they observed that SynDIG4 is positioned at the interface of

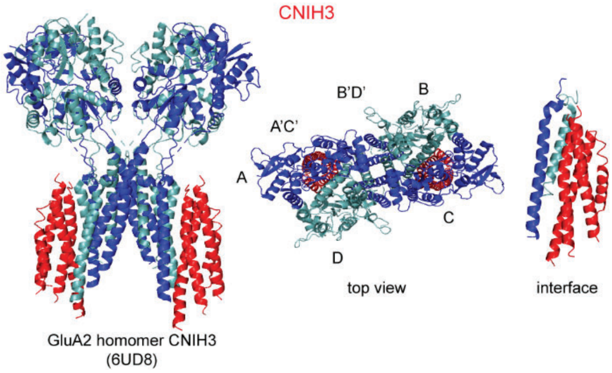

Figure 9: Architecture of the AMPAR-CNIH complex. Left panel, side view of the AMPAR visualizing the tetrameric LBD and TMD interface of a Glu2 homotetramer (GluA2 subunits positioned at AC and BD positions are coloured light and dark blue, respectively), and two CNIH3; middle panel, LBD top-down view depicting CNIH3 positioned at the A′C′ sites. Right panel, diagram of the interface between CNIH3 and M1 and M4 of AMPARs viewed from the side in parallel to the membrane (PDB 6UD8)[164].

CNIH2 and GluA1[135], in agreement with the initially proposed CNIH2-SynDIG4 co-assembling and GluA1-containing AMPAR[110,166,167]. SynDIG4 runs parallel to GluA1 M4 as well as CNIH2 M1 and M4, placing SynDIG4 in the periphery of A'C' sites[135], the 'outer' core of the AMPAR complex[109].

3.3.5 The stoichiometry of native AMPAR complexes

Over the last decade, massive progress has been accomplished towards the understanding of the structural composition of AMPAR complexes and how auxiliary subunits differentially interact and structurally shape the receptor during channel gating modulation, reviewed in [140]. Nonetheless, the majority of those studies rely on recombinant AMPAR complexes, in particular homomeric GluA2 receptors and/or GluA subunits tethered to auxiliary subunits. With at least ten different assemblies of GluA tetramers, and a handful of auxiliary subunits, the observations made in recombinant AMPAR complexes represent only a fraction of the story, and that is if those observations are applied to native AMPAR complexes; an example being the architecture of recombinant GluA2/GluA3 receptors which adopt an 'O'-like shape with GluA2 at A/C positions and GluA3 at B/D positions[136], whereas native GluA2/GluA3 were shown to adopt a 'Y'-like shape with GluA2 at B/D positions and GluA3 at A/C positions[100]. That said, if not taken with caution, these observations in recombinant AMPARs can, potentially, mislead us in pursuit of understanding the vast and intricate architecture of native AMPAR-auxiliary subunits complexes.

Recently, it has been observed that in the rodent brain the majority of the AMPARs (~29%) are GluA1/GluA2/GluA3 triheteromeric assemblies, followed by GluA1/GluA2 (~24%) and GluA2/GluA3 (~18%) diheteromeric assemblies[100]. While in the hippocampus, the GluA1/GluA2 diheteromeric assembly represents the majority of the AMPAR complexes (~56%), followed by the GluA1/GluA2/GluA3 triheteromeric assembly (~36%)[135].

Understanding the architecture of AMPAR complexes implies to not only solve the pore-forming core assembly but also knowing the stoichiometry of different auxiliaries in a given complex. Recently, Yu and colleagues[135] using γ8-labeled single-molecule photobleaching, observed that in the hippocampus most of the receptors bleached in 2-steps (69%), an indication of the stoichiometry of two γ8 subunits per AMPAR, 26% bleached in 1-step and 5% in 3-steps. This is consistent with the fact that

γ8 is the most abundant auxiliary subunit in the hippocampus[110,138], and at the same time sheds light on the vast heterogeneity of native AMPAR complexes. Moreover, Yu and colleagues observed that in the hippocampus CNIH (likely CNIH2) is often associated with γ8-containing AMPAR complexes and that a vast portion of SynDIG4 is associated with γ8-containing AMPAR complexes[135].

Lipid-like densities have been observed at the interfaces between AMPAR and the auxiliary subunits γ8 and CNIHs, both in recombinant[46,164] and native[135] AMPARs. The exact function of these lipids is yet unknown, but given the location could potentially regulate receptor assembly and/or gating[137].

4. The rise of AMPAR: a journey towards the synaptic transmission

At this point, it is clear that when we talk about AMPARs we also must talk about all these proteins that are part of AMPAR complexes at a given point of the receptor lifetime. While the auxiliary subunits often come along when discussing AMPAR-mediated transmission, these proteins are just a handful of the ~30 identified AMPAR interacting proteins. And the reason for that is that most of the time we do not understand the function of some of these proteins, therefore we do not talk about them, but also because they do not seem to be relevant for the most important function of the receptor, that is the regulation of excitatory transmission.

As abovementioned, during my stay in the lab of Dr. Daniel Choquet, I have been particularly interested in understanding the function and mechanism of some of these AMPAR interacting proteins, and how they relate to each other. When I picture the AMPAR, *i.e.*, the pore-forming core surrender by a collective of interacting proteins, it often resembles the normal structure of the society, or even the organization of a research team; the core-constituent principal investigator, supported by the exquisite members of the team. Therefore, as a co-worker of this AMPAR-oriented team and given my research topic, the most reasonable way for me to discuss the following AMPARs lifecycle topics is none other than from the perspective of the AMPAR co-workers themselves.

Before I emerge in this vast and complex journey of the AMPARs, I would like to bring attention to one particular point. While by definition when we talk about auxiliary subunits it is implied that these proteins are associated with AMPARs at the plasma membrane[108], the same does not, necessarily, apply to the remaining AMPAR interacting proteins. Indeed, Brechet and colleagues have recently identified two distinct pools of interacting proteins; one that only associates with intracellular AMPARs (herein termed endoplasmic reticulum (ER)-interacting subunits) and a second pool that can also be detected associated with the receptor at the plasma membrane, of which the auxiliary subunits[168].

4.1 The beginning of life: AMPAR biogenesis

Decades had passed since the identification of AMPARs and the first auxiliary subunit, yet the biogenesis process of AMPAR remains poorly understood. The recent discovery of a handful of proteins that specifically interact with AMPARs exclusively at intracellular compartments suggested that, perhaps, such proteins may play a role during AMPAR biogenesis[168]. Until recently, AMPAR assembly has been considered to occur as early as chain translocation[169]. This would prevent targeting of newly emerged GluA monomers by the ER protein quality control mechanism – the ER-associated protein degradation (ERAD) – as a consequence of misfolding by exposure of the unprotected hydrophilic surfaces of AMPAR pore[170,171]. However, new data suggests that auxiliary subunits may have something to say in that matter.

The α/β-hydrolase domain-containing protein 6 (ABHD6) is an integral membrane protein that belongs to the serine hydrolase family (Figure 6). Collectively, ABHD6, ABHD12, and the monoacylglycerol lipase account for about 99% of brain endocannabinoid neurotransmitter 2-arachidonylglycerol hydrolase activity[172-174]. ABHD6 transcripts are relatively abundant across the different brain regions, and ABHD6 levels gradually increase during development and remain fairly stable throughout adulthood[175,176]. ABHD6 is mainly expressed by principal glutamatergic neurons, and by some GABAergic neurons and astrocytes[173]. Recently, ABHD6 was identified as one of the constituents of AMPAR complexes in the ER[168,177]. Overexpression of ABHD6 in heterologous cells increases intracellular levels of AMPARs but has a negative effect on the delivery of AMPAR to the plasma membrane[176]. This was recently shown to be the result of the assembly of ABHD6 with the newly translocated GluA monomers, which traps GluA subunits as monomers (Figure 10), preventing the formation of functional tetramers and forward trafficking[177].

The porcupine O-acyltransferase (PORCN) is another protein that like ABHD6, belongs to the group of ER-interacting subunits[168]. PORCN belongs to the membrane-bound O-acyltransferase enzymes family; it encompasses an eight transmembrane helices multi-pass ER-resident protein involved in the secretion and signaling of Wnt proteins[178-181] (Figure 6). Like ABHD6, PORCN is suggested to associate with GluA monomers and prevent their oligomerization[170,177] (Figure 10). Little is known about the mechanism behind the functional interaction of ABHD6 and PORCN with GluA subunits but given their topology, ABHD6 and PORCN are likely to interact with GluA TMD[170,182]. While not the case of PORCN, the interaction with the GluA CTD seems to be necessary for proper interaction with ABHD6[176,182,183]. However, neither ABDH6 nor PORCN enzymatic activity is required for the proper physical or functional interaction with GluA subunits[176,184]. Given the putative physical interaction with GluA TMD, the association of ABHD6 or PORCN may protect GluA monomers from ERAD targeting by shielding the GluA 'hydrophilic pore-lining' surface from the lipids of the membrane environment[170]. ABHD12 also associates with native AMPARs[109,168], however, the relevance of this interaction, either a redundant or distinct function of ABHD6, remains unclear[176].

Dimerization of GluA subunits has long been attributed to ATD self-dimerization. GluA ATD dimers affinities range from nano- to micromolar, and together with the local concentration of different GluA subunits account for AMPAR homo- and heteromeric diversity. On the other hand, the assembly of a fully functional AMPAR tetramer requires the interaction of the remaining domains[113,116]. However, what triggers the dimerization of those trapped GluA monomers remains unknown. A clue to understanding this next step on AMPAR biogenesis may reside in two other ER-interacting subunits, the ER-resident carnitine palmitoyltransferase 1c (CPT1c) and ferric-chelate reductase 1-like (FRRS1l, also known as C9orf4)[168,177,185].

CPT1c is a brain-specific isoform of the carnitine long-chain acyltransferases family, mainly characterized for its role in food intake and energy homeostasis[186,187]; reviewed in [188]. Composed by two transmembrane helices that segregate the small cytoplasmic ATD from the large and catalytic CTD (Figure 6), CPT1c is exclusively expressed in neurons and has been implicated in the regulation of ceramide metabolism in the ER[189,190]. Opposed to the prominent cytosolic CPT1c, FRRS1l is a single transmembrane helix containing an ER-luminal N-terminal dopamine beta-monooxygenase domain[168,191] (Figure 6). FRRS1l is widely expressed throughout the adult brain[191-193] and it is mainly localized at the ER as a consequence of its interaction with CPT1c[168]. CPT1c and FRRS1l make up 15-20% of all the AMPAR complexes in the brain[168], an interaction suggested to regulate the oligomerization of GluA-ABHD6 complexes, and subsequent removal of ABHD6 from the complex[177] (Figure 10). Similar to ABHD6 and PORCN, the mechanism involved in this functional interaction with AMPARs is unknown, but given the topology of CPT1c and FFRS1l, it is likely to interact with GluA1 TMD. The interaction of CPT1c further requires GluA CTD interaction[194], and FRRS1l/CPT1c-induced AMPAR dimerization is independent of CPT1c enzymatic activity[177]. Worth mention, loss of CPT1c or FRRS1l shifts the balance of native AMPAR complexes, it decreases γ8-, Shisa6- and Shisa9-containing AMPAR complexes, but increases ABHD6/ABHD12/PORCN-containing AMPARs[168,177], which favors the theory of ABHD6/PORCN as one of the first interactors of GluA subunits. Moreover, loss of FRRS1l results in higher levels of immature GluA2 and GluA4 subunits[195]. AMPAR maturation process involves N-glycosylation of the receptor in the ER lumen (immature receptor) and Golgi apparatus (mature receptor), which impacts receptor trafficking and channel gating[35,196], and further discussed below. Altogether, highlighting the importance of CPT1c/FRRS1l interaction with AMPARs in the formation of mature functional AMPAR complexes.

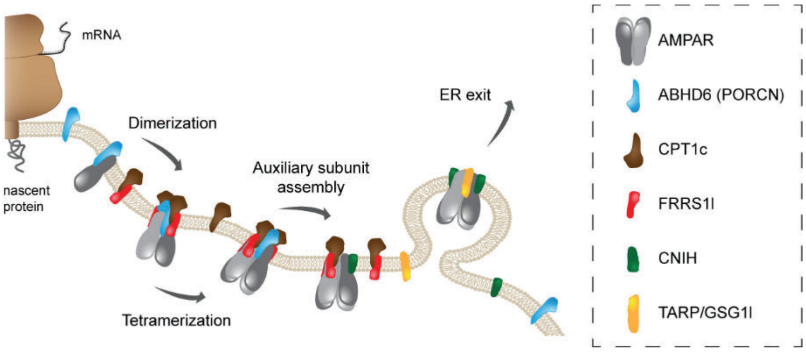

Figure 10: Biogenesis of AMPAR in the ER. Current understanding of the assembly line of AMPAR pore-forming core in the ER. Nascent GluA subunits associate with ABHD6 as monomers; formation of GluA dimers driven by co-assembly of CPT1c/FRRS1l complexes; GluA tetramerization via dimer-of-dimer formation and dissociation of ABHD6; binding of the cargo proteins and auxiliary subunits CNIHs and TARPs and dissociation of CPT1c/FRRS1l complexes; and initiation of ER export via induction of transport vesicles.

Despite the recent progress, the mechanisms and triggers behind each AMPAR building step remain to unveil. As ABDH6, CPT1c, and PORCN are ER-residents, a switch of proteins must occur before the ER-exit of functional AMPAR complexes.

4.2 Towards the light: forward trafficking of AMPARs

The ER-exit of functional AMPARs requires dissociation of AMPARs from the ER-resident CPT1c, and likely FRRS1l[177]. While there is some evidence of what the next steps are, this topic remains largely unexplored. Furthermore, there are some observations which still have some unclear implications for AMPAR biogenesis, for example regarding additional functions of CPT1c and FRRS1l discussed below.

As an ER-resident protein, CPT1c does not leave the ER, consequently it is not an ER cargo exporter. Recently, CPT1c was suggested to play a role in AMPAR trafficking via depalmitoylation of Cys585 in the M2 segment of GluA1[197,198]. However, the palmitoylation of GluA1 Cys585 occurs in the Golgi apparatus by the Golgi apparatus-resident palmitoyl acyl transferase DHHC3/GODZ; palmitoylation of GluA1 Cys585 results in inhibition of AMPAR forward trafficking and accumulation in the Golgi apparatus[105,199]. To date, no DHHC protein capable of palmitoylating GluA1 M2 has been identified in the ER which raises the possibility of retrograde traffic of palmitoylated GluA1 receptors. And, therefore, could represent an additional step in the quality control mechanism of AMPARs.

Additionally, the CPT1c co-assembly with FRRS1l creates a binding opportunity to Sac1, which otherwise is not present in AMPAR complexes[168]. Sac1 is a phosphatidyl-inositol-4-phosphate (PI(4)P) phosphatase that tightly regulates PI(4)P levels in different cellular compartments; it is primarily localized in the ER, but has the ability to shuttle between the ER and the trans-Golgi network (TGN)[200,201]. Stress-induced JNK3 palmitoylation entraps Sac1 in the Golgi, which results in Golgi-resident PI(4)P depletion, and subsequent inhibition of secretory trafficking, thereby reducing GluA1 surface trafficking[202]. Under normal conditions, CPT1c down-regulates Sac1 phosphatase activity, enabling proper GluA1 trafficking. In contrast, under metabolic stress, CPT1c-dependent inhibition of Sac1 is released, which results in Sac1 translocation to the ER-TGN contact sites and subsequent downregulation of GluA1 trafficking[194].

FRRS1l, on the other hand, remains more mysterious. While CPT1c-bound FRRS1l is trapped in the ER, the fraction not associated with CPT1c is subject to proteolytic cleavage – the transmembrane domain is replaced by a GPI-anchor – before exiting the ER[168]. Native FRRS1l and GluA1 were observed in hippocampal dynein vesicles[193] – crucial for AMPAR trafficking[203,204] –, whereas overexpression of recombinant FRRS1l was observed associated with AMPAR at extrasynaptic sites[193]. Nonetheless, whether GPI-anchored FRRS1l plays a role during AMPAR ER-exit or has any other function at the plasma membrane remains to be investigated. In sum, whereas a role other than AMPAR assembly is possible, the association of CPT1c and FRRS1l with AMPARs at physiological levels seems restricted to the ER[168,177].

Therefore, a switch of minions before the ER exit is a prerequisite. A job carried out by the auxiliary subunits of the CNIH and type-I TARP families[148,177,205,206] (Figure 10).

In *Drosophila*, chicken, and yeast, CNIH homologs are a well-known class of ER cargo transporters[207-209]. CNIH2 and CNIH3 are 'Golgi-resident' proteins that shuttle between ER and TGN, with ER-export being carried out in a coat protein complex II (COPII)-dependent manner. Evidence from the yeast homolog suggests that COPII-dependent CNIH trafficking requires the interaction with the COPII component Sec24 through the conserved M3-M4 linker[210]. Cryo-EM structure of CNIH2 and

CNIH3 revealed that CNIHs interact with AMPARs through the CNIH M1 and M2 domains, whereas the M3 and M4 domains face the outside of the complex[164,165], and potentially interact with COPII components[170]. Of the population of auxiliary subunits-containing AMPAR, CNIH2 and CNIH3 co-assemble with ~70% of the receptors, whereas type-Ia TARPs (γ2 and γ3) with the remaining ~30%[109,211]. Whether TARPs act directly as cargo transporters or indirectly via association with other proteins remains unclear. To note, unlike other cargo transporters, neither CNIHs nor TARPs dissociate from their cargo upon exiting the ER. Indeed, CNIH2 and CNIH3 are only present at the plasma membrane when associated with AMPAR[206]. Interestingly, CNIH2 has a greater ability to promote ER-export of AMPARs than γ2[177], and shows preferential association with GluA1-containing AMPARs[212]. Therefore, given the preferential CNIH association with GluA1-containing receptors, the fast ER-export of GluA1/GluA2 heteromers is likely due to the presence of CNIHs as cargo transporters. In contrast, the increased ER-retention and slow trafficking of GluA2/GluA3 heteromers could be a result of the replacement of CNIHs with type-Ia TARP[212,213]. Additionally, the cargo transporter protein interacting with C-kinase 1 (PICK1), a Ca^{2+}-responsive PDZ protein, promotes ER-export and maturation of GluA2/GluA3 heteromers[213,214].

The maturation status of AMPAR has long been suggested to impact AMPAR trafficking and likely receptor function and ligand affinity, reviewed in [35,196]. This process starts in the ER with high-mannose glycosylation, which can be trimmed down and modified into more complex sugars in the Golgi apparatus[196,215,216]. And again, a process that seems to be mediated through the association of AMPAR with auxiliary subunits. Both γ2 and γ8 promote maturation of AMPARs and therefore surface delivery of AMPAR[148,217,218]. An ability that depends on TARPs maturation itself, as overexpression of unglycosylated γ8 mutant was unable to restore the maturation levels of GluA1 and surface delivery in γ8 KO mice[217]. Loss of γ8 was shown to increase the levels of immature GluA2/GluA3 receptors[147], probably due to an increased ER retention. Interestingly, a large population of native AMPARs at the PM is immature, which indicates a bypass of the Golgi apparatus[219,220]. Given the required glycosylation of γ8, it is likely that those immature AMPARs at the plasma membrane are γ8-free AMPARs.

To conclude, it is necessary to know the AMPAR complex composition to properly understand the forward trafficking of AMPARs, as different auxiliary subunits will most likely be involved in specific AMPAR trafficking pathways.

4.3 The blossoming of AMPAR: surface anchoring and AMPAR-mediated excitatory transmission

Over 20 years have passed since the discovery of the first auxiliary subunit, yet, it was not until very recently that we started to put the pieces together and understand how all these different auxiliary subunits control the different aspects of AMPAR-mediated excitatory transmission. Nonetheless, despite the vast and exhaustive data collected over the years, I must say that we barely scratch the surface. As Aristotle once said: '*The more you know, the more you know you don't know*'.

I must say that this topic was perhaps the most difficult to structure. I have initially planned to introduce the function of the different auxiliary subunits by brain region, yet not so much is known about the role of these proteins during AMPAR-mediated transmission beyond the hippocampus. Therefore, the obvious structure would be the classic description of their function by protein family, starting with the prototypical γ2, and maybe stratify by regional and cellular expression followed by their modulatory role of the AMPAR gating in cell lines, and conclude with their role during AMPAR-mediated excitatory transmission in neurons. Yet, that did not seem correct, as AMPARs often contain more than one type of auxiliary subunits. Even if that is not the case for all the receptors, some auxiliary subunits are better explained together due to their particular abundance in a given brain region or cell type. Therefore, here I introduce the different auxiliary subunits one by one following their order of co-association at AMPAR complexes followed by cellular co-expression when no co-assembly is confirmed. While it might seem a bit confusing, this is the way that best describes what we know, *i.e.*, a lot and at the same time, not so much. So before I start, let me take the opportunity to rename this section a '*beautiful mess*'.

Importantly, although not within the scope of the work presented here, and therefore not discussed, it is important to point out that AMPARs interact with proteins other than the auxiliary subunits when at the plasma membrane. Those interactions occur through GluA CTDs or NTDs and have implications on several aspects, such as receptor trafficking, synaptic stabilization, endocytosis, and synaptic transmission and synaptic scaling. The AMPAR CTD is subjected to several post-translation modifications, such as phosphorylation, palmitoylation, ubiquitination, and S-nitrosylation, many of which have been implicated in synaptic plasticity and synaptic scaling, and even behavior; see [221]. In addition, several proteins have been suggested to directly interact with GluA CTDs and are necessary for synaptic plasticity and synaptic scaling. In particular, GluA2 and GluA3 share a consensus sequence, Ser-Val-Lys-Ile, at their C-terminus, through which GRIP family proteins (GRIP1, GRIP2, and AMPAR-binding protein) and PICK1 interact. Whereas, GluA1 CTD contains a 4.1N and SAP97 binding site[127,129].

Despite the extensive work on the role of GluA CTDs in receptor trafficking and plasticity, one big debate in the past decade stands out. Is GluA1 CTD really required for synaptic plasticity? Early molecular replacing studies from Granger and colleagues reported that GluA1 CTD was not required for LTP, but rather suggested a requirement for the extrasynaptic pool AMPARs as demonstrated by overexpression of Arg-unedited GluA2 in triple-flox Gria1/2/3 mice[222]. This was recently supported by Díaz-Alonso and colleagues[223], who used knock-in mice lacking the GluA1 CTD, and replacement strategies to overexpress a chimeric GluA1 containing the GluA2 CTD ($\text{GluA1}_{\text{GluA2CTD}}$) into triple-flox Gria1/2/3 or CRISPR/Cas9-deleted GluA1 knockout neurons. In another study, Zhou and colleagues used a different approach. They generated knock-in mice in which the CTD of either GluA1 or GluA2 was swapped with the CTD of the opposite subunit; $\text{GluA1}_{\text{GluA2CTD}}$ or the CTD of GluA2 with the CTD of GluA1 ($\text{GluA2}_{\text{GluA1CTD}}$)[130]. Zhou and colleagues observed that in $\text{GluA1}_{\text{GluA2CTD}}$, *i.e.*, in animals lacking the GluA1 CTD, LTP was absent. Moreover, in $\text{GluA2}_{\text{GluA1CTD}}$, the authors observed that LTP was enhanced by the presence of the extra copy of GluA1 CTD. These results indicate a role of GluA1 CTD during LTP and contradict[222,223]. However, in a follow-up study, using the $\text{GluA1}_{\text{GluA2CTD}}$ knock-in mice the authors observed that the requirement of GluA1 CTD during hippocampal LTP was age- and induction protocol-dependent[224], and therefore, could explain the discrepancy observed in previous studies; discussed in [123,221].

AMPAR NTDs have also been suggested to play an important role in the regulation of AMPAR stabilization at synapses[118,119,121], although this aspect of GluA biology is still very undeveloped and promises to be equally interesting, although its discussion is beyond the scope of this introduction. Altogether, while auxiliary subunits play a crucial role during AMPAR-mediated transmission (see below), it is important not to forget that several other factors directly or indirectly direct the course of transmission.

4.3.1 AMPAR Biophysics

As mentioned above, AMPARs are the hallmark of fast excitatory transmission. At the plasma membrane and in the absence of an agonist, AMPARs are in a resting – non-conducting closed – state. Glu release at synaptic sites triggers a conformational change and activation of the receptors to an open – ion conductive – state in the order of sub-milliseconds and is responsible for the rapid depolarization of the postsynaptic membrane. Worth mentioning, while full agonists induce maximal activation of the ion channel, partial agonists induce a submaximal activation as a consequence of stabilization of conformations that are less advantageous in the channel activation. Continuous exposure to the agonist induces a rearrangement of the receptor to an active but non-conducting – desensitized – state. Agonist dissociation induces the recovery of the receptor back to the resting state[225]. One of the first steps to unveil the function of each auxiliary subunit is to learn their key signature, *i.e.*, how each one of these proteins differentially modulate the AMPAR gating properties I have just mentioned. However, this is not always helpful, as in some cases those key signatures can be masked by the presence of other auxiliary subunits in the AMPAR complex.

The presence of TARPs in the AMPAR complex produces a moderate slowdown of receptor deactivation and desensitization, with type-Ib TARPs exerting a further slowdown than type-Ia TARPs. Additionally, the presence of type-I TARPs accelerates AMPAR recovery from desensitization in heterologous cells[144,145,155,226-228]. While the magnitude of the AMPAR gating modulation is dependent on the TARP subunit, GluA subunits and splice variants play an equal role in the extent of TARP-induced AMPAR gating modulation as different GluA subunits will have a different response[146]. That said, different brain regions and cell types will have different degrees of modulation mediated by the same TARP subunit as a consequence of different GluA tetramer combinations. Similar to type-Ia TARPs, GSG1l moderately slows deactivation and desensitization of AMPARs. Whereas in contrast to TARPs, GSG1l dramatically slows AMPAR rate of recovery from desensitization in heterologous cells[109,160,161]. CNIHs on the other hand, dramatically slow down AMPAR deactivation and desensitization but do not seem to modulate the receptor recovery from desensitization in heterologous cells[211,212,229,230]. In addition, auxiliary subunits modify the AMPAR pharmacological profile, of each enhanced Glu response as observed by the presence of TARPs or CNIHs in the AMPAR complex[146,155,226,228,230,231].

In sum, it is of utmost importance to understand the AMPAR complex composition, as it is the auxiliary subunit composition that will ultimately shape and confer the vast heterogeneity of AMPAR-mediated responses observed across the different brain regions and cell types, and further discussed below.

4.3.2 Regulation of AMPAR-mediated excitatory transmission by γ2

To not break the tradition, I will start with the prototypical AMPAR auxiliary subunit, γ2. This prototypical AMPAR auxiliary subunit is highly expressed in the cerebellum and at low levels in the hippocampus[71,148,232]. It is particularly important for the delivery of AMPAR to the plasma membrane of cerebellar granule cells[71]. Additionally, γ2 has also been implicated in several other AMPAR-related functions such as surface diffusion[69,233-235], stabilization[231], endocytosis[236], and synaptic targeting of AMPARs[70,71,78], and consequently, highly involved during synaptic plasticity[237,238] and synaptic scaling[239,240].

As mentioned above, γ2 contains the canonical PDZ-binding motif (Figure 11), which has been shown to interact particularly with PSD95, – but also PSD93[71,241], in a phosphorylation-dependent manner[235,242,243]. Consequently, γ2 and PSD95 interaction has been proposed to mediate AMPARs synaptic abundance by regulating receptor diffusion-trapping at synaptic sites from extrasynaptic receptors[69,70,244]. Indeed, deletion of the γ2 PDZ-binding motif destabilizes synaptic AMPARs, as observed by their increased mobility at PSD sites, and decreased AMPAR-mediated synaptic currents[69,70]. Note that the PDZ-binding motif is not the only motif at the TARPs CTD responsible for the interaction with PSD95. In addition to the PDZ-binding motif, type-I TARPs CTD display three additional conserved motifs (Figure 11), the Ser-rich motif, Arg-rich motif, and three aromatic residues-containing hydrophobic motifs (φ1/2/3)[245]. The positively charged stretch of conserved Arg residues mediate TARPs CTD interaction with the negatively charged phospholipids of lipid membranes via electrostatic interactions[235,246], crucial during AMPAR-mediated plasticity[245]. Whereas, some of the Ser residues that compose the Ser-rich motif have been implicated in the regulation of TARPs-dependent AMPAR-mediated plasticity via PSD95 interaction, as further discussed below. Recently, Zeng and colleagues observed that the γ2 CTD undergoes liquid-liquid phase separation with PSD95[245], a characteristic of several PSD proteins[247-249]. Interestingly, all four domains of TARPs CTD were shown to influence the formation of the liquid-liquid phase separation with PSD95; while the aromatic residues-containing hydrophobic motifs exert a moderate-to-strong effect on the formation of the liquid-liquid phase separation, both PDZ-binding motif, and the Ser- and Arg-rich motifs are crucial in the formation of this lipid-like droplet between γ2 and PSD95[245]. In neurons, the two first PSD95 PDZ domains (PDZ1 and PDZ2) have been suggested as the preferential binding sites of γ2-containing AMPARs[70,250]. It is worth highlighting that γ2 CTD and PSD95 binding affinity is one the strongest PSD95 PDZ1/PDZ2-target interactions ever reported[245]. Zeng and colleagues observed that whereas the PDZ-binding motif of γ2 binds with the PSD95 PDZ2 domain, the Arg-rich motif binds to the PSD95 PDZ1 domain[245]. However, phosphorylation of the Ser-rich motif causes elongation of the γ2 CTD into the cytosol, which shifts the γ2 CTD binding to the deepest and highest affinity PDZ2/PDZ3 domains of PSD95[235]. Altogether, the multivalent interaction between TARPs CTD and PSD95 is essential for trapping and stabilization of TARP-containing AMPARs at PSD sites, and consequently, for synaptic transmission.

At the hippocampal Schaffer collateral-commissural synapses, γ2 is expressed at perforated synapses – which contain a high density of AMPARs –, but not at non-perforated synapses that on the contrary have a low density of AMPARs[251]. AMPARs diffusion in and out from synaptic sites is a well-established requirement during synaptic plasticity[98]. Hence, phosphorylation/dephosphorylation of the γ2 PDZ-binding motif and subsequent binding to PSD95 has been associated with synaptic plasticity. In dissociated hippocampal neurons, phosphorylation of Thr321 in the PDZ-binding motif of γ2 by protein kinase A (PKA) (Figure 11) promotes synaptic targeting of γ2 and is required during chemical LTP induction, whereas LTD requires dephosphorylation of Thr321 of γ2 by mitogen-activated protein kinases (MAPKs)[237]. To add another level of complexity, in addition to the phosphorylation at the PDZ-binding motif, γ2 can be phosphorylated at the conserved Ser-rich motif. Phosphorylation of the Ser-rich motif prevents binding of the γ2 CTD to the lipid bilayer by neutralizing the positively charged Arg-rich motif. Consequently, phosphorylation of the Ser-rich motif induces effective extension of the CTD into the cytosol, which favors γ2 interaction with the PSD95; the opposite is observed during dephosphorylation[235,246]. NMDAR-dependent synaptic activity was shown to regulate both phosphorylation and dephosphorylation of the γ2 Ser-rich domain[252]. NMDAR-dependent LTP triggers CaMKII-dependent phosphorylation of γ2[252,253], which in turn immobilizes γ2-containing AMPARs at the synaptic sites[234]. Also, hippocampal activation of ghrelin was shown to trigger protein kinase C (PKC)-dependent phosphorylation of γ2 Ser-rich domain in an activity-dependent manner during LTP[254]. On the other hand, NMDAR-dependent LTD promotes γ2 dephosphorylation by phosphatase 1 (PP1) – downstream of calcium/calmodulin-dependent protein phosphatase 2B protein phosphatase-2B (PP2B)/calcineurin[252], and subsequent association with adaptor proteins to induce clathrin-dependent AMPAR endocytosis[236]. Consistently, cerebellar LTD at parallel fiber (PF) onto Purkinje cell synapses requires calcineurin-mediated dephosphorylation of γ2 Ser-rich domain[238].

In addition to synaptic plasticity, γ2 is also involved in AMPAR-mediated synaptic scaling (or homeostatic scaling), a form of homeostatic plasticity in which neurons adjust their synaptic strength in response to chronic alterations in the network activity by regulating the number of synaptic receptors[255]. Tetrodotoxin-induced synaptic upscaling triggers AMPAR synaptic delivery that is dependent on phosphorylation of γ2 Ser-rich domain[239]. In contrast, synaptic downscaling triggers dephosphorylation of γ2 Ser-rich domain, which increases γ2 and AMPAR mobility at the plasma membrane, and AMPAR endocytosis[240].

A topic that has raised a lot of controversy, and no consensus has been achieved to date, is whether auxiliary subunits dissociate or not from the receptor at the plasma membrane. Upon AMPA-induced AMPAR internalization, Tomita and colleagues observed that γ2 and γ3 internalized levels were unaffected by AMPA treatment, while AMPARs were heavily internalized. Moreover, AMPA-induced internalization led to a decrease in AMPAR and γ3 association at the surface, which suggested a possible dissociation of TARPs from the AMPAR complex[231]. These observations were later backed up by the observation that Glu induced a transient dissociation of γ2 from AMPAR complexes[233,256]. However, the veracity of that dissociation has also been questioned by others' work[257-259].

Given the importance of TARPs in the stabilization of AMPAR at the plasma membrane and synaptic targeting, it is of utmost importance to comprehend if dissociation of auxiliary subunits does occur at the plasma membrane of neurons.

4.3.3 Regulation of AMPAR-mediated excitatory transmission by γ8

γ2 is not the only TARP member to be detected in the hippocampus. Indeed, γ3 and γ8 are also present in the hippocampal *Cornu Ammonis* (CA) region[130,148,251,260]. Highly expressed and the most abundant TARP subtype in the hippocampus[148,261], γ8 is widely distributed through the surface of pyramidal neurons dendrites[261,262]. Interestingly, at Schaffer collateral-commissural onto CA1 synapses, γ8 is the only TARP expressed at nonperforated synapses, and to a lower extent in perforated synapses along with γ2[251]. Interestingly, while loss of γ2 results in similar AMPAR densities between both nonperforated and perforated synapses, as a result of the decrease of AMPAR in the latter, loss of γ8 severely decreases AMPAR density at nonperforated synapses. In conclusion, γ8 contributes to the regulation of AMPAR expression at nonperforated synapses, while γ2 plays a crucial role in the high expression of AMPARs at perforated synapses[251]. Unlike γ2, γ8 mostly regulates the AMPARs basal transmission in the CA1 neurons. Loss of γ8 leads to a nearly complete depletion of extrasynaptic AMPAR-mediated currents, but only to a mild reduction of the synaptic AMPAR-mediated currents[147]. As above mentioned, LTP requires AMPAR recruitment and trapping at synapses. Consistently, loss of γ8 drastically impairs LTP at CA1 synapses[147] and dentate gyrus medial perforant path synapses[263], but not LTD[147]. γ8 CTD is subjected to phosphorylation[262,264], of which, the γ8 CaMKII-dependent phosphorylation sites Ser277 and Ser281 at the Ser-rich motif were shown to mediate hippocampal LTP and, learning and memory[264]. Compared to other TARPs, γ8 has a unique long CTD containing a Pro/Ala-rich domain that binds to calcineurin/PP2B[265] (Figure 11). It is, therefore, possible that such interaction mediates trafficking and phosphorylation of AMPARs. γ8 PDZ-binding motif was shown to regulate AMPAR-mediated basal synaptic transmission, but not synaptic plasticity, *i.e.*, LTP[266]. Conversely, Sheng and colleagues observed that γ8 PDZ-binding motif was necessary for LTP at CA1 synapses, but not phosphorylation of the γ8 Ser-rich motif [267]. However, the striking difference of Sheng *et al.* from previous studies is most likely due to different experimental strategies, as Sheng and colleagues relied on overexpression of GluA1 and γ8 in triple-floxed *Gria1-3* mice. Therefore, the authors hypothesized that in the case of GluA1 homomeric AMPARs, γ8 PDZ interaction, but not Ser-rich motif phosphorylation, was necessary for synaptic targeting, and consequently LTP induction[267]. While γ8 PDZ-binding motif is crucial for the synaptic targeting and transmission of GluA1 homomeric AMPARs, this is not necessarily valid for other GluA2-containing AMPARs[121]. To note, the Arg-rich motif of γ8 was recently shown to mediate PSD95 interaction and required for hippocampal LTP[245].

In sum, phosphorylation of the Ser residues at the Ser-rich motif of γ8 mediates hippocampal LTP[264]; phosphorylation of γ2 Ser-rich motif prevents γ2 Arg-rich motif and plasma membrane interaction, which results in an effective extension of the γ2 CTD into the cytosol and access to deeper domains of PSD95[235]; and, TARPs Arg-rich motif binds PSD95 PDZ1 and is required for hippocampal LTP[245]. Taken together, one of the mechanisms involved in γ8-dependent AMPAR-mediated LTP is likely to occur as followed: 1) NMDAR-dependent CaMKII activation induces phosphorylation of Ser residues 277 and 281 at the Ser-rich motif; 2) phosphorylation of the Ser-rich motif neutralizes the interaction of the positively charged Arg residues and negatively charged phospholipids; 3) γ8 CTD detaches from the plasma membrane and stretches into the cytosol; 4) lengthening of γ8 CTD into the cytosol allows binding of the Arg-rich motif to the PSD95 PDZ1, and access of the γ8 PDZ-binding to the deeper domains of PSD95; 5) multivalent γ8/PSD95 interaction further enhances trapping and stabilization of γ8-containing AMPARs at PSD, and enhances synaptic response. This phosphorylation-dependent Ser-rich motif-induced Arg-rich motif binding to PSD95 PDZ domains is likely to be translated to all the type-I TARPs. It is, however, important to note that other mechanisms might be involved in different transmission pathways, as for example the phosphorylation of the TARPs PDZ domains.

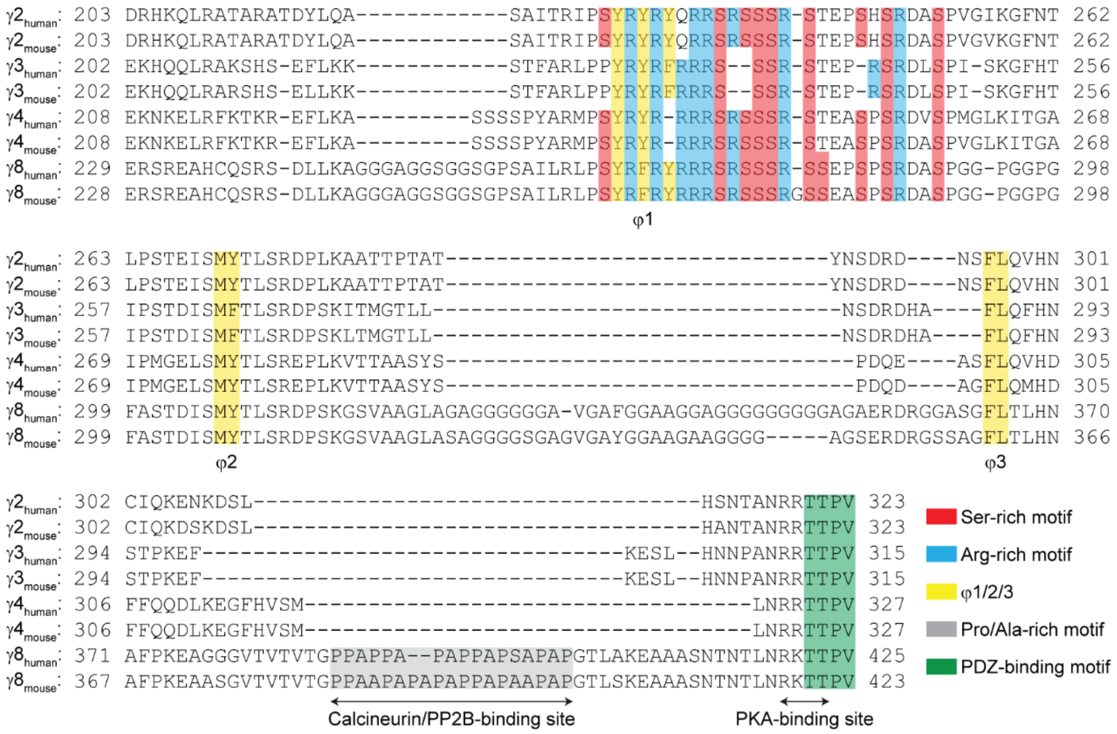

Figure 11: TARPs CTD conserved domains. Detailed sequence alignment of the type-I TARP CTDs from different species. Highlighted the conserved Ser-rich motif (red), Arg-rich motif (blue), three aromatic residues-containing hydrophobic motifs (φ1/2/3; yellow), PDZ-binding motif (green), and the conserved γ8 Pro/Ala-rich motif. Arrows indicate the predicted TARPs PKA-binding site and γ8 calcineurin/PP2-binding.

4.3.4 Regulation of AMPAR-mediated excitatory transmission by CNIH2

One cannot talk about γ8 without talking about CNIH2. Identified by Schwenk and colleagues[211] as one of the AMPAR auxiliary subunits in 2009, CNIH2 and CNIH3 are expressed throughout the brain[211,229,268], with CNIH2 having the highest expression in the hippocampus[229]. In the hippocampus, CNIH2 co-assembles with γ8-containing GluA1/GluA2 heteromers[135,212,229], thus, CNIHs follow the same surface distribution of γ8 in pyramidal cells[211,261,262]. To note, CNIHs are practically excluded from type-Ia TARP (γ2 and γ3)-containing AMPAR complexes[211]. Consequently, CNIHs are not expressed, at least at detectable levels, at the plasma membrane of the cerebellar granule cells[211], where expression of γ2 is crucial for the forward trafficking of AMPARs and synaptic transmission[149].

CNIHs strongly slows AMPAR decay kinetics and modulates pharmacology[211,230,269,270]. In the CA1 neurons, CNIH2 and γ8 synergistically modulate AMPAR kinetics[165,229,270,271]. γ8 (also γ4 and γ7) induces resensitization of recombinant AMPARs, which is suppressed by the presence of CNIH2[229,270]. The loss of γ8 drastically decreases the pool of CNIH2-containing AMPARs[212,229,270], suggesting that association with γ8 is crucial for stabilization of CNIH2-containing AMPARs, while CNIH2 fine-tunes the γ8-mediated AMPAR gating modulation. Moreover, similar to the loss of γ8[147], loss of CNIH2/CNIH3 results in a depletion of extrasynaptic AMPARs[212,229], and subsequently, impairs LTP at CA1 synapses[212]. In hilar mossy cells of the dentate gyrus, CNIH2 slows AMPAR kinetics[272]. Unfortunately, not so much is known about the role of CNIH3.

Altogether, CNIHs have as primary role to promote forward trafficking of GluA1-containing AMPARs, but can also be implicated in the fine tuning of AMPAR gating kinetics.

4.3.5 Regulation of AMPAR-mediated excitatory transmission by SynDIG4

Like for CNIH proteins, knowledge about SynDIG4 remains scarce. Recently, cryo-EM data of native hippocampal AMPAR complexes identified a single helix structure at the periphery of CNIH2/γ8-containing AMPARs presumed to be SynDIG4[135]. Thus, it would make no sense other than to introduce SynDIG4 right after having discussed CNIH2 and γ8. This ‘outer’ core auxiliary subunit is a peculiar auxiliary subunit that similarly to γ8 has been suggested to regulate the extrasynaptic pool of AMPARs. SynDIG4 is highly enriched in the hippocampus[166], preferentially associated with CNIH2/γ8/GluA1-containing AMPARs[109,110,135]. SynDIG4 is enriched at the extrasynaptic sites where it stabilizes GluA1-containing AMPARs through the phosphorylation of Ser845 in the CTD of GluA1[167,273], probably, via interaction with PP2B[274]. The activity-dependent phosphorylation of GluA1 Ser845 stabilizes extrasynaptic GluA1-containing AMPARs – especially, Ca^{2}-permeable AMPARs – at the plasma membrane by blocking endocytosis[104,275-277] enhancing synaptic strength during LTP[278,279]. In agreement, SynDIG4 knockout mice exhibit impaired GluA1-dependent LTP, but not GluA1-independent (NMDAR-dependent) LTP[167,273]. Interestingly, previous work reported that a single weak tetanus failed to elicit LTP, but not theta-burst stimulus in GluA1 knockout mice[280], suggesting a potential contribution of Ca^{2+}-permeable AMPARs in the single weak tetanus-induced LTP. In contrast, NMDAR-dependent LTD was impaired in SynDIG4 knockout mice. NMDAR-dependent LTD requires transient synaptic incorporation of Ca^{2+}-permeable AMPARs, which is dependent on PKA-dependent phosphorylation of GluA1 Ser845[281]. Of note, SynDIG4 was shown to decrease desensitization of recombinant GluA1 homotetramers but not of GluA1/GluA2 heterotetramers[167].

Altogether, SynDIG4 plays a crucial role in the maintenance of extrasynaptic GluA1-containing AMPARs, and, likely, contributes to Ca^{2+}-permeable AMPAR-dependent synaptic plasticity.

4.3.6 Regulation of AMPAR-mediated excitatory transmission by γ3 and γ4

γ3 is the most abundant type-I TARP in the cerebral cortex, but is also expressed in the hippocampus' pyramidal layer[148,260]. Unlike γ2 and γ8, the existence of γ3 tends to be neglected as no major differences in AMPAR expression are observed upon loss of γ3[251], therefore, its role is still unknown. Interestingly, immunostaining against γ3 reveals a moderate-to-strong expression of γ3 at pyramidal cell bodies, but practically absent from the dendritic network[260]. Taken together, it is likely that at the hippocampus each TARP plays a specific role in the organization of AMPARs at the plasma membrane. During hippocampal basal transmission, γ2 would be in charge of synaptic delivery and anchoring of AMPARs, γ8 in the regulation of extrasynaptic pool of AMPARs, whereas γ3 could potentially regulates the somatic population of AMPARs; to note, this is just a possibility based on the expression pattern of the three TARP subtypes, and apparent absence of compensatory effect observed by γ3 on knockout γ2 or γ8 mice. Also, no differences in AMPAR levels and response were observed in hippocampus of γ3 knockout[251] or γ3/γ4 double-knockout[282] mice, respectively. It is, however, possible that different expression patterns of TARP subunits across different brain regions and cell types may result in different TARP-specific AMPAR regulations. In the cerebellar cortex, where it is most abundant, γ3 is enriched at synapses, therefore, and similarly to γ2, γ3 may be involved in AMPAR synaptic delivery and anchoring in a brain region-specific manner[231,241].

Similarly to γ3, not much is known regarding γ4. The fact that γ4 is the major TARP subtype widely expressed throughout the brain in early developmental stages[110,148,232], suggests that γ4 might regulate synaptogenesis, by providing a particular increased sensitivity to Glu compared to other TARPs[145,227]. In the adult brain, γ4 is expressed in glial cells[148,232] suggesting a potential role in regulatory or communication processes through regulation of glial AMPARs. Interestingly, in the nucleus accumbens, subcellular fractionation assays revealed an almost exclusive enrichment of γ4 at extrasynaptic membranes, whereas γ2 was mostly found at synaptic membranes[283]. It is important to note that like γ4, γ8 is also highly expressed in the nucleus accumbens[110], but not in dissociated nucleus accumbens medium spiny neurons[283]. This is of particular interest as similar distribution between the type-Ia γ2 and type-Ib γ8 is observed in the hippocampus[261,262], where γ8 is crucial for the regulation of the extrasynaptic pool of AMPARs and maintenance of hippocampal LTP[147]. Therefore, it would be interesting to observe if in the nucleus accumbens, type-Ib γ4 regulates extrasynaptic AMPARs and AMPAR-dependent LTP in medium spiny neurons, and thus understand if such processes are common to type-Ib TARPs.

Of note, similar to γ2 and γ8, both γ3 and γ4 contain all four CTD domains above described, and it would be interesting to investigate their impact during γ3- and γ4-mediated AMPAR transmission. However, given the redundancy of TARPs and possible compensatory mechanisms, it is important to first identify the cell types that best rely on either γ3 or γ4 during AMPAR-mediated transmission.

4.3.7 Regulation of AMPAR-mediated excitatory transmission by GSG1l

As already discussed, GSG1l is a distant homolog of TARPs to which it is structurally related[109,160], and it binds to the same surface AMPARs as TARPs[161]. Similarly to type-I TARPs, GSG1l slows desensitization of recombinant AMPARs, but contrary to TARPs, it slows AMPAR recovery from desensitization in heterologous cells[109,160,161]. GSG1l is expressed in the hippocampus, cortex, thalamus, and striatum[160,284,285]. In CA1 neurons, GSG1l negatively regulates surface trafficking of AMPARs and promotes AMPAR endocytosis[163]. Interestingly, in CA1 neurons, GSG1l increases deactivation and desensitization of AMPARs, as well as, recovery from desensitization[163], contrary to the observations in heterologous cells[160,163], which could be a result of altered AMPAR complex composition upon overexpression or loss of GSG1l. Of note, co-expression of GSG1l and CNIH2 in heterologous cells abolishes CNIH2 slowdown of AMPAR kinetics[163]. Moreover, while hippocampal LTP at Schaffer collateral-CA1 synapses is drastically impaired in γ8[147,263] and CNIH2/CNIH3[212] knockout mice, loss of GSG1l enhances LTP at CA1 synapses[163]. Similarly to its function in CA1 neurons, GSG1l negatively modulates basal AMPAR-dependent synaptic transmission in dentate gyrus granule cells[286]. However, while GSG1l modulates AMPAR kinetics and LTP at CA1 neurons[163], endogenous GSG1l seems to not modulate AMPAR kinetics neither LTP at dentate gyrus granule cells[286]. Additionally, in the anterior thalamic nuclei, GSG1l is highly expressed at anterodorsal and anteroventral nucleus, but absent at anteromedial nucleus[285]. The anterior thalamic nuclei are at the core of the hippocampal-diencephalic-cingulate network with implications in spatial learning and memory[287-289]. In the anterodorsal and anteroventral nucleus neurons, GSG1l negatively regulates short-term plasticity at corticothalamic synapses, whereas in the subiculum-thalamic and mammillothalamic synapses, in which both γ2 and GSG1l are co-expressed, γ2 outcompetes GSG1l modulation over AMPARs[285].

Overall, GSG1l negatively regulates AMPAR-mediated synaptic transmission.

4.3.8 Regulation of AMPAR-mediated excitatory transmission by Shisa9

The Shisa family, previously known as cysteine-knot AMPAR modulating proteins (CKAMPs), is composed of four AMPAR auxiliary subunits – Shisa6/CKAMP52, Shisa7/CKAMP59, Shisa8/CKAMP39, and Shisa9/CKAMP44 – of type-I transmembrane proteins, with a conserved extracellular cysteine-knot motif and a cytosolic CTD containing a PDZ type II motif[290-292], for review see [293,294]. While the cysteine-knot domain is fundamental for the modulation of AMPAR gating[263], the PDZ type II motif is important for synaptic delivery of AMPARs[263,295,296]. Given the fact that for the moment there is no available data on the neuronal function of Shisa8, Shisa8 cannot be considered as a true auxiliary subunit, and therefore, it is not discussed here.

Like SynDIG4, Shisa proteins are suggested to occupy the periphery of the AMPAR macromolecular complex[109]. Shisha9 was the first member to be identified. It is widely expressed throughout the brain but particularly enriched at the dentate gyrus of the hippocampus[290]. Interestingly, proteomic correlation analysis suggested a likelihood of Shisa9 to co-assemble with GSG1l- and GluA3-containing AMPARs[110]. Shisa9 is highly enriched at synaptic sites[290,297], and it was shown to modulate AMPAR gating by slowing recovery from desensitization, similarly to GSG1l[160,290]. However, Shisa9 and

GSG1l have opposite effects on the modulation of AMPAR desensitization[160,290]. In dentate gyrus granule cells, most AMPARs are likely to be associated with Shisa9, where it modulates short-term plasticity[263,290]. Moreover, in dentate gyrus granule cells, Shisa9 and γ8 are part of the same AMPAR complex and are crucial for surface delivery and stabilization of AMPARs, including synaptic targeting of AMPARs[263,298]. Of note, Shisa9 interacts with PICK1[299], which promotes the ER-export of AMPARs[300]. Shisa9 and γ8 both modulate AMPAR-dependent synaptic short-term plasticity in dentate gyrus granule cells, but in the opposite manner due to their differential modulation of AMPAR gating. γ8, but not Shisa9, is necessary for LTP in dentate gyrus granule cells[263]. In addition to dentate gyrus granule cells, Shisa9 was also observed to promote surface trafficking of AMPARs and modulation of AMPAR-mediated synaptic short-term plasticity in dorsal lateral geniculate nucleus relay neurons[139].

4.3.9 Regulation of AMPAR-mediated excitatory transmission by Shisa6

Shisa6 is highly expressed in the hippocampus, cerebellum, and septum[291,295], but in contrast to Shisa9, Shisa6 is highly expressed in pyramidal neurons[293]. In the CA1 region, Shisa6 is enriched at PSD areas associated with AMPARs[295]. Interestingly, overexpression of Shisa6 in dissociated hippocampal neurons decreases lateral surface mobility of AMPARs through a PDZ-dependent PSD anchoring of AMPARs[295]. Like Shisa9, Shisa6 slows desensitization of recombinant GluA1- and GluA2-containing AMPARs in both HEK293T cells and Xenopus oocytes[291,295]. However, in contrast to Shisa9, Shisa6 enhances the steady-state current[290,295]. Moreover, while in dentate gyrus granule cells, Shisa9 reduces synaptic facilitation[290], Shisa6 modulates AMPAR-dependent synaptic short-term plasticity in a frequency-dependent manner in CA1 pyramidal neurons by slowing down the entry of AMPARs into a desensitized state[295]. Additionally, in the cerebellum, Shisa6 was found to facilitate Purkinje cell synaptic excitability[301]. While Shisa6 does not significantly affect the synaptic fraction of AMPARs in CA1 neurons[295], loss of Shisa6 in Purkinje cells results in a robust decrease of surface expression of GluA2- and GluA3-containing AMPARs[301]. Interestingly, Shisa6 is required for parallel fiber onto Purkinje cell synapses LTP, but not LTD[301].

4.3.10 Regulation of AMPAR-mediated excitatory transmission by Shisa7

Shisa7 is highly expressed in the cortex, hippocampus, amygdala, striatum, and olfactory bulb[291,296]. In CA1 neurons, and as Shisa6[295], Shisa7 is enriched at PSD associated with AMPARs[296]. Of note, in contrast to Shisa6 and Shisa9, Shisa7 does not modulate short-term plasticity in the hippocampus[263,290,295,296]. However, Shisa7 is important for LTP initiation and maintenance in CA1 neurons[296]. Of note, Shisa7 is also localized at GABAergic synapses as a $GABA_A$ receptor-auxiliary subunit, where promotes surface trafficking and modulation of channel kinetics of these receptors[302,303].

Like TARPs, different Shisa subtypes show differential regional distribution, as well as different modulation over AMPAR-mediated transmission. Therefore, more studies must be conducted to address the different roles of Shisa proteins across the different brain regions and cell types, and investigate if Shisa8 is indeed a true AMPAR auxiliary subunit.

4.3.11 Regulation of AMPAR-mediated excitatory transmission by γ7

To wrap up this section, nothing better to end where this vast world of auxiliary subunits started, the cerebellum of the stargazer mice. But, this time the spotlight goes to γ7, as γ2 was already discussed. As suggested by this introduction, this type-II TARP is highly expressed in the cerebellum, more particular, at inhibitory Purkinje cells, Golgi cells granule cells, and stellate cells[304]. It retains most of the canonical TARP-mediated AMPAR gating modulation[304], including the resensitization of AMPARs of TARPs type-Ib[229,270,304], but differentially modulates AMPAR pharmacology[304,305]. Interestingly, γ7 modulatory function on GluA2-containing AMPARs is dependent on GluA2 Gly/Arg editing[305].

The exact role of γ7 remains unclear as no phenotype is displayed by γ7 knockout mice[306,307], which together with the severe phenotype observed in stargazer mice[71,149], suggests that γ7 has minimal contribution to excitatory transmission. Nevertheless, it has been proposed that γ2 and γ7 cooperatively regulate AMPAR synaptic targeting and synaptic transmission in the cerebellum[306,308,309]. γ7 shows preferential association with GluA1- and GluA4-containing AMPARs[304,306]. In addition, whereas loss of γ2 leads to a drastic reduction of GluA2- and GluA3-containing AMPARs, and a lesser extent GluA4-containing AMPARs in the cerebellum, loss of γ7 results in a moderate reduction of GluA1- and GluA4-containing AMPARs but not GluA2- or GluA3-containing AMPARs[306], suggesting that γ2 and γ7 are required for forwarding trafficking of Ca^{2+}-impermeable and Ca^{2+}-permeable AMPARs, respectively. The overall loss of GluA1- and GluA4-containing AMPARs in the cerebellum of γ7 knockout mice was primarily a result of loss of these receptors in Bergmann glial cells[306]. γ7 is enriched at PSD[304,306], specifically, at asymmetric synapses, similarly to γ2[306]. Consistently, in cerebellar granule cells and stellate cells, γ7 was proposed to selectively promote synaptic targeting of Ca^{2+}-permeable AMPARs, but is also found associated with those receptors at extrasynaptic sites. Interestingly, while γ7 is not required for synaptic targeting of Ca^{2+}-permeable AMPARs – as TARPless AMPARs can be observed at synapses of both cerebellar granule cells and stellate cells in stargazer mice –, the presence of both TARPs (*i.e.*, γ2 and γ7) is required for the proper balance of surface AMPARs and incorporation of γ7-containing AMPAR at these synapses[308,309].

At climbing fiber onto Purkinje cell synapses, loss of γ7 had no apparent impact on the climbing fiber response, contrary to selective loss of γ2 at Purkinje cells, which drastically reduced AMPAR-mediated excitatory transmission. However, the loss of both γ2 and γ7 further impaired the climbing fiber response on Purkinje cells. Whereas, selective loss of γ2 at Purkinje cells had minimal impact on the motor behavior, the additional loss of γ7 severely impaired motor behavior. Thus, γ7 alone can sustain excitatory transmission at Purkinje cells compatible with normal motor behavior[307].

Altogether, while more work is necessary to clarify the role of γ7, the data so far supports a minimal role of γ7 over AMPAR-mediated transmission, yet, together with γ2, it coordinates the cerebellar synaptic transmission and motor behavior.

4.3.12 The importance of auxiliary subunits in AMPAR-mediated transmission

In the past two decades, several groups have done incredible work in deciphering the role of each one of the different auxiliary subunits. While initial work conducted in heterologous cells suggested redundancy of the function of several of these proteins, studies conducted in neuronal cells have helped us to demystify the true role of some of these proteins in native conditions. It is interesting to see that while some proteins, like γ2 and γ8, play very distinctive but vital roles for proper AMPAR-mediated transmission, others like CNIH2 and SynDIG4 have a more subtle role, more like a fine tuning of AMPAR-mediated transmission. In the hippocampus, γ8 pairs up with CNIH2 to promote trafficking and stabilization of extrasynaptic AMPARs, important for hippocampal LTP[147,212,229,263]. In this scheme, SynDIG4 would potentially support the regulation of extrasynaptic Ca^{2+}-permeable CNIH2/γ8-containing AMPARs[135,167,273]. In turn, γ2 plays a pivotal role on surface diffusion[69,233-235], synaptic targeting and anchoring of AMPARs[70,71,78], consequently implicated during AMPAR-mediated synaptic plasticity (LTD and LTD)[237,238], and homeostatic plasticity (downscaling and upscaling)[239,240]. GSG1l is an interesting auxiliary subunit, its role seems to be brain region and cell-type specific. Nonetheless, GSG1l is a negatively regulator of AMPAR-mediated synaptic transmission[163,285,286]. As for Shisa proteins, they are enriched at synaptic sites. Both Shisa6 and Shisa9 are implicated in the regulation of hippocampal[295] and dorsal lateral geniculate nucleus AMPAR-mediated synaptic short-term plasticity[139]. In contrast, Shisa7 mediates initiation and maintenance of LTP at CA1 neurons[296]. Finally, in the cerebellum, γ2 is fundamental for AMPAR-mediated synaptic transmission[71,149,310]. Whereas, γ7 pairs up with γ2 for synaptic incorporation of γ7-containing AMPARs[308,309].

An interesting aspect is the fact that CNIHs and type-Ia TARPs form distinct AMPAR complexes[211]. However, at the hippocampus CNIH2 is preferentially associated with type-Ib TARP γ8-containing AMPARs[135,212,229], where CNIH2 occupies the AMPAR A'C' sites (typically GluA1), and γ8 the AMPAR B'D' sites (GluA2)[135,165]. First, it is unclear why in neurons CNIHs associate with γ8, but not with γ2/γ3-containing AMPARs. Second, in recombinant cells, CNIHs are capable to associate with all four AMPAR subunit[206,230,311], and given that the binding residues in GluA1 and GluA2 TMD are fully conserved, it is unclear why this preferential configuration. It is, however, possible that these preferential auxiliary subunits arrangement are based on different affinities of auxiliary subunits towards different GluA subunits, as well as, the local concentration of auxiliary proteins. However, there is another aspect that may explain why CNIHs and γ8 occupy AMPAR A'C' and B'D' positions, respectively. As discussed above, auxiliary subunits at the A'C' positions are locate beneath the LBD dimers, whereas the ones at the B'D' positions are positioned beneath the LBD dimer-of-dimers interface and thus spatially less restricted than the ones located at the A'C' positions. Like γ8[46,135,165], GSG1l also has a 'bulky' ECD and shows preferential association towards the B'D' positions[161]. Moreover, outside-out patches from oocytes co-expressing GSG1l and γ2 with AMPAR show identical AMPAR gating properties to the cells expressing γ2 with AMPAR[109], which could suggest that either γ2 dominates the gating modulation of AMPAR over GSG1l, or simply, that in the presence of equal amounts of γ2, GSG1l is unable to associate/compete for a position in the AMPAR complex. Taken together, from a simplistic point-of-view, TARPs seem to have higher affinity towards AMPARs than other auxiliary subunits. However, spatial constrains might favour binding of alternative auxiliary subunits. This would explain why CNIHs are not present in type-Ia TARP-containing AMPARs – which have small ECDs –, but are able to co-assemble with the 'bulky' γ8.

Unfortunately, several proteins remain poorly investigated such as CNIH3, Shisa8 and γ4, among others. And, most of the knowledge about the function of these proteins arrives from one or two brain regions, usually hippocampal CA1 and dentate gyrus, or cerebellum. Additionally, the fact that more than one auxiliary subunit can be associated at the same AMPAR complex, and that overexpression or loss of a specific auxiliary subunit likely shifts the balance of AMPAR and auxiliary subunit complexes, makes the study and translation to other brain regions practically impossible. Nevertheless, it is clear that auxiliary subunits are fundamental for AMPAR-mediated excitatory transmission in a healthy brain, and that more work is necessary.

Given the crucial role of AMPAR interacting proteins at different stages of the AMPAR lifecycle and their close apposition, one of the main problems when attempting to study them is the lack of proper tools. Therefore, my main goal during these four years within the team of Dr. Daniel Choquet was to develop different tools and strategies that could be potentially used for the study of mechanisms implicated in the interaction with AMPAR and different interacting proteins. In particular, the development of tools to study the early steps of AMPAR biogenesis, but also during AMPAR-mediated transmission by designing new tools to target specific surface populations of auxiliary subunits.

Methods

Plasmid constructs

Plasmid amplification was performed via transformation in E. coli DH5α (Thermo Fisher Scientific, #EC0111), and DNA isolation via MAXI-prep ZymoPURE II Plasmid kits (Zymo Research).

The mCherry was inserted at position 886 aa of GluA1 (flop isoform; GluA1::mCherry) coding sequence in pRK5 vector using the restriction sites AgeI/NheI after PCR amplification using the oligonucleotides: GluR1_F, 5’-GCTAGCGGAGGAGGTGGTTCTGGTAAGTCCATGCAATCCATTCC-3’ and GluR1_R, 5’-GTCAGCCAGGACTTCCCCGGAGGAGGTGGTTCTGGTACCGGT-3’.

The plasmid for the expression of FRRS1l was a gift from Laurence Colleaux.

The eGFP was subcloned at the N-terminus of FRRS1l (eGFP::FRRS1l) using the AgeI/BspEI sites.

AgeI/NheI restriction sites were introduced after the signal peptide of FRRS1l to insert mScarlet-I or mCherry at N-terminus of FRRS1l (mScarlet::GluA1 and mCherry::FRRS1l, respectively) coding sequence in Clontech N1 vector.

The mScarlet-I was inserted at the C-terminus of FRRS1l (FRRS1l::mScarlet) using the oligonucleotides: FRRS1l_F, 5’-ACCGGTCGCCACCATGGTGAGCAAGGGCGAGG-3’ and FRRS1l_R, 5’-ATGGCTAGCCTTGTACAGCTCGTCCATGCCG-3’.

The plasmid for the expression of ABHD6, CPT1c and PORCN were a gift from Jochen Schwenk and Bernd Fakler[168,177].

The plasmid for the expression of γ2 was a gift from Stefan Dübel.

The plasmid for the expression of γ8 was a gift from Susumu Tomita.

The plasmid for the expression of Shisa6 was a gift from Remco Klaassen and August Smit.

The plasmid for the expression of CNIH2 was initially purchased from Addgene (pCMV-SPORT6-CNIH2) and subsequently subcloned into a cDNA3 vector.

The ARIAD CNIH2::mScarlet was generated as followed: BamHI/AgeI restriction sites were introduced at CNIH2 N- and C-terminus, respectively, using the oligonucleotides: CNIH2_F: 5’-GGATCCCTTGGAAATGGCGTTCACCTTCGC-3’ and CNIH2_R: 5’-CGTCATCCTTGTAATCAC CGGTAGAGAAGCTCACCAACGTATAAACC-3’. AgeI restriction site and, Furin cleavage site and XbaI restriction were inserted at N- and C-terminus of mScarlet-I, respectively using the oligonucleotides: mScarlet-I_F, 5’- TCAGGCGCGCCGGAGGAAGTGGTTCAACCGGTGTGAGC AAGGGCGAGGCCG-3’, and mScarlet-I_R, 5’-GGCTCTAGATCTCTTCTGACGGTTTCTGCTAGCCTTGTACAGCTCGTCCA TGCCGCCG-3’. The mScarlet/Furin was subcloned at the C-terminus of CNIH2 using the AgeI/XbaI sites. CNIH2::mScarlet::Furin was subcloned into the vector pEGFP-C1 using the NdeI/BglII sites. The conditional aggregation sites, composed of four repeats of the human FKBP12^{F36M}, was subcloned after the Furin sequence site using XbaI/SpeI sites.

The plasmid for the expression of EGFP GluA2 (flip isoform) was a gift from Maria Passafaro.

The plasmid for the expression of EGFP GluA1 (flop isoform)

The plasmid for the expression GluA1 (flip isoform) was a gift from James Howe. Gene synthesis of a double-stranded DNA fragment of GluA1 (104 aa to 347 aa) containing the msfGFP was ordered from Eurofins. The msfGFP was inserted at position D260/T261 (GluA1::msfGFP261) or P286/K287 (GluA1::msfGFP287) of GluA1. The msfGFP was flanked by the restriction sites MluI/NheI followed by a 7 aa GS linker. The synthesized double-stranded DNA fragment was subcloned into the GluA1 using the ApaI/BstBI sites.

The plasmid for the GluA1 (flip isoform) Tn5 ME SEP +396 aa was a gift by Andrew Plested. SEP was replaced by msfGFP using the AscI sites.

The eGFP was inserted after GluA1 (flop isoform) signal peptide by overlapping PCR as described in[312].

Heterologous cell culture

HeLa cells (ECACC, # 93021013) were cultured at 37 ºC under 5% CO_2 in DMEM supplemented with 10% FBS, 1% L-glutamine and 1% penicillin/streptomycin.

Transfection

HeLa cells plated at a density of 12,000-15,000 cells.cm^{-2} on a 12-well plate containing ⌀ 18 mm coverslips were transfected with 1 μg of total cDNA using X-tremeGENE™ HP DNA (Sigma, #6366236001) transfection reagent for ~24 h or 48 h. When co-transfected, different cDNA ratios were used according to the respective set of experiments, see section Results: Chapter I.

Animals

All experiments were performed in accordance with the European guidelines for the care and use of laboratory animals, and the guidelines issued by the University of Bordeaux animal experimental committee (CE50; Animal facilities authorizations A3306940 and A33063941).

Tissue for dissociated hippocampal cultures was harvested from embryos of an unascertained mixture of sexes prevenient from gestant Sprague-Dawley rat females at the age of 9 to 12 weeks old purchased weekly from Janvier Labs, Saint-Berthevin, France. Animals were housed at PIV-EOPS facility of the IINS under a 12 hour light/dark cycle at normal room temperature (22ºC) and humidity between 40-70% (typically 60%) with unrestricted access to food and water.

Primary dissociated hippocampal neurons

Gestant rat females were purchased weekly (Janvier Labs, Saint-Berthevin, France). Animals were handled and euthanized according to European ethical rules and protocols approved by the local ethics committee office 50. Dissociated hippocampal neurons from embryonic day 18 (E18) Sprague-Dawley rats' embryos of either sex were prepared as previously described[313]. Briefly, dissociated neurons were plated at a density of 250,000 cells per 60 mm dish on 0.1 mg.mL^{-1} PLL pre-coated 1.5H, ⌀ 18 mm coverslips (Marienfeld Superior, #0117580). Neurons cultures were maintained in Neurobasal™ Plus Medium (Thermo Fisher Scientific) supplemented with 0.5 mM GlutaMAX (Thermo Fisher Scientific) and 1X B-27™ Plus Supplement (Thermo Fisher Scientific). 2 μM Cytosine β-D-arabinofuranoside (Sigma Aldrich) was added after 72 h. At DIV7, cells were transfected with the respective cDNAs using a calcium phosphate procedure. Cultures were kept at 37 ºC under 5% CO2 up to 16 days.

Astrocytes feeder layers were prepared from the similar embryos, plated between 20,000 to 40,000 cells per 60 mm dish and cultured in Minimum Essential Medium (Thermo Fisher Scientific) containing 4.5 g.L^{-1} glucose, 2 mM GlutaMAX and 10% heat-inactivated horse serum for 14 days.

Calcium phosphate transfection

Neurons from DIV6-7 days were transfected with GluA1::msfGFP287 following calcium phosphate procedure; calcium phosphate procedure is based on formation of a calcium phosphate-DNA precipitate which binds to the cell surface and enters the cell by endocytosis.

Briefly, 2 mL of pre-warmed Neurobasal was added to the 60 mm culture dish (containing 4 coverslips). The cDNA (1 μg) diluted in 1 M tris-HCl and 250 mM EDTA solution was mixed in a $CaCl_2$ solution (2.5 M $CaCl_2$ and 10 mM HEPES), and added dropwise to a HEPES-buffered saline solution (HEBS; in mM): 40 HEPES, 270 NaCl, 10 KCl, 1.5 Na_2HPO_4, and 10 D-glucose. The mixture was gently mixed by vortexing to ensure the formation of a fine precipitate necessary to efficiently enter the cell. The DNA/$CaCl_2$/HEBS mix was then incubated for 15 min at room temperature in the dark. In the meantime, the coverslips were transferred to a 12-well plate in 450 μL of culture media from the initial Petri dish. The DNA/$CaCl_2$/HEBS mix (50 μL per well) was added dropwise, and the 12-well plate was placed in the incubator for ~1.5 h. The coverslips are rinsed with Neurobasal media containing 10 mM kynurenic acid; coverslips were returned back to their initial 60 mm Petri dish.

FRRS1l immunostaining

HeLa cells were transfected with WT FRRS1l (1 μg) as above described. Upon fixation with 4% PFA for 10 min, cells were rinsed three times with PBS and permeabilized with 0.2% Triton-X100 for 5 min. Reactive aldehydes groups were blocked for 10 min with 50 mM NH_4Cl. After 30 min blocking in 3% BSA diluted in PBS, cells were incubated with the mouse anti-FRRS1l (Santa Cruz Biotechnology, #SC-39862) diluted at 1:500 in 3% BSA for 1h at room temperature. Cells were incubated with secondary antibody anti-mouse AF568 (Thermo Fisher Scientific) diluted at 1:1000 in 3% BSA for 1h at room temperature. Imaging was performed on an up-right widefield fluorescence microscope (Leica Microsystems, Leica DM5000 B) microscope controlled by Metamorph software (Molecular Devices). Fluorescence excitation of AF568 was done by a LED SOLA Light (Lumencor). Images were acquired using an oil-immersion objective (Leica, HCX PL APO 63x/NA 1.4 oil) and appropriate filter set. Fluorescent emission was collected using a sCMOS camera (Hamamatsu Photonics, ORCA-Flash4.0 V2).

CNIH2 aggregation-induced experiment

HeLa cells transfected with ARIAD CNIH2::mScarlet or in combination with GluA1::msfGFP396 for a period of ~24 h were rinsed with PBS and imaged. Disaggregation of the ARIAD CNIH2::mScarlet was induced by addition of 2 μL.mL^{-1} D/D Solubilizer to the PBS. Cells were recorded every 3 s for a period of 10 min. Live-cell imaging was performed in PBS at 37 °C using an incubator box with an air heater system (Life Imaging Services) installed on an inverted Leica DMI6000 B (Leica Microsystem) spinning disk microscope controlled by Metamorph software (Molecular Devices). Cells were imaged with an oil-immersion objective (Leica, HCX PL Apo CS 63x/NA 1.4 oil) using an appropriate GFP filter set.

Frequency domain-based fluorescence lifetime imaging (FLIM)-Förster resonance energy transfer (FRET) measurements

HeLa cells transfected with 1 μg total DNA for a period of 24 h or 48 h were rinsed once and imaged in PBS.

Experiments were performed at 37°C using an incubator box with an air heater system (Life Imaging Services) installed on an inverted Leica DMI6000 B (Leica Microsystem) spinning disk microscope and using the LIFA frequency-domain lifetime attachment (Lambert Instruments) and the LI-FLIM software. Cells were imaged with an oil-immersion objective (Leica, HCX PL Apo CS 63x/NA 1.4 oil) using an appropriate GFP filter set. Cells were excited using a sinusoidally-modulated 3 W 477 nm light-emitting diode at 40 MHz under widefield illumination. Fluorescence emission was collected using an intensified CCD LI2CAM MD camera (Lambert Instruments, FAICM). Lifetimes were referenced to a 1 mg.mL^{-1} erythrosine B that was set at 0.086 ns[235]. The lifetime of the sample was determined from the fluorescence phase-shift between the sample and the reference from a set of 12 phase settings using the manufacturer's LI-FLIM software. All data are pulled measurements from a minimum of 20 cells (otherwise stated) per individual preparation.

Statistics

Statistical significance was calculated using GraphPad Prism. Statistical values are given as mean ± SD; ***$p < 0.001$, **$p < 0.01$, *$p < 0.05$, n.s. $p > 0.05$. Violin plot represents median, lower and upper quartiles, mean (cross), and mean of independent set of experiments (dots). Multiple sample comparisons were carried out using unpaired Welch's ANOVA. When only a single or two set of experiments were performed, the statistical analysis was pulled from the whole data points rather than the mean of the each individual set of experiments, and when statistical difference is observed it is reported as *$p < 0.05$.

Results

Chapter I

The stepwise assembly of AMPARs

Just before I started my journey in the lab of Dr. Daniel Choquet, Brechet and colleagues at the University of Freiburg had just published their most recent observations. In that study, from the lab of Bernd Fakler, Brechet and colleagues[168] used a combination of reverse proteomic and serial affinity purifications with high-resolution mass spectrometry to identify a set of AMPAR-interacting proteins that were only found associated with AMPARs within intracellular compartments, more specifically, in the ER. More intriguing was the fact that those AMPAR complexes were devoid of other auxiliary subunits. Considering the cellular compartment where those complexes were found and the requirement of auxiliary subunits for forwarding trafficking of AMPARs, the authors proposed a possible role of those ER-interacting subunits during the early steps of AMPAR biogenesis, with emphasis on the CPT1c/FRRS1l pair.

Until that point, most of the AMPAR-interacting proteins were thought to participate in the forward trafficking, surface stabilization, and anchoring and/or fine-tune of AMPAR-mediated excitatory transmission. Yet, no AMPAR-interacting protein to that date had been proposed to mediate the early steps of AMPAR biogenesis, *i.e.*, before the TARP/CNIH-mediated ER-exit of AMPARs. Therefore, as our group is interested in several aspects of the AMPAR lifetime, from intracellular trafficking to AMPAR-mediated transmission, those new observations caught our attention.

However, while Brechet and colleague’s observations were robust, especially if considering that some of those proteins are ER-resident proteins, their function as an AMPAR-interacting protein remained to unveil. Moreover, for a team like ours, with strong roots in electrophysiology and live-cell imaging, it was clear that not only the function of those proteins in regard to AMPAR was missing (if any), but also their dynamics.

To decipher the ‘snapshot’ captured by Brechet and colleagues, we establish a collaboration with Dr. Bernd Fakler and Dr. Jochen Schwenk at the time I started my PhD, around September 2017. Later on the road, Dr. Bernd Fakler and Dr. Jochen Schwenk presented us with their most recent theory, ‘the stepwise assembly of AMPARs’, and recently published as Schwenk, et al. (2019)[177]. Using blue native polyacrylamide gel electrophoresis (BN-PAGE), they observed that ABHD6 (and PORCN) retain GluA subunits as monomers, whereas the pair CPT1c/FRRS1l triggers GluA oligomerization, followed by ER-export of AMPAR by association with CNIH or TARPs. The complete transition to the next step requires dissociation of the previous group of proteins (Figure 12).

This led me to pursue a strategy to rebuild and study the proposed sequential assembly of GluA subunits and required proteins in living cells. Here, I used FLIM-based FRET microscopy to study the dynamics of FRRS1l and AMPAR interaction in living cells. I was able to corroborate Brechet *et al*. observations that CPT1c cooperates and enhances FRRS1l association with AMPARs. Additionally, I verified that ABHD6 and PORCN do not share the same AMPAR complexes as FRRS1l. FRET microscopy was then used to investigate the impact of ABHD6 during GluA subunits oligomerization. Surprisingly and contrary to the observations of Schwenk *et al*., the results here presented suggest that ABHD6 is unable to hold GluA subunits as monomers.

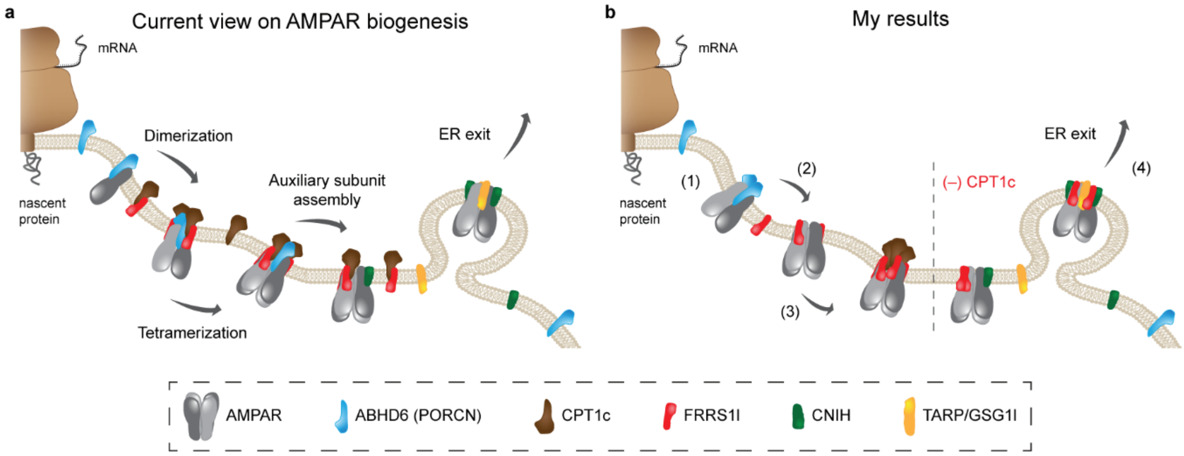

Figure 12: Comparison of the AMPAR biogenesis model proposed by Fakler and colleagues and my results. (**a**) Current understanding of assembly line of AMPAR pore-forming core in the ER purposed by Fakler and colleagues (Schwenk et al., 2019; Schwenk and Fakler, 2021). Nascent GluA subunits associate with ABHD6 as monomers; formation of GluA dimers driven by co-assembly of CPT1c/FRRS1l complexes; GluA tetramerization via dimer-of-dimer formation and dissociation of ABHD6; binding of the cargo proteins and auxiliary subunits CNIHs and TARPs and dissociation of CPT1c/FRRS1l complexes; and initiation of ER export via induction of transport vesicles. (**b**) Model of early steps of AMPAR biogenesis supported by the results here obtained and taken in consideration the model proposed by Fakler and colleagues. (1) The results here presented failed to demonstrate that ABHD6 holds nascent GluA subunits as monomers. Instead supports that AMPAR and ABHD6 can form a complex. (2) The FRET results between AMPAR and FRRS1l in the presence of either ABHD6 or PORCN, support that FRRS1l and ABHD6/PORCN are not part of the same AMPAR complex. Therefore, a switch of proteins needs to occur to transit to the next step. (3) CPT1c and FRRS1l are part of the same complex. Moreover, CPT1c enhances FRRS1l interaction with AMPARs. (4) In the absence of CPT1c, auxiliary subunits and FRRS1l can become part of the same AMPAR complex, and exit the ER as a single complex.

Visualization of AMPAR and FRRS1l interaction using FRET microscopy

Fluorescence labeling of FRRS1l

The recent data from the lab of Dr. Bernd Fakler suggests that CPT1c and FRRS1l cooperatively regulate GluA tetramerization. Subsequently, CNIHs and TARPs bind to the newly assembled AMPAR and promote its ER-exit upon dissociation of the CPT1c/FRRS1l pair from the receptor. In this model, CPT1c and FRRS1l are transiently associated with AMPARs. However, one of the major gaps in their work is the lack of dynamics and duration of the intermediary interactions.

Here, to investigate if the interaction of FRRS1l with AMPAR was indeed a transient interaction and so, study their dynamics, I selected FLIM-based FRET microscopy. FRET provides a reliable and robust way to study the interaction between proteins and their dynamics – given the reasonable temporal resolution – in living cells. Moreover, FLIM measurements provide a more robust and quantitative FRET analysis than the other FRET detection techniques, such as sensitized emission or acceptor photobleaching.

Here, I aimed to develop a robust FRET pair between FP-tagged AMPAR and FRRS1l. The FRET pair will then be used to investigate the dynamics of the AMPAR and FRRS1l interaction when in the presence of other AMPAR-interacting proteins.

The luminal NTD represents around 90% of the FRRS1l structure, therefore the acceptor fluorescent protein (FP) was inserted at the N-terminus after the FRRS1l signal peptide. To verify if FP insertion at FRRS1l N-terminus impacted FRRS1l cellular localization, different FPs were inserted at the N-terminus and compared to C-terminal tagged and recombinant wild-type (WT) FRRS1l in HeLa cells (Figure 13 and Figure 14a). FRRS1l is mainly localized at the ER, and to a lesser extent at the plasma membrane in the absence of CPT1c[168]. As shown in Figure 13, overexpressed WT FRRS1l shows a reticular pattern, characteristic of ER-resident proteins. A similar result was obtained when using FP (eGFP, mCherry, and mScarlet-I – herein termed mScarlet)-tagged FRRS1l (Figure 13 and Figure 14a).

Thus, N- or C-terminal FP-tagging does not compromise FRRS1l cellular localization.

Identification of permissive sites at AMPAR ECD

At the ER level, AMPAR ECD is facing the ER lumen. To develop a possible FRET pair between AMPAR and the N-terminus tagged FRRS1l, a donor FP was inserted at different positions of GluA1 ECD. Three different regions were selected for the insertion of the FP based on their location at the structural level: the linkers connecting the lateral-facing Helix H (position 261 and 287), and the flexible ATD-LBD linker (position 396)[314] (Figure 14d and Figure 15).

The presence of strong oxidizers in the ER imposes a challenge for proper folding of cysteine-containing FPs due to inter- and intrachain disulfide bonds formation between cysteines, which can result in half of the proteins being misfolded, dark, and of unclear functionality[315]. The monomeric superfolder GFP (msfGFP) is a stable and rapidly folding mutant of the enhanced GFP (eGFP). The msfGFP is a true monomeric FP with a lower pKa of 5.5 resistant to disulfide bond formation, making it

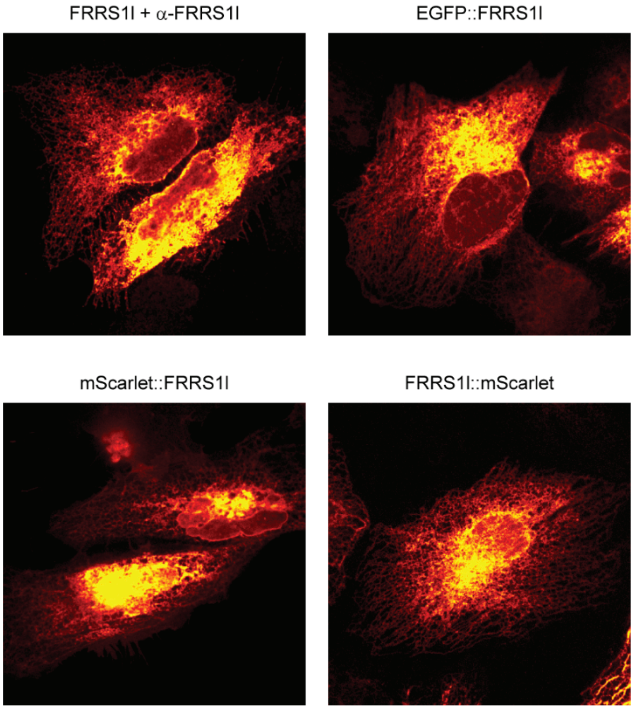

Figure 13: FP-tagging of N- or C-terminal of FRRS1l does not affect FRRS1l subcellular localization. Representative spinning disk confocal images of fixed HeLa cells expressing wildtype FRRS1l and labeled with an antibody against FRRS1l upon permeabilization (top left), eGFP::FFRS1l (top right), mScarlet::FRRS1l (bottom left), or FRRS1l::mScarlet (bottom right). Scale bar: 25 μm.

an ideal candidate for the labeling of proteins in the secretory pathway[315-317], and therefore, used in this study as donor FP in the FRET assays.

To verify if the insertion of msfGFP at positions 261, 287, and 396 of GluA1 impaired protein folding or cellular localization, HeLa cells were transfected with the different msfGFP-tagged GluA1s and compared to N-terminus msfGFP::GluA1. As shown in Figure 14b, all the different msfGFP-tagged GluA1s displayed similar cellular distribution in HeLa cells. Expression of msfGFP-tagged GluA1 at position 287 (GluA1::msfGFP287) in dissociated hippocampal neurons showed synaptic targeting (Figure 14d).

In sum, GluA1 tolerates msfGFP insertion at Helix H and ATD-LBD linker.

Design of possible FRET pairs between GluA1 subunit and FRRS1l

Among the three components that determine FRET efficiency, the spectral overlap between the donor emission spectrum and acceptor absorption spectrum is perhaps the easiest to control due to the vast array of FPs nowadays. As a first attempt to develop a robust FRET pair between GluA1 and FRRS1l, I decided to use the mScarlet as the acceptor molecule of the donor msfGFP. mScarlet is a bright and true monomeric red FP[318] with an integral overlap of 2.84 with msfGFP, compared to the integral overlap of 1.84 of msfGFP-mCherry pair[319].

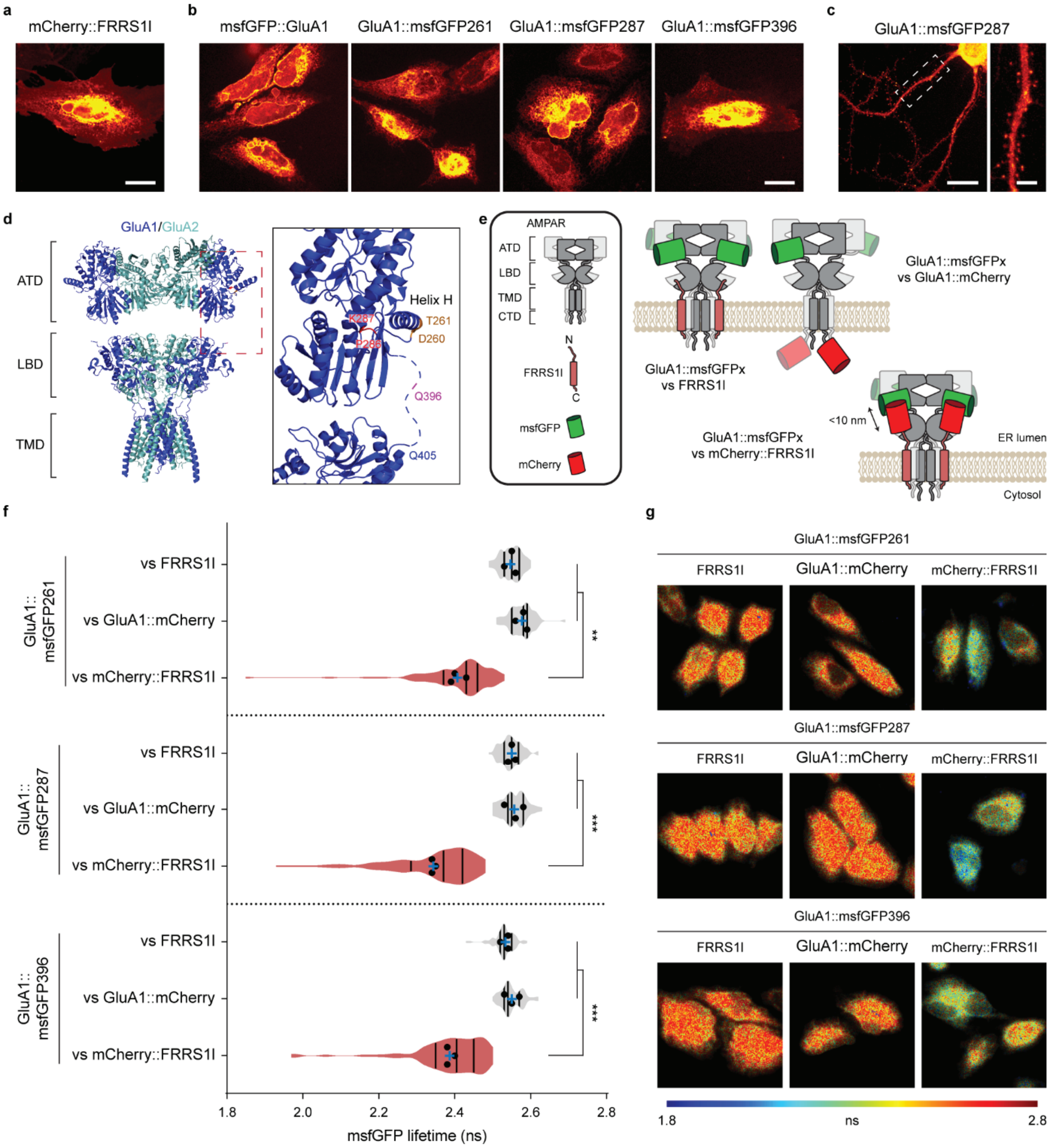

Figure 14: Design of FRET pairs between msfGFP-tagged GluA1 and mCherry-tagged FRRS1l. Representative spinning disk confocal images of fixed HeLa cells expressing (**a**) mCherry::FRRS1l or (**b**) from left to right, msfGFP::GluA1, GluA1::msfGFP261, GluA1::msfGFP287, and GluA1::msfGFP396. (**c**) Representative spinning disk confocal image of a living dissociated hippocampal neurons expressing GluA1::msfGFP287. On the right, magnified view of a fragment of a dendrite highlighted on the overview image. (**d**) Y-shaped global architecture of GluA1/GluA2 heterotetramer (7OCA). GluA1 subunits are colored dark blue, whereas GluA2 subunits are colored light blue. Each domain layer (ATD, LBD, and TMD) is labeled and separated by a dashed gray line. Inset of side view of GluA1 subunit highlighting the insertion sites of msfGFP of the tagged-GluA1. (**e**) Schematic illustration of the principle used for the design of controls (top) and Förster resonance energy transfer (FRET) pairs (bottom) for the study of GluA1 and FRRS1l interaction by FRET microscopy. (**f**) Analysis of msfGFP-tagged GluA1 subunits and mCherry-tagged FRRS1l interaction using fluorescence lifetime imaging microscopy, FLIM-FRET. Average msfGFP lifetime measured by FLIM in (top) GluA1::msfGFP261, (middle) GluA1::msfGFP287, or (bottom) GluA1::msfGFP396-positive HeLa cells co-expressing either (control) WT FRRS1l, (negative control) GluA1::mCherry, or (test condition) mCherry::FRRS1. GluA1::msfGFP261: + FRRS1l, τ_{msfGFP} = 2.55 ± 0.02 ns, n = 73; + GluA1::mCherry, τ_{msfGFP} = 2.58 ± 0.02 ns, n = 63; + mCherry::FRRS1l, τ_{msfGFP} = 2.41 ± 0.02 ns, n = 91. GluA1::msfGFP287: + FRRS1l, τ_{msfGFP} = 2.55 ± 0.01 ns, n = 76; + GluA1::mCherry, τ_{msfGFP} = 2.56 ± 0.03 ns, n = 67; + mCherry::FRRS1l, τ_{msfGFP} = 2.34 ± 0.01 ns, n = 90. GluA1::msfGFP396: + FRRS1l, τ_{msfGFP} = 2.53 ± 0.01 ns, n = 75; + GluA1::mCherry, τ_{msfGFP} = 2.55 ± 0.02 ns, n = 68; + mCherry::FRRS1l, τ_{msfGFP} = 2.39 ± 0.01 ns, n = 96. Mean msfGFP lifetime pulled out from the average of 3 independent set of experiments. (**g**) Representative widefield illumination fluorescence lifetime imaging microscopy (FLIM; msfGFP lifetime) images of living HeLa cells expressing, from the left to the right, FRRS1l, GluA1::mCherry, or mCherry:FRRS1l, and, from the top to bottom, GluA1::msfGFP261, GluA1::msfGFP287, or GluA1::msfGFP396. Scale bar: (**a**) and (**b**) = 25 µm, (**c**) overview image = 20 µm, and magnified image = 5 µm.

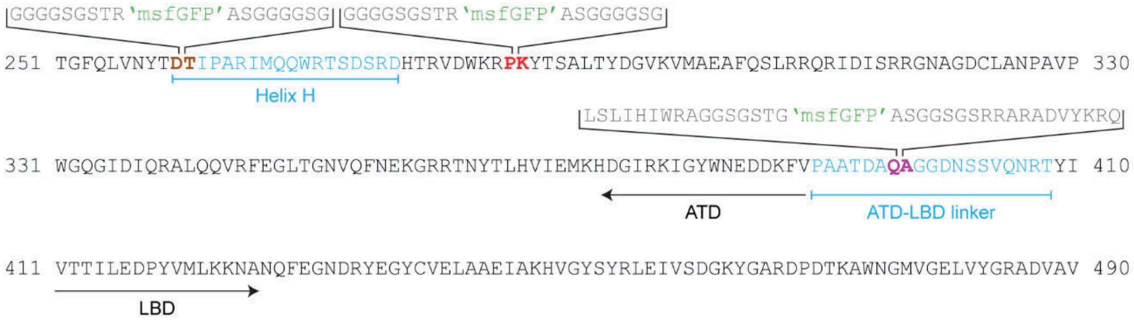

Figure 15: Amino acid sequence of msfGFP-tagged GluA1 constructs. Fragment of the amino acid sequence of GluA1 N-terminal domain (ATD) and ligand binding domain (LBD). The insertion sites of the msfGFP into GluA1 sequence are coloured as in Figure 1d; GluA1::msfGFP261 (brown), GluA1::msfGFP287 (red), and GluA1::msfGFP396 (purple).

At the time I started testing the possible GluA1::msfGFP (261, 287, or 396) and mScarlet::FRRS1l as possible FRET pair candidates, I did not have any other protein tagged with mScarlet, and as a consequence, no negative control was performed; negative control represents a condition where the donor and acceptor molecule do not interact. I started by transfecting HeLa cells for approximately ~24 h with one of the three GluA::msfGFP together with wild-type (control, *i.e*. donor alone) or mScarlet-tagged FRRS1l using a cDNA ratio of 1. Upon analyzing the donor's lifetime of the three FRET pair candidates, I verified a similar reduction of msfGFP lifetime when in the presence of mScarlet::FRRS1l as compared to the respective donor alone condition. Here, I decided to select the GluA1::msfGFP287 vs mScarlet::FRRS1l pair as it performed slightly better than the other two pairs (Figure 16a).

In an attempt to quickly perceive if it would be possible for me to use this tool to study the several steps of AMPAR biogenesis *i.e.*, the exchange of AMPAR-auxiliary subunits, γ2 and γ8 were used as a 'competitor' of FRRS1l, as TARPs type-I promote AMPAR ER-exit[148,177]. As FRRS1l partners up with CPT1c to regulate AMPAR at the ER level, HeLa cells were co-transfected with GluA1::msfGFP287, mScarlet::FRRS1l and CPT1c, in the presence or absence of TARPs (Figure 16b). During the course of this experiment, I obtained the FRRS1l bearing mScarlet at the C-terminus (FRRS1l::mScarlet) (Figure 13 bottom right), which was designed to function as the acceptor for the GluA1::msfGFP287 in the negative control condition.

To properly validate the GluA1::msfGFP287 and mScarlet::FRRS1l as a reliable FRET pair, HeLa cells were then co-transfected with GluA1::msfGFP287 and, mScarlet::FRRS1l (test condition), FRRS1l::mScarlet (negative control) or wild-type FRRS1l (control, donor alone). To my surprise, in the negative control condition, the msfGFP lifetime was lower than in the donor alone: + mScarlet::FRRS1l, τGluA1::msfGFP287 = 2.44 ± 0.05 ns versus +FRRS1l, τGluA1::msfGFP287 = 2.54 ± 0.03 ns (Figure 16c). As FRET between these two proteins is not possible to occur because the donor and acceptor are located on opposite sides of the membrane, this result suggests the occurrence of mScarlet fluorescence bleed-through in the donor's lifetime measurements. To confirm this possibility, HeLa cells were transfected either with mScarlet::FRRS1l or γ2::mCherry, a red FP that has been widely used in our lab for FLIM-FRET experiments when using GFP-variants. Cells were then excited with a 478 nm laser as normally used for the msfGFP. As expected, mScarlet signal, but not mCherry, was captured by the FLIM camera (CCD LI2CAM MD) confirming the occurrence of spectral bleed-through in the

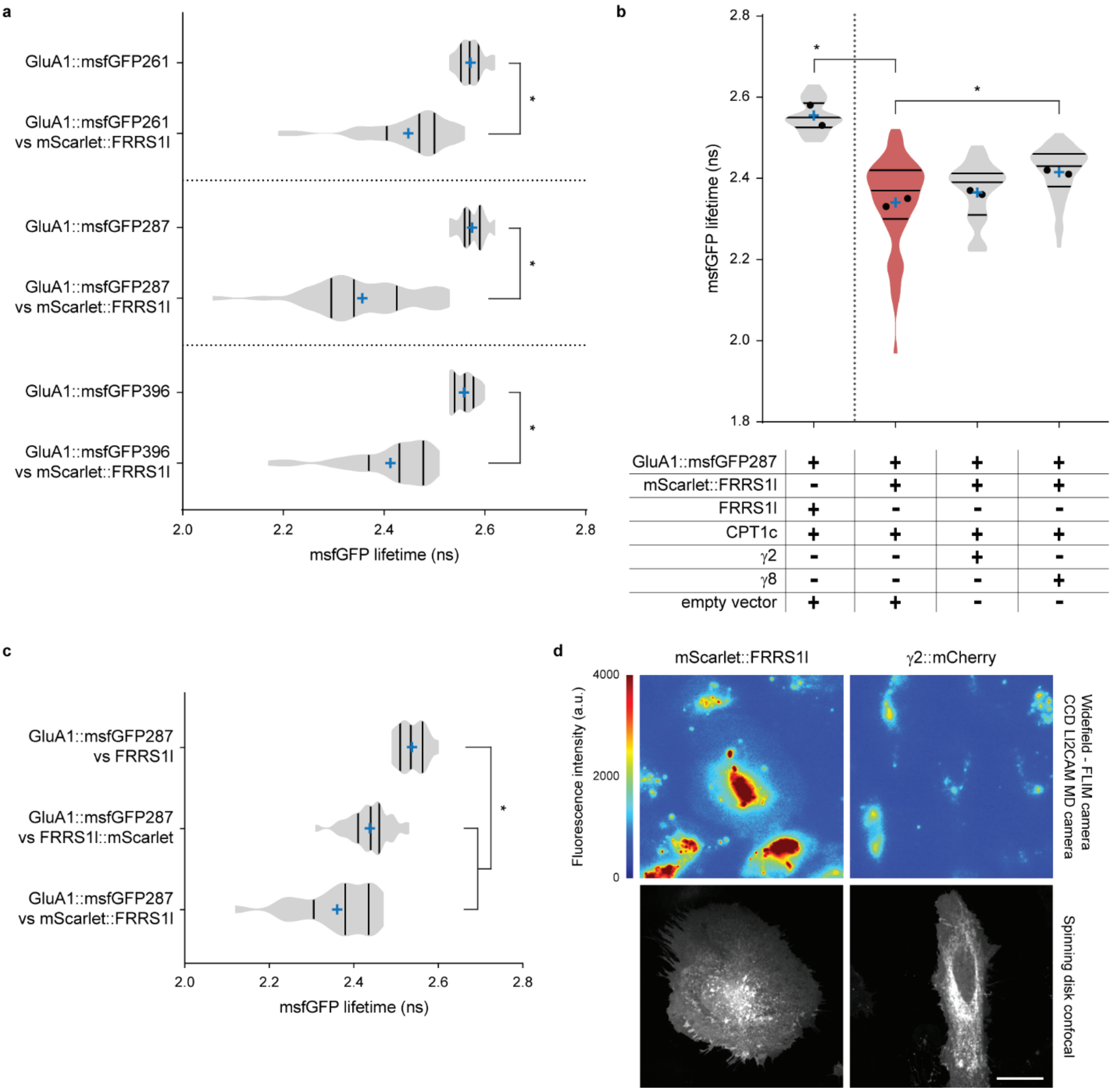

Figure 16: msfGFP lifetime contaminated by spectral bleed-through of the acceptor mScarlet-I. (**a**) Average msfGFP lifetime measured by FLIM in HeLa cells expressing: GluA1::msfGFP261 (donor alone), τ_{msfGFP} = 2.57 ± 0.02 ns, n = 16; GluA1::msfGFP261 + mScarlet::FRRS1l, τ_{msfGFP} = 2.45 ± 0.09 ns, n = 32; GluA1::msfGFP287 (donor alone), τ_{msfGFP} = 2.57 ± 0.03 ns, n = 21; GluA1::msfGFP287 + mScarlet::FRRS1l, τ_{msfGFP} = 2.36 ± 0.10 ns, n = 37; GluA1::msfGFP396 (donor alone), τ_{msfGFP} = 2.56 ± 0.02 ns, n = 20; GluA1::msfGFP396 + mScarlet::FRRS1l, τ_{msfGFP} = 2.41 ± 0.08 ns, n = 40. (**b**) Average msfGFP lifetime measured by FLIM in GluA1::msfGFP287- and CPT1c-positive HeLa cells co-expressing, from left to right: + FRRS1l and e.v. (donor alone), τ_{msfGFP} = 2.56 ± 0.04 ns, n = 57; + mScarlet::FRRS1l and e.v., τ_{msfGFP} = 2.34 ± 0.01 ns, n = 75; + mScarlet::FRRS1l and γ2, τ_{msfGFP} = 2.37 ± 0.01 ns, n = 54; + mScarlet::FRRS1l and γ8, τ_{msfGFP} = 2.42 ± 0.01 ns, n = 75. (**c**) Average msfGFP lifetime measured by FLIM in GluA1::msfGFP287-positive HeLa cells co-expressing: + FRRS1l (donor alone), τ_{msfGFP} = 2.54 ± 0.03 ns, n = 18; FRRS1l::mScarlet (negative control), τ_{msfGFP} = 2.44 ± 0.05 ns, n = 31; mScarlet::FRRS1l (test condition), τ_{msfGFP} = 2.36 ± 0.09 ns, n = 25. Mean msfGFP lifetime from (**a** and **c**) an individual set of experiments or (**b**) 2 independent set of experiments. (**d**) Representative widefield illumination FLIM (top) and spinning disk confocal (bottom) images of living HeLa cells expressing either mScarlet::FRRS1l (left column) or γ2::mCherry (right column). Scale bar: 25 μm.

msfGFP lifetime measurements when using mScarlet as a donor (Figure 16d). Given the following observations, all the FRET data related to the mScarlet::FRRS1l was discarded. The mScarlet in FRRS1l was replaced by mCherry and experiments remade using mCherry::FRRS1l as an acceptor for the GluA1::msfGFP donor.

To identify the best possible FRET pair between msfGFP-tagged GluA1 and mCherry-tagged FRRS1l, and similarly to the previous experiments, HeLa cells were co-transfected with mCherry::FRRS1l and one of the different GluA1::msfGFP (261, 287, or 396). As a control, each msfGFP-tagged GluA1 was co-expressed with wild-type FRRS1l; GluA1 bearing a mCherry at the cytosolic C-tail (GluA1::mCherry) was used as a control negative (Figure 14e). As shown in Figure 14f, all the three GluA1::msfGFP had similar msfGFP lifetime (~2.55 ns), both in the control and negative control conditions. Moreover, when in the presence of mCherry::FRRS1l, a robust decrease in msfGFP lifetime was observed for all the three GluA1::msfGFP constructs: $\tau_{\text{GluA1::msfGFP261}}$ = 2.41 ± 0.02 ns, $\tau_{\text{GluA1::msfGFP287}}$ = 2.34 ± 0.01 ns, and $\tau_{\text{GluA1::msfGFP396}}$ = 2.39 ± 0.01 ns (Figure 14f,g). As the pair msfGluA1::msfGFP287 vs mCherry::FRRS1l ($\tau_{\text{GluA1::msfGFP287}}$ = 2.34 ± 0.01 ns) performed slightly better, this FRET pair was used in the follow-up experiments.

Here, I demonstrate the development of three robust FRET pairs between FP-tagged GluA1 and FRRS1l, confirming the interaction of GluA1 and FRRS1l in living cells.

CPT1c promotes AMPAR and FRRS1l interaction, but not ABHD6 and PORCN

In earlier experiments, while I was still using mScarlet::FRRS1l, I chose to co-transfect cells with CPT1c when assessing the impact of TARPs in the AMPAR and FRRS1l interaction (Figure 16b). The reason behind this was, as already explained, the cooperative interaction of CPT1c and FRRS1l during AMPAR biogenesis[168]. Despite the inaccurate msfGFP lifetime measurements as a consequence of mScarlet fluorescence bleed-through, no evident dissociation of FRRS1l from the AMPAR complex was observed in the presence of TARPs (Figure 16b), *i.e.*, no increase in the msfGFP lifetime was observed when compared to the GluA1::msfGFP287 vs mScarlet::FRRS1l + CPT1c.

Given the unsuccessful previous experiment (Figure 16b), a new and more ambitious experimental design was prepared, with the intent to decipher the impact of different AMPAR-interacting proteins in the AMPAR-FRRS1l interaction. To decrease the number of conditions analyzed in a single set of experiments, I divided the AMPAR-interacting proteins into two groups, the ER-resident subunits (ABHD6, CPT1c, and PORCN) and the auxiliary subunits (CNIH2, γ2, γ8, and Shisa6). Here I chose to not co-transfect CPT1c in all the conditions to weaken the AMPAR-FRRS1l interaction[168]. Moreover, a cDNA ratio of 0.5 between FRRS1l and the second AMPAR-interacting protein was chosen to tip the balance towards the FRRS1l 'competitor'. The cDNA ratio between FRRS1l and AMPAR was 1. With this in mind, if FRRS1l is not part of a given AMPAR macromolecular complex, a decrease in FRET should be observed which is accompanied by an increase in the donor's lifetime.

Together with FRRS1l, three other proteins – ABHD6, CPT1c, and PORCN – mainly interact with AMPARs at the ER level. To better understand the role of these proteins during AMPAR biogenesis, I designed a new FRET assay where AMPAR and FRRS1l interaction was evaluated when in the presence of a second ER-resident subunit.

Similarly to the experiment in Figure 14f, HeLa cells were co-transfected with GluA1::msfGFP287 and mCherry::FRR1l at a cDNA ratio of 1. To increase the likelihood of potential alteration in FRET efficiency between GluA1 and FRRS1l (msfGFP and mCherry, respectively), the competitor protein (ABHD6, CPT1c, or PORCN) was used at a cDNA ratio of 2 in relation to FRRS1l. As the amount of

GluA1 and FRRS1l cDNA was reduced with the introduction of a third protein, cells were allowed to express for ~48 h to ensure proper levels of expression; contrary to the ~24 h used in Figure 14f,g.

Before I proceed, I would like to disclose that the following results concern the data gathered in two different experiments, therefore, one must be careful when considering those results.

Due to the complications that arose, *i.e.*, delays in design and production of new constructs, the mScarlet fluorescence bleedthrough, and the not so satisfactory overall results, we (Dr. Daniel Choquet and I, together with Dr. Bernd Fakler) agreed to stop the project here as it was not fulfilling our expectations. Therefore, the results below presented correspond to the data gathered until the decision was taken.

Unlike most of the AMPAR-interacting proteins, CPT1c and FRRS1l can self-assemble in the absence of AMPARs. Moreover, not only do CPT1c and FRRS1l specifically bind AMPARs, they exert a cooperative interaction, as the absence of one of the two strongly reduces the interaction of the second with AMPAR[168]. In line with that view, I observed that the presence of CPT1c promotes FRRS1l and AMPAR interaction as indicated by a decrease of the donor's lifetime, $\tau_{GluA1::msfGFP287}$ = 2.29 ± 0.01 ns; control: + empty vector – e.v., $\tau_{GluA1::msfGFP287}$ = 2.41 ± 0.04 ns (Figure 17a). On the contrary, the presence of ABH6 or PORCN results in an increase of GluA1::msfGFP287 lifetime suggesting a potential dissociation of the complex AMPAR/FRRS1l; +ABHD6: $\tau_{GluA1::msfGFP287}$ = 2.51 ± 0.01 ns, and +PORCN: $\tau_{GluA1::msfGFP287}$ = 2.51 ± 0.02 ns (Figure 17a).

Interestingly, the presence of twice the amount of wild-type FRRS1l was not enough to reduce the interaction between GluA1::msfGFP287 and mCherry::FRRS1l (Figure 17a).

The results here presented show that CPT1c enhances FRRS1l interaction with GluA1, as previously demonstrated. In contrast, ABHD6 and PORCN compete with FRRS1l for a position on AMPAR complexes.

FRRS1l and, CNIHs and TARPs, share the same AMPAR macromolecular complex

While ABHD6, PORCN, CPT1c, and FRRS1l have recently been implicated in the early stages of AMPAR biogenesis, the auxiliary subunits CNIH2/3 and TARP type-I are known to regulate the late stages of AMPAR biogenesis, of which ER-exit of AMPARs[148,177,205,206]. Similar to the previous experiment, HeLa cells were co-transfected with an auxiliary subunit (γ2, γ8, CNIH2 or Shisa6) in addition to GluA1::msfGFP287 and mCherry::FRRS1l for a period of ~48 h. To my surprise, neither the presence of TARPs nor CNIH2 was able to disrupt the interaction between GluA1 and FRRS1l (Figure 17b). While somehow surprising, such observation can be explained by a co-existence of FRRS1l and the auxiliary subunit in the same AMPAR complex, as FRRS1l – an outer core protein – binds to distinct pairs of AMPAR bindings sites to those of auxiliary subunits – inner core protein[109]. CNIH2 and TARPs are expected to promote ER-exit of AMPARs, therefore, a dissociation of FRRS1l from the AMPAR complex is expected as their interaction in neurons is restricted to the ER[168,177]. However, the ER retention of FRRS1l only occurs when in the presence of CPT1c[168] which was not the case of these

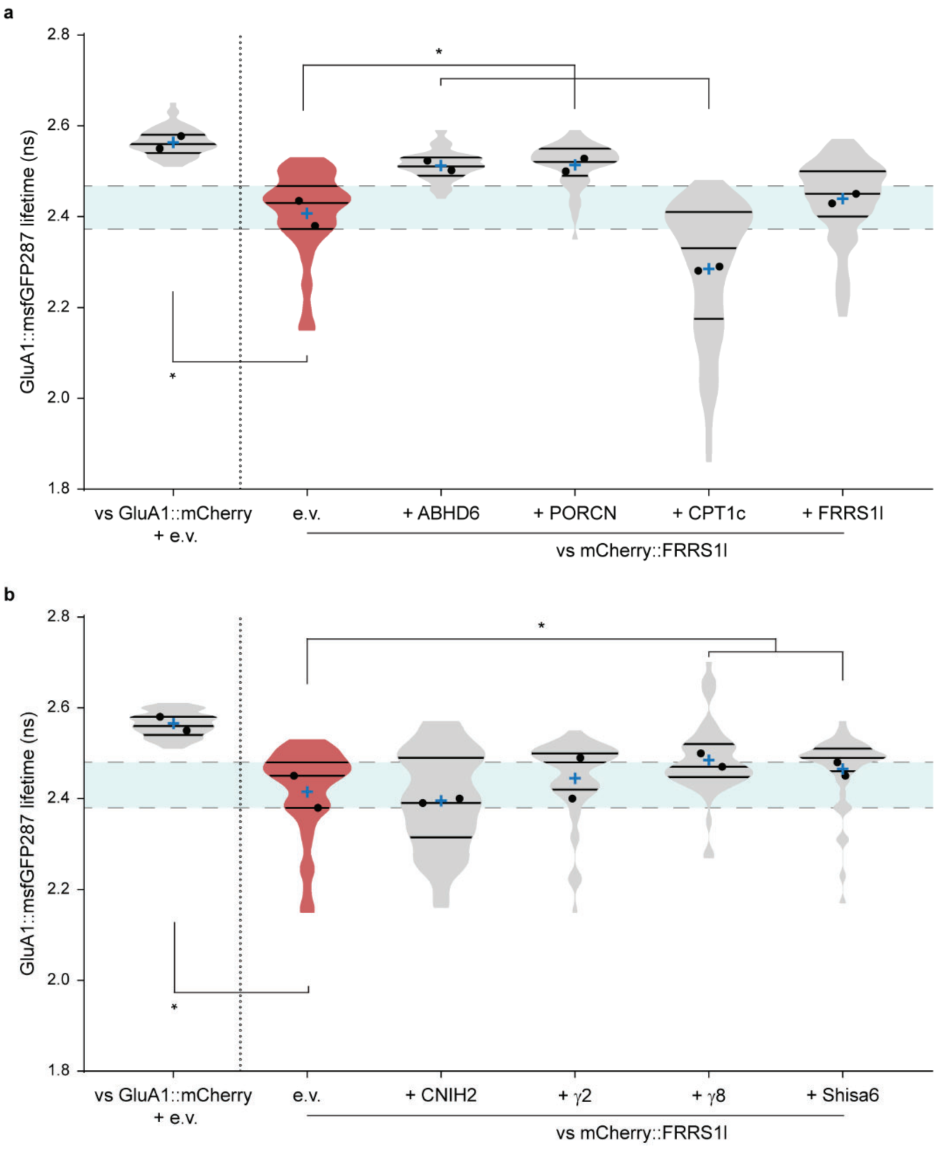

Figure 17: CPT1c enhances FRRS1l interaction with GluA1, whereas ABHD6 and PORCN exert an opposite effect. Analysis of GluA1::msfGFP287 and mCherry::FRRS1l interaction when in the presence of (**a**) ER-interacting proteins or (**b**) AMPAR-auxiliary subunits using FLIM-FRET. (**a**) Average msfGFP lifetime measured by FLIM in GluA1::msfGFP287-positive HeLa cells co-expressing, from left to right: GluA1::mCherry + empty vector (e.v.) (τ_{msfGFP} = 2.56 ± 0.02 ns, n = 59), or mCherry::FRRS1l: + e.v., τ_{msfGFP} = 2.41 ± 0.04 ns, n = 52; + ABHD6, τ_{msfGFP} = 2.51 ± 0.01 ns, n = 55; + PORCN, τ_{msfGFP} = 2.51 ± 0.02 ns, n = 51; + CPT1c, τ_{msfGFP} = 2.29 ± 0.01 ns, n = 56, or + FRRS1l, τ_{msfGFP} = 2.44 ± 0.01 ns, n = 53. (**b**) Average msfGFP lifetime measured by FLIM in GluA1::msfGFP287-positive HeLa cells co-expressing, from left to right: GluA1::mCherry + e.v., (τ_{msfGFP} = 2.57 ± 0.02 ns, n = 59), or mCherry::FRRS1l: + e.v., τ_{msfGFP} = 2.42 ± 0.05 ns, n = 54; + CNIH2, τ_{msfGFP} = 2.40 ± 0.01 ns, n = 60; + γ2, τ_{msfGFP} = 2.45 ± 0.06 ns, n = 55; + γ8, τ_{msfGFP} = 2.49 ± 0.02 ns, n = 54, or + Shisa6, τ_{msfGFP} = 2.47 ± 0.02 ns, n = 43. Mean msfGFP lifetime pulled out from the average of 2 independent set of experiments.

experiments; HeLa cells do not express CPT1c[320]: Human Protein Atlas available from http://www.proteinatlas.org.

In conclusion, while my results failed to demonstrate a dissociation of FRRS1l from the AMPAR complex upon CNIH2 or TARPs binding to the AMPAR, they support that FRRS1l and auxiliary proteins do not share the same AMPAR interaction sites, as previously suggested.

A controlled release of CNIH2 using aggregation domains

While the transient expression of all the constructs at once was the quickest and most practical way to check which AMPAR-auxiliary subunits would destabilize the AMPAR-FRRS1l complex, *i.e.*, not constitute part of FRRS1l-containing complexes, this approach lacks the capacity to reconstruct the stepwise assembly of AMPAR proposed by Schwenk and colleagues[170,177].

To overcome that limitation, a controlled release of the competitor AMPAR-auxiliary subunit would be required, ideally, in a matter of seconds to minutes. As the early steps of AMPAR biogenesis occur at the ER level, I took advantage of the ER release synchronization system from ARIAD Gene Therapeutics[321], previously used by our group to control the release of AMPARs to study intracellular transport of AMPARs[322]. In this strategy (herein termed ARIAD), the ER-luminal domain of the target protein is fused with a conditional aggregation domain consisting of four repeats of the mutant human FKBP12^{F36M} that accumulates as aggregates in the ER. Secretion can then be stimulated by a synthetic membrane-permeant ligand, as D/D Solubilizer, that induces protein disaggregation in the order of seconds[321].

To implement this strategy into CNIH2, CNIH2::mScarlet was C-terminal fused to the conditional aggregation domain (ARIAD CNIH2::mScarlet) (Figure 18a). Additionally, a Furin cleavage site was introduced in between the mScarlet and the conditional aggregation domain, which allows removal of the condition aggregation domain from the CNIH2::mScarlet by the ubiquitously expressed trans-Golgi Furin[321,323]. To validate the tool, HeLa cells were transfected with ARIAD CNIH2::mScarlet. As observed at the time 0 sec (Figure 18b), the introduction of the conditional aggregation domain at the C-terminus of the CNIH2::mScarlet efficiently aggregates and accumulates at the ER. Moreover, upon the treatment of the cells with the D/D Solubilizer ligand, disaggregation of the ARIAD CNIH2::mScarlet was observed as early as 30 sec after treatment (Figure 18b).

To verify if AMPARs were able to associate with aggregated CNIH2, HeLa cells were co-transfected with ARIAD CNIH2::mScarlet and GluA1::msfGFP396. As observed in Figure 18c, GluA1 was still able to interact with CNIH2 despite the aggregation of the latter as suggested by the accumulation of GluA1::msfGFP around the CNIH2::mScarlet aggregates. When I stimulated the disaggregation of ARIAD CNIH2::mScarlet, those same aggregates of GluA1 gradually started to disappear together with those of CNIH2::mScarlet. That said, while able to control the ER accumulation and release of CNIH2, the tool cannot be used for the study of AMPAR stepwise assembly as CNIH2 remains able to interact with GluA subunits.

In conclusion, while I succeeded to retain and aggregate CNIH2 within the ER, the aggregation using the ARIAD system does not prevent the binding of CNIH2 to GluA1. Therefore, the ARIAD system cannot be used for the controlled release of CNIH2 during the study of the dynamics of AMPAR and FRRS1l interaction.

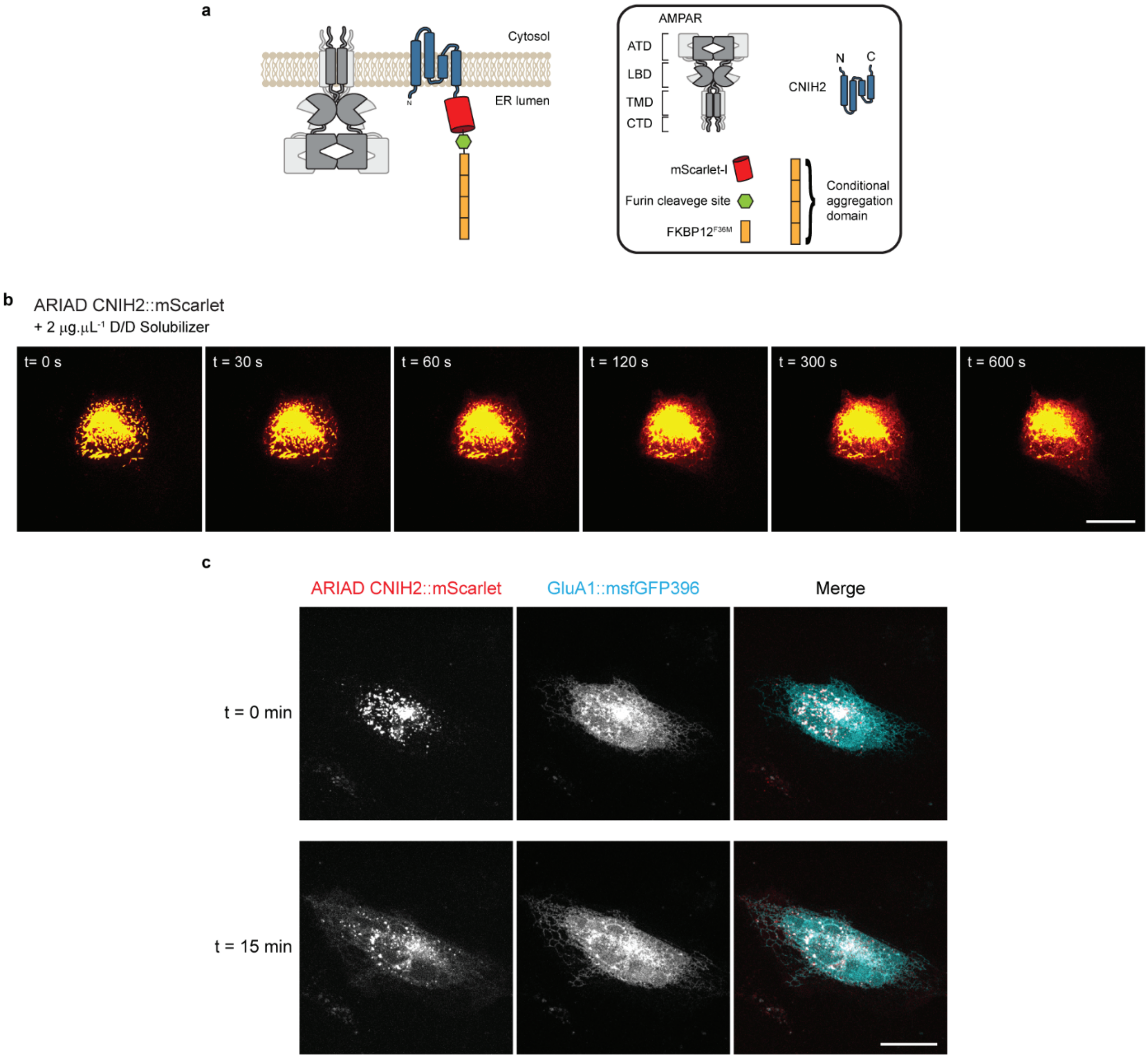

Figure 18: Aggregation-induced of CNIH2 at the ER. (**a**) Schematic representation of the ARIAD CNIH2::mScarlet construct used for the aggregation of CNIH2 in the ER. Four repeats of the mutant human FKBP12F36M – the conditional aggregation domain – were added at the C-terminus of the CNIH2::mScarlet. (**b**) Time-lapse acquisition of living HeLa cells transfected with the ARIAD CNIH2::mScarlet during 10 min upon addition of the disaggregation ligand D/D Solubilizer. (**c**) Representative spinning disk confocal images of living HeLa cells co-expressing ARIAD CNIH2::mScarlet (red) and GluA1::msfGFP396 (blue) before and after 15 min upon addition of the D/D Solubilizer, respectively, top and bottom panel. Despite the induction of CNIH2 aggregation, CNIH2 remains capable of interact with GluA1. Scale bar: (**b**) and (**c**) = 25 µm.

Accessing AMPAR multimerization

Design of FRET pairs between GluA subunits

Another protein that we were particularly interested in was ABHD6, which interaction with AMPAR favors the AMPAR monomer state[177].

As the formation of AMPARs dimers and tetramers requires the interaction of GluA subunits, a FRET-based approach was once again chosen. To study AMPAR dimerization/tetramerization, I designed possible FRET pairs between different GluA subunits. If dimerization/tetramerization of donor-tagged and acceptor-tagged GluA subunits occurs, a decrease in the donor's lifetime should be observed. Therefore, if indeed ABHD6 favors AMPAR monomers rather than dimers/tetramers, no FRET should be observed (Figure 19a).

Given the importance of AMPAR CTD for ABHD6 modulation[176,183], donor and acceptor were placed at the N-terminus of either GluA1 or GluA2 subunits. Two combinations were tested, donor::GluA1 vs acceptor::GluA1 and donor::GluA2 vs acceptor::Glua1. As a donor, eGFP (and not msfGFP) was used as the constructs were already available, whereas mCherry was used as an acceptor molecule. GluA1 bearing mCherry at C-tail (GluA1::mCherry) was used as the negative control. Interestingly, while a decrease in eGFP lifetime was observed in the condition eGFP::GluA2 vs mCherry::GluA1 ($\tau_{eGFP::GluA2}$ = 2.41 ± 0.02 ns), no change in donor's lifetime was observed in eGFP::GluA1 vs mCherry::GluA1 ($\tau_{eGFP::GluA1}$ = 2.55 ± 0.02 ns) and the negative control ($\tau_{eGFP::GluA2}$ = 2.55 ± 0.01 ns) (Figure 19b). The failure of eGFP::GluA1, but not eGFP::GluA2, to FRET with mCherry::GluA1 suggests a different structural rearrangement of GluA1 homotetramer and GluA1/GluA2 heterotetramer.

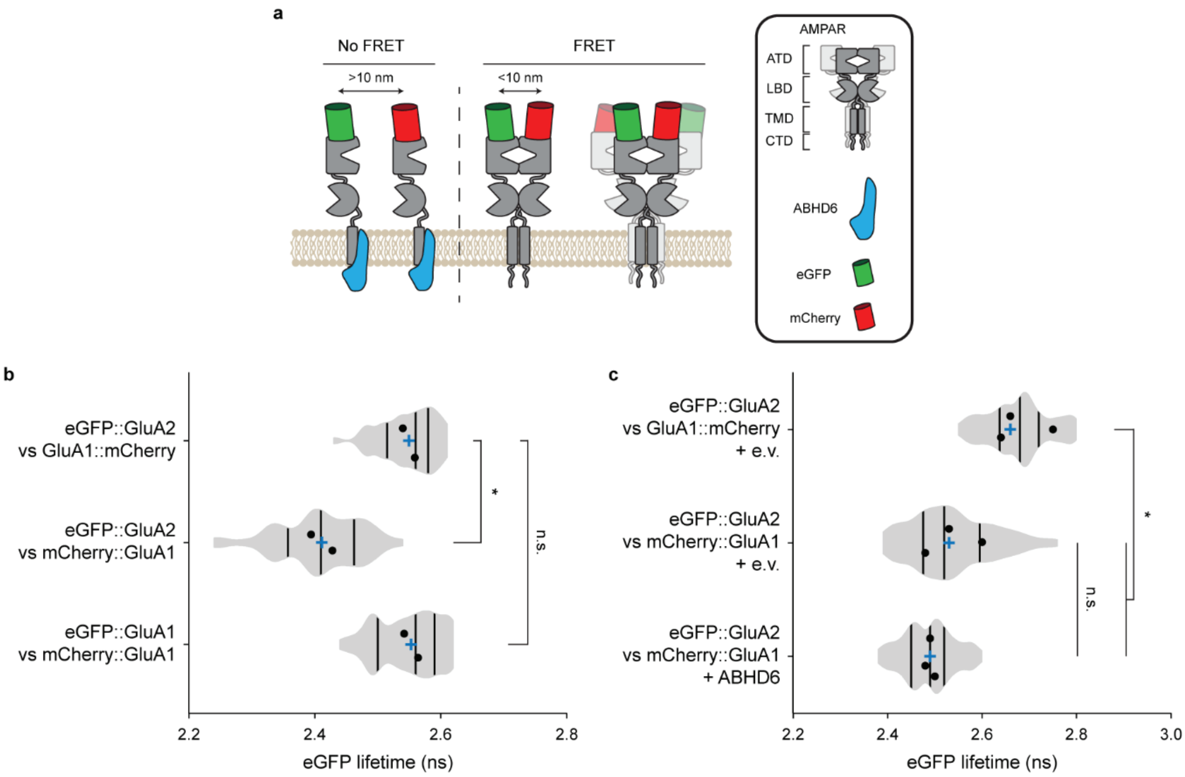

Figure 19: FRET between GluA1 and GluA2 subunits suggests that ABHD6 is unable to hold GluA subunits as monomers. (**a**) Schematic illustration of the fundament used for the design of FRET pairs for the study of GluA subunits assembly. If GluA subunits (grey) are hold in monomers by association with ABHD6 (blue) no FRET should be observed between msfGFP and mCherry. However, if dimerization and tetramerization of GluA subunits occurs, FRET between msfGFP- and mCherry-tagged GluA subunits should be observed. (**b**) Average eGFP lifetime measured by FLIM in HeLa cells co-expressing eGFP::GluA2 + GluA1::mCherry, τ_{eGFP} = 2.55 ± 0.01 ns, n = 45 (negative control); eGFP::GluA2 + mCherry::GluA1, τ_{msfGFP} = 2.41 ± 0.02 ns, n = 46; eGFP::GluA1 + mCherry::GluA1, τ_{msfGFP} = 2.55 ± 0.02 ns, n = 48. (**c**) Average eGFP lifetime measured by FLIM in eGFP::GluA2-positive HeLa cells co-expressing: GluA1::mCherry + e.v., τ_{eGFP} = 2.64 ± 0.06 ns, n = 66 (negative control); mCherry::GluA1 + e.v., τ_{eGFP} = 2.54 ± 0.06 ns, n = 57; mCherry::GluA1 + ABHD6, τ_{eGFP} = 2.49 ± 0.01 ns, n = 51. Mean eGFP lifetime pulled out from the average of (**b**) 2 and (**c**) 3 independent set of experiments.

In summary, here I report the development of a FRET pair between eGFP- and mCherry-tagged GluA2 and GluA1 subunits, respectively. Interestingly, in contrast to the GluA1 and GluA2 pair, I observed that eGFP- and mCherry-tagged GluA1 subunits were unable to FRET.

ABHD6 failed to prevent AMPAR multimerization

Having identified a FRET pair between AMPAR subunits, HeLa cells were then co-transfected with the FRET pair eGFP::GluA2 vs mCherry::GluA1 using equal amounts of the two subunits. As for ABHD6, a cDNA ratio of 2 compared to the GluA2/GluA1 was used. Unfortunately, to my surprise, the presence of ABHD6 did not compromise the FRET between the eGFP::GluA2 and mCherry::GluA1: +ABHD6: $\tau_{eGFP::GluA2}$ = 2.49 ± 0.01 ns vs control: $\tau_{eGFP::GluA2}$ = 2.54 ± 0.06 ns (Figure 19c). Schwenk and colleagues using blue native polyacrylamide gel electrophoresis observed that ABHD6 holds GluA1 and GluA2 monomers in monomeric GluA-ABHD6 complexes in transiently transfected tsA201 cells[177]. This observation contrasts the result here obtained even though the same combination of proteins (GluA1, GluA2, and ABHD6) were used. Contrary to the GluAs used in Schwenk, et al. (2019)[177], here I used N-terminus FP-tagged GluAs, but as observed by Dr. Jochen Schwenk, the insertion of FP at the N-terminus of GluA1 and GluA2 did not compromise the ABHD6 interaction (personal communication). Therefore, a likely explanation for such contradictory results lays in the sensitivity and accuracy of the two approaches.

To note, the differences observed in the eGFP lifetime between the controls in Figure 19b and Figure 19c can be explained by differences in the measurement of the lifetime of the system internal control, erythrosin B.

In conclusion, the results presented here failed to demonstrate that ABHD6 prevents oligomerization of GluA subunits, contrary to what was previously reported.

Chapter II

Bioorthogonal labeling of transmembrane proteins with non-canonical amino acids unveils masked epitopes in live neurons

Right after the discovery of AMPAR auxiliary proteins at the turn of the century, Tomita and colleagues[231] reported that during AMPAR internalization, TARPs dissociate from the AMPAR complex and remain stable at the plasma membrane. This observation was of particular relevance for the perception of how AMPARs are regulated during synaptic plasticity and scaling, as AMPARs rely – not only, but mainly – on TARPs for surface stabilization and synaptic targeting of AMPARs.

This hypothesis was later backed up by the observation that Glu binding induces a transient dissociation of $\gamma 2$ from AMPAR complexes[233,256]. However, other studies failed to observe the dissociation of TARPs from the AMPAR complex upon Glu binding. Therefore, rather than dissociation from the AMPAR complex, they proposed that Glu binding induces an overall rearrangement of the structure of the complex[257-259]. This ultimately led to the split of the AMPAR community into two parts. The ones that agree that auxiliary subunits dissociate from the AMPAR complex at the plasma membrane, and the ones that support that auxiliary subunit composition is predetermined at intracellular compartments with no further exchange of the complex composition.

To date, no clear evidence over one theory or the other exists. Faced with this gap in knowledge and at the same time the existence of conflicting data, I aimed to develop a strategy to study the dynamics of AMPAR and TARPs interaction in an attempt to decipher the conflicting data.

As our question was to understand if TARPs were able to dissociate from AMPARs at the plasma membrane – and the fact that at the time I was working with FLIM-FRET microscopy in the AMPAR biogenesis project, Chapter I –, we reasoned that the best way to address this particular question in living cells was through the use of FRET microscopy. As the ECD of TARPs comprises two small loops apposed to the AMPAR LBD and the low tolerance of these loops to protein tagging, the use of conventional tagging systems as FP or self-labeling SNAP- or HaloTag was out of question to label TARPs. The same could be said of smaller tags like biotin-acceptor peptide (bAP)- or hemagglutinin (HA)-tag which use bulky ligands. Confronted with such limitations, we established a collaboration with Dr. Markus Sauer and co-workers at the University of Würzburg in late 2017, which at the time were already working with non-canonical amino acids (ncAA) for labeling of recombinant proteins in heterologous cells. Therefore, we set the goal to come up with a strategy to label TARPs ECD using that approach as it is sterically minimally demanding when compared to conventional tagging strategies.

While the initial goal was to develop a tool for the study of AMPAR and TARPs interaction, given the success of the tool, here I present the development of a complete pipeline to label surface TARPs in both living dissociated neurons and slice cultures as complementary to the development of a tool to study AMPAR and TARPs interaction based on FRET. It should be noted the crucial contribution of Dr.

Alexander Kuhlemann and Dr. Gerti Beliu through the many enlightening discussions throughout the project, and who, together with Dr. Sören Doose, performed the acquisition and analysis of the super-resolution microscopy data.

In sum, using high-resolution and super-resolution microscopy, here I demonstrate that γ2 and γ8 are differentially organized at the plasma membrane of hippocampal neurons.

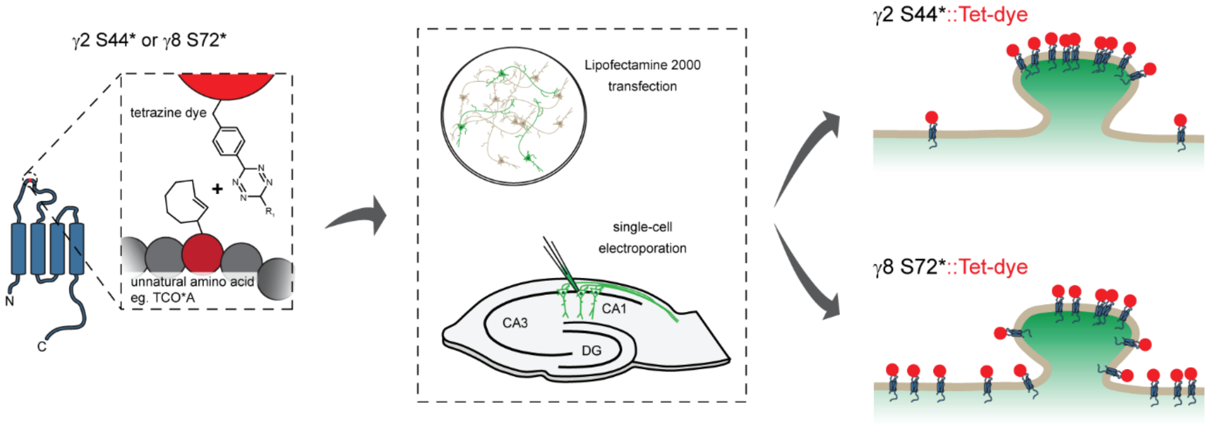

Figure 20: Bioorthogonal labeling of TARPs in living neurons. Schematic overview of click chemistry labeling via genetic code expansion. γ2 and γ8 carrying an Amber mutation (γ2 S44* and γ8 S72*, respectively) were tagged with the non-canonical amino acid (ncAA) TCO*A. TCO*A tagged TARPs were live stained with tetrazines functionalized with cell impermeable organic dyes in a catalysis-free reaction via the strain-promoted inverse electron-demanding Diels-Alder cycloaddition (SPIEDAC) reaction. ncAA-tagged TARPs experiments were conducted both in dissociated hippocampal neurons or hippocampal slice cultures. Surface labeling of γ2 S44* in dissociated neurons or slice cultures revealed enrichment of γ2 S44* at synaptic sites, whereas γ8 S72*-positive neurons revealed a homogeneous distribution of γ8 S72* throughout the dendrite.

Manuscript published in BioRxiv

DOI: https://doi.org/10.1101/2021.02.27.433189

Accepted in Nature Communication pending editorial modifications

Bioorthogonal labeling of transmembrane proteins with non-canonical amino acids unveils masked epitopes in live neurons

Diogo Bessa-Neto[1*], Gerti Beliu[2,3*], Alexander Kuhlemann[2*], Valeria Pecoraro[1], Sören Doose[2], Natacha Retailleau[1], Nicolas Chevrier[1], David Perrais[1], Markus Sauer[2#], Daniel Choquet[1,4#]

[1]University of Bordeaux, CNRS, Interdisciplinary Institute for Neuroscience, IINS, UMR 5297, F-33000 Bordeaux, France.
[2]Department of Biotechnology and Biophysics, University of Würzburg, Biocenter, Am Hubland, 97074 Würzburg, Germany.
[3]Rudolf Virchow Center for Integrative and Translational Bioimaging, University of Wuerzburg, Wuerzburg, Germany.
[4]University of Bordeaux, CNRS, INSERM, Bordeaux Imaging Center, BIC, UMS 3420, US 4, F-33000 Bordeaux, France.
[*]These authors contributed equally.
[#]Corresponding authors: M.S. (m.sauer@uni-wuerzburg.de), D.C. (daniel.choquet@u-bordeaux.fr)

ABSTRACT

Progress in biological imaging is intrinsically linked to advances in labeling methods. The explosion in the development of high-resolution and super-resolution imaging calls for new approaches to label targets with small probes. These should allow to faithfully report the localization of the target within the imaging resolution – typically nowadays a few nanometers - and allow access to any epitope of the target, in the native cellular and tissue environment. We report here the development of a complete labeling and imaging pipeline using genetic code expansion and non-canonical amino acids in neurons that allows to fluorescently label masked epitopes in target transmembrane proteins in live neurons, both in dissociated culture and organotypic brain slices. This allows us to image the differential localization of two AMPA receptor (AMPAR) auxiliary subunits of the transmembrane AMPAR regulatory protein family in complex with their partner with a variety of methods including widefield, confocal, and *d*STORM super-resolution microscopy.

INTRODUCTION

Over the past 15 years, advances in light-based super-resolution microscopy have revolutionized the way neuroscientists perceive key neuronal processes such as synaptic and axonal nanoscale organization or protein trafficking at the single-molecule level[99,324,325]. The improvements in the various super-resolution imaging methods, and particularly in single-molecule localization microscopy (SMLM), have made it possible to routinely reach imaging resolutions in the order of ~20 nanometers. However, elucidating target protein organization at virtually molecular resolution requires not only a high localization precision of individual emitters but also a high labeling density and specificity, and a distance between the fluorescent reporter and the target (linkage error) substantially smaller than the desired imaging resolution[326,327]. Classical labeling methods used for fluorescence imaging such as labeling the target protein with an antibody-dye complex or genetic fusion with a reporter fluorescent protein are limited in their use, particularly in live neurons. Antibodies are quite bulky, even when reduced to their monovalent forms, and only have access to exposed epitopes. Incorporation of fluorescent protein to a target protein can impede its native function, accounting for biased interpretations and severely limiting its possible site of insertion. There is thus a pressing need for the development of alternative labeling methods that do not depend on epitope accessibility and with sizes compatible with the nanometer precision of super-resolution imaging.

The nanoscale organization of synapses is an ideal model system for the application of innovative imaging and labeling methods because of its exquisite complexity and diversity as well as because of the tight link between synapse dynamic organization and function[99]. Among synaptic proteins, the complex involved in regulation of the function, localization, and trafficking of AMPA receptors (AMPAR) – the glutamate receptors that mediate most excitatory synaptic transmission, has historically raised large interest. Transmembrane AMPAR regulatory protein (TARP) family are four transmembrane proteins characterized by an intracellular amino- and carboxyl-terminal domain, and two extracellular loops (Ex1 and Ex2)[328] (Supplementary Fig. 1a). TARPs are key modulators of AMPAR-mediated synaptic transmission and plasticity, as they promote surface targeting, AMPAR pharmacology and gating modulation fundamental for proper AMPAR-mediated transmission[69,144,147,264,329-331]. Among the different members of the TARP family, γ2 (also known as stargazin) is the prototypical AMPAR auxiliary subunit and has been the most widely studied, followed, more recently, by γ8 that is the most abundant TARP in the hippocampus[110]. While sharing a large homology[148], γ2 and γ8 not only exert a differential modulation of AMPAR[144-146] but also display differential plasma membrane distribution, with γ2 suggested to bear an almost exclusive synaptic localization and γ8 a more widespread dendritic distribution, as seen in electron microscopy studies[261,262]. This was never, to the best of our knowledge, confirmed in living neurons by optical microscopy due to the lack of adequate tools.

Our understanding of TARPs localization and trafficking has been hampered by a lack of suitable labeling and imaging tools. The close association of the extracellular domains of TARPs to the AMPAR ligand-binding domain (LBD)[46,151,259,332,333] that confer their role in TARP-specific AMPAR modulation[144,145,334,335] has hindered the development of ligands recognizing the extracellular domains of TARPs as well as genetic fusion tagging[231,336]. Deciphering the respective surface diffusion and synaptic organization properties of γ2 and γ8 at the nanoscale is of particular interest given their presumptive key role in AMPAR regulation and modulation as well as the control of synaptic plasticity, but their molecular organization unfortunately remains widely unknown. This question is becoming particularly relevant given the recent increased interest in their differential role in synapse organization and function[245,333].

Click chemistry labeling via genetic code expansion (GCE) offers the possibility for site-specific incorporation of non-canonical amino acids (ncAAs) containing bioorthogonal groups into a target protein[337,338]. By replacing a native codon at a selected position in the target protein with a rare codon, such as the Amber (TAG) stop codon, the modified protein can then be expressed in the desired host cells along with an engineered amino acyltransferase (aaRS) and tRNA pair orthogonal to the host translational machinery. The engineered aaRS is modified in a way to only recognize a specific ncAA, which is then attached to a tRNA that matches the rare codon. Among a collection of different possibilities, the trans-cyclooct-2-ene (TCO*)-modified amino acids, such as TCO*-L-lysine (termed TCO*-A, where A stands for Axial isomer), is of interest when it comes to targeting and labeling the desired target proteins in living organisms. TCO* can react with a 1,2,4,5-tetrazine in a catalyst-free, fast, specific, and bioorthogonal strain-promoted inverse electron-demand Diels-Alder cycloaddition reaction (SPIEDAC). Due to the high selectivity and fast kinetics of this click chemical reaction, a large number of fluorophore-tetrazine conjugates and TCO*-functionalized molecules are now commercially available, making labeling of mammalian cells and whole organisms with organic dyes accessible for live and fixed samples[339-341].

Here, we explored the potential of bioorthogonal labeling as a strategy to tag and visualize surface TARPs in living neurons by conventional and superresolution microscopy with minimal to non-perturbation of TARPs modulation over AMPAR, opening new doors to the study of hard-to-tag proteins in living neurons. We describe a complete pipeline that allows for the first-time labelling proteins in live neurons in both primary and organotypic hippocampal cultures by GCE. Using this approach, we report the differential subcellular distribution of γ2 and γ8 for the first time at the light microscopy and single-molecule level. Also, our antibodies directed against extracellular loops of γ2 and γ8 allow us to establish that there are virtually no free surface γ2 and γ8 in hippocampal neurons.

RESULTS

Epitope masking by close interaction of TARPs extracellular loops with AMPAR LBD

As a first attempt to create specific ligands for γ2 and γ8 that could be used to study their organization and trafficking in live neurons, we generated antibodies against the γ2 Ex2 and γ8 Ex1 (Supplementary Fig. 1b). We first evaluated the antibodies specificity by incubating living COS-7 cells expressing either γ2 or γ8 bearing mEos2 as a reporter. As shown in Supplementary Fig. 1c, both antibodies are specific towards their respective target protein. We then analyzed if we could use these antibodies to label endogenous TARPs in dissociated hippocampal neurons, as both γ2 and γ8 are expressed in the hippocampus[148,232,251]. To our surprise, our antibodies were unable to recognize endogenous γ2 or γ8 in our primary hippocampal cultures. The presence of γ8 was confirmed by post-fixation immunostaining against the intracellular C-terminal domain of γ8 (Supplementary Fig. 1d), whereas γ2 immunostaining was inconclusive due to the poor sensitivity of the tested commercial α-γ2 antibodies. To understand the lack of TARPs staining in neurons, we overexpressed in neurons γ2 fused to eGFP at the C-terminus (γ2::eGFP) or GluA2 tethered to γ2::eGFP (GluA2::γ2::eGFP) in which the GluA2 C-terminus is fused to the γ2 N-terminus by in-frame expression[256]. When labeled with the α-γ2 Ex2, neurons overexpressing γ2::eGFP displayed specific antibody labeling that co-localized with the eGFP signal, likely revealing AMPAR-free γ2::eGFP. In contrast, in neurons overexpressing GluA2::γ2::eGFP and labeled with the α-γ2 Ex2, no antibody labeling was observed (Supplementary Fig. 1e). Structural data of γ2 or γ8 in complex with AMPARs revealed close proximity of both Ex1 and Ex2 to the AMPAR ligand-binding domain (LBD)[46,151,332], which likely results in epitope masking. This finding leads to the conclusion that antibodies fail to recognize endogenous TARPs in dissociated hippocampal neurons as well as in GluA2::γ2::eGFP-overexpressing neurons because of steric inaccessibility. Altogether, our results indicate that at the plasma membrane endogenous TARPs are always associated with AMPARs that mask the extracellular epitopes.

Genetic code expansion and bioorthogonal labeling of TARPs

Bioorthogonal labeling of proteins by replacing a single natural amino acid with a ncAA has emerged in the past years as an alternative strategy to target and visualize proteins in living mammalian cells with minimal to no perturbation[339,340,342]. Because click chemistry labeling of ncAAs with tetrazine-dyes is efficient and sterically minimally demanding, we hypothesized that it might be the method of choice to label masked epitopes on TARPs. We first designed Amber mutants (herein termed ncAA-tagged) of γ2 and γ8 by site-direct mutagenesis (Figure 21a), with respect to previously conducted work on γ2 with ncAAs[259]. Additionally, we replaced the endogenous Amber termination codon of γ8 with the Ochre codon (TAA) to prevent erroneous ncAA incorporation at the C-terminus (see Methods section). To identify the best position for the insertion of the Amber codon, three mutants of γ2 (S44*, S51* and S61*) and γ8 (S72*, S84* and K102*) were tested for ncAA incorporation and labeling efficiency in HEK293T cells (Figure 21b-d and Supplementary Fig. 1f,g).To check the efficiency of ncAA

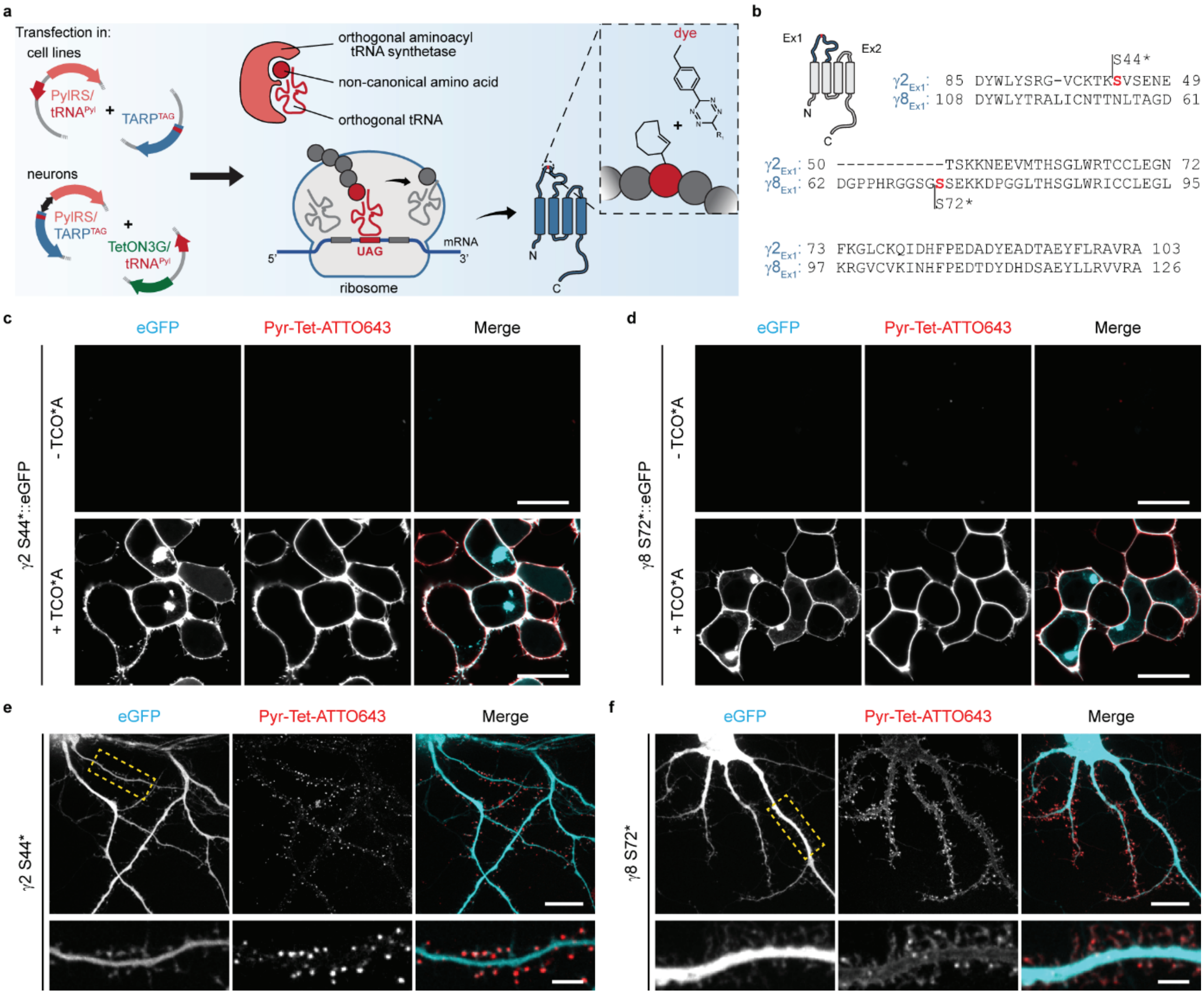

Figure 21: Bioorthogonal labeling of TARPs. (**a**) Schematic overview of click chemistry labeling via genetic code expansion. Amber mutants of ncAA-tagged γ2 and γ8 were designed by standard site-direct mutagenesis to incorporate the ncAAs carrying a TCO*A for click labeling. Protein expression occurs through endogenous and orthogonal tRNA-synthetases in the presence of appropriate tRNAs. Labeling of ncAA-tagged proteins occurs through a catalysis-free reaction between TCO*A and tetrazine-functionalized dyes via the strain-promoted inverse electron-demanding Diels-Alder cycloaddition (SPIEDAC) reaction. (**b**) Sequence alignment of the first extracellular loops of γ2 and γ8 from *rattus norvegicus*. Amber substitution mutations are represented in red. (**c-d**) Representative confocal images of living HEK293T cells co-expressing PylRS/4xtRNA^{Pyl} and (**c**) γ2 S44*::eGFP or (**d**) γ8 S72*::eGFP in the absence (upper) or presence of 250 μM TCO*A (lower) stained with 1.5 μM Pyr-Tet-ATTO643. Scale bar: 20 μm. Images are representative of three independent experiments. (**e-f**) Representative spinning disk confocal images of living dissociated hippocampal neurons co-expressing eGFP, Tet3G/tRNA^{Pyl} and (**e**) pTRE3G-BI PylRS/γ2 S44* or (**f**) pTRE3G-BI PylRS/γ8 S72* in the presence of 250 μM TCO*A and 100 ng.mL^{-1} doxycycline labeled with 0.5 μM Pyr-Tet-ATTO643. Bottom panels, magnified views of segments of dendrites highlighted in the eGFP panel (dashed yellow boxes) of the overview images showing the distribution of γ2 S44* and γ8 S72*. Scale bar: 20 μm (overview images) and 5 μm (magnified images). All representative images are representative of at least three independent preparations.

incorporation in the different mutants, eGFP was fused within the C-tail of γ2 and γ8–downstream the Amber mutation. Hence, inefficient incorporation or absence of ncAAs would result in premature translation termination and loss of eGFP signal (Figure 21c,d). HEK293T cells were co-transfected with one of the different ncAA-tagged TARPs, and an engineered pyrrolysine aminoacyl tRNA synthetase (PylRS) and its cognate tRNA: single-copy tRNA^{Pyl} (tRNA^{Pyl})[343] or four copies (4xtRNA^{Pyl})[344]. The clickable trans-cyclooctene derivatized lysine (TCO*A) was added to the cell media at the time of transfection for a period of approximately 24 h. Surface expression of the ncAA-tagged TARPs was accessed by bioorthogonal labeling via SPIEDAC using cell-impermeable tetrazine-dyes (H-Tet-Cy3, H-Tet-Cy5 and Pyr-Tet-ATTO643, Supplementary Fig. 2); tetrazines and TCO* react in a catalysis-free 'click-reaction'[339,340,345]. Afterward, excess of tetrazine-dyes was removed by subsequent washes and cells were live-imaged using confocal microscopy. As indicated by the eGFP signal, all ncAA-tagged TARPs showed equivalent expression levels as compared to γ2::eGFP, revealing efficient incorporation of TCO*A. However, the mutant γ8 K102*::eGFP displayed decreased Pyr-Tet-ATTO643 labeling as compared to mutants γ8 S72*::eGFP and γ8 S84*::eGFP. No noticeable difference in tetrazine-dye labeling efficiency was observed within the different γ2 mutants (Supplementary Fig. 1f,g). Additionally, tetrazine-dye labeling was entirely due to the incorporation of TCO*A as no labeling was detected in cells transfected with γ2::eGFP in the presence of TCO*A nor in cells transfected with γ2 S44*::eGFP or γ8 S72*::eGFP in the absence of TCO*A (Figure 21c,d and Supplementary Fig. 1f).

ncAA-tagged TARPs physically and functionally interact with AMPAR-subunit GluA1 as seen by FRET and electrophysiology

TARPs are auxiliary subunits to AMPARs that bind and interact closely with GluA subunits, as demonstrated by biochemical[231,331], functional[331], and structural[46,151,332] data. We thus aimed to study whether ncAA-tagged TARPs could still physically and functionally interact with GluA subunits using both Förster Resonance Energy Transfer (FRET) measurements and electrophysiology. As we were able to insert ncAAs into the Ex1 loops of γ2 and γ8 that are in close apposition to the extracellular domain of GluA subunits[46,151,332], we first sought to use FRET to measure AMPAR-TARP interactions. We designed a set of possible FRET pairs between the ncAA-tagged γ2/γ8 and the AMPAR-subunit GluA1. To label surface GluA1, a SNAP-tag was either inserted at the N-terminus (SNAP::GluA1; no FRET expected) or within the ATD-LBD linker of GluA1 at position 396 aa (GluA1::SNAP396; potential FRET pair) (Figure 22a). HEK293T cells were co-transfected with PylRS/tRNA^{Pyl}, SNAP-tagged GluA1, and the various ncAA-tagged TARPs in the presence of TCO*A. Cells were stained with 5 μM BG-AF488 (donor) and 1.5 μM H-Tet-Cy3 (acceptor) at 37 ºC for 30 minutes. Excess dye was removed by subsequent washing steps with HBSS. Fluorescence lifetime imaging microscopy (FLIM) was used to estimate the degree of FRET-based changes of the donor AF488 fluorescence lifetime[346]. As expected, when co-expressed with the SNAP::GluA1-AF488, neither γ2 S44*-Cy3 nor γ8 S72*-Cy3 were able to quench the donor, *i.e.*, no decrease in AF488 fluorescence lifetime was observed as compared to the donor alone condition (no H-Tet-Cy3, GluA1::SNAP396-AF488 + γ2 S44*); SNAP::GluA1-AF488 + γ2 S44*-Cy3: τ_{AF488} = 3.07 ± 0.03 ns, SNAP::GluA1-AF488 + γ8 S72*-Cy3: τ_{AF488} = 3.04 ± 0.01 ns, and GluA1::SNAP396-AF488 + γ2 S44*: τ_{AF488} = 3.01 ± 0.01 ns, respectively.

In contrast, we observed a robust decrease in GluA1::SNAP396-AF488 fluorescence lifetime when co-expressed with γ2 S44*-Cy3 or γ2 S61*-Cy3 as compared to the SNAP::GluA1-AF488 + γ2 S44*-Cy3, with the FRET pair GluA1::SNAP396-AF488 + γ2 S44*-Cy3 showing a stronger reduction in AF488 lifetime (Figure 22b,c). Moreover, when we forced a one to one interaction between GluA1 and γ2 using a tethered GluA1 SNAP396 to γ2 S61* (GluA1::SNAP396::γ2 S61*-AF488/Cy3), we did not observe a significant difference in AF488 lifetime compared to the condition in which we expressed the two proteins separately (GluA1::SNAP396-AF488 + γ2 S61*-Cy3). This suggests a full occupancy of the AMPAR subunits with four TARPs under our experimental conditions. Similar to ncAA-tagged γ2-Cy3,

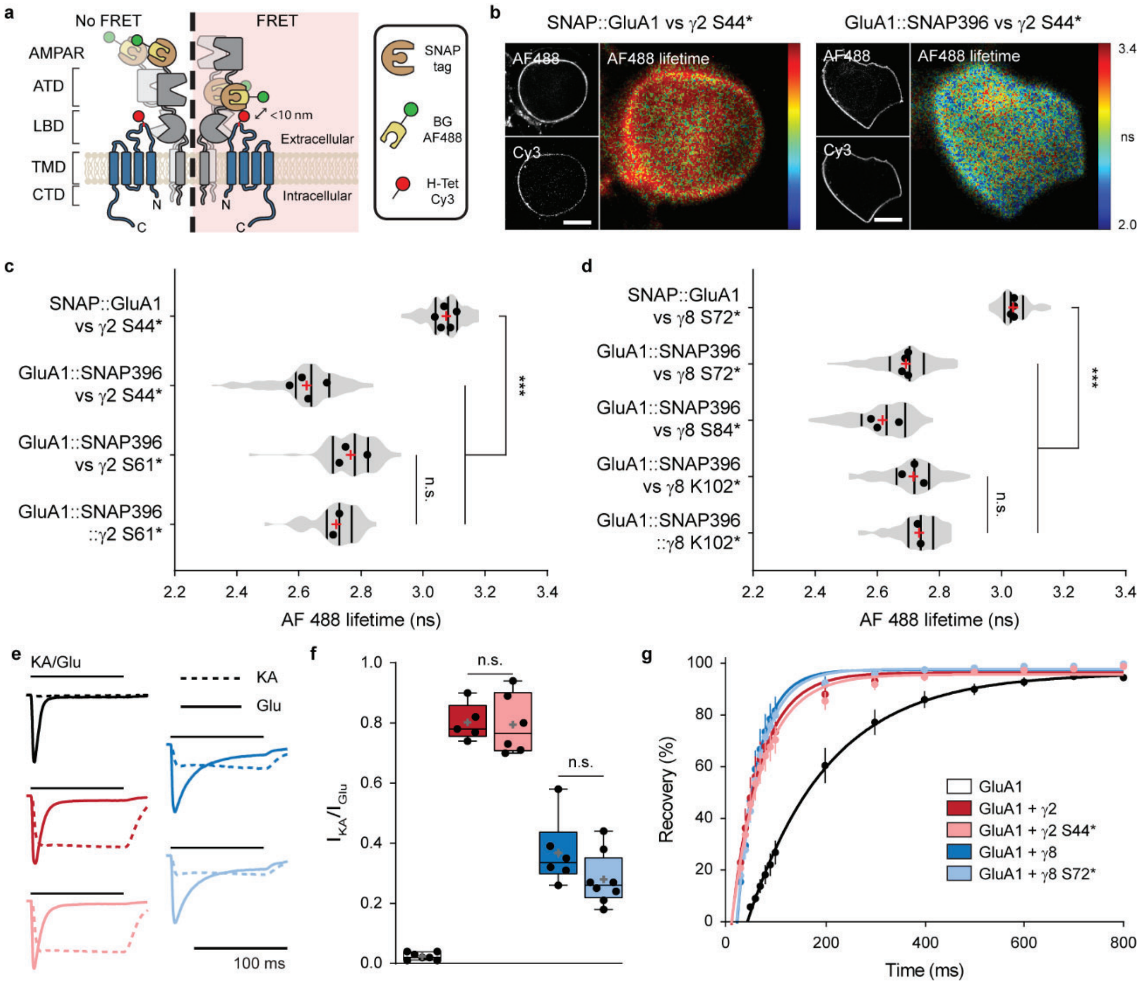

Figure 22: ncAA incorporation in the Ex1 loop of TARPs does not impair physical or functional interaction with AMPAR-subunit GluA1. (**a**) Strategy to label GluA1 and TARPs for FRET microscopy. SNAP-tag was inserted at GluA1 N-terminus (SNAP::GluA1) or ATD-LBD linker (GluA1::SNAP396) and labeled with BG-AF488 (donor). ncAA-tagged TARPs were labeled with tetrazine Cy3 (acceptor). (**b**) Representative spinning disk (AF488 and Cy3) and widefield illumination FLIM (AF488 lifetime) images of living HEK293T cells co-expressing PylRS/tRNA$^{\text{Pyl}}$, γ2 S44*, and SNAP GluA1 (left) or GluA1 SNAP396 (right) used in (**c**). Scale bar: 10 μm. (**c** and **d**) Average AF488 lifetime in HEK293T cells co-expressing PylRS/tRNA$^{\text{Pyl}}$, SNAP-tagged GluA1 (SNAP::GluA1 or GluA1::SNAP396), and (**c**) ncAA-tagged γ2 (γ2 S44* or γ2 S61*) or (**d**) ncAA-tagged γ8 (γ8 S72*, γ8 S84*, or γ8 k102*), or alternatively PylRS/tRNA$^{\text{Pyl}}$ and (**c**) GluA1::SNAP396::γ2 S61* or (**d**) GluA1::SNAP396::γ8 K102*. From top-to-bottom, cell numbers were (**c**) 117, 108, 66, 51; (**d**) 87, 104, 111, 84, 53. Data was pulled from two-to-five independent preparations. Statistical significance was analyzed using Welch's ANOVA test; *** $p < 0.001$, n.s. specifies no significance. (**e**) Whole-cell currents and (**f**) ratios of KA- to Glu-evoked currents in response to 0.1 mM KA (dashed) or 10 mM Glu (line), or (**g**) recovery of desensitization to two pulses of 100 ms Glu applied at different intervals from HEK293T cells co-transfected with PylRS/tRNA$^{\text{Pyl}}$, GluA1 and, eGFP (control, black, (**f**) 7 and (**g**) 6 cells), γ2::eGFP (dark red, 5 cells), γ2 S44*::eGFP (light red, 6 cells), γ8::eGFP (dark blue, 6 cells), or γ8 S72*::eGFP (light blue, 8 cells) from three-to-four independent preparations. Statistical difference was analyzed using one-way ANOVA with a Fisher's LSD multiple comparisons test; n.s. specifies no significance. All data represent mean ± SD. Box and violin indicates 25th to 75th percentiles, with median represented as a centre line, mean represented as a cross, and on box plot: whiskers represent max to min. Source data are provided as a Source Data file.

the presence of ncAA-tagged γ8-Cy3 led to a robust decrease in GluA1::SNAP396-AF488 lifetime, with the GluA1::SNAP396-AF488 + γ8 S84*-Cy3 pair outperforming the pairs GluA1::SNAP396-AF488 + γ8 S72*- and γ8 K102*-Cy3 (Figure 22d). As for γ2, we did not observe a difference between the GluA1::SNAP396-AF488 + γ8 K102*-Cy3 and the tethered GluA1 SNAP396 to γ8 K102* (GluA1::SNAP396::γ8 K102*-AF488/Cy3). Altogether, our FRET experiments indicate that ncAA-tagged TARPs physically interact with AMPAR and provide thus a new tool to study the regulation of AMPAR-TARP interactions.

TARPs type-I, including γ2 and γ8, modulate AMPAR gating in a TARP subtype-specific manner[144-146,226,334]. To determine if the incorporation of TCO*A within the Ex1 loop compromises TARP function, notably interaction with and modulation of AMPARs, we performed whole-cell patch-clamp recordings in HEK293T cells co-expressing GluA1 (flip isoform) alone (eGFP, control) or in the presence of WT or ncAA-tagged γ2/γ8, bearing eGFP as a reporter. When compared to GluA1 alone and GluA1 in the presence of WT γ2 or γ8, the incorporation of TCO*A into the Ex1 loop did not impair the ability of TARPs to increase the efficacy of the partial agonist kainate (KA) over GluA1 (ratio peak current amplitude KA/Glu mean ± SD: GluA1 = 0.02 ± 0.01; GluA1 + γ2 = 0.80 ± 0.06; GluA1 + γ2 S44* = 0.80 ± 0.10; GluA1 + γ8 = 0.37 ± 0.11; GluA1 + γ8 S72* = 0.28 ± 0.09) (Figure 22e,f). Additionally, we did not observe perturbations on TARPs ability to decrease receptor desensitization (τ_{des}: GluA1 = 4.34 ± 0.59; GluA1 + γ2 = 8.44 ± 1.50; GluA1 + γ2 S44* = 9.02 ± 2.14; GluA1 + γ8 = 17.41 ± 3.72; GluA1 + γ8 S72* = 15.43 ± 2.82 ms) (Supplementary Fig. 3a) or increase receptor recovery from desensitization (τ_{rec}: GluA1 = 162.6; GluA1 + γ2 = 57.1; GluA1 + γ2 S44* = 62.3; GluA1 + γ8 = 40.9; GluA1 + γ8 S72* = 45.8 ms) (Figure 22g). Furthermore, the presence of endogenous intracellular polyamines leads to a block of calcium-permeable AMPARs, like GluA1 homomers; better illustrated by a strong inwardly rectifying I-V curve. TARPs attenuate polyamine block of calcium-permeable AMPARs reducing AMPAR rectification[347]. No difference was observed between WT TARP and respective ncAA-tagged TARP ability to reduce the GluA1 rectification (Supplementary Fig. 3b). Altogether, the patch-clamp experiments indicate ncAA-tagged TARPs retain a normal functional ability to modulate AMPAR gating.

Distinct surface distributions of ncAA-tagged γ2 and γ8 in hippocampal neurons

After verification of the proper ncAA incorporation into TARPs extracellular loop and the normal receptor function in heterologous cells, we exploited the use of GCE to label recombinant TARPs in living neurons. The occurrence of the Amber codon in mammalian cells is rare, (~0.5 ‰), and represents 20-23% of all stop codons. It is however important to keep in mind that GCE might induce toxicity due to tRNA suppression of endogenous proteins containing Amber codon terminations. A good practice is to restrict the concentration of PylRS to prevent suppression of naturally occurring Amber codon terminations, as in the gene *Cacng8*, encoding the protein γ8. In addition, the presence of TARPs, especially γ8, increases AMPAR Glu affinity as well as channel conductance[335,348], as a result, overexpression of TARPs triggers Glu-induced excitotoxicity[349]. Hence, we decided to overexpress the PylRS and ncAA-tagged TARPs under a bidirectional doxycycline-inducible promoter, pTRE3G-BI, *i.e.* pTRE3G-BI PylRS/γ2 S44* and pTRE3G-BI PylRS/γ8 S72*. To make it easier to follow, we will simply refer to these constructs by the name of the respective ncAA-tagged TARP (γ2 S44* or γ8 S72*), however it should be noted that different DNA constructs were used for the expression of ncAA-tagged TARPs in heterologous cells and neurons. To further decrease the complexity of our tool, we combined in a single vector the $tRNA^{Pyl}$ and the Tet-On 3G transactivator (herein termed $Tet3G/tRNA^{Pyl}$), which binds to and activates expression from TRE3G promoters in the presence of doxycycline (see Methods section).

To estimate the potential off-target surface labeling level in our neuronal experiments, dissociated hippocampal neurons at days *in vitro* (DIV) 3-4 were co-transfected with the Tet3G/tRNA^{Pyl}, pTRE3G-BI PylRS (no TARP, only the PylRS), and clickable-GFP. Five days before H-Tet-Cy5 labeling, expression of PylRS was induced by doxycycline, and TCO*A was added to the cell media. Approximately 24 h before labeling, half of the cell media was replaced by fresh media supplemented with doxycycline and TCO*A (see Methods section). As shown in Supplementary Fig. 4, expression of clickable-GFP indicates the success of the GCE experiment, while the transfected cell does not express more H-Tet-Cy5 labeling than non-transfected neighboring neurons, demonstrating the absence of any detectable off-target surface labeling in the absence of clickable surface proteins.

To express TARPs, dissociated hippocampal neurons were transfected with the necessary machinery for the expression of γ2 S44* or γ8 S72* together with eGFP. At DIV 16-17, 100 ng.mL^{-1} doxycycline and 250 μM TCO*A were added to the cell media for approximately 20 h. Similar to bioorthogonal labeling of HEK293T cells, surface labeling of ncAA-tagged TARPs was obtained by live incubation with 0.5 μM of cell-impermeable tetrazine-dyes (H-Tet-Cy5, Pyr-Tet-ATTO643, Pyr-Tet-AF647). Excess of tetrazine-dye was removed by subsequent washes with warm Tyrode's solution before imaging of live or fixed neurons (Figure 21e, f and Figure 23). Similar to what we observed in HEK293T cells, TCO*A-supplemented neurons transfected with either WT γ2 or WT γ8 displayed no tetrazine-dye labeling (Figure 23a-c upper panel and d-f upper panel, respectively). Surface labeling of γ2 S44*-positive neurons showed a strong enrichment of γ2 S44* in the dendritic spines with low expression in the dendritic shaft (Figure 21e and Figure 23a-c lower panel). In contrast, γ8 S72* was distributed throughout the dendritic arbor (Figure 21f and Figure 23d-f lower panel). Of note, in Figure 21e-f, only surface TARPs are revealed, contrary to the images of GFP in neurons expressing γ2::GFP (Supplementary Fig. 1e) that display both, surface and intracellular γ2::GFP, explaining the more diffuse labeling in the latter case.

Using eGFP as a cell marker, we compared the enrichment of γ2 S44* and γ8 S72* in spines versus dendritic shafts, at the base of the measured spine (extraspine). We observed an average of 2.60 ± 0.69 fold higher enrichment in the spines as compared to the neighboring shaft for γ2 S44* (Figure 23g). Furthermore, γ2 S44* showed a pronounced tendency to accumulate in clusters heterogeneously distributed in the spine head. In contrast, γ8 S72* had a more homogeneous distribution in dendrites and spines with a lower tendency to form clusters. When comparing the fluorescence levels in the spine to the neighboring extraspine area, γ8 S72* was only slightly enriched at the spines (1.17 ± 0.25 fold increase) (Figure 23g).

One of the drawbacks of overexpression systems, in particular transfection, is the heterogeneous expression levels of the protein of interest from cell to cell and the potential higher expression level as compared to the endogenous protein, which might lead to artifacts like mislocalization of proteins. We directly estimated the overexpression level of γ8 by immunocytochemistry based on the total γ8 levels in γ8 S72*-positive neurons compared to non-transfected neurons (Supplementary Fig. 5). Our data showed that, while some neurons display up to 3-4 fold higher γ8 expression levels than the average,

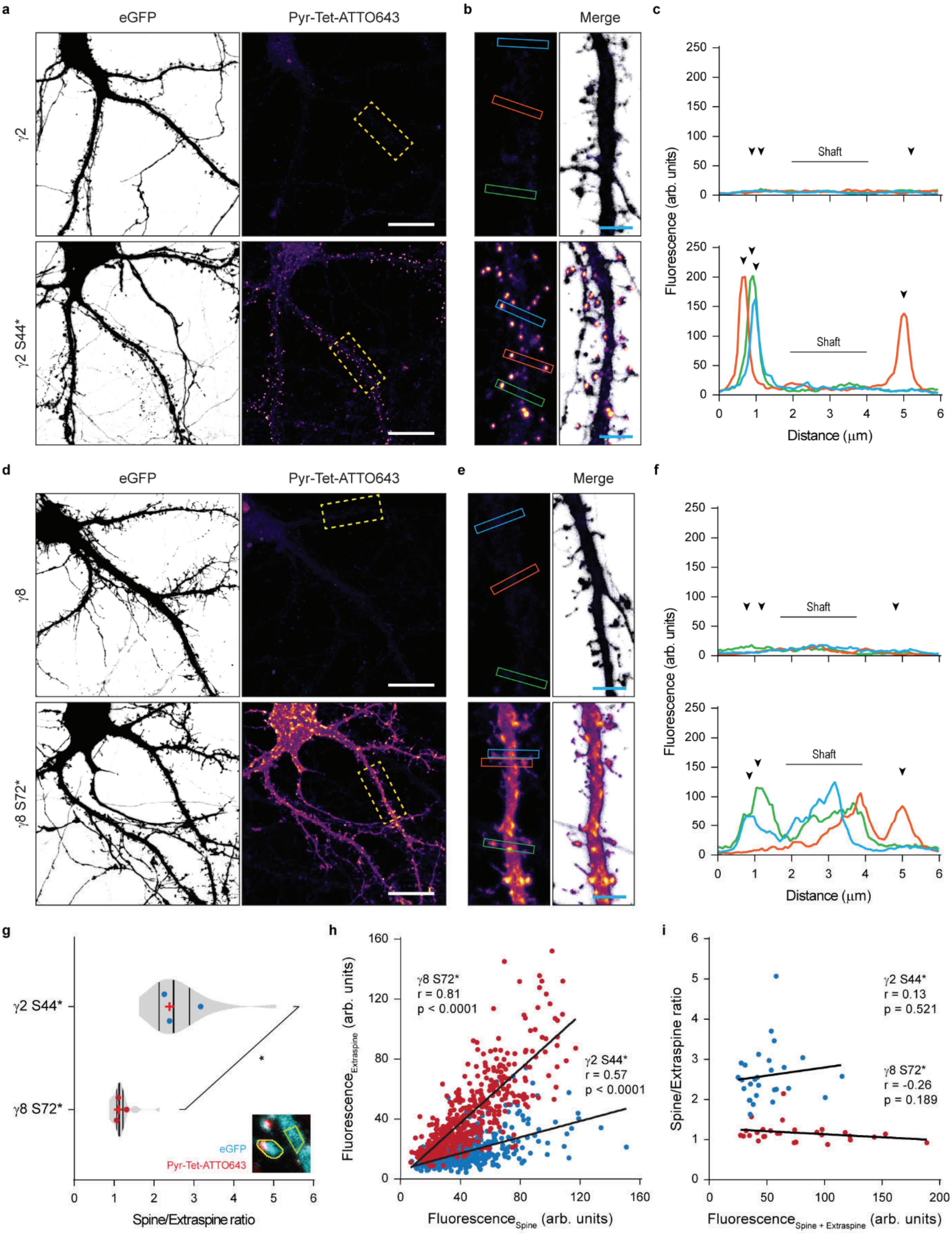

Figure 23: Distinct dendritic surface distribution of γ2 S44* and γ8 S72* in dissociated neurons. (**a**-**d**) Representative confocal images of fixed dissociated hippocampal neurons co-expressing eGFP, Tet3G/tRNA^{Pyl} and (**a**) pTRE3G-BI PylRS/γ2 (upper panel), pTRE3G-BI PylRS/γ2 S44* (lower panel), (**d**) pTRE3G-BI PylRS/γ8 (upper panel), or pTRE3G-BI PylRS/γ8 S72* (lower panel) in the presence of 250 μM TCO*A and 100 ng.mL^{-1} doxycycline live stained with 0.5 μM Pyr-Tet-ATTO643. (**b**) and (**e**) Magnified views of segments from the respective overview images (dashed rectangles). Scale bar: (**a** and **d**) 20 μm and (**b** and **e**) 4 μm (magnified images). (**c**) and (**f**) Line scan measurements of Pyr-Tet-ATTO643 across spines and dendritic shaft based on eGFP signal represented in (**b**) and (**e**). (**g**) Average spine to extraspine intensity ratio of the ncAA staining indicating a spine enrichment of 2.60 ± 0.69 folds for γ2 S44* (blue), and of only 1.17 ± 0.25 fold for γ8 S72* (red). Statistical significance was analyzed using a two-tailed unpaired Welch's t-test; *p < 0.05. (**h**) Plot of all the analyzed spines fluorescent intensities as a function of the intensity in a corresponding neighboring equivalent extraspine area in the dendrite for γ2 S44* (blue) and γ8 S72*

(red) expressing neurons. The Pearson's correlation coefficients are γ2 S44*: blue, r = 0.57, p < 0.0001, 872 spines; and, γ8 S72*: red, r = 0.81, p < 0.0001, 521 spines. (**i**) Plot of the average ratio per neuron of spine to extraspine intensities as a function of the sum of spine and extraspine intensities for γ2 S44* (blue, r = 0.13, p = 0.521) and γ8 S72*: and γ8 S72* (red, r = 0.-26, p = 0.189) expressing neurons. (**g**, **h**, and **i**) Data relative to γ2 S44* and γ8 S72* pulled from 28 cells each from three independent biological replicates. All representative images are representative of three independent preparations. Source data are provided as a Source Data file.

the mean γ8 expression level in all transfected neurons was not significantly different from that in non-transfected neighboring neurons. We could not perform this control for γ2 levels due to the poor quality of the staining we obtained with the C-terminal γ2 antibody. Interestingly, this might be related to poor accessibility of the antibody to the γ2 C-terminus in the packed PSD, as was previously observed in TEM[262]. This effect would be less prominent for γ8 that is more extrasynaptic. As a note, the fact that we observed strong synaptic localization of γ2 by GCE labeling confirms that our observation does not result from overexpression-induced γ2 mislocalization. Indeed, overexpression would tend to saturate γ2 binding sites in the PSD and lead to more extrasynaptic γ2.

To further explore the impact of γ2 and γ8 expression levels on their distribution, we plotted the mean fluorescence intensity level measured on all analyzed extraspine areas versus the neighboring spine levels. We observed a poor correlation between γ2 S44* labeling at spines versus extraspine, while γ8 S72* displayed a strong correlation between these two areas, independently of the expression level (Figure 23h). Furthermore, the average enrichment ratio per neuron of both γ2 S44* and γ8 S72* was independent of the expression level (Figure 23i). This indicates that the difference observed between γ2 S44* and γ8 S72* distribution is independent of their expression level, and likely due to the intrinsic nature of the proteins and their targeting properties.

Bioorthogonal labeling of TARPs in organotypic hippocampal slice cultures

While dissociated primary neuronal cultures are a well-established experimental model, they lack the physiological cellular environment, network, and regional specificity of the intact brain. Given the small size of tetrazine-dyes, high specificity, and ultrafast bioorthogonal reaction with TCO*, we aimed to exploit the potential of this approach as a tool to label surface proteins in the more physiological system of organotypic hippocampal slice cultures (OHSC). We used single-cell electroporation (SCE) to deliver the cDNAs in identified target CA1 pyramidal neurons from 300 μm thick slices. Similar to what we achieved in dissociated neurons, we used the doxycycline-inducible expression system for the controlled expression of ncAA-tagged TARPs and PylRS. TCO*A and doxycycline were added to the media approximately 22 h before tetrazine-dye labeling. Excess of TCO*A and tetrazine-dye in the extracellular space were removed by subsequent washes with warm Tyrode's solution (Figure 24a, see Methods section). Confocal images of fixed slices of SCE CA1 neurons co-expressing eGFP and γ2 S44* or γ8 S72* demonstrated good tissue penetrability and high specificity of H-Tet-Cy5 towards TCO* for tissue applications as indicated by the eGFP signal (Figure 24b,c,e). Similar to what we observed in dissociated neurons (Figure 23a-f lower panel), γ2 S44* expressed into CA1 neurons showed a remarkable fluorescence signal enrichment at spines of both apical and basal dendrites with reduced labeling in the dendritic shaft (Figure 24d,g,h). To verify γ2 S44* accumulation along the Z-projected

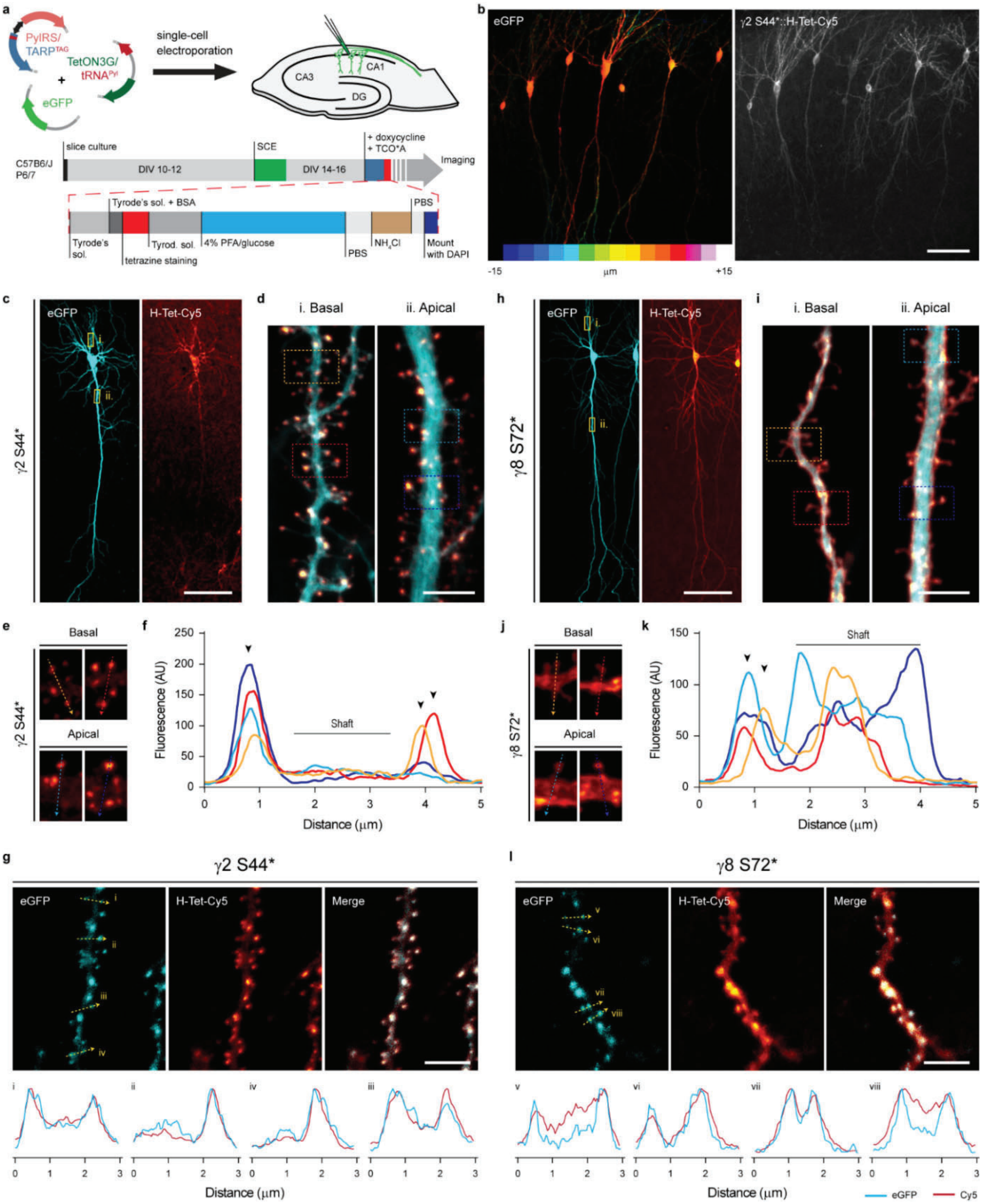

Figure 24: Bioorthogonal labeling of γ2 S44* and γ8 S72* in organotypic hippocampal slice cultures report a distinct surface distribution of TARPs. (**a**) Depiction of the workflow used for expression of ncAA-tagged TARPs in CA1 pyramidal cells in OHSC using single-cell electroporation (SCE), and live staining with tetrazine-dyes. (**b**) Example confocal image of fixed CA1 neurons co-expressing eGFP and γ2 S44* in OHSC. Images are projections of a z-stack taken by 1 μm increments, eGFP signal is color-coded with respect to sample depth. (**c, e**) Representative confocal images of CA1 neurons co-expressing eGFP, and (**c**) γ2 S44*- or (**h**) γ8 S72* live stained with 1 μM H-Tet-Cy5. (**d, f**) Magnified views of segments of the basal and apical dendrites from (**d**) γ2 S44*- and (**f**) γ8 S72*-overexpressing CA1 neurons highlighted in the corresponding overview images (yellow boxes). (**g, i**) Close up of representative spines from (**g**) γ2 S44*- and (**i**) γ8 S72*-overexpressing CA1 neurons highlighted (dashed squares) in the overview images (**d**) and (**f**), respectively. (**h**) and (**j**) Line scan measurements of Cy5 signal across spines in (**g**) and (**i**) respectively. (**k, l**) Confocal images of segments of basal dendrites from CA1 neurons co-expressing either (**k**) γ2 S44* or (**l**) γ8 S72, and the PSD-95 marker, XPH20::eGFP. Bottom insets: line scans of the GFP and Cy5 signal for the 3 μm segments indicated in the above images. Scale bar: (**b**, **c**, and **h**) 100 μm and (**d**, **g**, **i**,and **l**) 5 μm. (**b-e**, and **h-j**) representative images are representative of three or four independent preparations, and (**g** and **l**) from two independent preparations.

dendritic shaft (Figure 24d), we co-expressed γ2 S44* with the PSD-95 marker XPH20 fused with eGFP (XPH20::eGFP)[350,351] as a reporter and found that γ2 S44* accumulation was indeed always colocalized with the XPH20 eGFP signal (Figure 24k). In contrary to γ2 S44*, but in line with the observations made in dissociated neurons overexpressing γ8 S72* (Figure 23d-f lower panel), γ8 S72*-overexpressing CA1 neurons showed a more homogeneously distributed H-Tet-Cy5 fluorescence signal along the dendrites (Figure 24f,i,j).

This highlights the reliability of bioorthogonal labeling as a versatile, fast, and specific tool for live labeling of proteins in neuronal tissue.

*d*STORM imaging reveals differences in nanoscale distribution of TARPs

To investigate the peculiar difference found in the distribution of γ2 S44* and γ8 S72* in neurons by confocal microscopy in more detail, we used SMLM by *direct* stochastic optical reconstruction microscopy (*d*STORM)[352,353]. *d*STORM images revealed the molecular distribution of γ2 S44* and γ8 S72* in hippocampal neurons (Figure 25a,b) and indicated that γ2 S44* accumulates in synaptic spines (Figure 25b-d), in agreement with confocal data. To quantify the distribution of ncAA-tagged and H-Tet-Cy5 clicked TARPs, we co-expressed again the PSD-95 marker XPH20::eGFP as a reporter to identify synaptic sites and compared the localization densities determined from *d*STORM data of extrasynaptic and synaptic sites. While both TARPs show a homogeneous distribution in extrasynaptic sites, the absolute localization density determined for γ8 S72* is ~3-fold higher (Figure 25c). Together with the slightly higher localization density of γ2 S44* in synaptic sites (Figure 25c), our data thus demonstrate that the localization density measured for y2 S44* is ~9 fold higher in synaptic as compared to extrasynaptic sites, whereas γ8 S72* exhibits only a ~2 fold higher localization density in synaptic compared to extrasynaptic sites (Figure 25 c, inset).

Next, we calculated Ripley's K-function of several regions of interest (ROIs) in synaptic and extrasynaptic areas to analyze the distribution of TARPs in neurons (Supplementary Fig. 6) and compared them to simulated data with spatial distributions following complete spatial randomness or a clustered Neyman-Scott process (accounting for multiple localizations from each fluorophore) in identical ROIs. Ripley's K-functions showed for both TARPs in and outside of synapses randomly distributed localization clusters with a size of ~20 nm, which can be attributed to multiple localized Cy5 dye molecules. Only γ2 S44* in synaptic areas showed strong deviation from the simulations with a maximum at ~100 nm indicating cluster formation (Supplementary Fig. 6). Individual cluster analysis for each ROI in and outside of synapses confirmed the existence of γ2 S44* clusters in synapses and the absence of extrasynaptic γ2 S44* and γ8 S72* clusters (Figure 25d). In addition, the synaptic ROIs exhibited a higher localization density for γ2 S44* clusters with an average size of ~80 nm (Figure 25c,d and Supplementary Fig. 7).

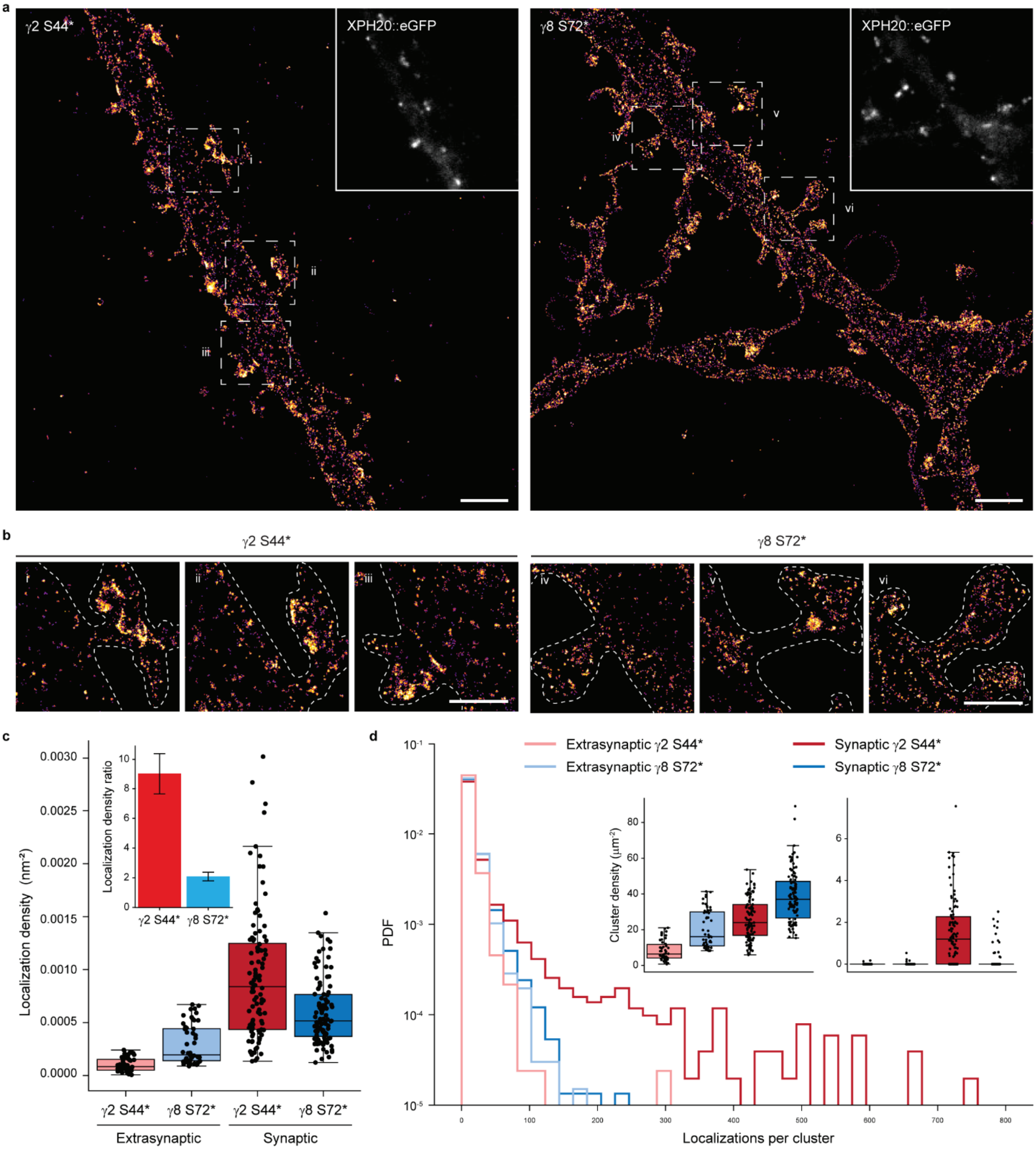

Figure 25: *d*STORM imaging and analysis reveal nano-scale organization of bioorthogonal labeled γ2 S44* and γ8 S72* in dissociated neurons. (**a**) Representative *d*STORM image of Pyr-Tet-AF647 (0.5 µM) live labeled neurons expressing γ2 S44* or γ8 S72* co-expressed with XPH20::eGFP. Scale bar: 2 µm. (**b**) Magnified views of spine and dendrite of the respective overview images in (**a**) (dashed rectangles). Scale bar: 1 µm. (**c**) Boxplots displaying higher synaptic localization densities for γ2 S44* ((0.93 ± 0.06)*10E-3 nm^{-2}, n = 104, dark red) compared to γ8 S72* ((0.60 ± 0.03)*10E-3 nm^{-2}, n = 102, dark blue). γ8 S72* showed higher extrasynaptic localization densities ((0.29 ± 0.03)*10E-3 nm^{-2}, n = 52, light blue) in comparison to γ2 S44* ((0.10 ± 0.01)*10E-3 nm^{-2}, n = 50, light red). Inset: Ratio of synaptic to extrasynaptic mean localization densities indicate a spine enrichment of 9.0 ± 1.4 folds for γ2 S44* (red) and of 2.1 ± 0.3 for γ8 S72* (blue). (**d**) Histograms showing localizations number per cluster for synaptic (dark), extrasynaptic (light) γ2 S44* (red) and γ8 S72* (blue), displayed as probability density function (PDF) (n = 2039, 3243, 2486, 3644 cluster from 50, 52, 104, 102 ROIs of five preparations for extrasynaptic γ2, extrasynaptic γ8, synaptic γ2, synaptic γ8, respectively). Insets display boxplots of ROI cluster densities for clusters with less (left inset) and more than 100 clustered localizations (right inset). Only synaptic γ2 S44* shows clusters with >100 localizations (1.93 ± 0.19 µm^{-2}) compared to nearly no clusters for synaptic γ8 S72* (0.21 ± 0.06 µm^{-2}) and extrasynaptic γ2 S44* (0.01 ± 0.01 µm^{-2}) or γ8 S72* (0.03 ± 0.01 µm^{-2}). For a selection of clusters with <100 localizations, γ8 S72* presents larger densities in synaptic (38 ± 1 µm^{-2}) as well as extrasynaptic areas (20 ± 2 µm^{-2}) in comparison to γ2 S44* clusters (synaptic: 26 ± 1 µm^{-2}, extrasynaptic: 8 ± 0.8 µm^{-2}). Boxplots show lower to upper quartile and median values of the data with whiskers extending 1.5 * interquartile range. All data represent mean ± SEM. Source data are provided as a Source Data file.

DISCUSSION

The ability to label target proteins with small ligands, and at sterically hard-to-access epitopes, represents an important challenge in biology, in particular for live-cell and super-resolution imaging studies in neurons. TARPs represent an interesting case study as their limited extracellular loops and close association with AMPARs has prevented the development of adequate ligands, in particular for the study of TARPs organization and trafficking at the cell surface of living neurons. Our motivation to search for alternative labeling strategies was further reinforced by our initial finding that functional antibodies to the extracellular domains of γ2 and γ8 were unable to recognize native TARPs in neurons, likely due to epitope masking. We thus engineered the technology to incorporate ncAAs in these proteins at given edited sites by GCE to label them directly with fluorophores by click chemistry. Due to the potential of GCE for protein tagging, and emerging interest in using such strategy for protein labeling via click chemistry, in particular in the context of neuroscience[354], we worked with commercially available reagents for reproducibility and broader reach and developed a new pipeline to label neurons in two different model systems, including cultured brain slices that preserve the physiological network environment.

We demonstrate that γ2 and γ8 can be directly labeled with this approach both in dissociated primary cultures and organotypic slices of rodent hippocampal neurons. Labeled proteins can then be imaged by a panoply of different approaches, including widefield, confocal, or *d*STORM super-resolution imaging due to the vast combination possibilities with different tetrazine-dyes. As some tetrazine-dyes tend to bind non-specifically to intracellular compartments, previous work show that it is important to carefully select suitable tetrazine-dyes and establish proper control experiments for each specific application[340].

Our data reveal that γ2 and γ8 display profoundly different distributions on the neuronal surface, γ2 being much more concentrated and clustered at synapses than γ8. In addition, the ability to label the masked epitopes in close proximity to the associated AMPAR subunits allowed us to develop FRET pairs between γ2 or γ8 and GluA subunits. Further development of the FRET pairs with smaller tags on AMPARs, such as α-bungarotoxin binding site-tag[355] and development of CRISPR/Cas9 technology for the site-specific incorporation of a single ncAA will be of value for the study of AMPAR and TARP dynamic interaction in live neurons, in particular, in the context of synaptic plasticity. Of note, we recently used GCE in combination with self-labeling enzymes to study the association/dissociation of heterodimers at the cell surface[355]. We, therefore, envision multiple applications of FRET-based sensors to study the dynamics of the AMPAR-TARP interactions in the future.

In the attempt to label surface TARPs, we first developed antibodies against the extracellular domains of γ2 and γ8. While live labeling with our antibodies against γ2 Ex2 or γ8 Ex1 was able to specifically detect the respective recombinant protein in cell lines and dissociated neurons, this approach failed to detect endogenous TARPs in dissociated hippocampal neurons or recombinant γ2 genetically tethered to GluA2. This indicates that the extracellular loops of γ2 and γ8 are masked when associated or in contact with AMPAR, which is compatible with the published cryo-EM structures of

TARP/GluA subunit complexes[46,151,332]. It further importantly indicates that, at endogenous levels, most if not all γ2 and γ8 are associated with AMPAR on the surface of hippocampal neurons, as γ2 in particular only associates to AMPAR subunits[231]. This had remained an important open question in the field. This result does not preclude the potential existence of intracellular AMPAR-free TARPs, particularly along the biosynthetic pathway[177], a point not addressed by our study. Small tags like hemagglutinin (HA, 9 aa)[231] or biotin-acceptor peptide (bAP, 15 aa) were previously successfully inserted in the Ex1 loop of γ2, while the incorporation of bigger proteins such as mCherry in the Ex1 led to intracellular retention of γ2 possibly due to protein misfolding[336]. Surface labeling of γ2-bAP with streptavidin[336] or γ2-HA with specific antibodies[69,240] in the extracellular loops had previously been achieved in neurons, but most likely only revealed overexpressed TARP not associated with AMPARs.

In contrast, GCE combined with click chemistry labeling allowed the site-specific incorporation of ncAAs that can be functionalized and labeled with small tetrazine-dyes with a size of ~1 nm[340]. Both patch-clamp and FRET experiments demonstrate that GCE-labeled TARPs are fully functional and can interact normally with GluA subunits. Indeed, electrophysiological recordings show that the incorporation of ncAAs into the Ex1 of γ2 and γ8 did not compromise TARP-specific AMPAR gating modulation, while FRET experiments indicate close association between ncAA-tagged TARPs and GluA subunits. A parallel approach using cysteine tagging of AMPAR and ncAA-tagging of γ2 TARPs enabled luminescence resonance energy transfer and single-molecule FRET live cell measurements of the distance between GluA2 and γ2 in HEK293T cells and the study of its regulation[259]. Worth mentioning, while we did not observe a difference in terms of labeling efficacy among tested Pyr-Tet-dyes and H-Tet-dyes in both cell lines and dissociated neurons, we did observe that H-Tet-Cy5 outperformed Pyr-Tet-ATTO643 in OHSC. This observation could be explained by the faster reaction of H-Tet with TCO*A as well as the lower sterical demand compared to Pyr-Tet[356,357]. We also observed some decrease in H-Tet-Cy5 fluorescence intensity with depth in organotypic slices, usually accompanied by a decrease in eGFP fluorescence intensity, suggesting inefficient excitation due to scattering issues rather than inefficient tetrazine-dye labeling.

Previous EM studies have suggested γ2 plasma membrane distribution to be almost exclusively synaptic, with γ8 being more equally distributed between extrasynaptic and synaptic sites[261,262]. It is interesting to note however that TEM could only detect γ2 and γ8 peri-synaptically[262], likely due to epitope masking. The limits inherent to EM (sensitivity, antigen accessibility) thus make the development of TARP labeling tools applicable in light microscopy even more relevant. In addition, functional studies have indicated that γ2 promotes synaptic targeting of AMPARs[69,329,331] whereas γ8 controls extrasynaptic surface pool and synaptic delivery of AMPARs[147,261]. Furthermore, at Schaffer collateral/commissural (SCC) synapses in the adult mouse hippocampal CA1, synaptic inclusion of γ2 potently increases AMPAR expression and transforms low-density synapses into high-density ones, whereas γ8 is essential for low-density or basal expression of AMPARs at non-perforated synapses[251], which is fully compatible with our observations. Therefore, these TARPs are critically involved in AMPAR density control at SCC synapses. However, specific imaging of γ2 and γ8 distribution in live neurons was lacking due to the absence of adequate tools. Our data indicate that both in dissociated hippocampal and organotypic CA1 pyramidal neurons, γ2 S44* shows a strong accumulation and forms clusters with a size of ~80 nm at spines compared to lower appearance and more homogeneous distribution at the dendritic shaft. In contrast, γ8 S72* shows a more homogenous distribution between spines and dendritic shaft without any indication of cluster formation.

As mentioned, a limitation in our study is the fact that we had to use an overexpression approach. Recent advances in genome editing tools, such as CRISPR/Cas9, will likely make it possible in the future to deliver site-specific incorporation of ncAAs into endogenous proteins in post-mitotic cells, such as neurons. The combination of this approach with future whole-genome recoding in which all the endogenous Amber codons are replaced by Ochre codons[358] would be particularly valuable. Another alternative that might be more reachable in the near future is the use of orthogonal ribosomes[359,360] combined with quadruplet codons[361], eliminating the possibility of tRNA-induced suppression of endogenous Amber codons as well as improving the incorporation of ncAA. In a complementary work to ours in preprint, Arsíc and colleagues[362] showed the potential of using bioorthogonal labeling to tag intracellular proteins in live neurons using a similar approach, further expanding the versatility and high potential of GCE in the context of neuroscience. Using a second tag (FLAG-tag or GFP) carrying an Amber codon mutation, these authors could incorporate ncAAs into endogenous proteins using CRISPR/Cas9 strategy. However, this strategy relies on the use of ‘conventional’ tags to deliver the Amber codon at the C-terminus of the target protein and lacks the versatility to site-specific incorporation of ncAAs.

In conclusion, the robustness and versatility of the approach shown here, and the panoply of cell-permeable and impermeable tetrazine-dyes[340] opens a new spectrum of possibilities that will be fascinating to explore, including for multicolor imaging of the nanoscale organization, interactions, and trafficking of intracellular and/or extracellular proteins in living neurons. The minimal perturbation of the target protein by insertion of a single ncAA and small size of tetrazine-dyes enables stoichiometric labeling even of sterically shielded protein sites. The method will thus be particularly valuable for quantitative super-resolution microscopy as it provides a sterically minimally demanding labeling and in principle, a perfectly controlled stoichiometric labeling as TCO*-tetrazine labeling exhibits a ratio of 1, and each tetrazine is labeled with a single dye. Additionally, due to the panoply of tetrazine-dyes available nowadays, this tool can be easily combined with other smaller tags, like HA- or bAP-tag. A limitation however remains in the capacity to demonstrate a saturation of the labeling. Multicolor GCE has been achieved[363,364], but is still challenging as to achieve dual-color labeling with two different ncAAs requires not only two orthogonal click-reactions but also need two mutually orthogonal tRNA/RS pairs which can specifically incorporate two distinctly clickable ncAAs. While multicolor labeling using two mutually orthogonal tRNA/RS pairs capable of specifically incorporate two distinctly clickable ncAAs is difficult with the current technology, GCE can easily be combined with other labeling strategies, including relatively small tags.

Altogether, bioorthogonal labeling of TARPs in living neurons constitutes an important achievement in protein tagging in the field of neuroscience, as it not only introduces a robust and fast labeling strategy with minimal to no-perturbation but also allows the labeling of hard-to-access proteins that to date have been highly affected by the bulky size of previous labeling strategies355. This altogether opens the possibility to tackle new sets of biological questions.

METHODS

Reagents

Trans-Cyclooct-2-en-L-Lysine (TCO*A; #SC-8008) was purchased from SiChem (Bremen, Germany). Pyrimidyl-Tetrazine-Alexa Fluor 647 (Pyr-Tet-AF647; #CLK-102), Pyr-Tet-ATTO-643 (Pyr-Tet-ATTO643; #CLK-101), H-Tet-Cy3 (#CLK-014-05) and H-Tet-Cy5 (#CLK-015-05) were purchased from Jena Bioscience (Jena, Germany). SNAP-Surface® Alexa Fluor® 488 (BG-AF488; #S9129S) was purchased from New England Biolabs. 2,3-Dioxo-6-nitro-1,2,3,4-tetrahydrobenzo[f]quinoxaline-7-sulfonamide disodium salt (NBQX; #1044) and Kainate (KA; #0222) were purchased from Tocris. L-Glutamic acid monosodium salt (Glu; #G1626) and doxycycline (#D1822) were purchased from Sigma.

Plasmid constructs

Plasmid amplification was performed via transformation in *E. coli* DH5α (Thermo Fisher Scientific, #EC0111) or *E. cloni*® 10G (Lucigen, #60107) in the case of pTRE3G plasmids, and DNA isolation via MAXI-prep ZymoPURE II Plasmid kits (Zymo Research).

eGFP, mCherry or mEos2 were cloned into the coding sequence of γ2 (between residues 304 and 305) and γ8 (between residues 401 and 402) by introducing AgeI/NheI sites to the respective position. The respective Amber stop mutants (Supplementary Fig. 1c) were generated by introducing a TAG codon through PCR-based site-directed mutagenesis in pcDNA3 vector. For γ8, the endogenous TAG stop codon of WT γ8 was replaced by a TAA stop codon. The plasmid for the expression of the tRNA/aminoacyl transferase pair (pCMV tRNA^{Pyl}/NESPylRS^{AF}, herein termed PylRS/tRNA^{Pyl}) was kindly provided by Edward Lemke[365].

The NESPylRS^{AF} was inserted into a bidirectional doxycycline-inducible expression vector pTRE3G-BI (Takara Bio, #631332), herein termed pTRE3G-BI PylRS, using the restriction sites BamHI/BglII into the BamHI restriction site of the multiple cloning site of pTRE3G-BI after PCR amplification using the oligonocleotides: PylRS_F, 5’-CTTGGATCCGCCACCATGGATAAAAAACC-3’ and PylRS_R, 5’- TAGAAGCTTTTACAGGTTAGTAGAAATACCATTGTAATAG-3’.

To reduce TARPs expression toxicity in neurons, and reduce the number of plasmids to transfect, WT TARPs and ncAA-tagged TARPs were subcloned into the plasmid pTRE3G-BI PylRS using the restriction sites KpnI/XbaI.

The U6 promoter and tRNA^{Pyl} were inserted into the pEF1α-Tet3G (Takara Bio, #631336; Tet3G/tRNA) using the restriction site BsrGI after PCR amplification using the oligonucleotides: U6/tRNA_F, 5’- GCATGTACATTTCCCCGAAAAATGG-3’ and U6/tRNA_R, 5’- GGTCATATTGGACAT GAGCC-3’ (primer located upstream the U6 promoter on the pCMV tRNAPyl/NESPylRSAF), and co-expressed with the pTRE3G-BI constructs.

γ2::eGFP and tethered GluA2 (flop isoform)::γ2::eGFP[233] were subcloned into the doxycycline-inducible expression vector pTRE3G-BI (Takara Bio, #631332) using the restriction sites XbaI/BamHI and EagI/BamHI, respectively.

MfeI/NheI restriction sites were introduced after the signal peptide of GluA1 to insert the SNAP-tag® at N-terminus of GluA1 (SNAP::GluA1) flip variant coding sequence in pRK5 vector.

The plasmid for the GluA1 Tn5 ME SEP +396 aa was kindly provided by Andrew Plested. AgeI/NheI restriction sites were introduced between the Tn5 ME sequences and SEP was replaced by SNAP-tag® (GluA1::SNAP396). The tethered GluA1::SNAP396::γ2 S61* and GluA1::SNAP396::γ8 K102* were performed as described for the tethered WT GluA1::γ2 in[256].

The plasmid for the expression of the tRNA/aminoacyl transferase pair (pNEU-hMbPylRS-4xU6M15, herein termed PylRS/4xtRNA^{Pyl}) was a gift from Irene Coin (Addgene, #105830)[344].

The plasmid for the expression of the Xph20 eGFP CCR5TC (XPH20::eGFP) was a gift from Matthieu Sainlos[350,351].

The plasmid for the expression of GFP39TAG (herein termed clickable-GFP) was kindly provided by Edward Lemke[343].

Heterologous cell culture

HEK293T cells (ECACC, #12022001) were cultured at 37ºC under 5% CO_2 in DMEM supplemented with 10% FBS, 1% L-glutamine and 1% penicillin/streptomycin. COS-7 cells (ECACC, #87021302) were cultured at 37 ºC under 5% CO_2 in DMEM supplemented with 10% FBS, 1% L-glutamine and 1% penicillin/streptomycin.

Animals

All experiments were performed in accordance with the European guidelines for the care and use of laboratory animals, and the guidelines issued by the University of Bordeaux animal experimental committee (CE50; Animal facilities authorizations A3306940 and A33063941).

Tissue for dissociated hippocampal cultures was harvested from embryos of an unascertained mixture of sexes prevenient from gestant Sprague-Dawley rat females at the age of 9 to 12 weeks old purchased weekly from Janvier Labs, Saint-Berthevin, France. Tissue for OHSC was harvested from WT C57Bl6/J mice of both sexes at postnatal day 5-7 raised at PIV-EOPS facility of the IINS. Animals were housed at PIV-EOPS facility of the IINS under a 12 hour light/dark cycle at normal room temperature (22ºC) and humidity between 40-70% (typically 60%) with unrestricted access to food and water.

Primary dissociated hippocampal neurons

Dissociated hippocampal neurons from embryonic day 18 (E18) Sprague-Dawley rats embryos of both sexes were prepared as previously described[313]. Briefly, dissociated neurons were plated at a density of 250,000 cells per 60 mm dish on 0.1 mg.mL^{-1} PLL pre-coated 1.5H, ⌀ 18 mm coverslips

(Marienfeld Superior, #0117580). Neurons cultures were maintained in Neurobasal™ Plus Medium (Thermo Fisher Scientific) supplemented with 0.5 mM GlutaMAX (Thermo Fisher Scientific) and 1X B-27™ Plus Supplement (Thermo Fisher Scientific). 2 μM Cytosine β-D-arabinofuranoside (Sigma Aldrich) was added after 72 h. At DIV3/4, cells were transfected with the respective cDNAs using Lipofectamine 2000 (Thermo Fisher Scientific, #11668019). Cultures were kept at 37 ºC under 5% CO2 up to 18 days.

Astrocytes feeder layers were prepared from the similar embryos, plated between 20,000 to 40,000 cells per 60 mm dish and cultured in Minimum Essential Medium (Thermo Fisher Scientific) containing 4.5 g.L^{-1} glucose, 2 mM GlutaMAX and 10% heat-inactivated horse serum for 14 days.

Organotypic hippocampal slice cultures (OHSC)

OHSC from animals at postnatal day 5-7 from wild type mice of both sexes (C57Bl6/J strain) were prepared as previously described[366]. Briefly, animals were quickly decapitated and hippocampi were dissected out and placed in ice-cold carbonated dissection buffer (in mM): 230 sucrose, 4 KCl, 5 $MgCl_2$, 1 $CaCl_2$, 26 $NaHCO_3$, 10 D-glucose, and phenol red. Coronal slices (300 μm) were cut using a tissue chopper (McIlwain), collected and positioned on interface-style Millicell® culture inserts (Millipore) in 6 well culture plates containing 1 mL of sterile serum-containing MEM medium (in mM): 30 HEPES, 5 $NaHCO_3$, 0.511 sodium L-ascorbate, 13 D-glucose, 1 $CaCl_2$, 2 $MgSO_4$, 5 L-glutamine, and 0.033% (v/v) insulin, pH 7.3, osmolarity adjusted to 317-320 mOsm, plus 20% (v/v) heat-inactivated horse serum. Brain slices were incubated at 35 °C under 5% CO_2 and the culture medium was changed from the bottom of each well every 2 to 3 days. After 14-15 days in culture, slices were transferred to an artificial cerebrospinal fluid containing (in mM): 130 NaCl, 2.5 KCl, 2.2 $CaCl_2$, 1.5 $MgCl_2$, 10 D-glucose, and 10 HEPES, pH 7.35, osmolarity adjusted to 300 mOsm. CA1 pyramidal cells were then processed for single-cell electroporation (SCE) using glass micropipettes containing K-gluconate-based intracellular solution (in mM): 135 K-gluconate, 4 NaCl, 2 $MgCl_2$, 2 HEPES, 2 Na_2ATP, 0.3 NaGTP, 0.06 EGTA, 0.01 $CaCl_2$ (pH 7.2-7.3 with KOH, osmolarity adjusted to 290 mOsm) with plasmids encoding Tet3G/tRNA^{Pyl} and pTRE3G-BI PylRS/γ2 S44* or pTRE3G-BI PylRS/γ8 S72* in equal proportions (26 ng. μl^{-1}) along with eGFP (13 ng.μl^{-1}) or XPH20 eGFP (13 ng.μl^{-1}). Patch pipettes were pulled from 1 mm borosilicate capillaries (Harvard Apparatus) with a vertical puller (Narishige, #PC-100). SCE was performed by applying 4 square pulses of negative voltage (−2.5 V, 25 ms pulse width) at 1 Hz. After SCE, slices were placed back in the incubator for 4-5 days before labeling.

Electrophysiology

cDNAs for GluA1 (250 ng), PylRS/tRNA^{RS} (375 ng), and WT/ncAA-tagged γ2/γ8 eGFP or soluble eGFP (375 ng) were co-transfected into HEK293T cells (90,000-100,000 cells.cm^{-2} in 12-well plate) using jetPRIME® (Polyplus-transfection, #114-01). 250 μM TCO*A and 40 μM NBQX were added to the cells at the time of the transfection. Cells were trypsinized 1 day after transfection and seeded on PLL-coated coverslips. Cells were transferred to the recording chamber, and brightly fluorescent isolated cells were selected. Whole-cell patch-clamp recordings were performed at room temperature in HEPES-buffered Tyrode's solution (HBSS) containing (in mM): 138 NaCl, 2 KCl, 2 $MgCl_2$, 2 $CaCl_2$, 10 D-glucose, and 10 HEPES, pH 7.4, osmolarity adjusted to 317-320 mOsm. Patch pipettes were filled with an internal solution containing (in mM): 120 $CsCH_3SO_3$, 2 NaCl, 2 $MgCl_2$, 10 EGTA, 100 HEPES, and 4 Na_2ATP, pH 7.4, osmolarity 312 mOsm. Pipette resistances for these experiments were typically 3–5 MΩ and cells with a series resistance higher than 15 MΩ were discarded. Glu (10 mM) or KA (0.1 mM) were dissolved in HEPES-buffered solution and applied using a theta pipette driven by a piezoelectric controller (Burleigh, #PZ-150M). Membrane potential was held at -60 mV. Currents were collected using an EPC10 amplifier (HEKA) and filtered at 2.9 kHz and recorded at a sampling frequency of 20 kHz.

TARPs immunostaining

cDNAs for Stg mEos2 or γ8 mEos2 (500 ng) were transfected into COS-7 cells (14,000-17,000 cells/cm^2 in 12-well plate) for 24 h using X-tremeGENE HP DNA (Roche, #06366236001). Cells were incubated for 7 min at 37 ºC with either 4 μg.mL^{-1} rabbit anti-γ2 Ex2 or 1:50 serum rabbit anti-γ8 Ex1 antibodies before fixation. Dissociated hippocampal neurons were co-transfected either with pTRE3G-BI γ2::eGFP or tethered pTRE3G-BI GluA2::γ2::eGFP, and Tet3G/$tRNA^{Pyl}$ in equal proportions (125 ng). Transfected neurons were treated with 200 ng.mL^{-1} doxycycline 18 h before use. Neurons were incubated for 7 min at 37 ºC with 10 μg.mL^{-1} mouse anti-GluA (Synaptic Systems, #182411) and anti-γ2 Ex2 or anti-γ8 Ex1 antibodies before 4% PFA/sucrose fixation. Reactive aldehydes groups were blocked for 10 min with 50 mM NH_4Cl. Alternatively, neurons were live incubated with the anti-GluA antibody, and after fixation neurons were permeabilized with 0.2% Triton-X100 for 5 min and incubated with 0.4 μg.mL^{-1} rabbit anti-γ8 antibody (Frontiers Institute, #TARPg8-Rb-Af1000) diluted in 3% BSA in PBS. Cells were incubated with the respective secondary antibodies anti-mouse AF568 and anti-rabbit AF647 (Thermo Fisher Scientific) diluted at 1:1000 in 3% BSA in PBS. Imaging was performed on an up-right widefield fluorescence microscope (Leica Microsystems, Leica DM5000 B) microscope controlled by Metamorph software (Molecular Devices). Fluorescence excitation of eGFP, AF568 and AF647 was done by a LED SOLA Light (Lumencor). Images were acquired using an oil-immersion objective (Leica, HCX PL APO 40x/NA 1.25 OIL) and appropriate filter set. Fluorescent emission was collected using a sCMOS camera (Hamamatsu Photonics, ORCA-Flash4.0 V2).

Bioorthogonal labeling in HEK293T cells

HEK293T cells plated at a density of 80,000-90,000 cells.cm^{-2} on a pre-coated PDL 4-well Nunc™ Lab-Tek™ II chamber (Thermo Fisher Scientific, #155382PK) were co-transfected with PylRS/4x$tRNA^{Pyl}$ (500 ng) and respective tagged TARPs (500 ng) using jetPRIME® transfection reagent for 24 h in the presence or absence of 250 μM TCO*A. Cells were washed once with cell media to remove excessive TCO*A prior to labeling with 1.5 μM Pyr-Tet-ATTO643 or H-Tet-Cy5 diluted in TCO*A-free medium for 30 min on ice. Subsequently, cells were rinsed 3 times with ice-cold HBSS and immediately live imaged or fixed for 15 minutes at RT with 4% FA in PBS followed by 3 washing steps with HBSS before imaging. Confocal imaging of living or fixed cells was performed using a LSM700 setup (Zeiss) equipped with an oil-immersion objective (Zeiss, Plan-Apochromat 63x/NA 1.4 OIL). eGFP and Pyr-Tet-ATTO643/H-Tet-Cy5 were excited using a 488 nm or 641 nm solid-state laser and respective filter settings. Images were processed in ImageJ (FIJI) adjusting brightness and contrast to identical values for comparison of experiments.

Bioorthogonal labeling in dissociated hippocampal neurons

Dissociated hippocampal neurons were co-transfected with Tet3G/tRNA^{Pyl} (104 ng), pTRE3G-BI PylRS/TARPs (γ2, γ8, γ2 S44* or γ8 S72*; 104 ng), along with eGFP or XPH20 eGFP (42 ng) at DIV 3-4 using lipofectamine 2000. At DIV16-18, 250 μM TCO*A and 100 ng.mL^{-1} doxycycline were added to the cell media for a period of ~20 h. Alternatively, neurons were co-transfected with Tet3G/tRNA^{Pyl} (104 ng), pTRE3G-BI PylRS (104 ng), and clickable-GFP (42 ng) at DIV 3-4. Five days prior to H-Tet-Cy5 labeling, 100 ng.mL^{-1} doxycycline and 250 μM TCO*A were added to the cell media. An extra 50 ng.mL^{-1} doxycycline and 125 μM TCO*A were added 24 h before labeling upon replacing half the media by fresh one. Cells were rinsed 3 times with warm Tyrode's solution containing (in mM): 100 NaCl, 5 KCl, 5 $MgCl_2$, 2 $CaCl_2$, 15 D-glucose, and 10 HEPES, pH 7.4, osmolarity adjusted to 243-247 mOsm followed by 3 min incubation in Tyrode's solution containing 1% BSA. Cells were then incubated with 0.5 μM tetrazine-dye for 7 min at 37 ºC and rinsed 4 times with Tyrode's solution.

Live-cell imaging was performed in Tyrode's solution at 37 °C using an incubator box with an air heater system (Life Imaging Services) installed on an inverted Leica DMI6000 B (Leica Microsystem) spinning disk microscope controlled by Metamorph software (Molecular Devices). Z-stacks of whole neurons were acquired using an oil-immersion objective (Leica, HCX PL APO 40x/NA 1.25 OIL) and appropriate filter set. Fluorescent emission was collected using a sCMOS camera (Hamamatsu, ORCA-Flash4.0 V2).

Alternatively, cells were fixed for 10 min using 4% PFA/glucose. Reactive aldehydes groups were blocked for 10 min with 50 mM NH4Cl. Images of fixed neurons were acquired with a Leica TCS SP8 confocal microscope controlled by Leica Application Suite X (LAS X) software and equipped with hybrid detectors. eGFP and Pyr-Tet-ATTO643 were excited at 488 nm and 638 nm, respectively. For quantification of γ2 S44* and γ8 S72* surface distribution in dissociated hippocampal neurons, Z-stacks of whole dendrite segments were acquired using an oil-immersion objective (Leica, HC PL APO CS2 63x/NA1.40 OIL) and a pinhole opened to one time the Airy disk.

Bioorthogonal labeling in OHSC

Single electroporated neurons from OHSC co-expressing pTRE3G-BI PylRS/γ2 S44* or pTRE3G-BI PylRS/γ8 S72*, Tet3G/tRNA^{Pyl} and eGFP were treated with 250 μM TCO*A and 100 ng.mL^{-1} doxycycline for ~22 h before labeling. Slices were washed three times 5 min with warm Tyrode's solution followed by 5 min in Tyrode's solution containing 1% BSA. Subsequently, slices were incubated for 10 min at 35 ºC with 1 μM H-Tet-Cy5 diluted in Tyrode's solution containing 1% BSA and washed four times 5 min with Tyrode's solution. Slices were fixed for 2 h at RT with 4% PFA/sucrose, washed with PBS. Reactive aldehydes groups were blocked for 20 min in 200 mM NH_4Cl. Slices were mounted in Fluoromount-G Mounting Medium (Thermo Fisher Scientific, #00-4958-02) and left to cure for 48 h at RT before imaging.

Images of fixed neurons were acquired with a Leica TCS SP8 confocal microscope controlled by Leica Application Suite X (LAS X) software and equipped with hybrid detectors. eGFP and Pyr-Tet-

ATTO643 were excited at 488 nm and 638 nm, respectively. Z-stacks of whole neuron were acquired using an oil-immersion objective (Leica, 20x/NA 0.70 IMM) and a pinhole opened to two times the Airy disk. For quantification of γ2 S44* and γ8 S72* surface distribution, Z-stacks of segments basal and apical dendrite were acquired using an oil-immersion objective (Leica, HC PL APO CS2 63x/NA 1.40 OIL) and a pinhole opened to one time the Airy disk.

Quantification of γ8 overexpression

To determine γ8 overexpression levels upon transfection with γ8 S72*, dissociated hippocampal neurons were transfected with Tet3G/tRNAPyl (104 ng), pTRE3G-BI PylRS/γ8 S72* (104 ng), along with XPH20 eGFP (42 ng); TCO*A and doxycycline was added to the media ~20 h prior to tretrazine labeling. Surface γ8 S72* was labeled with 0.5 μM H-Tet-Cy5 as above described. Upon fixation, cells were permeabilized and incubated with the anti-γ8 antibody (Frontiers Institute, #TARPg8-Rb-Af1000) (see TARPs immunostaining section). Cells were imaged using an inverted Leica DMI6000 B (Leica Microsystem) spinning disk microscope controlled by Metamorph software (Molecular Devices). Z-stacks of whole neurons were acquired using an oil-immersion objective (Leica, HCX PL APO 40x/NA 1.25 OIL) and appropriate filter set. Fluorescent emission was collected using a sCMOS camera (Hamamatsu, ORCA-Flash4.0 V2).

All images were analyzed using ImageJ (FIJI) software. Images of non-transfected and γ8 S72*-positive neurons were maximum intensity Z-projected. Masks of regions of interest (dendritic tree) generated based on AF568 (anti-γ8) images upon a median filter (radius = 1) were applied. Relative fluorescence intensity was calculated based on the average fluorescence intensity of non-trasfected cells.

γ2 S44* and γ8 S72* surface distribution in neurons

All images were analyzed using ImageJ (FIJI) software. Confocal images of dissociated neurons co-expressing eGFP, Tet3G/tRNA^{Pyl} and pTRE3G-BI PylRS/TARPs (γ2, γ8, γ2 S44* or γ8 S72*) were maximum intensity Z-projected. For tetrazine specificity, 3 pixel-width line scans across spines and dendritic shaft and cell-free areas were performed based on eGFP fluorescence. For surface distribution, masks of regions of interest (spine and adjacent dendritic draft area) generated based on thresholded eGFP images upon a Gaussian blur filter (radius = 1) were applied. Spine enrichment was calculated as the mean spine fluorescence intensity over the neighbor dendritic area mean fluorescence.

For surface distribution of γ2 S44*, γ8 S72*, and XPH20::eGFP in OHSC, confocal images of dendritic segments were integrated intensity Z-projected. Upon a Median filter (radius = 1) was applied, 3 pixel-width line scans across spines that were perpendicular to the dendritic shaft were performed based on eGFP fluorescence.

Confocal images of dissociated neurons co-expressing clickable-GFP, Tet3G/tRNA^{Pyl} and pTRE3G-BI PylRS labeled with H-Tet-Cy5 were maximum intensity Z-projected. For the purpose of accessing possible off-target surface labeling, 5 pixel-width line scans across random regions in the field-of-view were performed based on clickable-GFP fluorescence.

*d*STORM imaging

The TARP constructs γ2 S44* or γ8 S72*-positive neurons at DIV17-18 co-transfected with XPH20::eGFP were live stained with 0.5 μM Pyr-Tet-AF647 and fixed with 4% FA and 0.25% GA in PBS for 15 min.

The dSTORM images were acquired using an inverted wide-field fluorescence microscope (Olympus, IX-71). For excitation of Pyr-Tet-AF647 a 640-nm optically pumped semiconductor laser (OPSL) (Chroma, Genesis MX639-1000 STM, Coherent, Cleanup 640/10) was focused onto the back focal plane of the oil-immersion objective (Olympus, 60x, NA 1.45). Emission light was separated from the illumination light using a dichroic mirror (Semrock, FF 410/504/582/669 Brightline) and spectrally filtered by a bandpass filter (Semrock, 679/41 BrightLine HC). Images were recorded with an EMCCD (Andor, Ixon DU897). Resulting pixel size for data analysis was measured as 129 nm. For each dSTORM measurement, at least 15,000 frames at 50 Hz and irradiation intensities of ~2 kW cm^{-2} were recorded by TIRF (total internal reflection fluorescence) illumination. Experiments were performed in PBS-based photoswitching buffer containing 100 mM β-mercaptoethylamine (MEA; Sigma-Aldrich) adjusted to pH 7.4. Image reconstruction was performed using rapidSTORM3.3[367]. Overview images were reconstructed with pixel size of 20 nm, whereas insets were calculated with 10 nm pixel size. Prior to *d*STORM imaging, fluorescent image of XPH20::eGFP was acquired at 10 Hz using a 487 nm diode laser (TopticaPhotonics, iBEAM-SMART-488-S-HP), a dichroic mirror (Semrock, FF 410/504/582/669 Brightline) and a bandpass filter (Chroma, ET525/50).

*d*STORM imaging analysis

Cluster analysis was conducted using a custom custom-written python script applying DBSCAN algorithm as well as Ripley K analysis on localization data in determined region of interests (ROIs). In advance, XPH20::eGFP images were merged in ImageJ (Fiji) with the corresponding super-resolved reconstructed image to identify synaptic and extrasynaptic areas. Contrast and brightness of eGFP signal was dilated using ImageJ to determine ROIs of similar size in neuronal spines for γ2 S44* and γ8 S72* (Supplementary Fig. 4 b). Synaptic and extrasynaptic localization densities describe the number of localizations detected per ROI area. All dSTORM analysis was carried out on localizations in frames between 2 000 and 15 000, with intensity of more than 6500 camera counts and with a local background of less than 800. DBSCAN (with parameter epsilon of 20 nm and minPoints of 3) was applied for identification of clustered localizations of TARPs. Distributions for localizations per cluster and cluster area of synaptic and extrasynaptic γ2 S44* as well as γ8 S72* were displayed by their probability density function. The cluster density (number of clusters per ROI area) was calculated for clusters with less and more than 100 localizations per cluster. Cluster analysis was performed on 5 neurons of γ2 S44* (3 independent experiments) and γ8 S72* (4 independent experiments) resulting in analysis of synaptic γ2 S44* ROIs (n = 104), synaptic γ8 S72* ROIs (n = 102), extrasynaptic γ2 S44* ROIs (n = 50) and extrasynaptic y8 S72* ROIs (n = 52).

We calculated and displayed Ripley's H-function, a normalized Ripley's K-function, as previously described[368,369]. Computation was carried out for each ROI without edge correction. The averaged H-function was compared to H-functions and their 95% confidence intervals were computed from 100 simulated data sets with localizations distributed on the same ROIs (and identical number of localizations in each ROI) according to complete spatial randomness or a Neyman-Scott process. The Neyman-Scott clustering process has homogeneously distributed parent events with each parent having n offspring events, where n is Poisson distributed with mean 10, and with the offspring positions having a Gaussian offset with a standard deviation of 12 nm. The maximum of the H-function indicates a distance that is between cluster radius and diameter and thus provides an estimate for the average cluster size.

Frequency domain-based FLIM-FRET measurements

HEK293T cells plated at a density of 50,000-60,000 cells.cm^{-2} on a pre-coated PLL 4-well Nunc™ Lab-Tek™ II chamber were co-transfected with PylRS/tRNA^{Pyl} (166 ng), ncAA-tagged TARPs (166 ng) and SNAP-tagged GluA1 (166 ng), or PylRS/tRNA^{Pyl} and tethered GluA1 SNAP396::γ2 S61* or GluA1 SNAP396::γ8 K102* in equal amounts (250 ng) using jetPRIME®. 250 μM TCO*A and 40 μM NBQX were added to the cells at the time of the transfection. After 48 h, cells were incubated with 1.5 μM H-Tet-Cy3 and 5 μM BG-AF488 diluted in TCO*A-free medium for 30 min at 37ºC. Cells were rinsed three times with HBSS.

Experiments were performed in HBSS at 37°C using an incubator box with an air heater system (Life Imaging Services) installed on an inverted Leica DMI6000 B (Leica Microsystem) spinning disk microscope and using the LIFA frequency-domain lifetime attachment (Lambert Instruments) and the LI-FLIM software. Cells were imaged with an oil-immersion objective (Leica, HCX PL Apo 100x/NA 1.4 oil) using an appropriate GFP filter set. Cells were excited using a sinusoidally-modulated 3 W 477 nm light-emitting diode at 40 MHz under widefield illumination. Fluorescence emission was collected using an intensified CCD LI2CAM MD camera (Lambert Instruments, FAICM). Lifetimes were referenced to a 1 mg.mL^{-1} erythrosine B that was set at 0.086 ns[235]. The lifetime of the sample was determined from the fluorescence phase-shift between the sample and the reference from a set of 12 phase settings using the manufacturer's LI-FLIM software. All data are pulled measurements from a minimum of 20 cells per individual preparation. At least 20 cells in a minimum of three individual preparations were taken in consideration, except GluA1 SNAP396::γ2 S44*-AF488/Cy3 which are from two preparations.

Statistics

All electrophysiological recordings were analyzed with IGOR Pro 5 (WaveMetrics). Current amplitudes were measured with built-in tools, and τ_{des} was measured with exponential fit using a least-squares algorithm.

Statistical significance was calculated using GraphPad Prism 9. Statistical values are given as mean ± SD or SEM (as indicated); ***$p < 0.001$, **$p < 0.01$, *$p < 0.05$, n.s. specifies no significance. Box and violin plot indicate 25th to 75th percentiles, with median represented as a centre line, and mean represented as a cross. On the box plot, whiskers represent min to max values (Figure 22e and Supplementary Fig. 3a) or 1.5 times the interquartile range (Figure 25c,d, and Supplementary Fig. 7b).

Statistical significance for the levels of total γ8 between untransfected and γ8 S72* transfected neurons (Supplementary Fig.5), and TARPs spine vs extraspine ratios in dissociated neurons (Figure 23g) were analyzed using a two-tailed unpaired Welch's t-test. For multiple sample comparisons within electrophysiology experiments, one-way ANOVA with a Fisher's Least Significant Difference multiple comparisons test was used. For multiple sample comparisons within the FRET experiments, Welch's ANOVA multiple comparisons test was used. Sample sizes and biological replicates are given in the figure legends.

REPORTING SUMMARY

Further information on research design is available in the Nature Research Reporting Summary linked to this article.

DATA AVAILABILITY

All data supporting the findings of this study are provided within the paper and its supplementary information. All additional information will be made available upon reasonable request to the authors. Source data are provided with this paper.

CODE AVAILABILITY

Custom Python code for analysis procedures can be made available upon reasonable request to the corresponding author.

ACKNOWLEDGEMENTS

We thank Edward Lemke and Gemma Estrada Girona (European Molecular Biology Laboratory, Heidelberg, Germany) for the gift of the pCMV tRNAPyl/NESPylRSAF plasmid and expert training on how to use it. We wish to thank AS Hafner and F Coussen for early experiments to develop and characterize the γ2 and γ8 antibodies, and M Sainlos for the early gift of the Xph plasmids. We are gratefull to Andrew Plested and Ljudmila Katchan for suggesting some of the insertion sites in AMPAR subunits for FRET experiments and sharing the associated reagent. We thank the Bordeaux Imaging Center, part of the FranceBioImaging national infrastructure (ANR-10-INBS-04-0) for support in microscopy and in particular C. Poujol for advice and discussions on FLIM-FRET imaging; C. Martin and the IINS in vivo facility for animal husbandry. We thank the IINS cell biology core facilities (LABEX BRAIN [ANR-10-LABX-43]) and in particular C. Breillat and E. Verdier for cell culture and plasmid production. This work was supported by funding from the Ministère de l'Enseignement Supérieur et de la Recherche to D.C., Centre National de la Recherche Scientifique (CNRS), ERC grant ADOS (339541) and DynSynMem (787340) to D.C., grants from the conseil Régional d'Aquitaine to D.C., the MSCA-ITN-ETN SYNDEGEN (675554) to D.C. and D.B.N., Fondation Recherche Médicale (FDT202001010840) to D.B.N.. A.K., G.B. and M.S. acknowledge funding by the Deutsche Forschungsgemeinschaft (DFG, project SA829/19-1), the European Regional Development Fund (EFRE project 'Center for Personalized Molecular Immunotherapy') and the European Research Council (Synergy Grant

ULTRARESOLUTION). S.D. acknowledges funding by the Deutsche Forschungsgemeinschaft (DFG, project DO1257/4-1).

AUTHOR CONTRIBUTION

D.B.N. performed FRET, patch-clamp and imaging experiments, developed the strategy for GCE in neurons, developed part of the strategies for cDNA constructs and their production, prepared neuronal samples, performed corresponding data analysis and figure preparation, and co-wrote the MS. A.K. and G.B. developed strategies for site-specific ncAA incorporation by GCE, established click mutants, performed mammalian cell culture experiments and performed dSTORM imaging. A.K., G.B. and S.D. performed the cluster analysis of the dSTORM data, V.P. co-developed and co-performed the single-cell electroporation in organotypic slices, N.R. developed part of the strategies for cDNA constructs and their production and supervised the neuronal primary culture production, N.C. developed part of the strategies for cDNA constructs and their production, D.P. developed the patch-clamp approach and contributed to the corresponding analysis, M.S. and D.C. co-supervised the study and co-wrote the MS. All authors read and corrected the MS.

Supplementary Information for

Bioorthogonal labeling of transmembrane proteins with non-canonical amino acids unveils masked epitopes in live neurons

Diogo Bessa-Neto[1*], Gerti Beliu[2,3*], Alexander Kuhlemann[2*], Valeria Pecoraro[1], Sören Doose[2], Natacha Retailleau[1], Nicolas Chevrier[1], David Perrais[1], Markus Sauer[2#], Daniel Choquet[1,4#]

* These authors contributed equally; # for correspondence: M.S. (m.sauer@uni-wuerzburg.de), D.C. (daniel.choquet@u-bordeaux.fr)

Containing:
Supplementary Figures 1-7

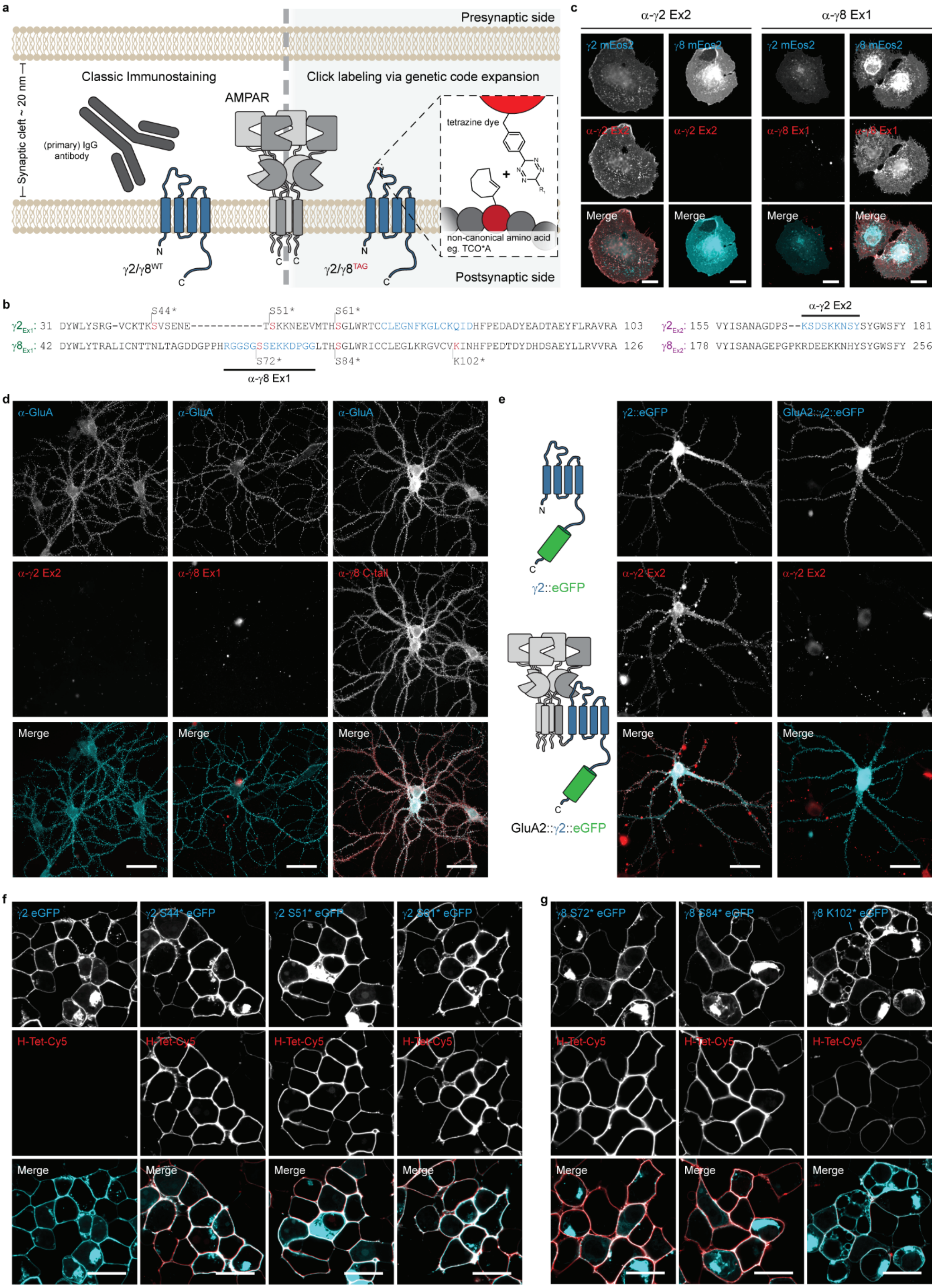

Supplementary Fig. 1: Unmasking the Ex1 loop of TARPs using bioorthogonal labeling. (**a**) Schematic illustration of the two approaches used to label the extracellular pool of γ2 and γ8. On the left side, the classic indirect immunostaining using whole IgG antibodies, and on the right, click chemistry labeling via genetic code expansion. (**b**) Sequence alignment of the extracellular loops, Ex1 and Ex2, of γ2 and γ8 from *rattus norvegicus*. Amber substitution mutations are represented in red. The epitopes recognized by the antibodies are represented in blue. (**c**) Representative widefield images of fixed COS7 expressing either γ2 or γ8 bearing mEos2 live stained with the antibodies against the extracellular loops of γ2 (α-γ2 Ex2) or γ8 (α-γ8 Ex1). (**d**) Representative widefield images of fixed untransfected dissociated hippocampal neurons co-stained live with α-GluA1/2/3/4, and α-γ2 Ex2 (left), α-γ8 Ex1 (middle), or post-fixation/permeabilization with α-γ8 C-tail (right). (**e**) Left: schematic illustration of the eGFP-tagged γ2 constructs used, respectively γ2::eGFP (upper) and GluA2:: γ2::eGFP (lower). Right: representative widefield images of fixed dissociated hippocampal neurons co-expressing Tet3G/tRNA^{Pyl}, and the doxycyline-inducible pTRE3G-BI γ2::eGFP (left) or pTRE3G-BI GluA2:: γ2::eGFP, live stained with α-γ2 Ex2. (**f**-**g**) Representative confocal images of live HEK293T cells co-expressing PylRS/4xtRNAPyl, and (**f**) γ2::eGFP or ncAA-tagged γ2::eGFP or (**g**) ncAA-tagged γ8::eGFP in the presence of 250 μM TCO*A stained with 1.5 μM Pyr-Tet-ATTO643. Scale bar: (**c**, **f**, and **g**) 20 μm, (**d** and **e**) 50 μm. All representative images are representative of two or three independent preparations.

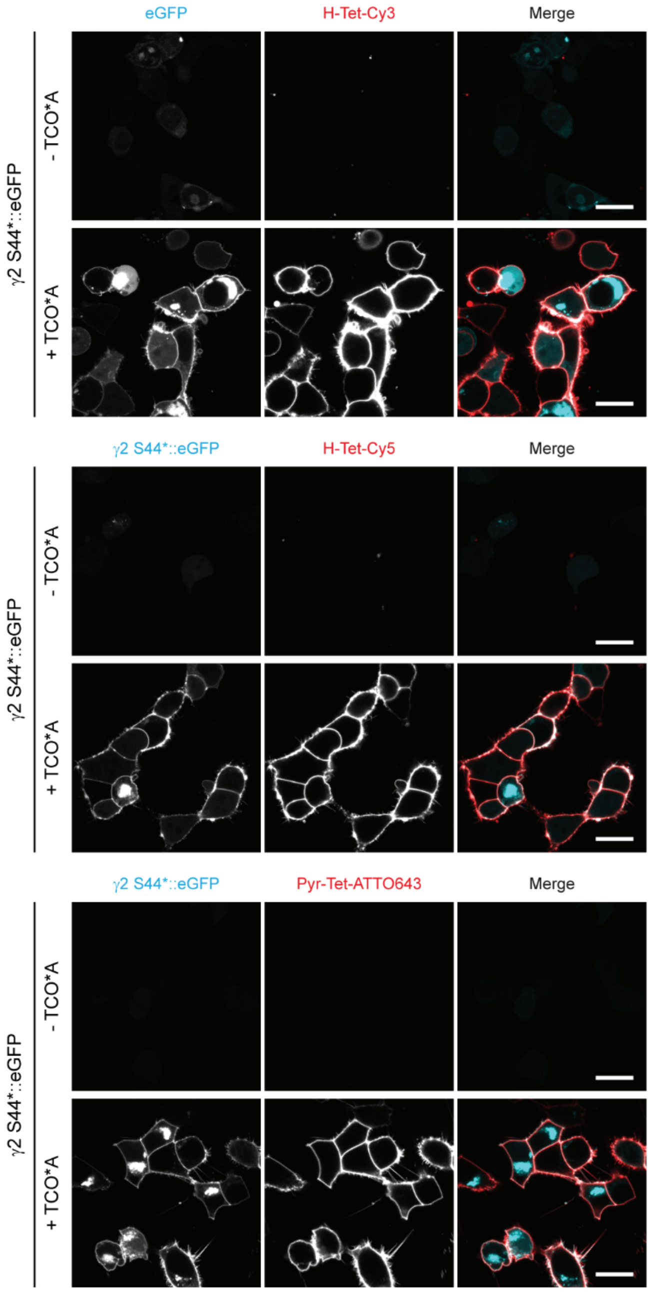

Supplementary Fig. 2: Bioorthogonal TARP click labeling with different tetrazine-dyes. Representative confocal images of living HEK293T cells co-expressing PylRS/4xtRNA^{Pyl} and γ2 S44*::eGFP without (-TCO*A) or with (+TCO*A) addition. Labeled with H-Tet-Cy3 (top), H-Tet-Cy5 (middle), and Pyr-Tet-ATTO643 (bottom). Scale bar: 20 μm. All representative images are representative of at least two independent preparations.

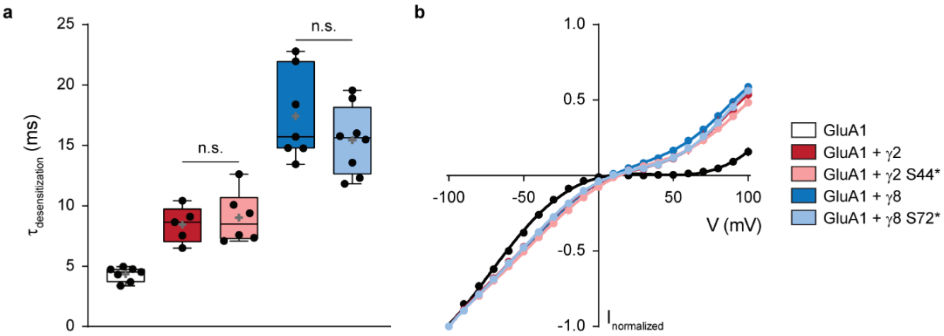

Supplementary Fig. 3: Incorporation of TCO*A within the Ex1 does not affect TARP subtype-induced AMPAR modulation. (**a**) Desensitization rates in response to 100 ms of 10mM Glu applied to whole-cell patches from HEK293T cells co-expressing PylRS/tRNA^{Pyl}, GluA1 and, eGFP (τ_{des} = 4.34 ± 0.06 ms; 7 cells; black), γ2::eGFP (τ_{des} = 8.44 ± 1.50 ms; 5 cells; dark blue), γ2 S44*::eGFP (τ_{des} = 9.02 ± 2.14 ms; 6 cells; light blue), γ8::eGFP (τ_{des} = 17.41 ± 3.72 ms; 7 cells; dark red), and γ8 S72*::eGFP (τ_{des} = 15.43 ± 2.82 ms; 8 cells; light red). Box indicates 25th to 75th percentiles, whiskers represent max to min, with median represented as a centre line, and mean represented as a cross. Statistical difference was analyzed using one-way ANOVA with a Fisher's Least Significant Difference multiple comparisons test; n.s. specifies no significance. (**b**) I-V relationships for 10 mM Glu-evoked peak currents applied to whole-cell patches from HEK293T cells co-expressing PylRS/tRNA^{Pyl}, GluA1 and, eGFP (control; 7 cells; black), γ2::eGFP (5 cells; dark blue), γ2 S44*::eGFP (6 cells; light blue), γ8::eGFP (7 cells; dark red), and γ8 S72*::eGFP (8 cells; light red). Current are normalized to -100 mV. All data is pulled from three-to-four independent biological preparations. All data represent mean ± SD. Source data are provided as a Source Data file.

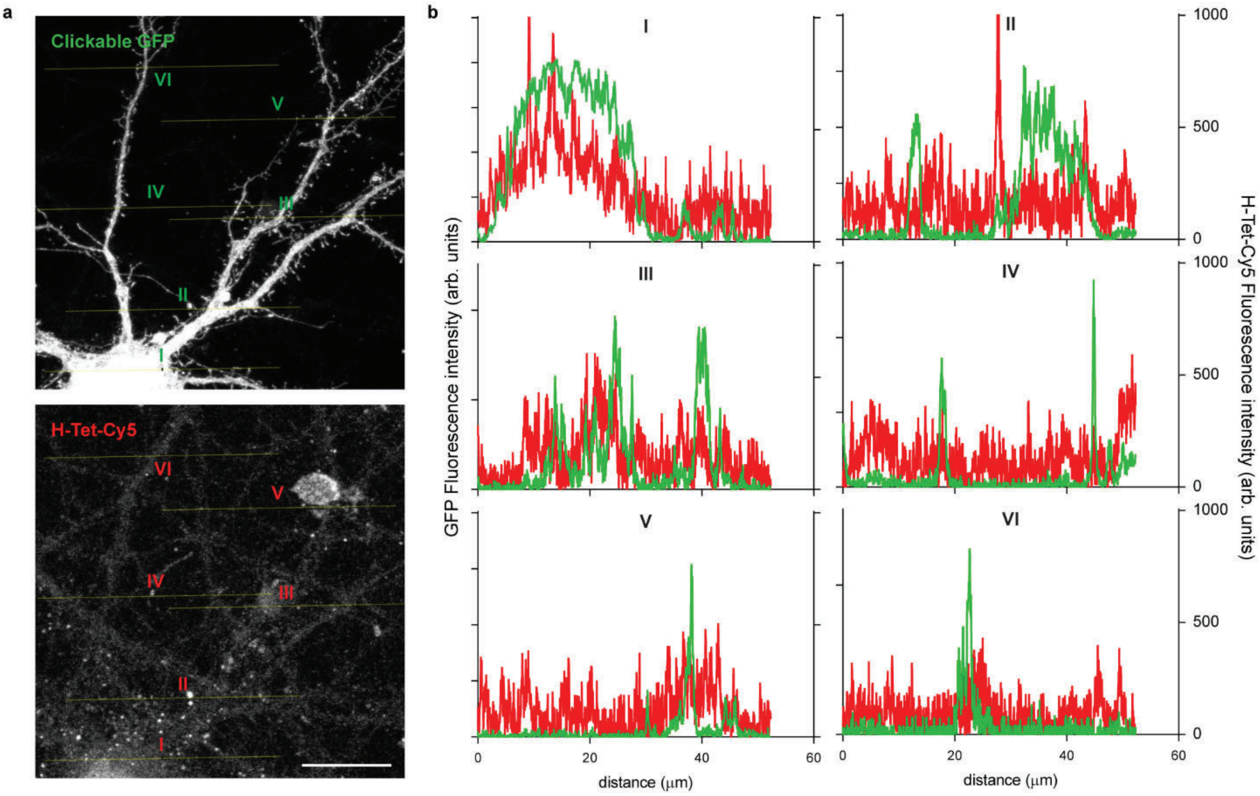

Supplementary Fig. 4: Absence of off-target surface labeling in PylRS/tRNA$^{\text{Pyl}}$ transfected neurons. (**a**) Representative confocal image of fixed dissociated neurons co-transfected with intracellular clickable GFP, Tet3G/tRNA$^{\text{Pyl}}$ and pTRE3G-BI PylRS at DIV15. Five days before H-Tet-Cy5 labeling, cells were treated with 250 μM TCO*A and 100 ng.mL^{-1} doxycycline. 24 h before labeling, an additional 125 μM TCO*A and 50 ng/mL was added to the cell media. Scale bar: 20 μm. (**b**) Line scan measurements of clickable-GFP (green) and H-Tet-Cy5 (red) across six different areas. On the left Y-axis (GFP fluorescence intensity) each tick interval corresponds to 1000 arbitrary units (arb. units), whereas on the right Y-axis (H-Tet-Cy5 fluorescence intensity) each tick interval corresponds to 500 arb. units. Expression of clickable-GFP indicates the success of the GCE experiment, while the transfected cell does not express more H-Tet-Cy5 labeling than non-transfected neighboring neurons, demonstrating the absence of any detectable off-target surface labeling in the absence of clickable surface protein. Representative images are representative of a single preparation.

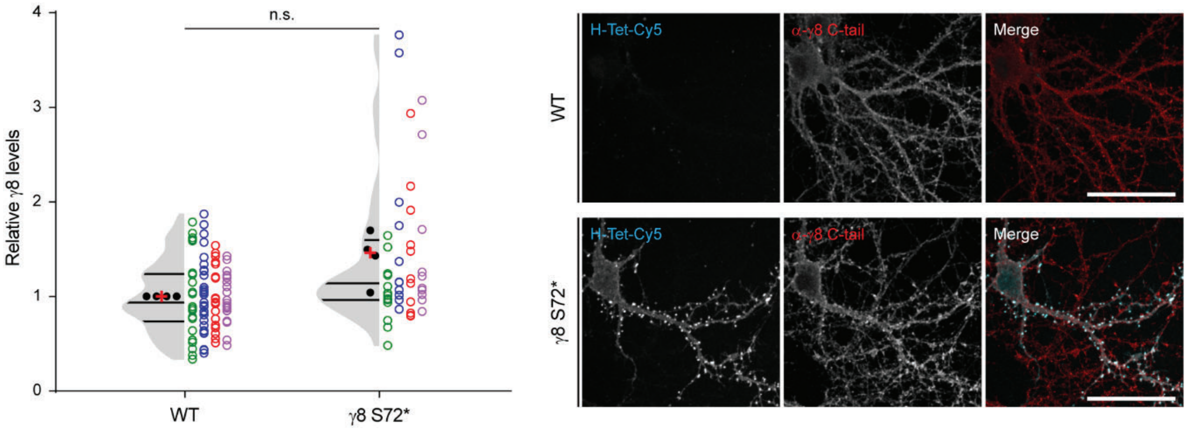

Supplementary Fig. 5: Comparison of γ8 levels between WT and γ8 S72*-positive neurons in dissociated hippocampal cultures. Normalized fluorescence intensity of α-γ8 C-tail antibody showed a slight increase of total γ8 protein in γ8 S72*-positive neurons (1.41 ± 0.27; $p < 0.0557$) in relation to non-transfected (WT) neurons. Circles on the right-half (green, blue, red and purple) of the violin plot represent the distribution of individual cells; 90 cells from four independent preparations. Violin indicates 25th to 75th percentiles (lower and upper lines, respectively), with median represented as a centre line, and mean represented as a cross; dots represent the mean value of relative γ8 levels per independent preparation. Statistical significance was analyzed using a two-tailed unpaired Welch's t test; n.s. specifies no significance. On the right side of the panel, representative spinning disk confocal images of WT (top) or γ8 S72*-positive (bottom) neurons labeled with α-γ8 C-tail antibody upon fixation and permeabilization of the cells. Scale bar: 50 μm. Source data are provided as a Source Data file.

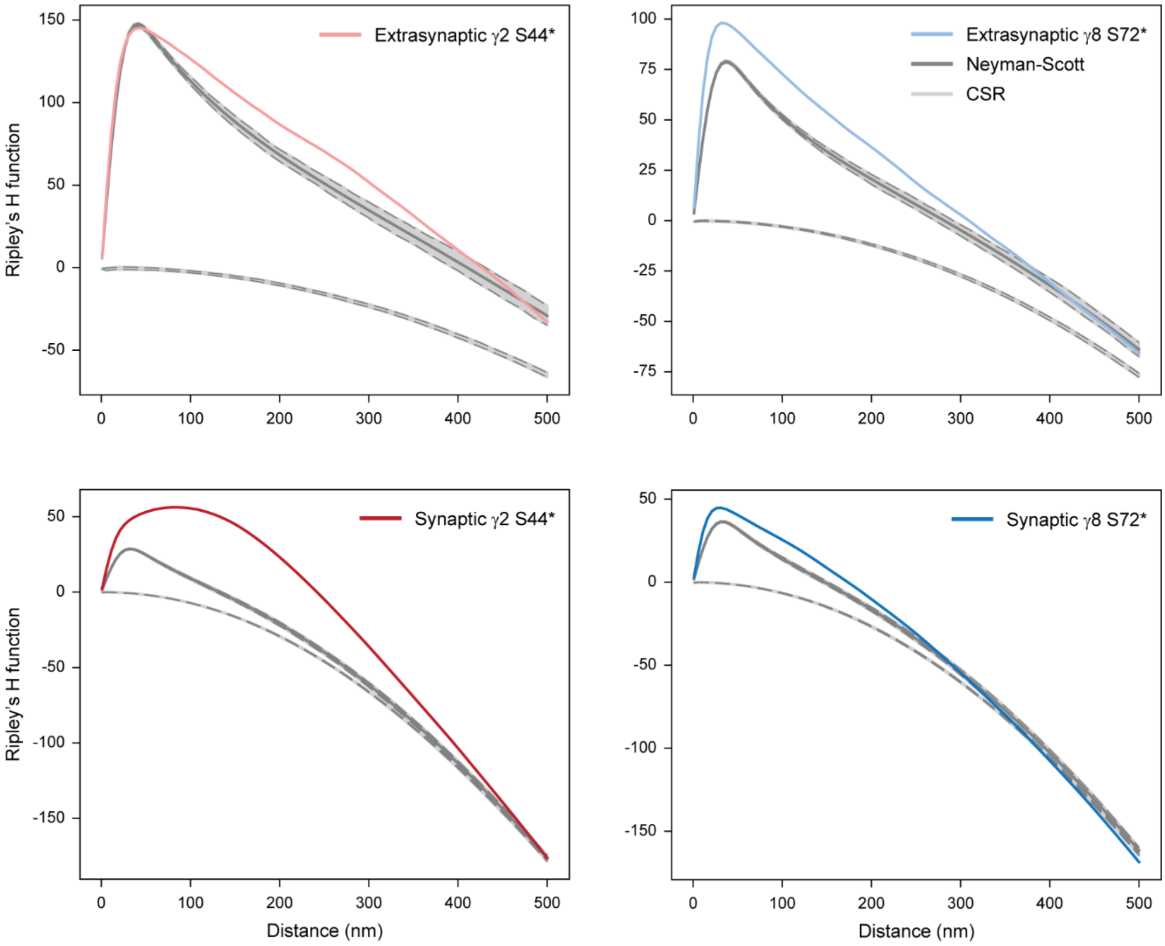

Supplementary Fig. 6: Ripley´s H function. γ2 S44* (red) as well as γ8 S72* (blue) show synaptic (dark) and extrasynaptic (light) random distributions of localization clusters with a size of ~20 nm. Only γ2 S44* (dark red) shows a non-random distribution in synaptic areas with a maximum at ~100 nm indicating cluster formation. Ripley´s H function from 100 replicates of simulated data with spatial distributions following complete spatial randomness (lower grey lines) or a clustered Neyman-Scott process (upper grey lines) in identical ROIs are displayed with 95% confidence intervals (dotted gray lines). Source data are provided as a Source Data file.

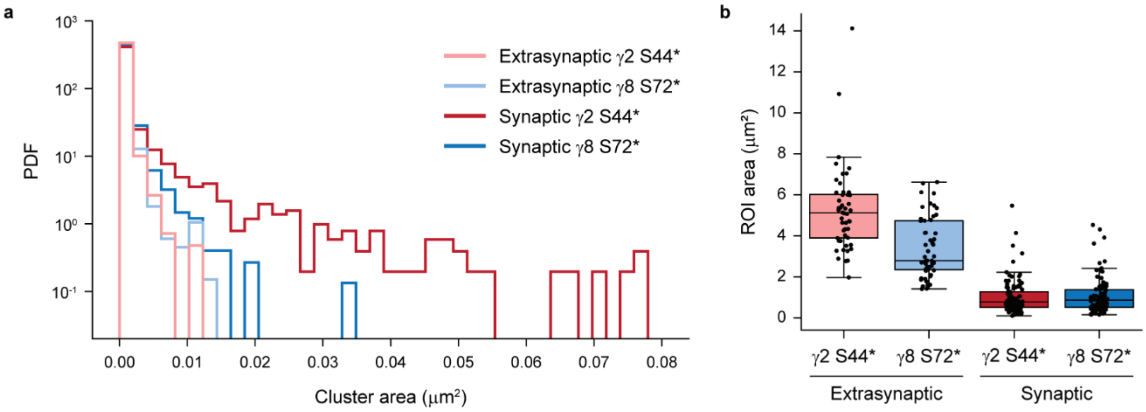

Supplementary Fig. 7: DBSCAN analysis of γ2 S44* and γ8 S72* localizations reveal the presence of clusters (>80nm) only for γ2 S44*in synapses. (**a**) Histograms of cluster areas displaying the probability density function (PDF) of the same cluster as analyzed in Figure 25 (n = 2039, 3243, 2486, 3644 cluster from 50, 52, 104, 102 ROIs of five independent preparations for extrasynaptic γ2, extrasynaptic γ8, synaptic γ2, synaptic γ8, respectively). Extrasynaptic γ8 S72* (light blue), extrasynaptic γ2 S44* (light red) and synaptic γ8 S72* (dark blue) show similar cluster areas for all clusters with areas < 0.02 μm², whereas synaptic γ2 S44* (dark red) exhibit also clusters with cluster areas > 0.02 μm² corresponding to cluster diameter > ~80 nm. (**b**) Boxplots displaying selected ROI areas that were included in cluster analysis. ROI areas were expanded to be similar for synaptic γ8 S72* and γ2 S44* as well as for extrasynaptic γ8 S72* and γ2 S44* to ensure comparable cluster analysis between γ8 and γ2. Boxplots show lower to upper quartile and median values of the data with whiskers extending 1.5 * interquartile range. Source data are provided as a Source Data file.

General discussion

Throughout ~20 years, since the discovery of the first AMPAR-auxiliary subunit, around 30 different proteins have been identified as core constituents of the AMPAR macromolecular complex[109,160,211,290]. While progress has been made in terms of understanding the function of these different proteins, the lack of tools to directly visualize how these proteins form complexes in living cells still underlies the major hindrance to understand how these proteins cooperate and interact with AMPARs.

In this study, I focused on the issue that is the lack of tools and, therefore, I developed two different strategies to tackle different sets of questions. In the first part, I developed strategies to study the interaction between AMPAR and the ER-resident subunits ABHD6 and FRRS1l through the use of FLIM-FRET microscopy. As for the second part, I primarily focused on the development of a labeling strategy based on GCE to specifically visualize the TARPs $\gamma2$ and $\gamma8$ in living neurons, and therefore, better understand how the two proteins are distributed and organized at the plasma membrane. While not the primary focus, this part is also related to the first one as I developed a strategy that allows the study of AMPAR and TARPs interaction based on FRET microscopy. As the second part is already published, I will not include it in this discussion to not repeat myself.

Tolerance for fluorescence protein insertion at GluA1 and FRRS1l

Bearing in mind the proposed role of FRRS1l in AMPAR tetramerization, a FRET-based strategy was chosen for the study of AMPAR and FRRS1l interaction as it is compatible with live cell experiments.

As FRRS1l is not structurally resolved and the luminal NTD comprises ~90% of its size, I inserted the FP after the FRRS1l signal peptide to FRET with GluA1 subunits tagged at the ECD. Here, I showed that the N-terminal insertion of different FPs (eGFP, mScarlet-I, or mCherry) did not disrupt the subcellular localization of FRRS1l. The selection of the permissive sites for the insertion of FPs at GluA1 ECD that could potentially FRET with N-terminal-tagged FRRS1l was based on the analysis of the GluA1 NTD (PDB: 3SAJ)[370] and full-length GluA2 homotetrameric structures (PDB: 5KBU)[151] as no full-length GluA1 was available at the time. As the ATD is more permissive for the insertion of FPs than the LBD[314], the linkers connecting the outer Helix H of GluA1 were selected (D260/T261 and P286/K287) and, the previously described linker connecting the ATD to the LBD (Q396/A397)[314]. Here, I showed that the insertion of the fast-folding msfGFP into the linkers flanking the Helix H showed a bright signal as well as displayed a normal subcellular distribution as compared to the N-terminal -tagged GluA1. Similar results to the ones observed by Sheridan, et al. (2006)[314] using GFP were produced with the insertion of msfGFP at the GluA1 ATD-LBD linker. Worth mentioning, while the interaction between AMPAR and the different AMPAR-interacting proteins is not entirely known, from what is known, AMPAR CTD and TMD, and in some cases LBD, are the only AMPAR regions responsible for the direct interactions[132,137]. Therefore, not only the AMPAR ATD makes a more permissive region for the insertion of FPs, as it is the safest region to avoid compromising the interaction of AMPAR with their associated proteins.

In the current study, FRET was measured based on the fluorescence donor's lifetime as it is independent of common problems like absorption spectral overlap of the donor and acceptor, and donor concentration[371]. The early stages of AMPAR biogenesis are constrained to the ER[170,177], a subcellular compartment that imposes a great challenge to most of the FPs[315]. In the current study, I took the advantage of the monomeric fast-folding GFP-variant, msfGFP, a best-suited GFP-variant for studies in the secretory pathway than commonly used eGFP[315-317]; msfGFP was used as donor fluorescent protein. FRET efficiency is dependent on three key factors: 1) the distance between the donor and acceptor molecule, R_0; 2) the spectral overlap of the donor emission and acceptor absorption, J; 3) the quantum efficiency in the absence of acceptor, Φ_{donor}[371]. The 2) is the only parameter that exclusively depends on the choice of the acceptor for a given donor. I initially chose the newly created red-FP mScarlet-I (mScarlet) as an acceptor molecule. mScarlet is a true monomeric and bright FP with a higher integral overlap with msfGFP than mCherry, *i.e.* $J(\lambda) = 2.84$ and $J(\lambda) = 1.84$, respectively[319]. Unfortunately, it was not until later I realized the occurrence of mScarlet fluorescence bleed-through in the donor lifetime measurements. Therefore, mScarlet was replaced by the red-shifted mCherry as it better suits the filter set available in our system. In the current study, three FRRS1l and GluA1 FRET pair candidates were identified, being the FRET pair GluA1::msfGFP287 vs mCherry::FRRS1l the one that best performed.

A cooperative interaction between FRRS1l and CPT1c

AMPAR-auxiliary proteins can be divided into two groups, the ones that are exclusively found as a part of the AMPAR macromolecular complex within the intracellular compartments (mostly implicated in the biogenesis), and the ones that are also present at the plasma membrane in complex with AMPARs[168]. Understanding the AMPAR macromolecular composition at a given stage, and the triggers that result in the exchange of proteins is of the utmost importance. It was not until very recently a glance of what the function of some of these proteins was shown; using BN-PAGE on rodent brain extracts or heterologous cells expressing different combinations of AMPAR and AMPAR-auxiliary subunits, Schwenk and colleagues observed that ABHD6 and PORCN control the AMPAR monomeric pool, whereas FRRS1l in cooperation with CPT1c promote AMPAR tetramerization. Upon tetramerization, AMPARs can then be exported from the ER, a process that requires the association of AMPARs with TARPs type-I and CNIHs proteins[170,177]. In sum, Schwenk and colleagues hypothesized that a sequential exchange of proteins must occur so that a transition between the different stages of AMPAR biogenesis is observed.

In the current study, to address this hypothesis of an AMPAR series-assembly, I started with a screening across several proteins to identify which proteins would compete against FRRS1l, in other words, the ones not part of the AMPAR-FRRS1l complex. Among the tested proteins, only three proteins induced a robust alteration of the donor lifetime, *i.e.*, modified the base GluA1-FRRS1l interaction. The results indicate that the presence of CPT1c leads to a decrease in donor lifetime which suggests an increase in AMPAR-FRRS1l interaction. However, the observed increase in FRET between FRRS1l and GluA1 upon binding of CPT1c does not prove an increase of the AMPAR and FRRS1l interaction. A structural rearrangement of GluA1 and FRRS1l upon CPT1c binding could also increase FRET efficiency. However, CPT1c and FRRS1l were previously shown to cooperatively associate and enhance the interaction with AMPARs[168].

Two other interesting candidates are ABHD6 and PORCN. Contrary to CPT1c, the presence of ABHD6 or PORCN leads to an increase in donor lifetime, suggesting that ABHD6 and PORCN are not part of the same AMPAR complex as FRRS1l. Again, a structural rearrangement of GluA1 and FRRS1l could explain a change in the donor lifetime. ABHD6 and PORCN were recently suggested to participate in holding GluA subunits as monomers, whereas FRRS1l together with CPT1c in the tetramerization of AMPARs[177], thus suggesting two different AMPAR complexes rather than structural changes.

To my surprise, no significant differences were observed in the FRET between GluA1 and FRRS1l when in the presence of the auxiliary subunits: CNIH2, γ2, γ8, or Shisa6. A possible scenario indicates that the competitor protein (CNIH2, γ2, γ8, or Shisa6) and FRRS1l share the same AMPAR complex. This would not be a surprise as CNIHs, TARPs, GSG1l, and CKAMPs are constituents of the AMPAR inner core, whereas FRRS1l forms part of the AMPAR outer core. These two categories of proteins have been suggested to interact with AMPAR using different AMPAR binding sites[109,135]. However, one cannot exclude the possibility that these two groups of proteins are not part of the same AMPAR complex, which would suggest a stronger AMPAR affinity of FRRS1l over the competitor protein. This scenario is very unlikely as in the brain, only 15-20% of the AMPARs are associated with FRRS1l, whereas the rest contain the core constituents, TARPs, CNIHs, and GSG1l[168]. Schwenk and colleagues hypothesized a stepwise assembly of AMPARs, where the interaction between ABHD6 GluA monomers is destabilized by the subsequent binding of CPT1c/FRRS1l complex that leads to GluA dimer and tetramer formation. This complex, AMPAR/CPT1c/FRRS1l, is then destabilized by the association of CNIH2 and type-I TARPs which work as cargo receptors for ER exit of FRRS1l-free AMPAR complexes[177].

I believe the main difference between my observations and the results from Schwenk and colleagues resides in the absence of the FRRS1l partner, CPT1c, in my experiments. The reason for that observation is the fact that without CPT1c, FRRS1l escapes the ER[168], and perhaps, escapes the ER while associated with the CNIH/TARP-containing AMPAR complex. While I was aware that CPT1c was necessary to restrict FRRS1l to the ER compartments, I expected that the absence of CPT1c would weaken the interaction of FRRS1l with AMPARs and therefore, lead to a striking difference of FRET between AMPAR and FRRS1l when in the presence of TARPs/CNIHs. Moreover, I reasoned the co-transfection of a fourth protein (CPT1c) would result in higher variability, as when increased the amount of total cDNA a decrease of cell viability was observed. In contrast, maintaining the same amount of total cDNA while introducing a new protein decreased transfection efficiency.

Therefore, in the absence of CPT1c, it is possible that CNIH2, γ2, or γ8 are unable to dissociate FRRS1l from the AMPAR complex, but instead, share the same complex. This scenario does not contradict the observations of Schwenk and colleagues but rather supports the importance of CPT1c in the stepwise assembly of AMPARs. Nevertheless, it would be interesting to repeat the same experiment but in the presence of CPT1c to verify if such a statement is truly valid. To decrease the complexity of the experiment, stable cell lines expressing at least one of the FRET pair constituents would most likely improve the transfection efficiency and thus, allow the addition of an extra protein like CPT1c.

Importantly, these results should be taken with caution since it is an unfinished experiment as we decided to put on hold due to unsatisfactory results. Nevertheless, this data suggests that ABHD6 and PORCN do not share the same AMPAR complex as FRRS1l, whereas CPT1c cooperates with FRRS1l and enhances its interaction with AMPARs.

ABHD6, the true gatekeeper of GluA monomers?

Perhaps one of the most intriguing and at the same time interesting points raised by Schwenk and colleagues is the ability of ABHD6 and PORCN to hold GluA subunits as monomers. To investigate it, different combinations of FP-tagged GluA1 and GluA2 subunits were tested. The results here presented showed that eGFP::GluA2, but not eGFP::GluA1, was able to FRET with the mCherry::GluA1. The observation that the pair eGFP::GluA1 and mCherry::GluA1 were unable to FRET was somehow unexpected given that eGFP::GluA2 and mCherry::GluA1 had such a robust FRET. This could be explained by the high heterogeneity of the NTD of different GluA subunits and differences in the overall structural arrangement of the GluA1 homotetramers and GluA1/GluA2 heterotetramers.

In the current study, the presence of ABHD6 had no impact on the FRET between eGFP::GluA2 and mCherry::GluA1 suggesting GluA subunits were able to form dimers and/or tetramers. This contrasts with the observations of Schwenk and colleagues which using BN-PAGE observed that in tsA201 cells and Xenopus oocytes, ABHD6 binds to GluA1 and GluA2 monomers and prevents their dimerization[177]. Here I used an AMPAR (GluA1 + GluA2) and ABHD6 cDNA ratio of 1. I initially wondered if the amount of ABHD6 compared to GluA subunits was insufficient. Upon a discussion with Dr. Schwenk, he confirmed that a cDNA ratio of 1 would be enough to robustly hold the GluA subunits as monomers, as well as, that ABHD6 was able to properly interact with N-terminal tagged GluA subunits. Therefore, the only explanation for such contradictory results lies in differences in the methodology used to determine AMPAR interaction. BN-PAGE is widely used to determine native masses and oligomeric states of protein complexes in the range of 10-10,000 kDa[372,373]. However, in some cases dissociation of less stable protein complexes under the BN-PAGE conditions might occur[374-376]. In this situation, clear-native PAGE can be used as an alternative to BN-PAGE, while it offers lower resolution than BN-PAGE, clear-native PAGE has the advantage of not using Coomassie-dye, which might lead to the dissociation of less stable protein complexes[374,376]. Therefore, it would be interesting to replicate the results obtained by Schwenk and colleagues using clear-native PAGE and verify if indeed the presence of ABHD6 promotes the monomeric state of GluA subunits or is simply an artifact of the BN-PAGE.

On the other hand, the FLIM-FRET strategy used here to measure the interaction between GluA subunits also presents some limitations. If indeed ABHD6 holds GluA subunits as monomers, the results here observed can be a result of a false positive. In FRET, false positives can be a result of acceptor fluorescence bleed-through, as was the case when using mScarlet-I as acceptor. However, this was not the case here, as no bleed-through was observed when using the eGFP-mCherry pair, otherwise, a decrease in eGFP lifetime would have been observed in the negative control. Another possibility for the presence of false positives can also result from a high local concentration of acceptors. This is particularly true when donor and acceptor are confined to subcellular compartments where as few as

100 acceptors per μm^2 can result in ‘random FRET’[377,378]. Therefore, one cannot exclude the possibility that the observed decrease of eGFP lifetime when in the presence of ABHD6 might be due to ‘random FRET’ as a consequence of jammed ER. While the total amount of cDNA was the same used in all the conditions, in the negative control, and the FRET condition without ABHD6, an empty vector was used instead, therefore fewer proteins were expressed. However, I doubt the obtained results are due to a jammed ER as the double amount of GluA subunits was used in the experiment of the identification of FRET pairs between GluA subunits, and no FRET was observed between eGFP::GluA1 vs mCherry::GluA1. When looking at the data distribution of the eGFP lifetime in the +ABHD6 condition, the data tends to favor a higher degree of FRET between GluA2 and GluA1 when in the presence of ABHD6 than without. This scenario is more likely to describe dimerization or tetramerization of AMPARs, rather than ‘random FRET’ interactions. It would have been however interesting to verify if decreasing the total amount of cDNA would produce the same results. That said, whether ABHD6 truly holds GluA subunits into monomers requires further investigation.

ER aggregation of CNIH2 does not prevent its interaction with AMPARs

In a pursue to clarify the role of different AMPAR-associated proteins in the early steps of AMPAR biogenesis and deciphering the stepwise assembly of AMPAR[170,177], in this project I fully relied on the transient expression of the different constructs at the same time. Additionally, analysis of FRET interaction was based on whole-cell FLIM-FRET measurements, which imposes several limitations. The use of a widefield epi-illumination to excite donor FP provides a fast acquisition when compared to TCSPC, but lakes in spatial resolution, which limits the data that can be extracted. As whole-cell measurements provide the average donor’s lifetime in the entire cell, it is not possible to discriminate different populations of AMPAR complexes. While this approach was particularly useful for the identification of FRET pairs and having a general idea of the impact of different auxiliary proteins in a given AMPAR complex, this strategy cannot be used for a comprehensive study on AMPAR stepwise assembly.

To overcome this limitation, one can resort to the controlled expression or release of proteins. Inducible gene expression, as the use of tetracycline-responsive promoters, allows a gradual expression of the target protein and usually in the timeframe of hundreds of minutes to hours[379-382]. As an alternative, proteins can be fused with specific domains which allow the newly synthesized proteins to be trapped in a given compartment. Under certain conditions, through small ligands[321,383] or light[384-386], synchronous and controlled release of the target protein can be achieved in a matter of seconds to minutes. Using whole-cell FLIM-FRET measurements, to recreate the stepwise assembly of AMPARs robustly and efficiently, a considerable amount of the competitor protein must be made available in a very short period for a better interpretation of the data. As the use of an inducible gene expression system would take several hundreds of minutes, a conditional aggregation system was chosen. As the ER is the first compartment in the secretory pathway, and as the AMPAR interactions I was interested in occur at the ER, the competitor protein needs to be trapped in the ER. Here, I chose the ER release system from ARIAD Gene Therapeutics which induces the ER aggregation of the newly synthesized target protein fused with a conditional aggregation domain – based on four repeats of the mutant the FKBP12^{F36M}. A synchronized release in the range of a few seconds to a couple of minutes can be obtained with the use of small synthetic membrane-permeant ligands[321]. Moreover, it is compatible with transmembrane proteins with ER-luminal domains. When I started this part of the project CNIH2 was picked among the other candidates as the ER-luminal C-terminus can be successfully tagged with FPs, and so, a good candidate for the introduction of conditional aggregation domains. Unfortunately, while I was able to successfully aggregate CNIH2 in the ER and control its disaggregation, CNIH2 remained able to interact with AMPARs nullifying the whole purpose of the tool.

What alternatives we might have to visualize the building of AMPAR complexes?

While the project was put on hold, a strategy that might deliver interesting results based on the tools I developed is to use a three-way FRET instead of the standard dual-color FRET. As the name suggests, three-way FRET relies on the use of three FPs instead of the standard two, and depending on the question, different variations of three-way FRET can be used[387-389]. To simplify, let's designate the three FPs as FP#1, FP#2, and FP#3. One possibility is a sequential two-step FRET, where the excited donor FP#1 transfers energy to the acceptor FP#2, which in turn works as a donor molecule to the second acceptor, FP#3. Alternatively, FP#1 can work as the donor for both acceptor FP#2 and FP#3, but in this case, FP#2 does not interact with FP#3. This strategy is of particular interest for the study of the stepwise assembly of AMPARs which requires a sequential exchange of proteins until a final assembly of AMPARs with auxiliary proteins is achieved. In this scenario, GluA subunits would be tagged with the donor FP#1, whereas FRRS1l and competitor protein (CNIHs, TARPs, GSG1L, and CKAMPs) tagged with the acceptors FP#2 and FP#3. Ideally, this strategy coupled to a controlled release of the auxiliary proteins would allow a precise and rather unique way to follow the building of new AMPAR macromolecular complexes in living cells. Perhaps, the pinnacle of the three-way FRET is what one could call the 'all-in' strategy, particularly relevant for multiple interactions in a complex. Here, FP#1 works as a donor for both FP#2 and FP#3, while FP#2 works as an acceptor of FP#1 and donor of FP#3. FRET detection between the donor-acceptor triple complex can be observed when the three FPs are within <10 nm range of each other. Additionally, this particular strategy requires some degree of spectral overlap between all three, which at the same time increases the complexity of analysis and interpretation of the data[387,389]. *Per se*, each one of the above strategies applied to conventional (ensemble) FRET would have the potential to deliver valuable new data about the early steps and overall equilibrium of different AMPAR macromolecular complexes in living cells. However, conventional FRET relies on ensemble- and time-averaging, making it impossible to detect individual species in transient, dynamic, and heterogeneous macromolecular complexes[390]. Single-molecule FRET comes with the possibility to track the dynamics of transient biomolecular complexes and provides accurate distance measurements[389,391]. Despite the challenges to implement it, three-way single-molecule FRET has been used to study Holliday junctions[392,393], and recently single-molecule FRET has been used to monitor the assembly and structural dynamics of G-protein-coupled receptors[394]. The constant development of new fluorescent dyes and, fast and smaller labeling strategies[355,395] coupled with the fast progress on single-molecule FRET could potentially lead to a whole new era on the structural dynamics of individual biomolecular complexes in living cells. And, perhaps, the answer to understanding the differences between the results here presented and the ones from Schwenk and colleagues.

In sum, while this project failed to recreate the stepwise assembly of AMPARs and prove the ability of ABHD6 to hold GluA subunits as monomers, I was able to confirm that CPT1c and FRRS1l form part of the same AMPAR complex and that CPT1c enhances FRRS1l and AMPAR interaction. While the role of the auxiliary proteins CNIH2 or, TARPs γ2 and γ8 in the AMPAR-FRRS1l complex was inconclusive, the results obtained advocate that ABHD6 and PORCN are not part of the same AMPAR complex as FRRS1l.

Bioorthogonal labeling TARPs in living neurons: where do we stand?

From an idea back in late 2017 to where we stand today in terms of click labeling of transmembrane proteins in living neurons, a tormented and sore path rests in between. Thanks to the cooperation of a group of enthusiastic people, I successfully established the use of GCE combined with click chemistry as a robust and sterically minimally demanding labeling technique to label transmembrane proteins in both dissociated neurons and organotypic slice cultures. It is now reasonable to ask what is the true utility of this approach. Could this be just another ‘fancy’ tool without any real advantage over well-established labeling techniques, or is there something else?

To properly answer this question, I will then use the tools here developed – the clickable TARPs, and see what gaps in the knowledge of TARPs can be filled while using these tools. I will start with probably one of the most controversial questions in this field, whether AMPAR-auxiliary subunits can or not dissociate from the AMPAR. It might not seem that relevant at a first glance, however, I would reckon to say that this is perhaps the ‘holy grail’ to understand AMPAR transmission. The one million dollars question, or shall I say euros? As previously mentioned, each auxiliary subunit exerts a different modulatory effect over AMPARs, as well as, different affinities for PSD proteins, which ultimately will determine AMPAR gating properties and localization, respectively. It is, therefore, of utmost importance to unravel this particular question so a clear and accurate understanding of the mechanism behind the AMPAR-mediated transmission can be achieved. Back in the early days after the discovery of TARPs, Tomita and colleagues observed that upon AMPA-induced AMPAR internalization, γ2 and γ3 internalized levels were unaffected by AMPA treatment in contrast to the AMPARs. Moreover, AMPA-induced internalization led to a decrease in AMPAR and γ3 association at the surface, which ultimately suggested the possibility of AMPAR to dissociate from TARPs[231]. These observations were later supported by the observation that Glu application induced a transient dissociation of γ2 from AMPAR complexes[233,256]. However, the veracity of dissociation of TARPs from AMPARs upon agonist binding has been questioned[257-259].

These conflicting results led me to design the FRET pairs between AMPAR and TARPs here reported. It would have been logical to assume the next step should be to simply treat some transfected cells with Glu and check if any alterations are observed. However, that is not as straightforward as one may think. First, as structural rearrangement upon ligand binding can affect the distance between the donor and the acceptor, it is important to assess if the FRET pairs here presented are sensitive to those conformational changes. To do that I used GluA1 mutants that are constitutively expressed in a given conformation; open state[396,397], closed-resting state[398], and desensitized state[399,400]. However, the insertion of SNAP-tag at position 396 aa of the GluA1 mutants drastically impaired their surface expression. As these controls are key for the use of these FRET pairs in functional studies, it will be important in the future to replace SNAP-tag with a smaller and sterically minimally demanding tag, as bungarotoxin binding site (BBS)-tag[355,401]. Additionally, a parallel approach using cysteine tagging of GluA2 and ncAA-tagging of γ2 observed by luminescence resonance energy transfer that Glu application does not induce GluA2 and γ2 dissociation in HEK293T cells, but rather a rearrangement of the proteins[259]. Moreover, previous work from our group reported that while Glu application induced dissociation of endogenous AMPAR and γ2 in neurons, the effect was abolished upon γ2 overexpression, likely due to a saturation of AMPARs with γ2. Thus, to properly investigate whether TARPs dissociate or not from AMPARs, AMPAR tagging needs to be improved, and a more relevant system than heterologous cells needs to be used, ideally, ncAA-tagging of endogenous TARPs in living neurons, as discussed below.

Faced with the limitations of the FRET assay here presented, an alternative was necessary. Biotinylation of surface proteins has been widely used to study receptor internalization, including AMPARs [402], and gave the first hint about a possible dissociation of TARPs from AMPARs[231]. The approach consists of a thiol-cleavable amine-reactive biotinylation reagent that reacts with primary amino groups, which includes the side chain of lysine residues and the N-terminus of proteins. Moreover, the amine-reactive group and the biotin group are separated by a spacer containing a disulfide bond that allows biotin to be removed using a reducing agent as DTT, glutathione, or MesNa. To be able to incorporate this strategy into the click labeling used here, I requested a custom-made cleavable-tetrazine to Jena Biosciences, Me-Tetrazine-SS-Cy5 (Figure 26a). When labeled with Me- Tetrazine-SS- Cy5, COS-7 cells expressing γ2::eGFP showed strong Cy5 labeling. Moreover, the treatment with the cell-impermeable reducing agent MesNa was able to efficiently cleave Cy5 from the tetrazine (Figure 26b). Although the strategy was a success in COS-7 cells, the translation to neurons (dissociated neurons and organotypic slice cultures) has proven to be a challenge due to the repetitive exposure of the cells to different solutions and temperatures. This of course aggravates when added to the low number of transfected neurons and the toxicity induced by TARPs overexpression. Nevertheless, given the success of the tool in heterologous cells, and the poor understanding of TARPs internalization, it is worth further develop the tool.

The third topic worth to be explored that would complement the abovementioned, and at the same time remains poorly understood, is TARPs mobility. Indeed, the only available information about TARPs mobility at the plasma membrane concerns γ2. Using single-particle tracking, our group gave the first insights about γ2 mobility. We observed that γ2 mobility is highly dependent on the environment; in synapses, γ2 is mostly immobile, contrary to the extrasynaptic sites where it is mostly mobile[69,403]. Moreover, we observed that the transient diffusional trapping of AMPAR at synapses is dependent on γ2[69,234]. Recently, Louros and colleagues observed that synaptic downscaling triggers γ2 dephosphorylation, and subsequent increase of γ2 mobility at the plasma membrane[240]. Though these

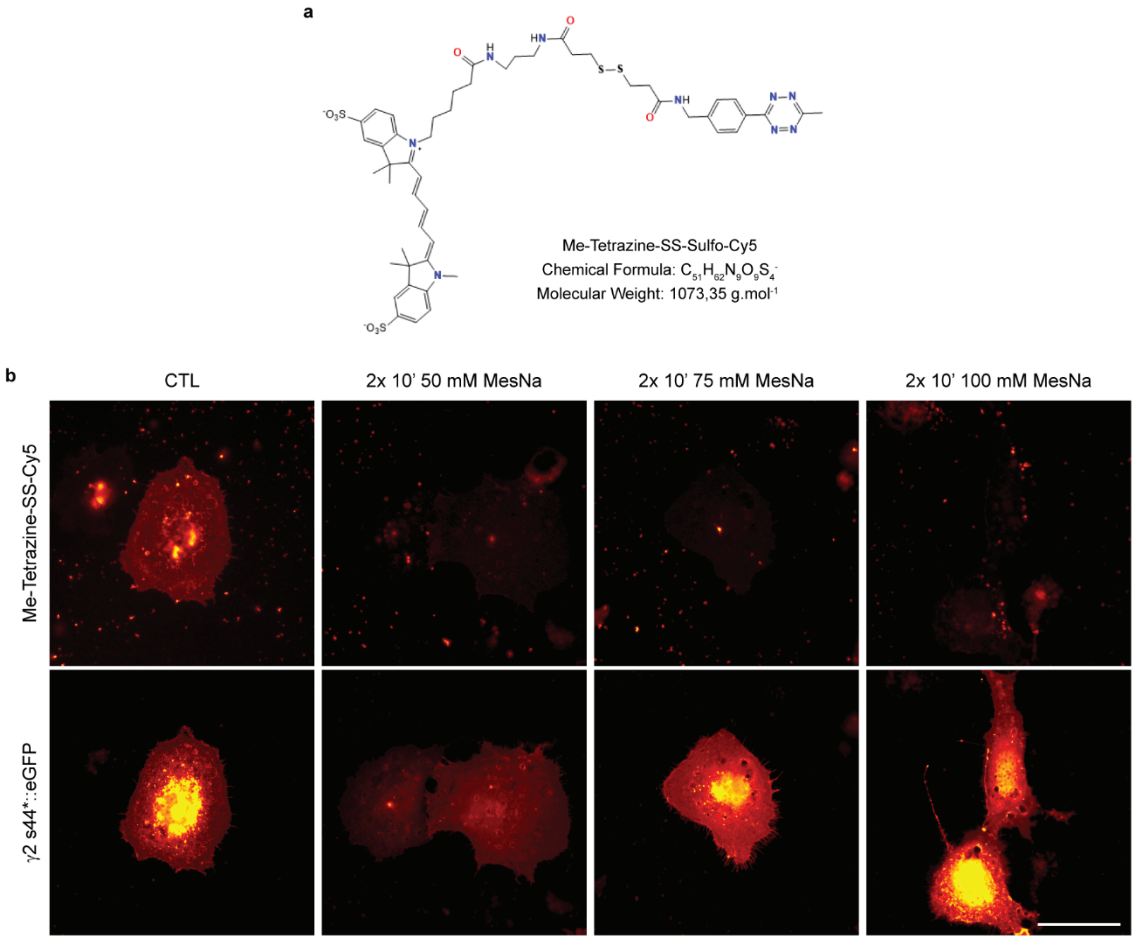

Figure 26: A cleavable tetrazine, Me-Tetrazine-SS-Cy5. (**a**) Chemical structure of the cleavable methyltetrazine-disulfide-amine-sulfo-Cyanine5 (Me-Tetrazine-SS-Cy5). (**b**) Representative widefield images of fixed γ2 S44*::eGFP-positive COS-7 cells live stained with 1.5 µM Me-Tetrazine-SS-Sulfo-Cy5 for 30 min at 4 ºC. From left to right: After labeling, live cells were not treated or treated twice with three different concentrations (50, 75, or 100 nM) of sodium 2-mercaptoethane sulfonate (MesNa) for 10 min. Scale bar: 50 µm.

data have helped to conceptualize how γ2 diffuses at the plasma membrane of neurons, they all have two important technical limitations that can easily lead to biased results. The overexpression of γ2 leads to the presence of AMPAR-free TARPs, as shown here, which could behave differently from the AMPAR-TARPs complexes. And, the use of bulky labeling strategies, HA-tag detected by indirect immunofluorescence[69,234,240] or bAP detected by monomeric streptavidin[403]. The use of a bulky labeling strategy can lead to two types of issues. First is the inaccessibility of the probe to detect the respective tag when γ2 is in complex with AMPARs. Second, the use of multivalent probes, such as antibodies, has the potential to induce protein crosslinking. In turn, the use of ncAA-click labeling allows the possibility to label TARPs even when in complex with AMPARs. As no information is available for γ8, it is now important to use the tools here develop to investigate γ8 mobility and compare it with γ2. Moreover, the use of ncAA-tagged γ2 will allow us to understand the impact of using bigger tags when studying protein mobility. I have tried in the past to set up this type of experiment either by under-labeling or by adding a diluted solution of tetrazine-dye to the acquisition media, but so far without success. A better alternative to the ones tested could be the use of tetrazines bearing a photoactivatable[404] or spontaneously blinking dye[340,405].

Finally, the icing on the cake would be to investigate TARPs surface mobility in a more complete and physiologic system. Given the excellent tetrazine click labeling obtained in organotypic slice cultures, it would be worthy to access TARPs mobility in slices using fluorescence recovery after photobleaching (FRAP) in a lattice light-sheet microscope; lattice light-sheet microscopy combines high spatial-temporal resolution with reduced photobleaching and phototoxicity[406]. This strategy would be of particular interest to study TARPs mobility in the context of synaptic plasticity. Yet, if used overexpression of TARPs the results are most likely biased; as above mentioned, AMPAR-free TARPs might have different mobility from the ones in complex with AMPARs.

I would guess at this point the reader has realized that I always bring the same old problem, the overexpression. I must confess that when it comes to this topic, I am more than biased. Though I appreciate the impact and progress that came along with the use of a transient expression of recombinant proteins, a part of me always had a hard time accepting it due to the potential introduction of artifacts. I tend to see the transient expression of recombinant proteins as a powerful and easy way to test and validate new tools, exactly as performed here. Yet, when it comes to the use of these same tools in the context of unveiling biological processes, I am usually hesitant. It is like introducing a new variable in equitation where most of the variables are unknown or poorly understood. Sometimes even the constants are a mystery.

The transient or stable knockdown of endogenous proteins either by using small interfering RNA[407-409] or short hairpin RNA[410,411], respectively, can mitigate or even abolish the problem of overexpression while focusing on the impact and function of the target recombinant protein. The same could be said when using knockout systems, but neither one of these strategies is ideal when the intent is to replace the target protein with a recombinant protein (either a mutant and/or tagged protein). Thanks to the development of CRISPR/Cas9 technology, which the pioneering work from Jennifer Doudna and Emmanuelle Charpentier won a Nobel Prize in 2020[412], genome editing is now much easier, faster, and cheaper. Using this strategy knock-in organisms can be generated to tag specific proteins in every cell, which includes post-mitotic cells, such as neurons[413-416]. In a complementary work to ours in preprint, Arsíc and colleagues[362] used a non-homologous end joining (NHEJ)-based CRISPR/Cas9 strategy to knock-in endogenous neurofilament light chain and tubulin with ncAA in dissociated neurons. Here the authors used an additional tag (FLAG or GFP) as a mechanism to successfully deliver the ncAA at the C-terminus of the target endogenous protein. While the experiment represents a new achievement in the field of GCE and further expands the versatility and high potential of this tool in the context of neuroscience, lacks the versatility to site-specific incorporation of ncAAs. The NHEJ approach is sensitive to insertion or deletion mutations, particularly when targeting other than the C-terminal region[414]. More importantly, the Cas9 cutting sites are not always present at the exact desired site which limits the applicability of this approach. Recently, Fang and colleagues[415] developed a new CRISPR/Cas9-based strategy, Targeted Knock-In with Two (TKIT), which uses two guide RNAs located in non-coding regions upstream and downstream of the coding sequence to be edited which allows the precise genomic knock-in. Given the recent advances in CRISPR/Cas9 technology, it will come as no surprise that within the near future we will achieve site-specific incorporation of single ncAA in endogenous proteins.

However, one of the major downsides of using ncAAs is the relatively low incorporation efficiency in mammalian cells. Different strategies have been used to boost Amber suppression efficiency in mammalian cells, either by adding a strong N-terminal nuclear export signal to the PylRS[365], increasing the levels of tRNAs[344,417], or co-transfection with a mutant eukaryotic release factor 1[417]. Despite the significant improvement of Amber suppression efficiency by those strategies, they are not 100% effective. A ncAA-knocked-in could, eventually, result in a decrease of the levels of the endogenous targeted protein with a high number of truncated proteins. And, often neglected, the occurrence of the Amber codon in mammalian cells represents 20-23% of all stop codons, thus it is important to consider this parameter when investigating a certain biological process. A solution to this problem could come along with the improvement of the quadruplet codons[361] and orthogonal ribosomes[359,360], or even a whole-genome recoding to replace all the endogenous Amber codons by Ochre codons[358]. Though it is still early to know how successful site-specific incorporation of ncAA into endogenous proteins in post-mitotic cells will be, it is important to keep in mind the limitations of the current technology.

In sum, I believe the use of GCE and click chemistry to label proteins will see large community support in the coming years, including in the field of neuroscience. Although we have a long way to go, it is already a great tool to study hard-to-tag proteins like TARPs.

Bibliography

1. Kuhn, T.S. The Copernican revolution: Planetary astronomy in the development of western thought, Edn. 18th. (Harvard University Press, 1957).
2. Gerlach, J.v. Über die struktur der grauen Substanz des menschlichen Grosshirns. *Zentralbl. med* **10**, 273-275 (1872).
3. Golgi, C. Sulla strutturea della sostanza grigia del cervello (Comunicazione preventiva). *Gaz. Med. Ital. Lomb.* **33**, 244-246 (1873).
4. Golgi, C. The impossible interview with the man of the hidden biological structures. Interview by Paolo Mazzarello. *J Hist Neurosci* **15**, 318-325 (2006).
5. Bentivoglio, M. in Encyclopedia of the Neurological Sciences, Vol. 3, Edn. Second Edition. (eds. M. Aminoff & R. Daroff) 464-468 (Elsevier, 2014).
6. Cajal, S.R. Estructura de los centros nerviosos de las aves. (1888).
7. Glickstein, M. Golgi and Cajal: The neuron doctrine and the 100th anniversary of the 1906 Nobel Prize. *Curr Biol* **16**, R147-151 (2006).
8. Sotelo, C. Camillo Golgi and Santiago Ramon y Cajal: the anatomical organization of the cortex of the cerebellum. Can the neuron doctrine still support our actual knowledge on the cerebellar structural arrangement? *Brain Res Rev* **66**, 16-34 (2011).
9. von Waldeyer-Hartz, W. Ueber einige neuere Forschungen im Gebeite der Anatomie des Centralnervensystems. (G. Thieme, 1891).
10. Cajal, S.R. Significación fisiológica de las expansiones protoplasmáticas y nerviosas de las células de la sustancia gris. *Congréso medico valenciano* (1891).
11. Van Gehuchten, A. La structure des centres nerveux. La moelle épinière et le cervelet. *La Cellule* **7**, 79-122 (1891).
12. Sherrington, C.S. Double (antidrome) conduction in the central nervous system. *Proceedings of the Royal Society of London* **61**, 243-246 (1897).
13. Berlucchi, G. Some aspects of the history of the law of dynamic polarization of the neuron. From William James to Sherrington, from Cajal and van Gehuchten to Golgi. *J Hist Neurosci* **8**, 191-201 (1999).
14. Foster, M. & Sherrington, C.S. in A text book of physiology, Vol. 3, Edn. 7th. (ed. L.M.a. Co) 929 (Lea Brothers & Company, 1897).
15. Robertson, J.D. Ultrastructure of two invertebrate synapses. *Proc Soc Exp Biol Med* **82**, 219-223 (1953).
16. Palade, G. & Palay, S. Electron microscope observations of interneuronal and neuromuscular synapses. *Anat Rec* **118**, 335-336 (1954).
17. De Robertis, E.D. & Bennett, H.S. Some features of the submicroscopic morphology of synapses in frog and earthworm. *J Biophys Biochem Cytol* **1**, 47-58 (1955).
18. De Robertis, E. & Bennett, H.S. in Fed. Proc, Vol. 13 35 (1954).
19. Palay, S.L. Synapses in the central nervous system. *J Biophys Biochem Cytol* **2**, 193-202 (1956).
20. Dosemeci, A., Weinberg, R.J., Reese, T.S. & Tao-Cheng, J.H. The Postsynaptic Density: There Is More than Meets the Eye. *Front Synaptic Neurosci* **8**, 23 (2016).
21. Valenstein, E.S. The War of the Soups and the Sparks The Discovery of Neurotransmitters and the Dispute Over How Nerves Communicate. (Columbia University Press, 2005).
22. Bennett, M.V. & Zukin, R.S. Electrical coupling and neuronal synchronization in the Mammalian brain. *Neuron* **41**, 495-511 (2004).
23. Bennett, M.V. Gap junctions as electrical synapses. *J Neurocytol* **26**, 349-366 (1997).
24. Faber, D.S. & Korn, H. Electrical field effects: their relevance in central neural networks. *Physiol Rev* **69**, 821-863 (1989).
25. Taber, K.H. & Hurley, R.A. Volume transmission in the brain: beyond the synapse. *J Neuropsychiatry Clin Neurosci* **26**, iv, 1-4 (2014).
26. Castaneda-Hernandez, G.C. & Bach-y-Rita, P. Volume transmission and pain perception. *ScientificWorldJournal* **3**, 677-683 (2003).
27. Elliott, T.R. The action of adrenalin. *J Physiol* **32**, 401-467 (1905).
28. Dale, H.H. The action of certain esters and ethers of choline, and their relation to muscarine. *Journal of Pharmacology and Experimental Therapeutics* **6**, 147-190 (1914).

29. Loewi, O. Über humorale übertragbarkeit der Herznervenwirkung. *Pflüger's Archiv für die gesamte Physiologie des Menschen und der Tiere* **189**, 239-242 (1921).
30. Mustafa, A. & Gazi, S. in Encyclopedia of the Neurological Sciences, Vol. 3. (eds. M. Aminoff & R. Daroff) 565-572 (Elsevier, 2014).
31. Langley, J.N. On the reaction of cells and of nerve-endings to certain poisons, chiefly as regards the reaction of striated muscle to nicotine and to curari. *J Physiol* **33**, 374-413 (1905).
32. Maehle, A.H. "Receptive substances": John Newport Langley (1852-1925) and his path to a receptor theory of drug action. *Med Hist* **48**, 153-174 (2004).
33. Hollmann, M., O'Shea-Greenfield, A., Rogers, S.W. & Heinemann, S. Cloning by functional expression of a member of the glutamate receptor family. *Nature* **342**, 643-648 (1989).
34. Lodge, D. The history of the pharmacology and cloning of ionotropic glutamate receptors and the development of idiosyncratic nomenclature. *Neuropharmacology* **56**, 6-21 (2009).
35. Traynelis, S.F. et al. Glutamate receptor ion channels: structure, regulation, and function. *Pharmacol Rev* **62**, 405-496 (2010).
36. Contractor, A., Mulle, C. & Swanson, G.T. Kainate receptors coming of age: milestones of two decades of research. *Trends Neurosci* **34**, 154-163 (2011).
37. Pinheiro, P. & Mulle, C. Kainate receptors. *Cell Tissue Res* **326**, 457-482 (2006).
38. Paoletti, P., Bellone, C. & Zhou, Q. NMDA receptor subunit diversity: impact on receptor properties, synaptic plasticity and disease. *Nat Rev Neurosci* **14**, 383-400 (2013).
39. Hansen, K.B. et al. Structure, function, and allosteric modulation of NMDA receptors. *J Gen Physiol* **150**, 1081-1105 (2018).
40. Ferraguti, F. & Shigemoto, R. Metabotropic glutamate receptors. *Cell Tissue Res* **326**, 483-504 (2006).
41. Niswender, C.M. & Conn, P.J. Metabotropic glutamate receptors: physiology, pharmacology, and disease. *Annu Rev Pharmacol Toxicol* **50**, 295-322 (2010).
42. Goncalves, J. et al. Nanoscale co-organization and coactivation of AMPAR, NMDAR, and mGluR at excitatory synapses. *Proc Natl Acad Sci U S A* **117**, 14503-14511 (2020).
43. Racca, C., Stephenson, F.A., Streit, P., Roberts, J.D. & Somogyi, P. NMDA receptor content of synapses in stratum radiatum of the hippocampal CA1 area. *J Neurosci* **20**, 2512-2522 (2000).
44. Tarusawa, E. et al. Input-specific intrasynaptic arrangements of ionotropic glutamate receptors and their impact on postsynaptic responses. *J Neurosci* **29**, 12896-12908 (2009).
45. Tajima, N. et al. Activation of NMDA receptors and the mechanism of inhibition by ifenprodil. *Nature* **534**, 63-68 (2016).
46. Herguedas, B. et al. Architecture of the heteromeric GluA1/2 AMPA receptor in complex with the auxiliary subunit TARP gamma8. *Science* **364** (2019).
47. Khanra, N., Brown, P.M., Perozzo, A.M., Bowie, D. & Meyerson, J.R. Architecture and structural dynamics of the heteromeric GluK2/K5 kainate receptor. *Elife* **10** (2021).
48. Koehl, A. et al. Structural insights into the activation of metabotropic glutamate receptors. *Nature* **566**, 79-84 (2019).
49. Sheng, M. & Kim, E. The postsynaptic organization of synapses. *Cold Spring Harb Perspect Biol* **3** (2011).
50. Sheng, M. & Hoogenraad, C.C. The postsynaptic architecture of excitatory synapses: a more quantitative view. *Annu Rev Biochem* **76**, 823-847 (2007).
51. Gray, E.G. Axo-somatic and axo-dendritic synapses of the cerebral cortex: an electron microscope study. *J Anat* **93**, 420-433 (1959).
52. Siekevitz, P. The postsynaptic density: a possible role in long-lasting effects in the central nervous system. *Proc Natl Acad Sci U S A* **82**, 3494-3498 (1985).
53. Carlin, R.K., Grab, D.J., Cohen, R.S. & Siekevitz, P. Isolation and characterization of postsynaptic densities from various brain regions: enrichment of different types of postsynaptic densities. *J Cell Biol* **86**, 831-845 (1980).
54. Takumi, Y., Ramirez-Leon, V., Laake, P., Rinvik, E. & Ottersen, O.P. Different modes of expression of AMPA and NMDA receptors in hippocampal synapses. *Nat Neurosci* **2**, 618-624 (1999).
55. Holler, S., Kostinger, G., Martin, K.A.C., Schuhknecht, G.F.P. & Stratford, K.J. Structure and function of a neocortical synapse. *Nature* **591**, 111-116 (2021).
56. Helm, M.S. et al. A large-scale nanoscopy and biochemistry analysis of postsynaptic dendritic spines. *Nat Neurosci* **24**, 1151-1162 (2021).
57. Peng, J. et al. Semiquantitative proteomic analysis of rat forebrain postsynaptic density fractions by mass spectrometry. *J Biol Chem* **279**, 21003-21011 (2004).

58. Cheng, D. et al. Relative and absolute quantification of postsynaptic density proteome isolated from rat forebrain and cerebellum. *Mol Cell Proteomics* **5**, 1158-1170 (2006).
59. Inoue, A. & Okabe, S. The dynamic organization of postsynaptic proteins: translocating molecules regulate synaptic function. *Curr Opin Neurobiol* **13**, 332-340 (2003).
60. Blanpied, T.A., Kerr, J.M. & Ehlers, M.D. Structural plasticity with preserved topology in the postsynaptic protein network. *Proc Natl Acad Sci U S A* **105**, 12587-12592 (2008).
61. Cho, K.O., Hunt, C.A. & Kennedy, M.B. The rat brain postsynaptic density fraction contains a homolog of the Drosophila discs-large tumor suppressor protein. *Neuron* **9**, 929-942 (1992).
62. Kistner, U. et al. SAP90, a rat presynaptic protein related to the product of the Drosophila tumor suppressor gene dlg-A. *J Biol Chem* **268**, 4580-4583 (1993).
63. Petersen, J.D. et al. Distribution of postsynaptic density (PSD)-95 and Ca2+/calmodulin-dependent protein kinase II at the PSD. *J Neurosci* **23**, 11270-11278 (2003).
64. Valtschanoff, J.G. & Weinberg, R.J. Laminar organization of the NMDA receptor complex within the postsynaptic density. *J Neurosci* **21**, 1211-1217 (2001).
65. Dani, A., Huang, B., Bergan, J., Dulac, C. & Zhuang, X. Superresolution imaging of chemical synapses in the brain. *Neuron* **68**, 843-856 (2010).
66. Kim, E. & Sheng, M. PDZ domain proteins of synapses. *Nat Rev Neurosci* **5**, 771-781 (2004).
67. Kornau, H.C., Schenker, L.T., Kennedy, M.B. & Seeburg, P.H. Domain interaction between NMDA receptor subunits and the postsynaptic density protein PSD-95. *Science* **269**, 1737-1740 (1995).
68. Niethammer, M., Kim, E. & Sheng, M. Interaction between the C terminus of NMDA receptor subunits and multiple members of the PSD-95 family of membrane-associated guanylate kinases. *J Neurosci* **16**, 2157-2163 (1996).
69. Bats, C., Groc, L. & Choquet, D. The interaction between Stargazin and PSD-95 regulates AMPA receptor surface trafficking. *Neuron* **53**, 719-734 (2007).
70. Schnell, E. et al. Direct interactions between PSD-95 and stargazin control synaptic AMPA receptor number. *Proc Natl Acad Sci U S A* **99**, 13902-13907 (2002).
71. Chen, L. et al. Stargazin regulates synaptic targeting of AMPA receptors by two distinct mechanisms. *Nature* **408**, 936-943 (2000).
72. Sturgill, J.F., Steiner, P., Czervionke, B.L. & Sabatini, B.L. Distinct domains within PSD-95 mediate synaptic incorporation, stabilization, and activity-dependent trafficking. *J Neurosci* **29**, 12845-12854 (2009).
73. Meyer, D., Bonhoeffer, T. & Scheuss, V. Balance and stability of synaptic structures during synaptic plasticity. *Neuron* **82**, 430-443 (2014).
74. Steiner, P. et al. Destabilization of the postsynaptic density by PSD-95 serine 73 phosphorylation inhibits spine growth and synaptic plasticity. *Neuron* **60**, 788-802 (2008).
75. Kim, M.J. et al. Synaptic accumulation of PSD-95 and synaptic function regulated by phosphorylation of serine-295 of PSD-95. *Neuron* **56**, 488-502 (2007).
76. El-Husseini, A.E. et al. Dual palmitoylation of PSD-95 mediates its vesiculotubular sorting, postsynaptic targeting, and ion channel clustering. *J Cell Biol* **148**, 159-172 (2000).
77. Noritake, J. et al. Mobile DHHC palmitoylating enzyme mediates activity-sensitive synaptic targeting of PSD-95. *J Cell Biol* **186**, 147-160 (2009).
78. El-Husseini Ael, D. et al. Synaptic strength regulated by palmitate cycling on PSD-95. *Cell* **108**, 849-863 (2002).
79. Opazo, P., Sainlos, M. & Choquet, D. Regulation of AMPA receptor surface diffusion by PSD-95 slots. *Curr Opin Neurobiol* **22**, 453-460 (2012).
80. Xu, W. PSD-95-like membrane associated guanylate kinases (PSD-MAGUKs) and synaptic plasticity. *Curr Opin Neurobiol* **21**, 306-312 (2011).
81. Chowdhury, D. & Hell, J.W. Homeostatic synaptic scaling: molecular regulators of synaptic AMPA-type glutamate receptors. *F1000Res* **7**, 234 (2018).
82. Bliss, T.V. & Lomo, T. Long-lasting potentiation of synaptic transmission in the dentate area of the anaesthetized rabbit following stimulation of the perforant path. *J Physiol* **232**, 331-356 (1973).
83. Lomo, T. The discovery of long-term potentiation. *Philos Trans R Soc Lond B Biol Sci* **358**, 617-620 (2003).
84. Bliss, T.V. & Collingridge, G.L. A synaptic model of memory: long-term potentiation in the hippocampus. *Nature* **361**, 31-39 (1993).
85. Cooke, S.F. & Bliss, T.V. Plasticity in the human central nervous system. *Brain* **129**, 1659-1673 (2006).

86. Lynch, G.S., Dunwiddie, T. & Gribkoff, V. Heterosynaptic depression: a postsynaptic correlate of long-term potentiation. *Nature* **266**, 737-739 (1977).
87. Dunwiddie, T. & Lynch, G. Long-term potentiation and depression of synaptic responses in the rat hippocampus: localization and frequency dependency. *J Physiol* **276**, 353-367 (1978).
88. Singer, S.J. & Nicolson, G.L. The fluid mosaic model of the structure of cell membranes. *Science* **175**, 720-731 (1972).
89. Axelrod, D. et al. Lateral motion of fluorescently labeled acetylcholine receptors in membranes of developing muscle fibers. *Proc Natl Acad Sci U S A* **73**, 4594-4598 (1976).
90. Young, S.H. & Poo, M.M. Rapid lateral diffusion of extrajunctional acetylcholine receptors in the developing muscle membrane of Xenopus tadpole. *J Neurosci* **3**, 225-231 (1983).
91. Rao, A., Kim, E., Sheng, M. & Craig, A.M. Heterogeneity in the molecular composition of excitatory postsynaptic sites during development of hippocampal neurons in culture. *J Neurosci* **18**, 1217-1229 (1998).
92. Triller, A. & Choquet, D. Synaptic structure and diffusion dynamics of synaptic receptors. *Biol Cell* **95**, 465-476 (2003).
93. Choquet, D. & Triller, A. The dynamic synapse. *Neuron* **80**, 691-703 (2013).
94. Meier, J., Vannier, C., Serge, A., Triller, A. & Choquet, D. Fast and reversible trapping of surface glycine receptors by gephyrin. *Nat Neurosci* **4**, 253-260 (2001).
95. Borgdorff, A.J. & Choquet, D. Regulation of AMPA receptor lateral movements. *Nature* **417**, 649-653 (2002).
96. Dahan, M. et al. Diffusion dynamics of glycine receptors revealed by single-quantum dot tracking. *Science* **302**, 442-445 (2003).
97. Tardin, C., Cognet, L., Bats, C., Lounis, B. & Choquet, D. Direct imaging of lateral movements of AMPA receptors inside synapses. *EMBO J* **22**, 4656-4665 (2003).
98. Choquet, D. Linking Nanoscale Dynamics of AMPA Receptor Organization to Plasticity of Excitatory Synapses and Learning. *J Neurosci* **38**, 9318-9329 (2018).
99. Groc, L. & Choquet, D. Linking glutamate receptor movements and synapse function. *Science* **368** (2020).
100. Zhao, Y., Chen, S., Swensen, A.C., Qian, W.J. & Gouaux, E. Architecture and subunit arrangement of native AMPA receptors elucidated by cryo-EM. *Science* **364**, 355-362 (2019).
101. Sommer, B. et al. Flip and flop: a cell-specific functional switch in glutamate-operated channels of the CNS. *Science* **249**, 1580-1585 (1990).
102. Penn, A.C. & Greger, I.H. Sculpting AMPA receptor formation and function by alternative RNA processing. *RNA Biol* **6**, 517-521 (2009).
103. Roche, K.W., O'Brien, R.J., Mammen, A.L., Bernhardt, J. & Huganir, R.L. Characterization of multiple phosphorylation sites on the AMPA receptor GluR1 subunit. *Neuron* **16**, 1179-1188 (1996).
104. Lee, H.K. et al. Phosphorylation of the AMPA receptor GluR1 subunit is required for synaptic plasticity and retention of spatial memory. *Cell* **112**, 631-643 (2003).
105. Hayashi, T., Rumbaugh, G. & Huganir, R.L. Differential regulation of AMPA receptor subunit trafficking by palmitoylation of two distinct sites. *Neuron* **47**, 709-723 (2005).
106. Cull-Candy, S.G. & Farrant, M. Ca(2+) -permeable AMPA receptors and their auxiliary subunits in synaptic plasticity and disease. *J Physiol* **599**, 2655-2671 (2021).
107. Cull-Candy, S., Kelly, L. & Farrant, M. Regulation of Ca2+-permeable AMPA receptors: synaptic plasticity and beyond. *Curr Opin Neurobiol* **16**, 288-297 (2006).
108. Yan, D. & Tomita, S. Defined criteria for auxiliary subunits of glutamate receptors. *J Physiol* **590**, 21-31 (2012).
109. Schwenk, J. et al. High-resolution proteomics unravel architecture and molecular diversity of native AMPA receptor complexes. *Neuron* **74**, 621-633 (2012).
110. Schwenk, J. et al. Regional diversity and developmental dynamics of the AMPA-receptor proteome in the mammalian brain. *Neuron* **84**, 41-54 (2014).
111. Martin, L.J., Furuta, A. & Blackstone, C.D. AMPA receptor protein in developing rat brain: glutamate receptor-1 expression and localization change at regional, cellular, and subcellular levels with maturation. *Neuroscience* **83**, 917-928 (1998).
112. Sobolevsky, A.I., Rosconi, M.P. & Gouaux, E. X-ray structure, symmetry and mechanism of an AMPA-subtype glutamate receptor. *Nature* **462**, 745-756 (2009).
113. Greger, I.H., Watson, J.F. & Cull-Candy, S.G. Structural and Functional Architecture of AMPA-Type Glutamate Receptors and Their Auxiliary Proteins. *Neuron* **94**, 713-730 (2017).

114. Jin, R. et al. Crystal structure and association behaviour of the GluR2 amino-terminal domain. *EMBO J* **28**, 1812-1823 (2009).
115. Moykkynen, T., Coleman, S.K., Semenov, A. & Keinanen, K. The N-terminal domain modulates alpha-amino-3-hydroxy-5-methyl-4-isoxazolepropionic acid (AMPA) receptor desensitization. *J Biol Chem* **289**, 13197-13205 (2014).
116. Rossmann, M. et al. Subunit-selective N-terminal domain associations organize the formation of AMPA receptor heteromers. *EMBO J* **30**, 959-971 (2011).
117. Suzuki, K. et al. A synthetic synaptic organizer protein restores glutamatergic neuronal circuits. *Science* **369** (2020).
118. Sia, G.M. et al. Interaction of the N-terminal domain of the AMPA receptor GluR4 subunit with the neuronal pentraxin NP1 mediates GluR4 synaptic recruitment. *Neuron* **55**, 87-102 (2007).
119. Watson, J.F., Ho, H. & Greger, I.H. Synaptic transmission and plasticity require AMPA receptor anchoring via its N-terminal domain. *Elife* **6** (2017).
120. Diaz-Alonso, J. et al. Subunit-specific role for the amino-terminal domain of AMPA receptors in synaptic targeting. *Proc Natl Acad Sci U S A* **114**, 7136-7141 (2017).
121. Watson, J.F., Pinggera, A., Ho, H. & Greger, I.H. AMPA receptor anchoring at CA1 synapses is determined by N-terminal domain and TARP gamma8 interactions. *Nat Commun* **12**, 5083 (2021).
122. Kuusinen, A., Abele, R., Madden, D.R. & Keinanen, K. Oligomerization and ligand-binding properties of the ectodomain of the alpha-amino-3-hydroxy-5-methyl-4-isoxazole propionic acid receptor subunit GluRD. *J Biol Chem* **274**, 28937-28943 (1999).
123. Diaz-Alonso, J. & Nicoll, R.A. AMPA receptor trafficking and LTP: Carboxy-termini, amino-termini and TARPs. *Neuropharmacology* **197**, 108710 (2021).
124. Jiang, C.H., Wei, M., Zhang, C. & Shi, Y.S. The amino-terminal domain of GluA1 mediates LTP maintenance via interaction with neuroplastin-65. *Proc Natl Acad Sci U S A* **118** (2021).
125. Mayer, M.L. Glutamate receptors at atomic resolution. *Nature* **440**, 456-462 (2006).
126. Malinow, R. & Malenka, R.C. AMPA receptor trafficking and synaptic plasticity. *Annu Rev Neurosci* **25**, 103-126 (2002).
127. Song, I. & Huganir, R.L. Regulation of AMPA receptors during synaptic plasticity. *Trends Neurosci* **25**, 578-588 (2002).
128. Bredt, D.S. & Nicoll, R.A. AMPA receptor trafficking at excitatory synapses. *Neuron* **40**, 361-379 (2003).
129. Shepherd, J.D. & Huganir, R.L. The cell biology of synaptic plasticity: AMPA receptor trafficking. *Annu Rev Cell Dev Biol* **23**, 613-643 (2007).
130. Zhou, Z. et al. The C-terminal tails of endogenous GluA1 and GluA2 differentially contribute to hippocampal synaptic plasticity and learning. *Nat Neurosci* **21**, 50-62 (2018).
131. Huganir, R.L. & Nicoll, R.A. AMPARs and synaptic plasticity: the last 25 years. *Neuron* **80**, 704-717 (2013).
132. Twomey, E.C., Yelshanskaya, M.V. & Sobolevsky, A.I. Structural and functional insights into transmembrane AMPA receptor regulatory protein complexes. *J Gen Physiol* **151**, 1347-1356 (2019).
133. Lu, W. et al. Subunit composition of synaptic AMPA receptors revealed by a single-cell genetic approach. *Neuron* **62**, 254-268 (2009).
134. Wenthold, R.J., Petralia, R.S., Blahos, J., II & Niedzielski, A.S. Evidence for multiple AMPA receptor complexes in hippocampal CA1/CA2 neurons. *J Neurosci* **16**, 1982-1989 (1996).
135. Yu, J. et al. Hippocampal AMPA receptor assemblies and mechanism of allosteric inhibition. *Nature* (2021).
136. Herguedas, B. et al. Structure and organization of heteromeric AMPA-type glutamate receptors. *Science* **352**, aad3873 (2016).
137. Kamalova, A. & Nakagawa, T. AMPA receptor structure and auxiliary subunits. *J Physiol* **599**, 453-469 (2021).
138. Jacobi, E. & von Engelhardt, J. Diversity in AMPA receptor complexes in the brain. *Curr Opin Neurobiol* **45**, 32-38 (2017).
139. Chen, X., Aslam, M., Gollisch, T., Allen, K. & von Engelhardt, J. CKAMP44 modulates integration of visual inputs in the lateral geniculate nucleus. *Nat Commun* **9**, 261 (2018).
140. Chen, S. & Gouaux, E. Structure and mechanism of AMPA receptor - auxiliary protein complexes. *Curr Opin Struct Biol* **54**, 104-111 (2019).
141. Maher, M.P. et al. Discovery and Characterization of AMPA Receptor Modulators Selective for TARP-gamma8. *J Pharmacol Exp Ther* **357**, 394-414 (2016).

142. Hoffman, J.L. et al. Inhibition of AMPA receptors (AMPARs) containing transmembrane AMPAR regulatory protein gamma-8 with JNJ-55511118 shows preclinical efficacy in reducing chronic repetitive alcohol self-administration. *Alcohol Clin Exp Res* **45**, 1424-1435 (2021).
143. Kato, A.S., Gill, M.B., Yu, H., Nisenbaum, E.S. & Bredt, D.S. TARPs differentially decorate AMPA receptors to specify neuropharmacology. *Trends Neurosci* **33**, 241-248 (2010).
144. Cho, C.H., St-Gelais, F., Zhang, W., Tomita, S. & Howe, J.R. Two families of TARP isoforms that have distinct effects on the kinetic properties of AMPA receptors and synaptic currents. *Neuron* **55**, 890-904 (2007).
145. Milstein, A.D., Zhou, W., Karimzadegan, S., Bredt, D.S. & Nicoll, R.A. TARP subtypes differentially and dose-dependently control synaptic AMPA receptor gating. *Neuron* **55**, 905-918 (2007).
146. Kott, S., Werner, M., Korber, C. & Hollmann, M. Electrophysiological properties of AMPA receptors are differentially modulated depending on the associated member of the TARP family. *J Neurosci* **27**, 3780-3789 (2007).
147. Rouach, N. et al. TARP gamma-8 controls hippocampal AMPA receptor number, distribution and synaptic plasticity. *Nat Neurosci* **8**, 1525-1533 (2005).
148. Tomita, S. et al. Functional studies and distribution define a family of transmembrane AMPA receptor regulatory proteins. *J Cell Biol* **161**, 805-816 (2003).
149. Hashimoto, K. et al. Impairment of AMPA receptor function in cerebellar granule cells of ataxic mutant mouse stargazer. *J Neurosci* **19**, 6027-6036 (1999).
150. Letts, V.A. et al. The mouse stargazer gene encodes a neuronal Ca2+-channel gamma subunit. *Nat Genet* **19**, 340-347 (1998).
151. Twomey, E.C., Yelshanskaya, M.V., Grassucci, R.A., Frank, J. & Sobolevsky, A.I. Elucidation of AMPA receptor-stargazin complexes by cryo-electron microscopy. *Science* **353**, 83-86 (2016).
152. Zhao, Y., Chen, S., Yoshioka, C., Baconguis, I. & Gouaux, E. Architecture of fully occupied GluA2 AMPA receptor-TARP complex elucidated by cryo-EM. *Nature* **536**, 108-111 (2016).
153. Chen, S. et al. Activation and Desensitization Mechanism of AMPA Receptor-TARP Complex by Cryo-EM. *Cell* **170**, 1234-1246 e1214 (2017).
154. Riva, I., Eibl, C., Volkmer, R., Carbone, A.L. & Plested, A.J. Control of AMPA receptor activity by the extracellular loops of auxiliary proteins. *Elife* **6** (2017).
155. Tomita, S. et al. Stargazin modulates AMPA receptor gating and trafficking by distinct domains. *Nature* **435**, 1052-1058 (2005).
156. Dawe, G.B. et al. Distinct Structural Pathways Coordinate the Activation of AMPA Receptor-Auxiliary Subunit Complexes. *Neuron* **89**, 1264-1276 (2016).
157. Shi, Y., Lu, W., Milstein, A.D. & Nicoll, R.A. The stoichiometry of AMPA receptors and TARPs varies by neuronal cell type. *Neuron* **62**, 633-640 (2009).
158. Kim, K.S., Yan, D. & Tomita, S. Assembly and stoichiometry of the AMPA receptor and transmembrane AMPA receptor regulatory protein complex. *J Neurosci* **30**, 1064-1072 (2010).
159. Hastie, P. et al. AMPA receptor/TARP stoichiometry visualized by single-molecule subunit counting. *Proc Natl Acad Sci U S A* **110**, 5163-5168 (2013).
160. Shanks, N.F. et al. Differences in AMPA and kainate receptor interactomes facilitate identification of AMPA receptor auxiliary subunit GSG1L. *Cell Rep* **1**, 590-598 (2012).
161. Twomey, E.C., Yelshanskaya, M.V., Grassucci, R.A., Frank, J. & Sobolevsky, A.I. Structural Bases of Desensitization in AMPA Receptor-Auxiliary Subunit Complexes. *Neuron* **94**, 569-580 e565 (2017).
162. Twomey, E.C., Yelshanskaya, M.V., Grassucci, R.A., Frank, J. & Sobolevsky, A.I. Channel opening and gating mechanism in AMPA-subtype glutamate receptors. *Nature* **549**, 60-65 (2017).
163. Gu, X. et al. GSG1L suppresses AMPA receptor-mediated synaptic transmission and uniquely modulates AMPA receptor kinetics in hippocampal neurons. *Nat Commun* **7**, 10873 (2016).
164. Nakagawa, T. Structures of the AMPA receptor in complex with its auxiliary subunit cornichon. *Science* **366**, 1259-1263 (2019).
165. Zhang, D., Watson, J.F., Matthews, P.M., Cais, O. & Greger, I.H. Gating and modulation of a hetero-octameric AMPA glutamate receptor. *Nature* **594**, 454-458 (2021).
166. Kirk, L.M. et al. Distribution of the SynDIG4/proline-rich transmembrane protein 1 in rat brain. *J Comp Neurol* **524**, 2266-2280 (2016).
167. Matt, L. et al. SynDIG4/Prrt1 Is Required for Excitatory Synapse Development and Plasticity Underlying Cognitive Function. *Cell Rep* **22**, 2246-2253 (2018).

168. Brechet, A. et al. AMPA-receptor specific biogenesis complexes control synaptic transmission and intellectual ability. *Nat Commun* **8**, 15910 (2017).
169. Greger, I.H., Ziff, E.B. & Penn, A.C. Molecular determinants of AMPA receptor subunit assembly. *Trends Neurosci* **30**, 407-416 (2007).
170. Schwenk, J. & Fakler, B. Building of AMPA-type glutamate receptors in the endoplasmic reticulum and its implication for excitatory neurotransmission. *J Physiol* **599**, 2639-2653 (2021).
171. Wu, X. & Rapoport, T.A. Mechanistic insights into ER-associated protein degradation. *Curr Opin Cell Biol* **53**, 22-28 (2018).
172. Blankman, J.L., Simon, G.M. & Cravatt, B.F. A comprehensive profile of brain enzymes that hydrolyze the endocannabinoid 2-arachidonoylglycerol. *Chem Biol* **14**, 1347-1356 (2007).
173. Marrs, W.R. et al. The serine hydrolase ABHD6 controls the accumulation and efficacy of 2-AG at cannabinoid receptors. *Nat Neurosci* **13**, 951-957 (2010).
174. Navia-Paldanius, D., Savinainen, J.R. & Laitinen, J.T. Biochemical and pharmacological characterization of human alpha/beta-hydrolase domain containing 6 (ABHD6) and 12 (ABHD12). *J Lipid Res* **53**, 2413-2424 (2012).
175. Fiskerstrand, T. et al. Mutations in ABHD12 cause the neurodegenerative disease PHARC: An inborn error of endocannabinoid metabolism. *Am J Hum Genet* **87**, 410-417 (2010).
176. Wei, M. et al. alpha/beta-Hydrolase domain-containing 6 (ABHD6) negatively regulates the surface delivery and synaptic function of AMPA receptors. *Proc Natl Acad Sci U S A* **113**, E2695-2704 (2016).
177. Schwenk, J. et al. An ER Assembly Line of AMPA-Receptors Controls Excitatory Neurotransmission and Its Plasticity. *Neuron* **104**, 680-692 e689 (2019).
178. Bornholdt, D. et al. PORCN mutations in focal dermal hypoplasia: coping with lethality. *Hum Mutat* **30**, E618-628 (2009).
179. Gao, X. & Hannoush, R.N. Single-cell imaging of Wnt palmitoylation by the acyltransferase porcupine. *Nat Chem Biol* **10**, 61-68 (2014).
180. Tanaka, K., Okabayashi, K., Asashima, M., Perrimon, N. & Kadowaki, T. The evolutionarily conserved porcupine gene family is involved in the processing of the Wnt family. *Eur J Biochem* **267**, 4300-4311 (2000).
181. Hofmann, K. A superfamily of membrane-bound O-acyltransferases with implications for wnt signaling. *Trends Biochem Sci* **25**, 111-112 (2000).
182. Wei, M. et al. PORCN Negatively Regulates AMPAR Function Independently of Subunit Composition and the Amino-Terminal and Carboxy-Terminal Domains of AMPARs. *Front Cell Dev Biol* **8**, 829 (2020).
183. Wei, M. et al. The Inhibitory Effect of alpha/beta-Hydrolase Domain-Containing 6 (ABHD6) on the Surface Targeting of GluA2- and GluA3-Containing AMPA Receptors. *Front Mol Neurosci* **10**, 55 (2017).
184. Erlenhardt, N. et al. Porcupine Controls Hippocampal AMPAR Levels, Composition, and Synaptic Transmission. *Cell Rep* **14**, 782-794 (2016).
185. Gratacos-Batlle, E., Yefimenko, N., Cascos-Garcia, H. & Soto, D. AMPAR interacting protein CPT1C enhances surface expression of GluA1-containing receptors. *Front Cell Neurosci* **8**, 469 (2014).
186. Price, N. et al. A novel brain-expressed protein related to carnitine palmitoyltransferase I. *Genomics* **80**, 433-442 (2002).
187. Dai, Y., Wolfgang, M.J., Cha, S.H. & Lane, M.D. Localization and effect of ectopic expression of CPT1c in CNS feeding centers. *Biochem Biophys Res Commun* **359**, 469-474 (2007).
188. Casals, N. et al. Carnitine palmitoyltransferase 1C: From cognition to cancer. *Prog Lipid Res* **61**, 134-148 (2016).
189. Carrasco, P. et al. Ceramide levels regulated by carnitine palmitoyltransferase 1C control dendritic spine maturation and cognition. *J Biol Chem* **287**, 21224-21232 (2012).
190. Sierra, A.Y. et al. CPT1c is localized in endoplasmic reticulum of neurons and has carnitine palmitoyltransferase activity. *J Biol Chem* **283**, 6878-6885 (2008).
191. Madeo, M. et al. Loss-of-Function Mutations in FRRS1L Lead to an Epileptic-Dyskinetic Encephalopathy. *Am J Hum Genet* **98**, 1249-1255 (2016).
192. Chadwick, B.P. et al. Cloning, mapping, and expression of a novel brain-specific transcript in the familial dysautonomia candidate region on chromosome 9q31. *Mamm Genome* **11**, 81-83 (2000).
193. Han, W., Wang, H., Li, J., Zhang, S. & Lu, W. Ferric Chelate Reductase 1 Like Protein (FRRS1L) Associates with Dynein Vesicles and Regulates Glutamatergic Synaptic Transmission. *Front Mol Neurosci* **10**, 402 (2017).

194. Casas, M. et al. Sensing of nutrients by CPT1C controls SAC1 activity to regulate AMPA receptor trafficking. *J Cell Biol* **219** (2020).
195. Stewart, M. et al. Loss of Frrs1l disrupts synaptic AMPA receptor function, and results in neurodevelopmental, motor, cognitive and electrographical abnormalities. *Dis Model Mech* **12** (2019).
196. Standley, S. & Baudry, M. The role of glycosylation in ionotropic glutamate receptor ligand binding, function, and trafficking. *Cell Mol Life Sci* **57**, 1508-1516 (2000).
197. Gratacos-Batlle, E. et al. Mechanisms of CPT1C-Dependent AMPAR Trafficking Enhancement. *Front Mol Neurosci* **11**, 275 (2018).
198. Gratacos-Batlle, E., Yefimenko, N., Cascos-Garcia, H. & Soto, D. AMPAR interacting protein CPT1C enhances surface expression of GluA1-containing receptors. *Front Cell Neurosci* **8**, 469 (2015).
199. Yang, G., Xiong, W., Kojic, L. & Cynader, M.S. Subunit-selective palmitoylation regulates the intracellular trafficking of AMPA receptor. *Eur J Neurosci* **30**, 35-46 (2009).
200. Faulhammer, F. et al. Growth control of Golgi phosphoinositides by reciprocal localization of sac1 lipid phosphatase and pik1 4-kinase. *Traffic* **8**, 1554-1567 (2007).
201. Blagoveshchenskaya, A. et al. Integration of Golgi trafficking and growth factor signaling by the lipid phosphatase SAC1. *J Cell Biol* **180**, 803-812 (2008).
202. Yang, G. et al. JNK3 couples the neuronal stress response to inhibition of secretory trafficking. *Sci Signal* **6**, ra57 (2013).
203. Kapitein, L.C. et al. Mixed microtubules steer dynein-driven cargo transport into dendrites. *Curr Biol* **20**, 290-299 (2010).
204. Kim, C.H. & Lisman, J.E. A labile component of AMPA receptor-mediated synaptic transmission is dependent on microtubule motors, actin, and N-ethylmaleimide-sensitive factor. *J Neurosci* **21**, 4188-4194 (2001).
205. Brockie, P.J. et al. Cornichons control ER export of AMPA receptors to regulate synaptic excitability. *Neuron* **80**, 129-142 (2013).
206. Harmel, N. et al. AMPA receptors commandeer an ancient cargo exporter for use as an auxiliary subunit for signaling. *PLoS One* **7**, e30681 (2012).
207. Hoshino, H. et al. Cornichon-like protein facilitates secretion of HB-EGF and regulates proper development of cranial nerves. *Mol Biol Cell* **18**, 1143-1152 (2007).
208. Castro, C.P., Piscopo, D., Nakagawa, T. & Derynck, R. Cornichon regulates transport and secretion of TGFalpha-related proteins in metazoan cells. *J Cell Sci* **120**, 2454-2466 (2007).
209. Bokel, C., Dass, S., Wilsch-Brauninger, M. & Roth, S. Drosophila Cornichon acts as cargo receptor for ER export of the TGFalpha-like growth factor Gurken. *Development* **133**, 459-470 (2006).
210. Pagant, S., Wu, A., Edwards, S., Diehl, F. & Miller, E.A. Sec24 is a coincidence detector that simultaneously binds two signals to drive ER export. *Curr Biol* **25**, 403-412 (2015).
211. Schwenk, J. et al. Functional proteomics identify cornichon proteins as auxiliary subunits of AMPA receptors. *Science* **323**, 1313-1319 (2009).
212. Herring, B.E. et al. Cornichon proteins determine the subunit composition of synaptic AMPA receptors. *Neuron* **77**, 1083-1096 (2013).
213. Greger, I.H., Khatri, L. & Ziff, E.B. RNA editing at arg607 controls AMPA receptor exit from the endoplasmic reticulum. *Neuron* **34**, 759-772 (2002).
214. Lu, W., Khatri, L. & Ziff, E.B. Trafficking of alpha-amino-3-hydroxy-5-methyl-4-isoxazolepropionic acid receptor (AMPA) receptor subunit GluA2 from the endoplasmic reticulum is stimulated by a complex containing Ca2+/calmodulin-activated kinase II (CaMKII) and PICK1 protein and by release of Ca2+ from internal stores. *J Biol Chem* **289**, 19218-19230 (2014).
215. Aebi, M., Bernasconi, R., Clerc, S. & Molinari, M. N-glycan structures: recognition and processing in the ER. *Trends Biochem Sci* **35**, 74-82 (2010).
216. Moremen, K.W., Tiemeyer, M. & Nairn, A.V. Vertebrate protein glycosylation: diversity, synthesis and function. *Nat Rev Mol Cell Biol* **13**, 448-462 (2012).
217. Zheng, C.Y., Chang, K., Suh, Y.H. & Roche, K.W. TARP gamma-8 glycosylation regulates the surface expression of AMPA receptors. *Biochem J* **465**, 471-477 (2015).
218. Shi, Y. et al. Functional comparison of the effects of TARPs and cornichons on AMPA receptor trafficking and gating. *Proc Natl Acad Sci U S A* **107**, 16315-16319 (2010).
219. Hanus, C. et al. Unconventional secretory processing diversifies neuronal ion channel properties. *Elife* **5** (2016).

220. Bowen, A.B., Bourke, A.M., Hiester, B.G., Hanus, C. & Kennedy, M.J. Golgi-independent secretory trafficking through recycling endosomes in neuronal dendrites and spines. *Elife* **6** (2017).

221. Diering, G.H. & Huganir, R.L. The AMPA Receptor Code of Synaptic Plasticity. *Neuron* **100**, 314-329 (2018).

222. Granger, A.J., Shi, Y., Lu, W., Cerpas, M. & Nicoll, R.A. LTP requires a reserve pool of glutamate receptors independent of subunit type. *Nature* **493**, 495-500 (2013).

223. Diaz-Alonso, J. et al. Long-term potentiation is independent of the C-tail of the GluA1 AMPA receptor subunit. *Elife* **9** (2020).

224. Liu, A. et al. The Requirement of the C-Terminal Domain of GluA1 in Different Forms of Long-Term Potentiation in the Hippocampus Is Age-Dependent. *Front Synaptic Neurosci* **12**, 588785 (2020).

225. Twomey, E.C. & Sobolevsky, A.I. Structural Mechanisms of Gating in Ionotropic Glutamate Receptors. *Biochemistry* **57**, 267-276 (2018).

226. Priel, A. et al. Stargazin reduces desensitization and slows deactivation of the AMPA-type glutamate receptors. *J Neurosci* **25**, 2682-2686 (2005).

227. Korber, C., Werner, M., Kott, S., Ma, Z.L. & Hollmann, M. The transmembrane AMPA receptor regulatory protein gamma 4 is a more effective modulator of AMPA receptor function than stargazin (gamma 2). *J Neurosci* **27**, 8442-8447 (2007).

228. Tomita, S., Sekiguchi, M., Wada, K., Nicoll, R.A. & Bredt, D.S. Stargazin controls the pharmacology of AMPA receptor potentiators. *Proc Natl Acad Sci U S A* **103**, 10064-10067 (2006).

229. Kato, A.S. et al. Hippocampal AMPA receptor gating controlled by both TARP and cornichon proteins. *Neuron* **68**, 1082-1096 (2010).

230. Coombs, I.D. et al. Cornichons modify channel properties of recombinant and glial AMPA receptors. *J Neurosci* **32**, 9796-9804 (2012).

231. Tomita, S., Fukata, M., Nicoll, R.A. & Bredt, D.S. Dynamic interaction of stargazin-like TARPs with cycling AMPA receptors at synapses. *Science* **303**, 1508-1511 (2004).

232. Fukaya, M., Yamazaki, M., Sakimura, K. & Watanabe, M. Spatial diversity in gene expression for VDCCgamma subunit family in developing and adult mouse brains. *Neurosci Res* **53**, 376-383 (2005).

233. Constals, A. et al. Glutamate-induced AMPA receptor desensitization increases their mobility and modulates short-term plasticity through unbinding from Stargazin. *Neuron* **85**, 787-803 (2015).

234. Opazo, P. et al. CaMKII triggers the diffusional trapping of surface AMPARs through phosphorylation of stargazin. *Neuron* **67**, 239-252 (2010).

235. Hafner, A.S. et al. Lengthening of the Stargazin Cytoplasmic Tail Increases Synaptic Transmission by Promoting Interaction to Deeper Domains of PSD-95. *Neuron* **86**, 475-489 (2015).

236. Matsuda, S. et al. Stargazin regulates AMPA receptor trafficking through adaptor protein complexes during long-term depression. *Nat Commun* **4**, 2759 (2013).

237. Stein, E.L. & Chetkovich, D.M. Regulation of stargazin synaptic trafficking by C-terminal PDZ ligand phosphorylation in bidirectional synaptic plasticity. *J Neurochem* **113**, 42-53 (2010).

238. Nomura, T. et al. Cerebellar long-term depression requires dephosphorylation of TARP in Purkinje cells. *Eur J Neurosci* **35**, 402-410 (2012).

239. Louros, S.R., Hooks, B.M., Litvina, L., Carvalho, A.L. & Chen, C. A role for stargazin in experience-dependent plasticity. *Cell Rep* **7**, 1614-1625 (2014).

240. Louros, S.R., Caldeira, G.L. & Carvalho, A.L. Stargazin Dephosphorylation Mediates Homeostatic Synaptic Downscaling of Excitatory Synapses. *Front Mol Neurosci* **11**, 328 (2018).

241. Dakoji, S., Tomita, S., Karimzadegan, S., Nicoll, R.A. & Bredt, D.S. Interaction of transmembrane AMPA receptor regulatory proteins with multiple membrane associated guanylate kinases. *Neuropharmacology* **45**, 849-856 (2003).

242. Choi, J. et al. Phosphorylation of stargazin by protein kinase A regulates its interaction with PSD-95. *J Biol Chem* **277**, 12359-12363 (2002).

243. Chetkovich, D.M., Chen, L., Stocker, T.J., Nicoll, R.A. & Bredt, D.S. Phosphorylation of the postsynaptic density-95 (PSD-95)/discs large/zona occludens-1 binding site of stargazin regulates binding to PSD-95 and synaptic targeting of AMPA receptors. *J Neurosci* **22**, 5791-5796 (2002).

244. Sainlos, M. et al. Biomimetic divalent ligands for the acute disruption of synaptic AMPAR stabilization. *Nat Chem Biol* **7**, 81-91 (2011).

245. Zeng, M. et al. Phase Separation-Mediated TARP/MAGUK Complex Condensation and AMPA Receptor Synaptic Transmission. *Neuron* **104**, 529-543 e526 (2019).

246. Sumioka, A., Yan, D. & Tomita, S. TARP phosphorylation regulates synaptic AMPA receptors through lipid bilayers. *Neuron* **66**, 755-767 (2010).
247. Zeng, M. et al. Reconstituted Postsynaptic Density as a Molecular Platform for Understanding Synapse Formation and Plasticity. *Cell* **174**, 1172-1187 e1116 (2018).
248. Zeng, M. et al. Phase Transition in Postsynaptic Densities Underlies Formation of Synaptic Complexes and Synaptic Plasticity. *Cell* **166**, 1163-1175 e1112 (2016).
249. Hosokawa, T. et al. CaMKII activation persistently segregates postsynaptic proteins via liquid phase separation. *Nat Neurosci* **24**, 777-785 (2021).
250. Xu, W. et al. Molecular dissociation of the role of PSD-95 in regulating synaptic strength and LTD. *Neuron* **57**, 248-262 (2008).
251. Yamasaki, M. et al. TARP gamma-2 and gamma-8 Differentially Control AMPAR Density Across Schaffer Collateral/Commissural Synapses in the Hippocampal CA1 Area. *J Neurosci* **36**, 4296-4312 (2016).
252. Tomita, S., Stein, V., Stocker, T.J., Nicoll, R.A. & Bredt, D.S. Bidirectional synaptic plasticity regulated by phosphorylation of stargazin-like TARPs. *Neuron* **45**, 269-277 (2005).
253. Tsui, J. & Malenka, R.C. Substrate localization creates specificity in calcium/calmodulin-dependent protein kinase II signaling at synapses. *J Biol Chem* **281**, 13794-13804 (2006).
254. Ribeiro, L.F. et al. Ghrelin triggers the synaptic incorporation of AMPA receptors in the hippocampus. *Proc Natl Acad Sci U S A* **111**, E149-158 (2014).
255. Turrigiano, G.G. The self-tuning neuron: synaptic scaling of excitatory synapses. *Cell* **135**, 422-435 (2008).
256. Morimoto-Tomita, M. et al. Autoinactivation of neuronal AMPA receptors via glutamate-regulated TARP interaction. *Neuron* **61**, 101-112 (2009).
257. Nakagawa, T., Cheng, Y., Ramm, E., Sheng, M. & Walz, T. Structure and different conformational states of native AMPA receptor complexes. *Nature* **433**, 545-549 (2005).
258. Semenov, A., Moykkynen, T., Coleman, S.K., Korpi, E.R. & Keinanen, K. Autoinactivation of the stargazin-AMPA receptor complex: subunit-dependency and independence from physical dissociation. *PLoS One* **7**, e49282 (2012).
259. Shaikh, S.A. et al. Stargazin Modulation of AMPA Receptors. *Cell Rep* **17**, 328-335 (2016).
260. Moss, F.J., Dolphin, A.C. & Clare, J.J. Human neuronal stargazin-like proteins, gamma2, gamma3 and gamma4; an investigation of their specific localization in human brain and their influence on CaV2.1 voltage-dependent calcium channels expressed in Xenopus oocytes. *BMC Neurosci* **4**, 23 (2003).
261. Fukaya, M. et al. Abundant distribution of TARP gamma-8 in synaptic and extrasynaptic surface of hippocampal neurons and its major role in AMPA receptor expression on spines and dendrites. *Eur J Neurosci* **24**, 2177-2190 (2006).
262. Inamura, M. et al. Differential localization and regulation of stargazin-like protein, gamma-8 and stargazin in the plasma membrane of hippocampal and cortical neurons. *Neurosci Res* **55**, 45-53 (2006).
263. Khodosevich, K. et al. Coexpressed auxiliary subunits exhibit distinct modulatory profiles on AMPA receptor function. *Neuron* **83**, 601-615 (2014).
264. Park, J. et al. CaMKII Phosphorylation of TARPgamma-8 Is a Mediator of LTP and Learning and Memory. *Neuron* **92**, 75-83 (2016).
265. Itakura, M., Watanabe, I., Sugaya, T. & Takahashi, M. Direct association of the unique C-terminal tail of transmembrane AMPA receptor regulatory protein gamma-8 with calcineurin. *FEBS J* **281**, 1366-1378 (2014).
266. Sumioka, A. et al. PDZ binding of TARPgamma-8 controls synaptic transmission but not synaptic plasticity. *Nat Neurosci* **14**, 1410-1412 (2011).
267. Sheng, N. et al. LTP requires postsynaptic PDZ-domain interactions with glutamate receptor/auxiliary protein complexes. *Proc Natl Acad Sci U S A* **115**, 3948-3953 (2018).
268. Mauric, V. et al. Ontogeny repeats the phylogenetic recruitment of the cargo exporter cornichon into AMPA receptor signaling complexes. *Mol Cell Neurosci* **56**, 10-17 (2013).
269. Shanks, N.F. et al. Molecular dissection of the interaction between the AMPA receptor and cornichon homolog-3. *J Neurosci* **34**, 12104-12120 (2014).
270. Gill, M.B. et al. Cornichon-2 modulates AMPA receptor-transmembrane AMPA receptor regulatory protein assembly to dictate gating and pharmacology. *J Neurosci* **31**, 6928-6938 (2011).
271. Gill, M.B., Kato, A.S., Wang, H. & Bredt, D.S. AMPA receptor modulation by cornichon-2 dictated by transmembrane AMPA receptor regulatory protein isoform. *Eur J Neurosci* **35**, 182-194 (2012).
272. Boudkkazi, S., Brechet, A., Schwenk, J. & Fakler, B. Cornichon2 dictates the time course of excitatory transmission at individual hippocampal synapses. *Neuron* **82**, 848-858 (2014).

273. Troyano-Rodriguez, E., Mann, S., Ullah, R. & Ahmad, M. PRRT1 regulates basal and plasticity-induced AMPA receptor trafficking. *Mol Cell Neurosci* **98**, 155-163 (2019).
274. Martin, E.E., Wleklinski, E., Hoang, H.T.M. & Ahmad, M. Interaction and Subcellular Association of PRRT1/SynDIG4 With AMPA Receptors. *Front Synaptic Neurosci* **13**, 705664 (2021).
275. Ehlers, M.D. Reinsertion or degradation of AMPA receptors determined by activity-dependent endocytic sorting. *Neuron* **28**, 511-525 (2000).
276. Man, H.Y., Sekine-Aizawa, Y. & Huganir, R.L. Regulation of {alpha}-amino-3-hydroxy-5-methyl-4-isoxazolepropionic acid receptor trafficking through PKA phosphorylation of the Glu receptor 1 subunit. *Proc Natl Acad Sci U S A* **104**, 3579-3584 (2007).
277. He, K. et al. Stabilization of Ca2+-permeable AMPA receptors at perisynaptic sites by GluR1-S845 phosphorylation. *Proc Natl Acad Sci U S A* **106**, 20033-20038 (2009).
278. Oh, M.C., Derkach, V.A., Guire, E.S. & Soderling, T.R. Extrasynaptic membrane trafficking regulated by GluR1 serine 845 phosphorylation primes AMPA receptors for long-term potentiation. *J Biol Chem* **281**, 752-758 (2006).
279. Esteban, J.A. et al. PKA phosphorylation of AMPA receptor subunits controls synaptic trafficking underlying plasticity. *Nat Neurosci* **6**, 136-143 (2003).
280. Romberg, C. et al. Induction and expression of GluA1 (GluR-A)-independent LTP in the hippocampus. *Eur J Neurosci* **29**, 1141-1152 (2009).
281. Sanderson, J.L., Gorski, J.A. & Dell'Acqua, M.L. NMDA Receptor-Dependent LTD Requires Transient Synaptic Incorporation of Ca(2)(+)-Permeable AMPARs Mediated by AKAP150-Anchored PKA and Calcineurin. *Neuron* **89**, 1000-1015 (2016).
282. Menuz, K., Kerchner, G.A., O'Brien, J.L. & Nicoll, R.A. Critical role for TARPs in early development despite broad functional redundancy. *Neuropharmacology* **56**, 22-29 (2009).
283. Ferrario, C.R., Loweth, J.A., Milovanovic, M., Wang, X. & Wolf, M.E. Distribution of AMPA receptor subunits and TARPs in synaptic and extrasynaptic membranes of the adult rat nucleus accumbens. *Neurosci Lett* **490**, 180-184 (2011).
284. Lein, E.S. et al. Genome-wide atlas of gene expression in the adult mouse brain. *Nature* **445**, 168-176 (2007).
285. Kamalova, A., Futai, K., Delpire, E. & Nakagawa, T. AMPA Receptor Auxiliary Subunit GSG1L Suppresses Short-Term Facilitation in Corticothalamic Synapses and Determines Seizure Susceptibility. *Cell Rep* **32**, 107921 (2020).
286. Mao, X., Gu, X. & Lu, W. GSG1L regulates the strength of AMPA receptor-mediated synaptic transmission but not AMPA receptor kinetics in hippocampal dentate granule neurons. *J Neurophysiol* **117**, 28-35 (2017).
287. Nelson, A.J.D. The anterior thalamic nuclei and cognition: A role beyond space? *Neurosci Biobehav Rev* **126**, 1-11 (2021).
288. Bubb, E.J., Kinnavane, L. & Aggleton, J.P. Hippocampal - diencephalic - cingulate networks for memory and emotion: An anatomical guide. *Brain Neurosci Adv* **1** (2017).
289. Wolff, M. & Vann, S.D. The Cognitive Thalamus as a Gateway to Mental Representations. *J Neurosci* **39**, 3-14 (2019).
290. von Engelhardt, J. et al. CKAMP44: a brain-specific protein attenuating short-term synaptic plasticity in the dentate gyrus. *Science* **327**, 1518-1522 (2010).
291. Farrow, P. et al. Auxiliary subunits of the CKAMP family differentially modulate AMPA receptor properties. *Elife* **4**, e09693 (2015).
292. Pei, J. & Grishin, N.V. Unexpected diversity in Shisa-like proteins suggests the importance of their roles as transmembrane adaptors. *Cell Signal* **24**, 758-769 (2012).
293. Abdollahi Nejat, M., Klaassen, R.V., Spijker, S. & Smit, A.B. Auxiliary subunits of the AMPA receptor: The Shisa family of proteins. *Curr Opin Pharmacol* **58**, 52-61 (2021).
294. von Engelhardt, J. AMPA Receptor Auxiliary Proteins of the CKAMP Family. *Int J Mol Sci* **20** (2019).
295. Klaassen, R.V. et al. Shisa6 traps AMPA receptors at postsynaptic sites and prevents their desensitization during synaptic activity. *Nat Commun* **7**, 10682 (2016).
296. Schmitz, L.J.M. et al. The AMPA receptor-associated protein Shisa7 regulates hippocampal synaptic function and contextual memory. *Elife* **6** (2017).
297. Karataeva, A.R. et al. C-terminal interactors of the AMPA receptor auxiliary subunit Shisa9. *PLoS One* **9**, e87360 (2014).

298. Harb, A. et al. Auxiliary Subunits Regulate the Dendritic Turnover of AMPA Receptors in Mouse Hippocampal Neurons. *Front Mol Neurosci* **14**, 728498 (2021).
299. Kunde, S.A., Rademacher, N., Zieger, H. & Shoichet, S.A. Protein kinase C regulates AMPA receptor auxiliary protein Shisa9/CKAMP44 through interactions with neuronal scaffold PICK1. *FEBS Open Bio* **7**, 1234-1245 (2017).
300. Pick, J.E. & Ziff, E.B. Regulation of AMPA receptor trafficking and exit from the endoplasmic reticulum. *Mol Cell Neurosci* **91**, 3-9 (2018).
301. Peter, S. et al. AMPAR Auxiliary Protein SHISA6 Facilitates Purkinje Cell Synaptic Excitability and Procedural Memory Formation. *Cell Rep* **31**, 107515 (2020).
302. Han, W. et al. Shisa7 is a GABAA receptor auxiliary subunit controlling benzodiazepine actions. *Science* **366**, 246-250 (2019).
303. Wu, K., Han, W., Tian, Q., Li, Y. & Lu, W. Activity- and sleep-dependent regulation of tonic inhibition by Shisa7. *Cell Rep* **34**, 108899 (2021).
304. Kato, A.S. et al. New transmembrane AMPA receptor regulatory protein isoform, gamma-7, differentially regulates AMPA receptors. *J Neurosci* **27**, 4969-4977 (2007).
305. Kato, A.S., Siuda, E.R., Nisenbaum, E.S. & Bredt, D.S. AMPA receptor subunit-specific regulation by a distinct family of type II TARPs. *Neuron* **59**, 986-996 (2008).
306. Yamazaki, M. et al. TARPs gamma-2 and gamma-7 are essential for AMPA receptor expression in the cerebellum. *Eur J Neurosci* **31**, 2204-2220 (2010).
307. Yamazaki, M. et al. Relative contribution of TARPs gamma-2 and gamma-7 to cerebellar excitatory synaptic transmission and motor behavior. *Proc Natl Acad Sci U S A* **112**, E371-379 (2015).
308. Studniarczyk, D., Coombs, I., Cull-Candy, S.G. & Farrant, M. TARP gamma-7 selectively enhances synaptic expression of calcium-permeable AMPARs. *Nat Neurosci* **16**, 1266-1274 (2013).
309. Bats, C., Soto, D., Studniarczyk, D., Farrant, M. & Cull-Candy, S.G. Channel properties reveal differential expression of TARPed and TARPless AMPARs in stargazer neurons. *Nat Neurosci* **15**, 853-861 (2012).
310. Chen, L., Bao, S., Qiao, X. & Thompson, R.F. Impaired cerebellar synapse maturation in waggler, a mutant mouse with a disrupted neuronal calcium channel gamma subunit. *Proc Natl Acad Sci U S A* **96**, 12132-12137 (1999).
311. Sun, J.H. et al. X-linked neonatal-onset epileptic encephalopathy associated with a gain-of-function variant p.R660T in GRIA3. *PLoS Genet* **17**, e1009608 (2021).
312. Perestenko, P.V. & Henley, J.M. Characterization of the intracellular transport of GluR1 and GluR2 alpha-amino-3-hydroxy-5-methyl-4-isoxazole propionic acid receptor subunits in hippocampal neurons. *J Biol Chem* **278**, 43525-43532 (2003).
313. Kaech, S. & Banker, G. Culturing hippocampal neurons. *Nat Protoc* **1**, 2406-2415 (2006).
314. Sheridan, D.L., Robert, A., Cho, C.H., Howe, J.R. & Hughes, T.E. Regions of alpha-amino-5-methyl-3-hydroxy-4-isoxazole propionic acid receptor subunits that are permissive for the insertion of green fluorescent protein. *Neuroscience* **141**, 837-849 (2006).
315. Costantini, L.M. & Snapp, E.L. Fluorescent proteins in cellular organelles: serious pitfalls and some solutions. *DNA Cell Biol* **32**, 622-627 (2013).
316. Pedelacq, J.D., Cabantous, S., Tran, T., Terwilliger, T.C. & Waldo, G.S. Engineering and characterization of a superfolder green fluorescent protein. *Nat Biotechnol* **24**, 79-88 (2006).
317. Aronson, D.E., Costantini, L.M. & Snapp, E.L. Superfolder GFP is fluorescent in oxidizing environments when targeted via the Sec translocon. *Traffic* **12**, 543-548 (2011).
318. Bindels, D.S. et al. mScarlet: a bright monomeric red fluorescent protein for cellular imaging. *Nat Methods* **14**, 53-56 (2017).
319. Lambert, T.J. FPbase: a community-editable fluorescent protein database. *Nat Methods* **16**, 277-278 (2019).
320. Uhlen, M. et al. A pathology atlas of the human cancer transcriptome. *Science* **357** (2017).
321. Rivera, V.M. et al. Regulation of protein secretion through controlled aggregation in the endoplasmic reticulum. *Science* **287**, 826-830 (2000).
322. Hangen, E., Cordelieres, F.P., Petersen, J.D., Choquet, D. & Coussen, F. Neuronal Activity and Intracellular Calcium Levels Regulate Intracellular Transport of Newly Synthesized AMPAR. *Cell Rep* **24**, 1001-1012 e1003 (2018).
323. Denault, J.B. & Leduc, R. Furin/PACE/SPC1: a convertase involved in exocytic and endocytic processing of precursor proteins. *FEBS Lett* **379**, 113-116 (1996).

324. Hussey, A.M. & Chambers, J.J. Methods to locate and track ion channels and receptors expressed in live neurons. *ACS Chem Neurosci* **6**, 189-198 (2015).
325. Sigal, Y.M., Zhou, R. & Zhuang, X. Visualizing and discovering cellular structures with super-resolution microscopy. *Science* **361**, 880-887 (2018).
326. Sauer, M. Localization microscopy coming of age: from concepts to biological impact. *J Cell Sci* **126**, 3505-3513 (2013).
327. Sauer, M. & Heilemann, M. Single-Molecule Localization Microscopy in Eukaryotes. *Chem Rev* **117**, 7478-7509 (2017).
328. Osten, P. & Stern-Bach, Y. Learning from stargazin: the mouse, the phenotype and the unexpected. *Curr Opin Neurobiol* **16**, 275-280 (2006).
329. Schnell, E. et al. Direct interactions between PSD-95 and stargazin control synaptic AMPA receptor number. *Proc Natl Acad Sci U S A* **99**, 13902-13907. (2002).
330. Choquet, D. & Hosy, E. AMPA receptor nanoscale dynamic organization and synaptic plasticities. *Curr Opin Neurobiol* **63**, 137-145 (2020).
331. Chen, L. et al. Stargazin regulates synaptic targeting of AMPA receptors by two distinct mechanisms. *Nature* **408**, 936-943. (2000).
332. Zhao, Y., Chen, S., Yoshioka, C., Baconguis, I. & Gouaux, E. Architecture of fully occupied GluA2 AMPA receptor-TARP complex elucidated by cryo-EM. *Nature* (2016).
333. Yu, J. et al. Hippocampal AMPA receptor assemblies and mechanism of allosteric inhibition. *Nature* **594**, 448-453 (2021).
334. Turetsky, D., Garringer, E. & Patneau, D.K. Stargazin modulates native AMPA receptor functional properties by two distinct mechanisms. *J Neurosci* **25**, 7438-7448 (2005).
335. Tomita, S. et al. Stargazin modulates AMPA receptor gating and trafficking by distinct domains. *Nature* **435**, 1052-1058 (2005).
336. Chamma, I. et al. Mapping the dynamics and nanoscale organization of synaptic adhesion proteins using monomeric streptavidin. *Nature Communications* **7** (2016).
337. Liu, C.C. & Schultz, P.G. Adding new chemistries to the genetic code. *Annu Rev Biochem* **79**, 413-444 (2010).
338. Chin, J.W. Expanding and reprogramming the genetic code of cells and animals. *Annu Rev Biochem* **83**, 379-408 (2014).
339. Nikic, I., Kang, J.H., Girona, G.E., Aramburu, I.V. & Lemke, E.A. Labeling proteins on live mammalian cells using click chemistry. *Nature protocols* **10**, 780-791 (2015).
340. Beliu, G. et al. Bioorthogonal labeling with tetrazine-dyes for super-resolution microscopy. *Communications biology* **2**, 261 (2019).
341. Ernst, R.J. et al. Genetic code expansion in the mouse brain. *Nat Chem Biol* **12**, 776-778 (2016).
342. Neubert, F. et al. Bioorthogonal Click Chemistry Enables Site-specific Fluorescence Labeling of Functional NMDA Receptors for Super-Resolution Imaging. *Angew Chem Int Ed Engl* **57**, 16364-16369 (2018).
343. Plass, T., Milles, S., Koehler, C., Schultz, C. & Lemke, E.A. Genetically encoded copper-free click chemistry. *Angew Chem Int Ed Engl* **50**, 3878-3881 (2011).
344. Serfling, R. et al. Designer tRNAs for efficient incorporation of non-canonical amino acids by the pyrrolysine system in mammalian cells. *Nucleic Acids Res* **46**, 1-10 (2018).
345. Blackman, M.L., Royzen, M. & Fox, J.M. Tetrazine ligation: fast bioconjugation based on inverse-electron-demand Diels-Alder reactivity. *J Am Chem Soc* **130**, 13518-13519 (2008).
346. Yasuda, R. Imaging spatiotemporal dynamics of neuronal signaling using fluorescence resonance energy transfer and fluorescence lifetime imaging microscopy. *Curr Opin Neurobiol* **16**, 551-561 (2006).
347. Soto, D., Coombs, I.D., Kelly, L., Farrant, M. & Cull-Candy, S.G. Stargazin attenuates intracellular polyamine block of calcium-permeable AMPA receptors. *Nat Neurosci* **10**, 1260-1267 (2007).
348. Jackson, A.C. et al. Probing TARP modulation of AMPA receptor conductance with polyamine toxins. *J Neurosci* **31**, 7511-7520 (2011).
349. Shanks, N.F., Maruo, T., Farina, A.N., Ellisman, M.H. & Nakagawa, T. Contribution of the global subunit structure and stargazin on the maturation of AMPA receptors. *J Neurosci* **30**, 2728-2740 (2010).
350. Rimbault, C. et al. Engineering selective competitors for the discrimination of highly conserved protein-protein interaction modules. *Nature Communications* **10** (2019).
351. Rimbault, C. et al. Engineering paralog-specific PSD-95 synthetic binders as potent and minimally invasive imaging probes. *bioRxiv*, 2021.2004.2007.438431 (2021).

352. Heilemann, M. et al. Subdiffraction-resolution fluorescence imaging with conventional fluorescent probes. *Angew Chem Int Ed Engl* **47**, 6172-6176 (2008).
353. van de Linde, S. et al. Direct stochastic optical reconstruction microscopy with standard fluorescent probes. *Nat Protoc* **6**, 991-1009 (2011).
354. Nikic-Spiegel, I. Expanding the Genetic Code for Neuronal Studies. *Chembiochem* **21**, 3169-3179 (2020).
355. Beliu, G. et al. Tethered agonist exposure in intact adhesion/class B2 GPCRs through intrinsic structural flexibility of the GAIN domain. *Mol Cell* **81**, 905-921 e905 (2021).
356. Oliveira, B.L., Guo, Z. & Bernardes, G.J.L. Inverse electron demand Diels-Alder reactions in chemical biology. *Chem Soc Rev* **46**, 4895-4950 (2017).
357. Karver, M.R., Weissleder, R. & Hilderbrand, S.A. Synthesis and evaluation of a series of 1,2,4,5-tetrazines for bioorthogonal conjugation. *Bioconjug Chem* **22**, 2263-2270 (2011).
358. Lajoie, M.J. et al. Genomically recoded organisms expand biological functions. *Science* **342**, 357-360 (2013).
359. Rackham, O. & Chin, J.W. A network of orthogonal ribosome x mRNA pairs. *Nat Chem Biol* **1**, 159-166 (2005).
360. Wang, K., Neumann, H., Peak-Chew, S.Y. & Chin, J.W. Evolved orthogonal ribosomes enhance the efficiency of synthetic genetic code expansion. *Nat Biotechnol* **25**, 770-777 (2007).
361. Neumann, H., Wang, K., Davis, L., Garcia-Alai, M. & Chin, J.W. Encoding multiple unnatural amino acids via evolution of a quadruplet-decoding ribosome. *Nature* **464**, 441-444 (2010).
362. Arsić, A., Hagemann, C., Stajković, N., Schubert, T. & Nikić-Spiegel, I. Minimal genetically encoded tags for fluorescent protein labeling in living neurons. *bioRxiv*, 2021.2001.2014.426692 (2021).
363. Nikic, I. et al. Minimal tags for rapid dual-color live-cell labeling and super-resolution microscopy. *Angew Chem Int Ed Engl* **53**, 2245-2249 (2014).
364. Meineke, B., Heimgartner, J., Eirich, J., Landreh, M. & Elsasser, S.J. Site-Specific Incorporation of Two ncAAs for Two-Color Bioorthogonal Labeling and Crosslinking of Proteins on Live Mammalian Cells. *Cell Rep* **31**, 107811 (2020).
365. Nikic, I. et al. Debugging Eukaryotic Genetic Code Expansion for Site-Specific Click-PAINT Super-Resolution Microscopy. *Angew Chem Int Ed Engl* **55**, 16172-16176 (2016).
366. Stoppini, L., Buchs, P.A. & Muller, D. A simple method for organotypic cultures of nervous tissue. *J Neurosci Methods* **37**, 173-182 (1991).
367. Wolter, S. et al. rapidSTORM: accurate, fast open-source software for localization microscopy. *Nat Methods* **9**, 1040-1041 (2012).
368. Kiskowski, M.A., Hancock, J.F. & Kenworthy, A.K. On the use of Ripley's K-function and its derivatives to analyze domain size. *Biophys J* **97**, 1095-1103 (2009).
369. Dixon, P.M. in Encyclopedia of Environmetrics (2001).
370. Yao, G. et al. Crystal structure of the glutamate receptor GluA1 N-terminal domain. *Biochem J* **438**, 255-263 (2011).
371. Selvin, P.R. Fluorescence resonance energy transfer. *Methods Enzymol* **246**, 300-334 (1995).
372. Schagger, H., Cramer, W.A. & von Jagow, G. Analysis of molecular masses and oligomeric states of protein complexes by blue native electrophoresis and isolation of membrane protein complexes by two-dimensional native electrophoresis. *Anal Biochem* **217**, 220-230 (1994).
373. Schagger, H. & von Jagow, G. Blue native electrophoresis for isolation of membrane protein complexes in enzymatically active form. *Anal Biochem* **199**, 223-231 (1991).
374. Pfeiffer, K. et al. Cardiolipin stabilizes respiratory chain supercomplexes. *J Biol Chem* **278**, 52873-52880 (2003).
375. Eubel, H., Braun, H.P. & Millar, A.H. Blue-native PAGE in plants: a tool in analysis of protein-protein interactions. *Plant Methods* **1**, 11 (2005).
376. Wittig, I. & Schagger, H. Advantages and limitations of clear-native PAGE. *Proteomics* **5**, 4338-4346 (2005).
377. Vogel, S.S., Thaler, C. & Koushik, S.V. Fanciful FRET. *Sci STKE* **2006**, re2 (2006).
378. Fung, B.K. & Stryer, L. Surface density determination in membranes by fluorescence energy transfer. *Biochemistry* **17**, 5241-5248 (1978).
379. Gossen, M. & Bujard, H. Tight control of gene expression in mammalian cells by tetracycline-responsive promoters. *Proc Natl Acad Sci U S A* **89**, 5547-5551 (1992).
380. Wang, Y., O'Malley, B.W., Jr., Tsai, S.Y. & O'Malley, B.W. A regulatory system for use in gene transfer. *Proc Natl Acad Sci U S A* **91**, 8180-8184 (1994).

381. No, D., Yao, T.P. & Evans, R.M. Ecdysone-inducible gene expression in mammalian cells and transgenic mice. *Proc Natl Acad Sci U S A* **93**, 3346-3351 (1996).
382. Rivera, V.M. et al. A humanized system for pharmacologic control of gene expression. *Nat Med* **2**, 1028-1032 (1996).
383. Boncompain, G. et al. Synchronization of secretory protein traffic in populations of cells. *Nat Methods* **9**, 493-498 (2012).
384. Wang, H. et al. LOVTRAP: an optogenetic system for photoinduced protein dissociation. *Nat Methods* **13**, 755-758 (2016).
385. Yang, X., Jost, A.P., Weiner, O.D. & Tang, C. A light-inducible organelle-targeting system for dynamically activating and inactivating signaling in budding yeast. *Mol Biol Cell* **24**, 2419-2430 (2013).
386. Kichuk, T.C., Carrasco-Lopez, C. & Avalos, J.L. Lights up on organelles: Optogenetic tools to control subcellular structure and organization. *Wiley Interdiscip Rev Syst Biol Med* **13**, e1500 (2021).
387. Ahmed, A., Schoberer, J., Cooke, E. & Botchway, S.W. Multicolor FRET-FLIM Microscopy to Analyze Multiprotein Interactions in Live Cells. *Methods Mol Biol* **2247**, 287-301 (2021).
388. Hoppe, A.D., Scott, B.L., Welliver, T.P., Straight, S.W. & Swanson, J.A. N-way FRET microscopy of multiple protein-protein interactions in live cells. *PLoS One* **8**, e64760 (2013).
389. Roy, R., Hohng, S. & Ha, T. A practical guide to single-molecule FRET. *Nat Methods* **5**, 507-516 (2008).
390. Ha, T. et al. Probing the interaction between two single molecules: fluorescence resonance energy transfer between a single donor and a single acceptor. *Proc Natl Acad Sci U S A* **93**, 6264-6268 (1996).
391. Lerner, E. et al. Toward dynamic structural biology: Two decades of single-molecule Forster resonance energy transfer. *Science* **359** (2018).
392. Hohng, S., Joo, C. & Ha, T. Single-molecule three-color FRET. *Biophys J* **87**, 1328-1337 (2004).
393. Person, B., Stein, I.H., Steinhauer, C., Vogelsang, J. & Tinnefeld, P. Correlated movement and bending of nucleic acid structures visualized by multicolor single-molecule spectroscopy. *Chemphyschem* **10**, 1455-1460 (2009).
394. Asher, W.B. et al. Single-molecule FRET imaging of GPCR dimers in living cells. *Nat Methods* **18**, 397-405 (2021).
395. Nikic, I. & Lemke, E.A. Genetic code expansion enabled site-specific dual-color protein labeling: superresolution microscopy and beyond. *Curr Opin Chem Biol* **28**, 164-173 (2015).
396. Stern-Bach, Y., Russo, S., Neuman, M. & Rosenmund, C. A point mutation in the glutamate binding site blocks desensitization of AMPA receptors. *Neuron* **21**, 907-918 (1998).
397. Sun, Y. et al. Mechanism of glutamate receptor desensitization. *Nature* **417**, 245-253 (2002).
398. Robert, A., Armstrong, N., Gouaux, J.E. & Howe, J.R. AMPA receptor binding cleft mutations that alter affinity, efficacy, and recovery from desensitization. *J Neurosci* **25**, 3752-3762 (2005).
399. Armstrong, N., Jasti, J., Beich-Frandsen, M. & Gouaux, E. Measurement of conformational changes accompanying desensitization in an ionotropic glutamate receptor. *Cell* **127**, 85-97 (2006).
400. Plested, A.J. & Mayer, M.L. AMPA receptor ligand binding domain mobility revealed by functional cross linking. *J Neurosci* **29**, 11912-11923 (2009).
401. Harel, M. et al. The binding site of acetylcholine receptor as visualized in the X-Ray structure of a complex between alpha-bungarotoxin and a mimotope peptide. *Neuron* **32**, 265-275 (2001).
402. Lin, J.W. et al. Distinct molecular mechanisms and divergent endocytotic pathways of AMPA receptor internalization. *Nat Neurosci* **3**, 1282-1290 (2000).
403. Chamma, I. et al. Mapping the dynamics and nanoscale organization of synaptic adhesion proteins using monomeric streptavidin. *Nat Commun* **7**, 10773 (2016).
404. Grimm, J.B. et al. Bright photoactivatable fluorophores for single-molecule imaging. *Nat Methods* **13**, 985-988 (2016).
405. Uno, S.N. et al. A spontaneously blinking fluorophore based on intramolecular spirocyclization for live-cell super-resolution imaging. *Nat Chem* **6**, 681-689 (2014).
406. Chen, B.C. et al. Lattice light-sheet microscopy: imaging molecules to embryos at high spatiotemporal resolution. *Science* **346**, 1257998 (2014).
407. Elbashir, S.M. et al. Duplexes of 21-nucleotide RNAs mediate RNA interference in cultured mammalian cells. *Nature* **411**, 494-498 (2001).
408. Hammond, S.M., Bernstein, E., Beach, D. & Hannon, G.J. An RNA-directed nuclease mediates post-transcriptional gene silencing in Drosophila cells. *Nature* **404**, 293-296 (2000).
409. Caplen, N.J., Fleenor, J., Fire, A. & Morgan, R.A. dsRNA-mediated gene silencing in cultured Drosophila cells: a tissue culture model for the analysis of RNA interference. *Gene* **252**, 95-105 (2000).

410. Brummelkamp, T.R., Bernards, R. & Agami, R. A system for stable expression of short interfering RNAs in mammalian cells. *Science* **296**, 550-553 (2002).
411. Paddison, P.J., Caudy, A.A., Bernstein, E., Hannon, G.J. & Conklin, D.S. Short hairpin RNAs (shRNAs) induce sequence-specific silencing in mammalian cells. *Genes Dev* **16**, 948-958 (2002).
412. Ozkan, J. Jennifer A. Doudna and Emmanuelle Charpentier. *Eur Heart J* **42**, 2143-2145 (2021).
413. Willems, J. et al. ORANGE: A CRISPR/Cas9-based genome editing toolbox for epitope tagging of endogenous proteins in neurons. *PLoS Biol* **18**, e3000665 (2020).
414. Suzuki, K. et al. In vivo genome editing via CRISPR/Cas9 mediated homology-independent targeted integration. *Nature* **540**, 144-149 (2016).
415. Fang, H., Bygrave, A.M., Roth, R.H., Johnson, R.C. & Huganir, R.L. An optimized CRISPR/Cas9 approach for precise genome editing in neurons. *Elife* **10** (2021).
416. Gao, Y. et al. Plug-and-Play Protein Modification Using Homology-Independent Universal Genome Engineering. *Neuron* **103**, 583-597 e588 (2019).
417. Schmied, W.H., Elsasser, S.J., Uttamapinant, C. & Chin, J.W. Efficient multisite unnatural amino acid incorporation in mammalian cells via optimized pyrrolysyl tRNA synthetase/tRNA expression and engineered eRF1. *J Am Chem Soc* **136**, 15577-15583 (2014).